PLASMA ENHANCED CHEMICAL VAPOUR DEPOSITION OF SILICA THIN FILMS

A thesis submitted to The University of Manchester for the degree of

Chemical Engineering

in the Faculty of Engineering and Physical Sciences

2010

DAVID ARTHUR GREGORY SAWTELL

THE SCHOOL OF CHEMICAL ENGINEERING AND ANALYTICAL SCIENCE

Contents

The total word count of this thesis is 73322 words.

List of Figures

List of Tables

Abstract

Atmospheric pressure chemical vapour deposition is an industrially significant process for forming functional thin films. There is a great opportunity for increased scientific understanding with the aim of improving current processes and helping to formulate new ones. This work is concerned with developing a methodology to assist this ongoing concern. A combination of spectroscopic and chemometric techniques are used to investigate several chemical vapour deposition processes.

The first investigation concerns the spatial concentration mapping of key by-products during the thermal chemical vapour deposition of tin oxide films through the use of near infra red laser diode spectroscopy. This novel two dimensional characterisation of the process has identified reaction hotspots within the process, and has identified the redundancy of part of the exhaust mechanism. Subsequently, there has been improvements to the head design, and the operation of the process.

The main thrust of the investigations are focussed towards the use of chemometric methods, such as experimental design and principal components analysis, in conjunction with a suite of spectroscopic measurement techniques, to analyse the plasma enhanced chemical vapour deposition of silica films. This work has shown the importance of active oxygen species on the chemistry. It has also been shown that the film properties are highly dependant on oxygen concentration in the reactor, and hence active oxygen species forming in the plasma. The identification of by-products in the silica deposition process has also been carried out for the first time. Finally, this work also presents the first rigorous studies of a new precursor for silica deposition, dichlorodimethylsilane.

Declaration

No portion of the work referred to in the thesis has been submitted in support of an application for another degree or qualification of this or any other university or other institute of learning.

Copyright

1. The author of this thesis (including any appendices and/or schedules to this thesis) owns any copyright in it (the Copyright) and he has given The University of Manchester the right to use such Copyright for any administrative, promotional, educational and/or teaching purposes.

2. Copies of this thesis, either in full or in extracts, may be made only in accordance with the regulations of the John Rylands University Library of Manchester. Details of these regulations may be obtained from the Librarian. This page must form part of any such copies made.

3. The ownership of any patents, designs, trade marks and any and all other intellectual property rights except for the Copyright (the Intellectual Property Rights) and any reproductions of copyright works, for example graphs and tables (Reproductions), which may be described in this thesis, may not be owned by the author and may be owned by third parties. Such Intellectual Property Rights and Reproductions cannot and must not be made available for use without the prior written permission of the owner(s) of the relevant Intellectual Property Rights and/or Reproductions.

4. Further information on the conditions under which disclosure, publication and exploitation of this thesis, the Copyright and any Intellectual Property Rights and/or Reproductions described in it may take place is available from the Head of School of (insert name of school) (or the Vice-President) and the Dean of the Faculty of Life Sciences, for Faculty of Life Sciences candidates.

Acknowledgements

Many thanks go to my supervisors Dr Philip Martin and Professor David Sheel for both the opportunity to carry out this work, and the help that they have provided. Both supervisors have provided a wealth of ideas and support over the past four years, and without them this thesis and the work it presents would not have come to fruition.

The author would like to thank Andrew Campen and John Riley for their invaluable help in the experimental work carried out for this report. Special thanks must also got to Andrew for numerous readthroughs and discussions about theory. Thanks must also go to Zaenab Abd Allah for the many work related discussions and help she has provided. Raja Ibrahim has also been a great source of knowledge concerning lasers. Robert Holdsworth and Vasili Kasyutich have also provided assistance with laser spectroscopy, both practical and theoretical. The students in C19 have provided much assistance with all things physics related, in particular Marcus Campbell Bannerman, Ben Embley, James Magee and Rafal Zatera. Gary Burns, Loris Doyle, Roy Kershaw, Paul Rothwell and Eric Wigget have all provided much appreciated assistance with the setting up of equipment. Also thanks must go to those who have helped me at Salford University, most notably Mathieu Delmas, Jeff Gaskell, John Hodgkinson, David Massey and Gerry Murray.

Thank you to the EPSRC, TDL Sensors and CVD Technologies who all provided funding for the project.

And finally much love and gratitude to my Parents, who have always provided me with support and inspiration.

Chapter 1

An introduction to thin film deposition processes

1.1 Introduction

The final goal of any good chemical vapour deposition process is the cost effective production of marketable, functional thin solid films, and as such, any studies carried out on the process should always be done with an eye to maximising profit. It is self evident from the long term use of the process over the course of decades that chemical vapour deposition has always had the potential to be a profitable one. As an established technology, research into this process should always have process optimisation or product development as one of its primary goals in order to enhance profitability.

Of primary importance in enhancement of the process, is the understanding of the science underpinning it. As is always the case with market driven technologies, the fundamental science of the production process gets overlooked. As such there are considerable areas of scientific interest that lie unexplored within the realm of chemical vapour deposition. As already stated, any investigations should be carried out with an eye towards opportunities for process optimisation and product optimisation.

Thin films

Thin films can vary in thickness from fractions of a nanometre to the order of several micrometres. The variety of functions of these thin films is vast, some of these are represented in figure 1.1. The best, most widely used, example of these thin films can perhaps

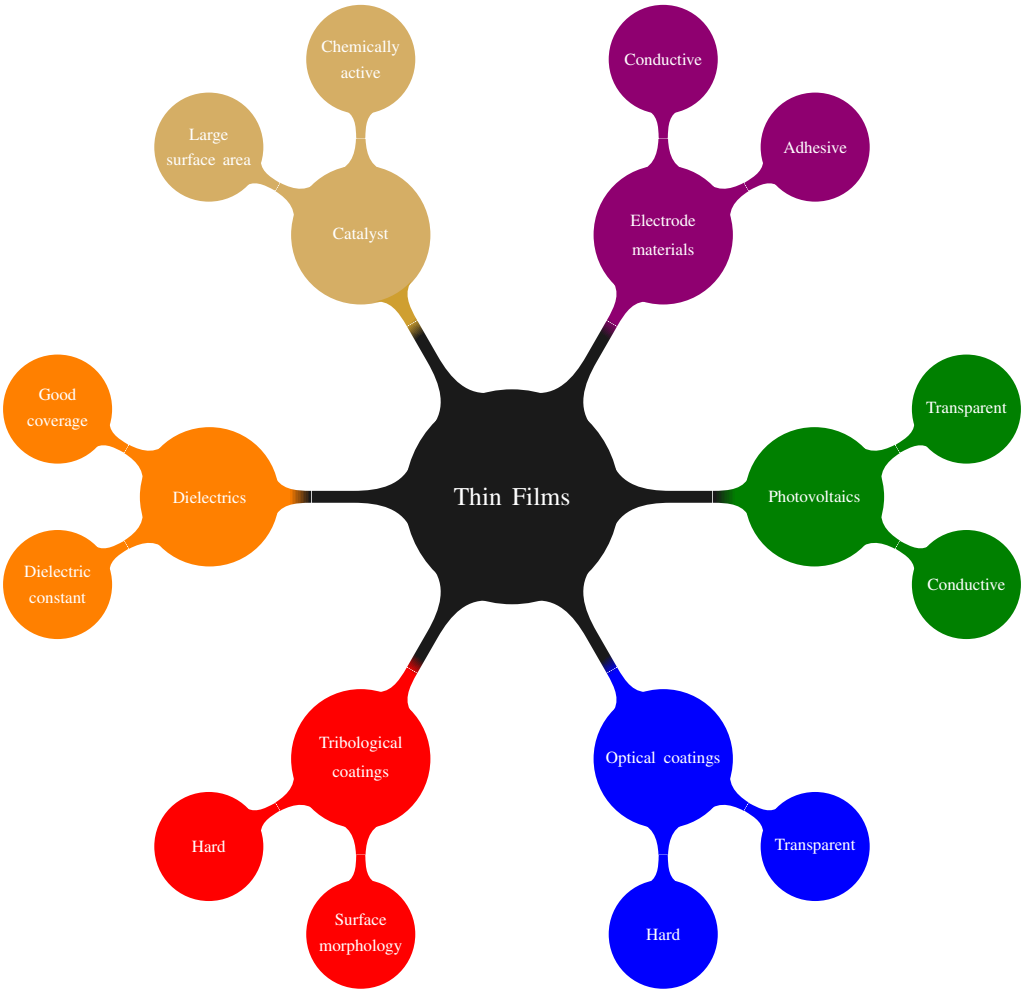

Figure 1.1: Range of thin film applications with important properties.

be found in the semiconductor industries. Several thin films are used in the production of microchips, from the semiconductor layers, to the dielectrics in between layers. It is safe to say that the microprocessor revolution relies on the production of these films.

There is a large market for optical coatings, and the properties required for these coatings covers a vast range. These range from hard, scratch proof coatings, to photochromic coatings that become semi-opaque in direct sunlight. The coatings are also used as a waveguide, and to produce reflective surfaces. The refractive index of such films is of great importance.

Transparent conductive oxides such as tin oxide, [5] are used in the manufacture of

solar panels. These films are both transparent to light, and allow a current to pass. They can also be used in situations where dissipation of electrostatic charge on the surface of glass is necessary, such as for flat panel televisions. Such films need to be both highly conductive and transparent to light. The surface morphology also plays a part, as incident light needs to be scattered onto lower layers of the solar panel.

Titanium dioxide, [9], [10], [11], is used by the glass industry as a self cleaning layer on the surface of glass. In the presence of ultraviolet light, titanium dioxide catalyses a cold combustion reaction of organics on the surface. This effect is limited to crystalline titanium dioxide.

Films made out of silver, [12], and copper have antibacterial properties, which have a variety of implications for the food and medical industries. The silver or copper tends to be toxic to bacteria, and so limits and destroys bacterial colony growth.

Silicon carbide, [13], and diamond-like carbon films can also provide a hard wear resistant layer, particularly on the surfaces of tools for example. These coatings are of great importance in the oil and gas industry, as drilling operations are getting ever more intensive. The key properties for such films are adherence and hardness.

There is a large market for tribological coatings for gears and tools. These are coatings that modify the friction of the surface in some manner, and so are important for a good grip of a tool on a surface. The surface morphology of such films is highly important, as is the adherence.

Corrosion protection coatings are another application of thin films. There are a variety of different properties required for corrosion protection that are application specific. However, the adherence and hardness of such films are highly important.

Thin films have seen use as battery electrodes. These films need to be conductive and

resistant to chemical corrosion.

Thin layers of catalytic material such as platinum are another product. Such materials require a high surface area to enduce catalytic reactions to occur.

1.2 Chemical Vapour Deposition

How is it possible to deposit a thin solid film using chemical vapour deposition? The process relies on a precursor molecule being transferred to a chemical vapour deposition reactor containing the substrate to be coated. This precursor is present in the vapour phase, hence chemical **vapour** deposition, [14]. This precursor is induced to react in the vapour phase, breaking down into intermediaries and by-products. The intermediaries can then diffuse towards the substrate, and are free to adsorb onto available sites on the surface of the substrate. The intermediaries can react and initiate the growth of the thin film. These surface reactions possibly involve reactions with other gas phase species, but can also be a simpler breakdown of the intermediary into the thin film species and by-products. Any by-product formed at the surface is then free to desorb. See figure 1.2 for an involved schematic of the process.

A typical film growth mechanism is where growth tends to occur at several nucleation sites over the surface of the substrate. Subsequent film growth occurs around these nucleation sites, with the film merging to cover the surface of the substrate. This process is commonly referred to as island growth. Layer by layer growth can also occur, whereby the film grows in layers across the surface of the substrate.

The combination of gas phase chemistry, mass transport and surface chemistry indicates that the average chemical vapour deposition process has a series of complicated reaction mechanisms. Coupling this with the fact that the process is, by it's nature, not

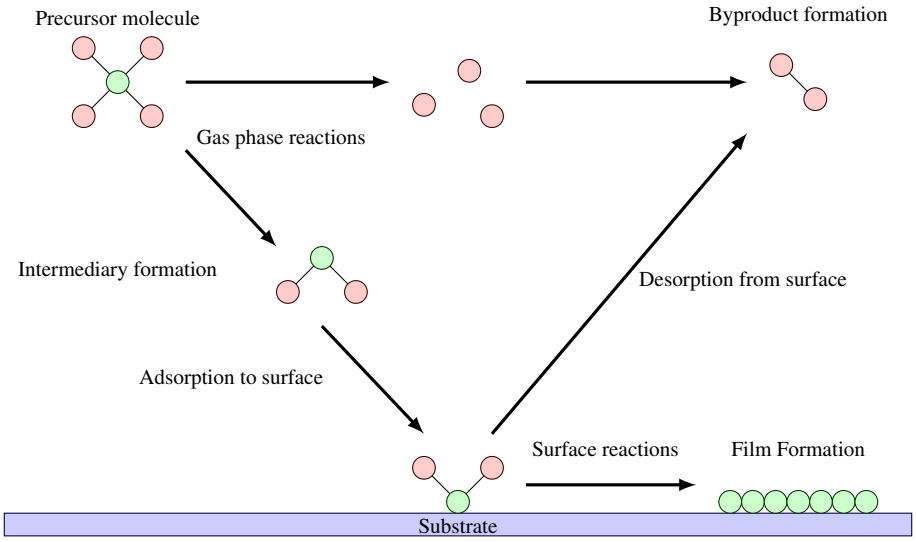

Figure 1.2: A generic chemical vapour deposition process.

a steady state process, makes the analysis of the fundamental chemistry of the process difficult. The usage of chemical species varies, and the nature of the surface reactions change, as the film grows. It is possible to simplify the process, depending on various factors. For example the gas phase reactions might be the slowest step within the reaction scheme, essentially meaning that we could ignore the other steps in a kinetic analysis of the process.

1.3 Atmospheric pressure chemical vapour deposition processes

The use of the process at atmospheric pressure has inherent advantages, notably the possibility of higher film growth rates, leading to higher processing rates. This has the key result of more product in a shorter amount of time, driving up productivity of the process. The removal of the need for expensive vacuum equipment should not be ignored either in assessing the viability of the process.

The advantages of low pressure chemical vapour deposition should perhaps be mentioned at this juncture. The primary advantage is the greater control of film growth and properties. This is due to the tighter control over the amount of precursor introduced to the process, and the reduced effects of flow patterns effecting the reaction zone. The choice of low pressure chemical vapour deposition, of course, is highly dependent on the intended aims of a given process, and for many applications, atmospheric pressure chemical vapour deposition is eminently suitable.

Atmospheric pressure chemical vapour deposition has a tendency to be limited by the gas phase reactions occuring, the mass transport and surface reactions being much slower in comparison.

There are a wide range of methods for initiating the chemical vapour deposition process at atmospheric pressure. No matter how novel a given technique may be, again it is always important to acknowledge the practical use of the technology in producing a profitable product. The differing methods are discussed here.

Thermal chemical vapour deposition

In thermal chemical vapour deposition gas phase reactions are initiated by high thermal temperatures. At atmospheric pressure, the substrate is located on some kind of heating plate, or heated by infrared heating lamps where it is usually heated to a temperature of 500 °C or greater. The process gas is passed in at a temperature high enough to stop the precursor condensing out prior to entry of the reactor chamber. The precursor reacts above the surface of the substrate, either thermally decomposing or reacting with some other process gas, to form the intermediaries for film growth. A range of the thin solid films produced by the thermal chemical vapour deposition process at atmospheric pressure are presented in table 1.1.

Coating	Precursor	References
Alumina (Al_2O_3)	Trimethylaluminium ($(CH_3)_3Al$)	[15]
Gold (Au)	Various dimethylgold(III) carboxylates	[16]
Tin oxide (SnO)	Trimethyltin ($(CH_3)_3Sn$)	[17]
Titanium dioxide (TiO_2)	Titanium tetraisopropoxide ($Ti_4(OCH_3)_{16}$) Titanium tetrachloride, ethyl acetate ($TiCl_4$), ($C_4H_8O_2$)	[18] [19]
Zinc selenide ($ZnSe$)	Dimethyl zinc, hydrogen selenide ($Zn(CH_3)_2$), (H_2Se)	[20]
Zinc sulphide (ZnS)	Dimethyl zinc, hydrogen sulphide ($Zn(CH_3)_2$), (H_2S)	[20]

Table 1.1: Thin films produced by thermal chemical vapour deposition at atmospheric pressure.

Thermal processes can be controlled by several of the reaction stages. At lower temperatures the gas phase chemistry is the limiting factor, with the formation of intermediaries diffusion to the surface being effectively instantaneous at the point of formation. As the temperature increases, there is a greater resistance to mass transfer, and diffusion is the slowest step in the overall reaction scheme. Of course the process depends on the chemistry involved in producing a film of a given substance, and the properties required.

Engineering problems arise due to the necessity of keeping the thermal heating homogeneous across the surface of the substrate so as to keep the film growth constant. In addition well mixed gas flows entering the reaction chamber or zone are of great importance for similar reasons.

Coating	Precursor	References
Alumina (Al_2O_3)	Aluminium acetylacetonate ($C_{15}H_{21}AlO_6$)	[22], [23]
Ceria (CeO_2)	Ce(III) 2-ethylhexanoate ($CeC_{16}H_{30}O_4$)	[24]
Copper (Cu)	Copper Nitrate ($Cu(NO_3)_2$)	[18]
Hydroxyapatite ($Ca_{10}(PO_4)_6(OH)_2$)	Calcium acetate, ammonium phosphate ($Ca(CH_3COO)_2$, $((NH_4)_2HPO_4)$	[25]
Molybdenum Oxide (MoO_3)	Ammonium molybdate ($(NH_4)_6Mo_7O_{24}$)	[26]
Silica (SiO_2)	Tetraethylorthosilicate ($SiC_8H_{20}O_4$)	[27]
Silver (Ag)	Silver Nitrate ($AgNO_3$)	[19]
Tantalum oxide (Ta_2O_5)	Tantalum ethoxide ($Ta(OC_2H_5)_5$)	[28]
Tin Oxide (SnO)	Tin(II)-2-ethylhexanoate ($SnC_{16}H_{30}O_4$)	[29]
Tungsten Oxide (WO_3)	Ammonium metatungstate ($(NH_4)_6H_2W_{12}O_{40}$)	[26]
Zinc Oxide (ZnO)	Zinc(II)-2-ethylhexanoate ($ZnC_{16}H_{30}O_4$)	[30], [31]

Table 1.2: Thin films produced by combustion chemical vapour deposition at atmospheric pressure.

Combustion chemical vapour deposition

Combustion, or flame enhanced chemical vapour deposition involves the use of a flame to break down the precursor to film growth, [21]. The temperature of the flame can be controlled with relative ease, enabling control of the gas phase reactions. Difficulty comes in investigation due to the large number of reactions occuring in such a system. Generally precursor is added by some kind of aerosol into the flame. A range of films that can be produced by this method at atmospheric pressure can be seen in table 1.2.

This method shares similar engineering difficulties to that of thermal chemical vapour deposition. In addition, the frequent use of aerosols to introduce precursors to the flame

also has its own difficulties, in terms of distribution of precursor and formation of intermediaries within the flame.

Plasma enhanced chemical vapour deposition

This technique can also be referred to as plasma assisted chemical vapour deposition, [32]. A plasma is a gas containing electrons, ions and radicals in addition to neutral species. The plasmas used are labelled non-thermal or non-equilibrium. This refers to the fact that the electrons are at a much higher temperature than the rest of the species present. The electrons are unable to impart this energy to the larger ions and neutrals, but are able to initiate reactions that would not occur at lower temperatures in a traditional thermal process.

The technique has seen widespread use at low pressures, particularly in the deposition of silica in the semiconductor industry. At atmospheric pressure, the technology is still newly emergent, and this will be expanded upon in subsequent chapters.

This process has commercial potential due to the ability to coat thin films at low thermal temperatures, allowing for coating on thermally sensitive substrates. Homogeneity of the plasmas used, and hence the films produced is a problem with the process. There is limited knowledge of how and why process parameters affect film properties.

Some of the films coated by this technique are presented in table 1.3.

Photon assisted chemical vapour deposition

The photon assisted form of the process involves the use of light at specific wavelengths to either break down the precursor in the vapour phase, activate the surface for

Coating	Precursor	References
Alumina (Al_2O_3)	Triethylaluminium ($(C_2H_5)_3Al$)	[33]
Silica (SiO_2)	Hexamethyldisiloxane ($Si_2C_6H_{18}O$)	[34], [35]
	Silane, nitrous oxide (SiH_4), (N_2O)	[36]
Silicon nitride (SiN)	Silane, nitrogen, ammonia (SiH_4), (N_2), (NH_3)	[37]
Titanium dioxide (TiO_2)	Titanium tetrachloride ($TiCl_4$)	[38], [9]
	Titanium tetraisopropoxide ($Ti_4(OCH_3)_{16}$)	[38]

Table 1.3: Thin films produced by plasma enhanced chemical vapour deposition at atmospheric pressure.

film growth, activate various reactants, or some combination of these effects, [39]. The light that is used is generally in the form of an ultraviolet lamp, or a laser. The process has the advantage of being able to grow patterned films without the use of some kind of mask. Some films coated using this technique are presented in table 1.4.

The process, in particular the laser activated form, grows films of low surface area. Therefore it is obviously not of use for large scale film growth in process industries such as glass production.

1.4 Thin film growing techniques

Chemical vapour deposition is not the sole thin solid film growth process, there are, in fact, a wide variety of thin film production techniques. The processes are either physical, as in the case of sputtering; or chemical, as in the sol-gel process. The choice of the process at an industrial level is, as always, due to the cost of the technology, and the value it adds to the films produced. This value can be in the form of enhanced qualities, or

Coating	Precursor	References
Boron carbide (BC)	Boron trichloride, methane (BCl_3), (CH_4)	[40]
Iridium (Ir)	Cyclopentadienyliridium ($C_5H_5Ir(C_2H_4)_2$)	[41]
Rhodium (Rh)	Cyclopentadienylrhodium ($C_5H_5Rh(C_2H_4)_2$)	[41]
Platinum (Pt)	Cyclopentadtrimethylplatinum ($C_5H_5Pt(CH_3)_3$)	[42]
Silicon (Si)	Dichlorosilane (SiH_2Cl_2)	[43]
Titanium Nitride (TiN)	Titanium tetrachloride, nitrogen ($TiCl_4$), (N_2)	[44]
Zinc Telluride ($ZnTe$)	Diethylzinc, diethyltellurium ($Zn(C_2H_5)_2$), ($Te(C_2H_5)_2$)	[45]

Table 1.4: Thin films produced by photon assisted chemical vapour deposition at atmospheric pressure.

Coating	References
Alumina (Al_2O_3)	[49]
Barium Titanate ($BaTiO_3$)	[50]
Lithium Cobalt Oxide ($LiCoO_2$)	[48]
Silica (SiO_2)	[51], [52], [53]
Tin Oxide (SnO_2)	[46], [54], [55]
Titanium Dioxide (TiO_2)	[47], [52]
Vanadium Oxide (VO_2)	[56]

Table 1.5: Thin films produced by the sol-gel process

cheaper production. A brief overview of these processes is now presented.

Sol-gel processing

One such process is the sol-gel process. This has seen use in producing a myriad of different thin films, from transparent conducting oxides such as tin oxide, [46], and titanium dioxide, [47], to dielectrics such as barium titanate, [48], and alumina, [49]. A more complete list of films coated by this method is presented in table 1.5.

Coating	References
Chromium (Cr)	[58]
Copper (Cu)	[59]
Gold (Au)	[60]
Indium (In)	[61]
Lead (Pb)	[62]
Nickel (Ni)	[63]
Osmium (Os)	[64]
Silver (Ag)	[65]
Tin (Sn)	[62]
Zinc (Zn)	[66]

Table 1.6: Thin films produced by electroplating.

The process first involves the generation of a "sol", which is a solvent that contains the metal ions that will constitute the final product, [57]. This sol is then turned into a semi-solid gel, which is either a colloidal or polymeric structure. This sol-gel is then applied to a surface and then heated, which does three things. First, all solvents and organics are removed. Secondly, the structure of the ions is rearranged and starts to become denser. Thirdly, crystallisation of the solid film occurs.

The process has some disadvantages. Firstly, it is a wet chemistry process that produces some waste. It is also a multiple stage process, and this has implications on processing times. Care has to be taken during film formation, as too high a rate of heating can cause films to fracture. The process still has a large amount of success, and is well used in a variety of situations.

Electroplating

A variety of metal coatings can be coated using electroplating, and a selection of these can be seen in table 1.6. It is also possible to plate films of alloys, but in the interest of brevity, these type of films have been left out of table 1.6.

Coating	References
Barium Cerate ($BaCeO_3$)	[70]
Lithium Manganese Oxide ($LiMn_2O_4$)	[71]
Silicon Carbide (SiC)	[72]
Silver (Ag)	[73]
Zirconia (ZrO_2)	[70], [74]

Table 1.7: Thin films produced by electrospraying.

Electroplating is where a conductive substrate is placed within an electrolytic solution with the desired coating material present in the solution, [67]. The substrate acts as the cathode, whilst an anode is also present. A current is passed between the cathode and the anode, inducing metal ions to reduce at the cathode. These metal ions form a plate or thin film over the cathode.

The obvious drawback of this process is that it is limited to production of metallic films. It is also a wet chemistry process that has the potential to generate a large amount of concentrated, toxic chemicals, [68]. The films that the process does produce are dense and adherent films.

Electrospraying

The process of electrospraying is where a liquid is sprayed out of a nozzle, which has a large voltage applied across it. The large electric field which is generated acts to turn what would be a spray into a fine mist of droplets, [69]. This is sprayed at a surface kept at a temperature suitable for thin film formation. Films coated by this technique are shown in table 1.7.

There is a wide variety of films produced by this method. In a lot of cases the films tend to require further annealling, [70], to be functional. Control of the spraying process is also limited to a handful of variables.

Coating	References
Alumina (Al_2O_3)	[77]
Barium ferrite ($BaFe_{12}O_{19}$)	[78]
Beryllium (Be)	[79]
Hydroxyapatite ($Ca_{10}(PO_4)_6(OH)_2$)	[80]
Lithium niobate ($LiNbO_3$)	[81]
Lithium niobate tantalate (Li_2NbTaO_6)	[82]
Titanium dioxide (TiO_2)	[83]
Titanium nitride (TiN)	[84]
Zirconia (ZrO_2)	[85], [86]

Table 1.8: Thin films produced by plasma spraying.

Plasma spraying

Plasma spraying, [75], describes a range of techniques where a thermal plasma is used. A thermal plasma is one in which all species (electrons, ions and neutrals) are at the same thermal temperature, [76]. The role of the thermal plasma is to provide a high temperature energy source to break down a source material into its constituent atoms, which can then be sprayed at a surface to form a thin film. A variety of films coated by this technique are presented in table 1.8.

The process produces hard films, with the required properties present without any further treatment of the films. Plasma spraying also exhibits very high growth rates, typically around one millimeter per hour, [76]. This process is an industrially established one, with perhaps the drawback being the high thermal temperatures involved.

Plasma assisted physical vapour deposition

Plasma is used to generate and direct ions towards a substrate, [87]. This is known as physical vapour deposition or plasma enhanced physical vapour deposition, [88]. The technique can be split into two primary methods, reactive sputtering and activated reactive

Coating	References
Alumina (Al_2O_3)	[89]
Magnesium Aluminate ($MgAl_2O_4$)	[89]
Magnesium Oxide (MgO)	[89]
Titanium Dioxide (TiO_2)	[90]
Titanium Nitride (TiN)	[91]
Vanadium Dioxide (VO_2)	[92]
Zinc Oxide (ZnO)	[93]

Table 1.9: Thin films produced by plasma assisted physical vapour deposition.

Coating	References
Alumina (Al_2O_3)	[96], [97]
Titanium Oxide (TiO_x)	[98], [99]
Zinc Oxide (ZnO)	[100]

Table 1.10: Thin films produced by HIPIMS.

sputtering. Both rely on ejecting metal atoms from a target, or source, and accelerating them towards the substrate requiring coating. A variety of sputtered films are presented in table 1.9

The control of the properties of the thin films is high, and generally better tribological coatings are produced. However, the coatings are carried out at low pressure, therefore there is a high cost to implement the process and a subsequent one to keep it running.

High Power Impulse Magnetron Sputtering

Recently the high power impulse magnetron sputtering process (HIPIMS), [94], has seen a lot of interest since the first patent being filed in 1997, [95]. This is another form of physical vapour deposition at low pressure. The technique is different due to the short pulses of high power coupled into the system. Sputtering is undertaken under vacuum, and involves atoms being fired at the substrate.

Coating	References
Alumina (Al_2O_3)	[103]
Iridium (Ir)	[104]
Lithium Carbonate (Li_2CO_3)	[105]
Strontium Titanate ($SrTiO_3$)	[106]
Ytterbium Oxide (Yb_2O_3)	[107]
Zinc Oxide (ZnO)	[108], [109]

Table 1.11: Thin films produced by atomic layer deposition.

Films coated by HIPIMS are presented in table 1.10. This is again a vacuum process, with all the drawbacks this implies.

Atomic layer deposition

Atomic layer deposition (also known as atomic layer epitaxy, [101]) is a process that is seeing ever more interest in terms of research. This process can almost be seen as a step wise chemical vapour deposition, [102]. The process goes through cycles of adding precursor, purging of the excess precursor and then a reactant of some kind is added. Finally the byproducts are purged. The film is built up over many cycles of precursor and reactant addition, generally in the region of two hundred reaction cycles. Films deposited by atomic layer deposition are presented in table 1.11.

This process does allow for greater control of film properties than an atmospheric pressure chemical vapour deposition process. There is, however, still the issue of processing time. Atomic layer deposition tends to take longer than a chemical vapour deposition process for a film of equivalent thickness.

1.5 Summary

The chemical vapour deposition process is an established one, proving itself versatile and cost effective against a range of competitive processes for producing thin films. Processing at atmospheric pressure has enhanced this process enormously, with higher throughputs being possible in combination with cheaper processing costs.

The issues then, lie with the characterisation and subsequent improvement of the process. The investigation of the gas phase and surface chemistry occuring during the process can be seen as the key to this improvement, as this information can establish the important process variables to produce a given film possessing certain qualities. This is not a trivial task, as the next chapter will establish.

1.6 Aims and Objectives

The atmospheric pressure chemical vapour deposition process is one that requires study. The aim of this work is to develop a variety of techniques that can be used in combination to enhance scientific understanding of the process, whilst still enabling process optimisation and control. The subsequent objective is to apply and illustrate the use of these techniques in characterising atmospheric pressure chemical vapour deposition processes.

Chapter 2

Techniques for *in situ* investigation of chemical vapour deposition.

2.1 Introduction

It is necessary to be familiar with the measurements that can be made during chemical vapour deposition, so as to be aware of the situations in which they can be applied. Knowledge of what still needs to be known about the process is also of great importance, and this was established in the previous chapter. Gas phase reactions, surface reactions, fluid dynamics and process specific phenomena give rise to a large number of unknowns about the process that need to be identified and investigated.

A range of techniques can be used for investigation of the chemical vapour deposition process. The techniques range from surface measurement techniques to analyse the surface chemistry, to fluid dynamics measurements of gas flows. On top of these there are measurement techniques that are process specific. For example the use of optical emission spectroscopy for monitoring combustion and plasma chemical vapour deposition.

For this indepth look the measurement techniques are split into four main areas; surface measurements; gas phase measurements; transport phenomena measurements; and process specific measurements. Emphasis will be placed upon *in situ* measurements, but some treatment will also be given to *ex situ* applications too. The analysis of these measurements will focus on how useful they will be in investigating atmospheric pressure chemical vapour deposition processes.

2.2 *In situ* measurements of the thin film surface.

Measurements of the surface of the thin film are of great use in identifying the surface chemistry, rate of film growth and various optical properties of the films. It could be argued that surface spectroscopy techniques are the most useful in enhancing understanding of the chemical vapour deposition process in terms of film properties. These techniques are also of use in process control, especially for monitoring film thickness. A discussion of the various techniques is now presented.

X-ray photoelectron spectroscopy

X-ray photoelectron spectroscopy relies on the action of x-ray photons on the surface atoms, causing ejection of electrons. The energy of the electrons can be used to identify the atomic species present on the surface of a thin film.

X-ray photoelectron spectroscopy has been used to measure what is occuring at the surface during low pressure chemical vapour deposition. Use of the technique during deposition of aluminium thin films from dimethylaluminium hydride [110] has led to an understanding of the surface chemistry, identifying that the growth mechanism is partially dependent on breakdown of precursor in the gas phase. Atomic layer deposition has also been investigated, with x-ray photoelectron spectroscopy being carried out between the coating of each monolayer of zinc oxide coating [111]. This enabled identification of the growth cycles with highest growth rate, whilst still allowing some commentary on the chemistry occuring at the surface. Another use of x-ray photoelectron spectroscopy (in combination with Auger electron spectroscopy) during deposition of diamond films on copper substrates [112], has allowed identification of a three stage surface process.

This technique cannot be used in the atmospheric pressure processes that are studied

here due to ultra high vacuum being required for the measurement techniques to work. The use of the term *in situ* is also perhaps a bit tenuous, due to the substrate being moved between coating chamber and measurement during the deposition process, however it is still under the same vacuum conditions under which deposition is being carried out.

Auger electron spectroscopy

Auger electron spectroscopy works by the action of a high energy electron beam incident on a surface. This beam has enough energy to ionise surface atoms, giving off Auger electrons, which are electrons that have been ejected from ionised surface atoms. The energy of the Auger electron is purely a function of the atom it is emitted from, and so measurement of the emitted electrons allows for identification of atomic species in a given thin film.

In situ studies have been carried out at low pressure. These studies rely on translation of the substrate being coated from the coater to the diagnostic equipment during the deposition cycle. The technique has been carried out during rhodium deposition[113], and was able to identify that less carbon and oxygen were incorporated into the rhodium films with increasing deposition time, thus helping to highlight the optimum processing conditions for a pure rhodium film. The technique has also been used in combination with x-ray photoelectron spectroscopy, as stated above [112].

This surface measurement technique has similar drawbacks to that of x-ray photoelectron spectroscopy when carried out *in situ*.

Ellipsometry

Ellipsometry can be used for monitoring film thickness and optical properties. The technique relies upon changes of polarization of light reflected from a surface, from which the refractive index and film thickness can be calculated. This requires easy optical access to the surface of the film at quite a high angle of incidence. This is not necessarilly practical for *in situ* measurements.

The technique has been used during diamond deposition [114] by hot filament chemical vapour deposition, where it has been applied to better control contamination, substrate temperature and particulate nucleation. Ellipsometry has been applied during plasma deposition of hydrocarbon films [115], where it was used to suggest a possible mechanism for film growth. It has also been used during the growth of crystalline silicon films [116], where it has been useful in showing at what point in time deposition ends.

Reflection absorption and attenuated total reflection infrared spectroscopy

Infrared spectrocopy of surfaces relies upon the reflection of the infrared beam from the surface to the detector. There are two primary methods of doing this. Reflection absorption infrared spectroscopy involves a polarised infrared beam reflecting off a surface at a very low angle of incidence. The adsorbed molecules on the surface absorb the incident radiation, [117]. Attenuated total reflection infrared spectroscopy (ATR-FTIR) generally uses a diamond crystal, transparent to infrared light, into which the infrared beam is passed such that it totally internally reflects within the crystal, [117]. Some infrared light penetrates slightly beyond the surface of the crystal as an evanescent wave. The thin film can be pressed against this crystal, and a spectrum can be recorded of its

surface.

In situ reflection absorption measurements during plasma deposition of amorphous silicon films, [118], have been carried out. This study showed the usefulness of the technique in measuring the composition and temperature of the surface, with absorption features due to the film visible after five minutes of deposition time. ATR-FTIR has also seen use during the plasma cleaning of silicon and gallium arsenide surfaces [119], where it was useful in identifying the end point of the cleaning process. A major drawback of this technique is that it would require a specially constructed chamber that can only be used for measurements of films depositing on the crystal surface.

Surface enhanced Raman spectroscopy

Surface enhanced Raman spectroscopy relies upon the effect of adsorbed surface molecules enhancing the Raman scattering effect. There was some debate as to how this measurement works, [120], with a disagreement as to whether it is due to an electric field or chemical effect. However, the use of Raman at the surface can be used to identify the formation of chemical bonds, in addition to the chemical species present. It is dependent on the surface undergoing coating, with silver and gold surfaces often being used. It is also used to assess crystal structure as well.

The use of surface enhanced Raman spectroscopy during the deposition of tantalum oxide films, [28], has indicated that the initial deposition mechanism is due to surface oxidation reactions. The technique has seen success in identifying the mechanism of film growth during deposition of diamond from methane [121], where it was used to identify poly-acetylene formation at the surface.

The limitation of substrate choice means that this technique provides information on initial growth processes under a very restricted set of conditions, specifically the choice

of substrate. It is not practical for anything more.

Summary

It is evident that *in situ* surface measurements are highly limited by the design of the reactor. However, at atmospheric pressure, gas phase reactions tend to dominate. It is maybe more pertinent to identify and investigate the formation of intermediates in the gas phase in any case.

2.3 *In situ* measurements of the gas phase.

As established in the previous chapter *in situ* measurements of gas phase chemistry have the potential to provide a wealth of information on the atmospheric pressure chemical vapour deposition process. The techniques for measurement are many, and need to be evaluated for their potential.

Fourier transform infrared absorption spectroscopy

Fourier transform infrared (FTIR) spectroscopy is used to investigate molecules that are active in the infrared region, subsequent chapters will expand upon this technique. It is a broad spectral range technique, and can be used to both identify chemical species and quantify their concentration. The technique is commonly used after the reactor to investigate by products of the process. However, there has been a significant amount of *in situ* use. During the deposition of silicon carbide from trichloromethylsilane, [122], the technique has been used to identify the intermediary products to film production and postulate a series of reaction mechanisms. The technique has also seen use during the plasma

enhanced deposition of copper at low pressure, [123]. In this case the FTIR spectroscopic measurements were used to establish the range of process conditions, in which high concentrations of active hydrogen species were generated. The use of FTIR spectroscopy during the low pressure plasma enhanced deposition of amorphous silicon, [118], has shown use in identifying the precursor usage and short lived intermediaries within the reaction scheme. The combination of *in situ* and *ex situ* use of FTIR spectroscopy has assisted in identification of intermediaries formed during indium gallium arsenide film production, [124]. *In situ* measurements during vanadium dioxide film growth, [125], [126]. *In situ* use during plasma etch dates back at least to 1982[127]. Some use has been seen in various studies of plasma etching processes in the intervening years, [128].

FTIR spectroscopy can also be used to investigate temporal behaviour of species, which is especially interesting in plasma chemical vapour deposition where the chemistry is governed by the discharge cycle of the plasma. Though no investigations have been carried out as yet for chemical vapour deposition processes, the technique has seen use for investigations of plasma chemistry, [129].

Raman spectroscopy

Raman spectroscopy relies on the inelastic scattering of light by molecules, the Raman effect, [130]. It is necessary for the light to be monochromatic, in order that the technique be quantitative. Photons excite the molecule to a virtual excited state, and then this excited state relaxes to a new vibrational or rotational state, emitting a photon in the process. The photons that are emitted can either gain or lose energy compared to the original incident photon. This is known as anti-stokes and stokes scattering respectively. Rayleigh scattering occurs when there is no net gain or loss in photon energy.

The potential for the use of this technique has long been associated with chemical

vapour deposition, [131], with studies being performed on the chemistry that leads to silicon nitride deposition.

Coherent anti-Stokes Raman spectroscopy involves the application of several lasers to cause electron oscillation between several energy levels within a measured molecule. The technique has been used to measure hydrogen concentration and temperature during deposition of diamond, [132], revealing information about the deposition process. Measurements have been made during deposition of silicon carbide to measure molecular hydrogen and tetramethylorthosilicate concentration and temperature, [133]. It has also been applied during plasma deposition of silicon nitride to measure silane concentrations, [134].

Ultraviolet-visible absorption spectroscopy

UV-vis spectroscopy is used to measure electronic transitions of atoms and molecules. Light in this region excites the electrons of the molecules and atoms it comes into contact with, with the light being absorbed to cause this excitation.

The technique has been applied during the chemical vapour deposition of gallium arsenide films, [135], where gallium intermediary species were identified in the gas phase which in turn lead to the reaction mechanism being identified. The technique has also seen use during the deposition of copper films, [136], where it was used to measure the concentration of copper atoms as the chemical vapour deposition process progressed.

The technique can be used for identification of simple atomic and molecular species. In the presence of a more complex chemical reaction scheme, with more complex chemical structures, the technique is not necessarily the primary technique for identifying reaction mechanisms.

Infrared laser diode absorption spectroscopy

Laser diode spectroscopy provides a line of sight measurement of an absorption feature in the infrared region. This absorption feature can be used to measure the concentration of the species responsible for it, the technique will be discussed in detail in the next chapter.

Multiple species measurements during the chemical vapour deposition of gallium arsenide have been carried out [137], these have been used in conjunction with film measurements to assess the film properties during the deposition process. The study also identified the methyl radical as an important species in the reaction, but was unable to identify where it was formed. Hydrogen bromide measurements during plasma etch in an inductively coupled plasma reactor, [138], were used to measure the temperature within the reactor, which remained constant over the experimental conditions examined. The results showed the dependance of hydrogen bromide dissociation on power coupled into the plasma, as well as the substrate condition. Measurements of hydrogen chloride made during the plasma etching of poly-silicon, [139], were successful in correlating hydrogen chloride concentration with etch rate. The dual use of laser diode measurements of hydrogen chloride and hydrogen flouride during the atmospheric pressure deposition of tin oxide films was successfully used to highlight process problems, [140]. Hydrogen flouride measurements during plasma etch, [141], have been shown to be useful in identifying the endpoint of the etch process.

The relatively recent development of quantum cascade lasers has made the instrumentation of mid-infrared laser diode measurement systems more light weight, and more readily applicable to industrial processes, [142]. The potential for further work in this field is promising as it is a non invasive, relatively cheap process analysis technology, [143].

Laser induced fluorescence spectroscopy

Laser induced fluorescence spectroscopy works by laser excitement of the species to be measured. After an amount of time, the species fluoresces and releases photons with higher wavelengths than the incident photons, which can be measured. The process has the advantage that these photons scatter light in all directions, coupled with effective measurement this can enable the measured species to be tracked spatially in three dimensions.

The technique has seen use for measurement of gas phase silicon atoms during silicon deposition [144], where it was used in combination with numerical modelling of the process to identify the reaction mechanisms occurring during the deposition process.

Summary

The gas phase measurements presented here provide a substantial approach to examining the chemistry of chemical vapour deposition as it is occurring. The use of several of these techniques at once would provide the information necessary to explore the gas phase chemistry, and can be correlated with the properties of the thin films grown during the chemical vapour deposition process.

2.4 Measurements of fluid dynamics and transport phenomena

The fluid dynamics and mass transfer occurring during these processes are highly complex. Typically there are large temperature, concentration and velocity gradients that can impact on the film formation. Presented here are some techniques for measurement of these factors.

Velocity measurements

There are a variety of techniques used to measure gas velocities in a chemical vapour deposition process [14]. A brief treatment of the techniques is given here.

One method involves the introduction of a tracer material into the gas stream, generally one that causes powder formation [145]. Results from this method have been used to aid in development of more complex models of the chemical vapour deposition process, [146]. Fluorescing materials can also be used as a tracer, [147]. The velocity of these powders can be tracked through the use of light scattering measurements, [148]. The gas flows can be visualised in three dimensions, however this technique involves the introduction of contaminants into the process, so it can not be used during production.

Another method is that of holographic interferometry, [149]. This is a complicated technique which involves measurement of the gas density changes within the reactor though the use of two or more laser beams, one of which is a reference beam, the other is aimed through the reactor. Both beams are trained on a holographic recording medium, [150]. Interference occurs between the two beams due to density changes causing the refractive index of the gas within the reactor to change, and hence the interference fringes can be reconstructed to identify density gradients, [151]. The density changes within the reactor are used to interpolate the flow regime, [149]. Most work with this technique tends to be more qualitative.

Yet another technique that can be used to measure gas velocities, is that of laser velocimetry, [152]. This is where several lasers are used to track particles seeded into the reactor, with the particles following the direction and velocity of gas flow. It has been used in combination with infrared thermography to better understand the transport phenomena occurring within a chemical vapour deposition reactor, [153].

These techniques tend to rely upon injection of some kind of tracer material into the reactor, which can not be used in normal production. Therefore they are not suitable for this work.

Gas and surface temperature

Several techniques can be used for temperature measurements, from infrared thermography ([153]) to thermocouple measurements ([145]). Not only is this information useful in characterising the process, but it can also be used to aid analysis results from other measurement techniques. In particular the optical techniques are dependent on the temperature of the gases being measured.

Thermocouples have seen a lot of use in characterisation of the substrate surface, but can also be used to measure temperatures of the gas stream [145]. Spatially resolved temperature measurements of the substrate surface are useful in improving homogeneity of films produced, as the growth rates can be strongly affected by temperature differences across the surface of the substrate.

Raman spectroscopy can be used to spatially measure the temperature of the gases, [154], albeit with the use of an extremely powerful laser. Generally the rotational transitions of the carrier gases are measured to resolve the temperature within the reactor, [155]. Due to Raman spectroscopy being a laser technique, this method of temperature measurement can be highly spatially resolved, [154]. The technique identified the importance of the volume of the hot region during the chemical vapour deposition of gallium arsenide in reducing undesired side reactions, [155].

It should be noted that holographic interferometry can also be used to measure the temperature, as the density of gases is also dependent on their temperature, [151]. Interpretation of results is very complex however, but the technique can resolve temperature

changes to within ten kelvin, [151].

Temperature measurements are useful, but do not provide a complete picture of the process in and of themselves. The use of *in situ* spectroscopic techniques presented above allows for temperature measurement, whilst providing additional information.

Summary

These measurements are an area of interest in chemical vapour deposition, however, the main unknowns are the chemical mechanisms that occur, and how these lead to film growth and film properties. These measurements do not assist in identifying these unknowns, and as so are of less importance in identifying the chemistry. They are of great use, however, in reactor improvement and subsequent redesigns of the process.

2.5 Plasma specific measurement techniques

Due to the unique nature of plasma, there are several techniques that can be applied to investigations of plasma enhanced chemical vapour deposition, that cannot be applied to the other chemical vapour deposition processes. These techniques are presented subsequently.

Langmuir probes

This is an electrical diagnostic. First developed by Irving Langmuir [156], [157], and takes advantage of the nature of plasma sheathes. The sheath region in a plasma is where initial electron build up on a surface acts to repel incident electrons upon that selfsame surface, the density of positive ions in the sheath is consequentially higher. The

diagnostic is used to measure the electron and ion density of a plasma. This works by placing an electrode into the plasma region and applying a voltage between the probe and the reactor. The electric field generated acts to retard the impact of electrons on the probe, allowing positive ions to hit the probe and generate a voltage that can be measured.

This technique can be used to build up a spatially resolved measurement of the plasma density and temperature within the plasma region. This is a huge advantage, as it allows the mapping of instabilities within the plasma region.

The technique has been used for measurements of atmospheric pressure plasmas [158]. In this case the Langmuir probe was used to successfully measure the plasma density at a variety of voltages and gas velocities, showing the probes use in measurements of atmospheric pressure plasmas.

There are two main problems with the technique. Firstly a Langmuir probe is invasive, and this can have an effect on gas flows and deposition chemistry. There are also issues in making sure that the correct interpretation of the results is applied. There are added complications in a reactor coating a dielectric film, as there will be coating on the probe itself.

Optical emission spectroscopy

Optical emission spectroscopy has seen much use for investigating plasmas as it relies on light emission from electronically excited species. It can be used to measure a range of plasma quantities such as electron density and excitation temperature. As such, the technique has been used for many investigations of plasma processes. See subsequent chapters for a more in depth explanation.

The use of the method during the low pressure deposition of titanium nitride[159]

identified the formation of positive titanium ions as important for the formation of films. The use during microwave plasma formation of diamond films [160] identified CH and C_2 radicals as the active species. The technique has been used to extensively study the chemistry during the plasma assisted chemical vapour deposition of silicon carbide thin films at low pressure [161], and helped to identify the importance of etching on the quality of the films grown.

Summary

Of course these techniques can only be applied to plasma, however, they are of great use in establishing the plasma mechanisms and properties. This is of importance in such a complex system as plasma, as the properties of plasma processes are vastly different to those of conventional chemical vapour deposition processes, and these differences require some method of measurement.

2.6 Overall summary

The variety of techniques available is perhaps daunting. The atmospheric chemical vapour deposition process itself is the limiting factor though, and the key investigation area should be that of the gas phase chemistry. This is so as to identify the precursor chemistry leading to film growth.

Gas phase diagnostics provide information on the gas phase chemistry. For atmospheric pressure chemical vapour deposition of all types, this point of the process is extremely important, as established in chapter one. Therefore, the use of gas phase diagnostics is perhaps the best way forward, with particular attention paid to those techniques which have the most potential for providing the most information. The use of Fourier

transform infrared spectroscopy has potential to provide wide ranging information on the chemical processes occurring, whilst laser diode spectroscopy could provide information on spatial and temporal concentration gradients, thus validating mechanisms and physical models.

In the case of plasma processes, the addition of optical emission spectroscopy enables the identification of a wider range of chemical species, in addition to providing a method to estimate the electron temperature. The technique can thus further enhance investigation of the process.

All these techniques are non-invasive, and do not involve the addition of contaminants to the process. Their use also minimises the need to specially design reactors solely for measurement activities, and have the potential to be used in a real process environment. Subsequent chapters will expand on the various techniques used for this work.

Chapter 3

Non thermal plasmas

3.1 An Introduction to Plasma

It is important to describe what a plasma is, and the type of plasma that is being used. A plasma is a gas that has undergone at least some partial ionisation. There can be a large quantity of ions and electrons present within plasmas, leading to extremely chemically active environments. There are many applications of these plasmas within an industrial context due to this reason. They can be applied to processes such as gaseous emission treatment, [162], [163], polymerisation reactions, [164], and surface treatment, [165]. Chemical vapour deposition is just one of many processes where plasmas can be applied, [166].

Methods of plasma generation are extremely varied. These range from the complex tokamaks that provide the high temperatures and magnetic containment necessary for nuclear fusion, [167] to the very simple silent discharge first reported by Siemens that was used for ozone generation, [168]. The dielectric barrier discharge reactors used for this work are a further adaptation of this original plasma generation method, which relies upon strong electric fields to ionise the gases involved. Practically they are easy to set up, however the theory is far more complex.

The plasmas involved in some of the more common industrial applications are not in thermal equilibrium, in other words the constituent particles of the plasma are not at the same effective temperature. The free electrons have a higher temperature than the ions and neutral species making up the rest of the plasma. This electron temperature, T_e, is high as

Process	Representation
Stepwise Ionisation	$A^* + A^* \rightarrow A^+ + A + e^-$
Penning Ionisation	$A^* + B_2 \rightarrow A + B_2^+ + e^-$
Ionic Conversion	$A^+ + 2A \rightarrow A_2^+ + A$
	$A_2^+ + A_2 + B \rightarrow A_4^+ + B$
Excitation	$A + e^- \rightarrow A^* + e^- + E$
Metastable deactivation	$A^* + e^- \rightarrow A + e^-$ - E
Atomic ion recombination	$A^+ + e^- \rightarrow A$
Molecular ion recombination	$A_2^+ + e^- + e^- \rightarrow 2A + e^-$
	$A_2^+ + e^- + A \rightarrow 3A$
	$A_4^+ + e^- \rightarrow 2A_2$

Table 3.1: Example plasma collision processes, [7], where the * represents metastable states and E represents energy released in the form of photons.

collisions that equalise the temperature of the plasma are less likely at the relatively low pressures involved, [169].

Within a plasma, the large amount of different particles present lead to many different collisional processes. These collision processes are summarised in table 3.1. In an atmospheric pressure plasma, there is the possibility for formation of a large number of different species, due to the density of the gases involved. This means that the potential is there for a lot of these collisional processes to occur, and so it is important to be aware of them.

The electric field required for a given gas to form a plasma is of a relatively high order. This is generally generated by passing a high voltage across two electrodes seperated by the gas to be ionised. The voltage required to ionise, or break down, the gas is known as the breakdown voltage (V_b).

The voltage required for the initial gas breakdown, [170] is dependent on the electrode gap (d); the gas used; the pressure (P); and the electrode or dielectric material, [171] facing the plasma. The electrode or dielectric material plays a role, as it sustains the plasma via the release of electrons or ions from its surface upon the incidence of electrons

from the plasma. The strong electric field induced by the electrodes also induces electrons to escape the dielectric surface, [172]. This secondary electron emission of the dielectric surface (γ_e) plays a role in sustaining the plasma[173], and can, in fact, act to quench the plasma. The breakdown voltage can be shown to be calculated using equation 3.1, [171]:

$$V_b = \frac{BPd}{\ln(APd) + \ln(\ln(1 + 1/\gamma_e))} \tag{3.1}$$

Where *A* and *B* are empirical values that vary depending on the gas used. Equation 3.1 is useful as it enables the calculation of not just the breakdown voltage necessary for a given set of conditions, but also the effective plasma generation range of a given transformer. At higher *Pd*, it is noticeable that any effects contributed by the dielectric are negligible, making the breakdown voltage effectively independent of the dielectric used. It is worth further examining the breakdown voltages required for plasma generation at atmospheric pressure for differing gas gaps. The gases used in appreciable amounts for the plasmas in this work are helium, argon, nitrogen and oxygen. The parameters *A* and *B* are taken from Lieberman and Lichtenberg, [174], and the secondary electron emission coefficient was also estimated from the same source.

The use of plasmas in a variety of surface processing roles is significant. Classic work carried out concerning etching, [175], [176], perhaps shows why. The work concerns the effects of chemical and ion bombardment on the etch rate of silica. Etching was carried out using these two processes separately, and the etch rate was quite low. When the two processes were occurring together, simulating a plasma, the etch rate increased by an order of magnitude. It is this synergistic effect that plasmas possess that leads to their use in a variety of surface processing roles.

This synergistic effect also applies to deposition processes, [177]. It is in the complexity of plasma surface interactions where this synergistic effect resides. Growth mech-

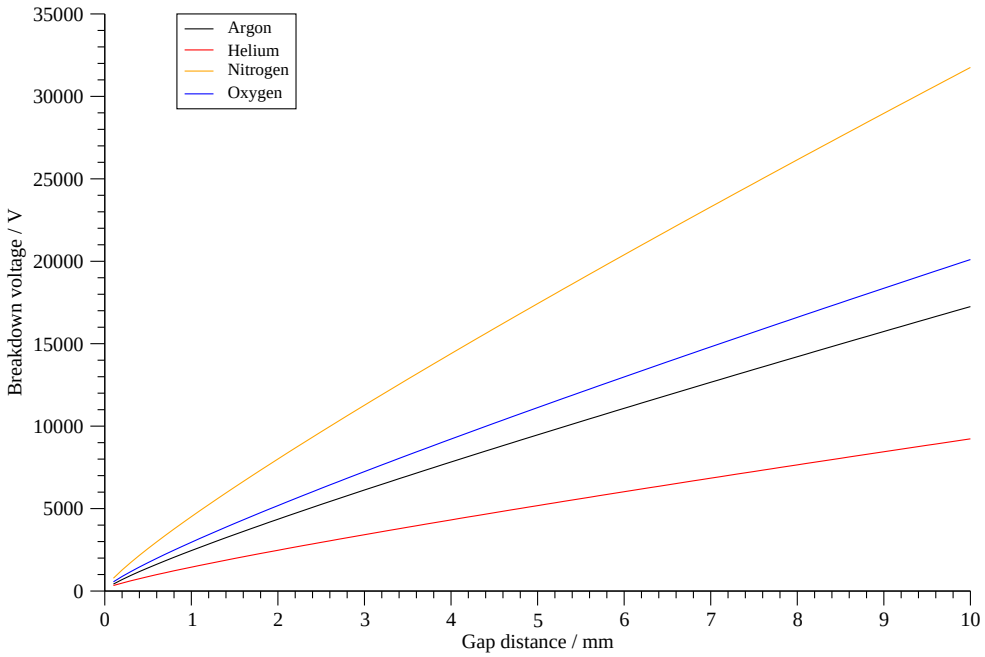

Figure 3.1: Breakdown voltage against gas gap at atmospheric pressure for different gases.

anisms are little known, and this is due to both the complexity of the plasma reactions as seen in table 3.1, and the growth and etching processes at the surface. This is why plasmas are used in a wide variety of surface processing industries, [178], and why the study of them is important. The limited knowledge of growth and etching mechanisms is a subject that needs considerable expansion. The area of plasma surface interactions are a definite key research topic for plasma researchers.

3.2 Glow Discharge Plasmas

To further the understanding of plasmas, or gas discharges, perhaps the first stage is to examine the direct current (DC) glow discharge plasma. This occurs at low gas pressures when a DC voltage is applied across the gas, [1]. Figure 3.2 illustrates the regions formed in a glow discharge tube. The distance between the electrodes is important, and governs

the regions that appear in the discharge. Each of the regions have a set of distinct processes occurring within them. They are also electrode separation dependant, for example, if the gas gap is too small the positive column and faraday dark space disappear, [171].

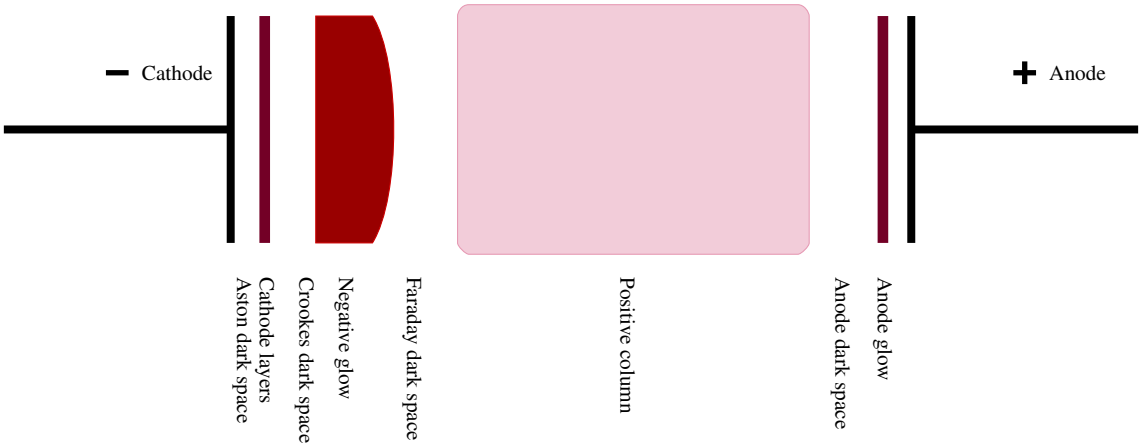

Figure 3.2: Illustration of low pressure glow discharge, [1].

The sheath regions are located at the electrodes, labelled Crookes and Anode dark space in figure 3.2. The electric field strength is strongest in the sheath regions, and this acts to repel electrons travelling to the electrodes, [179]. Some secondary electron emission occurs at the walls of the discharge tube, and at the electrodes due to ion and electron bombardment.

The cathode is a source of secondary electrons due to impacts with positive ions. These secondary electrons are necessary to sustain the discharge. This leads to many collisional processes in the cathode sheath as the electrons are accelerating through large electric fields. The ionisation processes that do occur however, are not sufficient to sustain the plasma, but they do play a role in maintaining the current through the plasma.

The sheath at the anode accelerates secondary electrons from the anode into the glow region, providing a source of ionisation and energy. The glow region in turn acts as an ion source for the anode sheath.

Within the glow region there are three different electron ‘types’. These consist of

primary electrons entering from secondary emissions within the sheath regions; secondary electrons, which are the product of ionising collisions; and ”ultimate” electrons, at the plasma temperature, which are the most prevalent type. Ions within this region are at a low relative energy, and so are not involved in further ionisation.

The glow discharge illustrates several facets of gas discharges. The sheath regions are common to all such plasmas. Secondary electron emission acts to sustain the plasma. The glow discharge also illustrates the use of electric field to couple energy into the plasma.

3.3 Dielectric Barrier Discharge Plasmas

The original dielectric barrier reactors consisted of two coaxial glass tubes, [168]. An alternating high voltage was passed across two electrodes located either side of the glass dielectric, and gas was passed through the annulus formed by the tubes, [180]. Dielectric barrier discharges may be arranged as in figure 3.3. Gas flows through the space between the two electrodes. The alternating current leads to a constantly changing electric field forming. This affects the atoms and molecules within the gas and at the dielectric barrier, [172], to the point whereby electrons are excited and released from their parent species, [169]. The electrons and ions present within the plasma region are now free to move, inducing electric fields. This in turn induces changes in the current in the power supply circuit, [181].

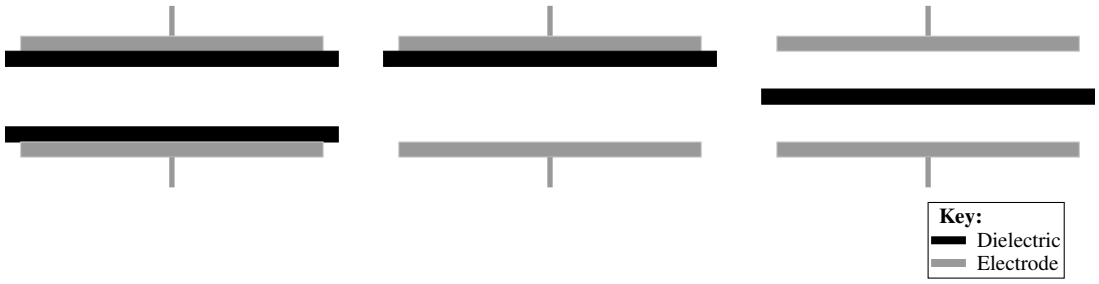

Figure 3.3: Dielectric barrier discharge arrangements, [2].

The dielectric acts as a limit on the current within the discharge, ensuring that the discharge does not undergo transition to the arc regime, [182]. The arc is a plasma which is under local thermal equilibrium, which causes scorching of the reactor chamber and is far more energised than many processes require.

The initial stage in the gas breakdown is referred to as a Townsend discharge. This can then undergo transition to a filamentary, semi-glow or glow discharge depending on several variables. Within a Townsend discharge, electrons are freed from their parent species by the electric field. The Townsend discharge is dominated by secondary electron emission at the dielectric surface. The resultant charged species collide with other species leading to further ionisation, [183]. This can be regarded as an avalanche of ionisation, resulting in the discharge being initiated, [184].

After this initial stage the plasma is relatively self-sustaining, requiring a reduced electric field. This reduces the voltage required from the power supply. This stage in the discharge is either the filamentary or glow discharge. The plasma can also stay in a Townsend regime. Filamentary discharge occurs when the plasma is dominated by streamers. Visually the plasma is contained within several intense localised regions, resembling lightning strikes. There is a charge build up on the surface of the dielectric, which leads to streamer formation over the course of a voltage cycle, [185].

The glow discharge occurs over the entire volume of the discharge, with the power more evenly dissipated.

The gases used for the plasma have an effect on the plasma. Helium is relatively easy to ionise at lower voltages, and leads to a glow discharge. As can be seen from figure 3.1, argon requires a higher voltage to break down, and leads to a filamentary discharge which can undergo transition to a semi glow at atmospheric pressure. This might seem counter intuitive, as the ionisation potential of argon is 15.8 eV, compared

to 24.6 eV for helium. This is because of the faster heat and mass transfer processes of helium, causing more efficient transfer of energy and increase of the ionisation avalanches leading to plasma formation, [184]. Nitrogen is a very electronegative molecule, and as such requires a stronger electric field and hence higher voltage to ionise and induce breakdown. It also tends to produce a filamentary discharge at atmospheric pressure but with suitable conditions a glow discharge can be formed, [186], [187].

3.4 Atmospheric Pressure Glow Discharge Plasmas

There has been some debate in the literature as to how the atmospheric pressure glow discharge differs from a conventional dielectric barrier discharge. It is either regarded as many overlapping filaments, [188] forming a pseudo-homogeneous plasma, or as a plasma in the glow regime, [189] as previously outlined. Several time resolved imaging studies of the plasma emission indicate that the glow discharge, [190] is an entirely different regime however, with emission being mostly uniform across the plasma, [189], [191], [192].

Work done in characterising the breakdown of these discharges under atmospheric pressure, has shown that it tends to be a Townsend discharge as characterised previously, [193]. For a discharge in nitrogen, the secondary electron emission continues to dominate throughout the discharge cycle, and so the nitrogen discharge can be referred to as an atmospheric pressure Townsend discharge, [183]. The helium discharge in comparison shares a lot of similarities with a low pressure glow discharge, some features of which are outlined previously. And so these are true atmospheric pressure glow discharges, [189].

Regions of instability in the electric field tend to become even more unstable at atmospheric pressure, these regions increasing in electron density and transitioning to the arc regime, [194]. It is important to control and prevent this transition in the case of chemical

vapour deposition, [195] as this can lead to inhomogeneous and damaged films. Perhaps the most important factor in forming a homogeneous discharge is the dielectric material, [196], [7], [173], [194]. Roughness and chemical impurities in the dielectric material contribute to changes in the electric field and ionisation rate in certain regions, leading to the arc transition. Plastics are suggested to limit the generation of instabilities.

Another method of enforcing the glow discharge at atmospheric pressure is by modification of the power supply. The use of an inductive choke is suggested, [194] to limit fast rates of current increase, thus limiting the instabilities in electric field in the plasma and the arc transition. Frequency, [197] of the alternating current is perhaps also relevant, [198], however atmospheric pressure glow discharges have been reported at many frequencies, [194], [199].

3.5 Electrical modelling of atmospheric pressure plasmas

There has been considerable work done on the modelling of atmospheric pressure gas discharges as electrical circuits in the past decade. This is of importance, as such models can provide insight into the mechanisms of the discharge. They also provide a way to benchmark and optimise power supplies, [200].

The initial work on such an electrical model, is to characterise and model the power supply. This is generally treated as a linear amplifier amplifying an audio frequency alternating current, which then supplies a step-up transformer. The transformer has an inherent resistance and stray capacitance due to its design. The resistance is due to both the resistance of the windings, and hysteresis losses in the transformer. These can be accommodated with relative ease into an electrical model.

The discharge region can be treated as a capacitor without a plasma present, as it is

essentially a capacitor with two or three dielectric layers. These consist of the gas gap, and the dielectric barriers.

The plasma has both resistive and capacitive characteristics, [201]. Electrical circuit models of the glow discharge have to take into account the breakdown and then the subsequent discharge.

A model of the atmospheric pressure Townsend discharge in nitrogen, [202], uses two Zener diodes to simulate the Townsend conditions. These represent the exponential rise of the voltage and current product with the discharge current. The characteristic parameters of such a model are set to represent the breakdown and current flow at high voltage. A resistor and capacitor in parallel with each other are used to simulate the effect the frequency of the power supply has on the breakdown voltage of the circuit.

The atmospheric pressure glow discharge in helium has also been simulated, [200]. Again, a pair of Zener diodes are used to simulate the initial Townsend breakdown conditions. The memory effect has to be taken into account however, as this acts to reduce the breakdown voltage of the gas gap. This is due to excited and metastable species still present in the gas from one discharge cycle to the next one. A resistive capacitive circuit that is connected to the discharge current is used, and this can modify the operating characteristics of the Zener diodes, simulating a decreased breakdown voltage.

3.6 Summary

Non-thermal plasmas are used in a variety of industrial situations. Most significantly they are of primary importance in the semiconductor industry, underpinning the creation of ever improving computer processors. These chemically reactive environments that plasmas provide are significant, and can assist with more energy efficient processes.

These non-thermal plasmas also have potential at atmospheric pressure, especially in the form of the atmospheric pressure glow discharge. For chemical vapour deposition, such discharges are ideal. They are homogeneous, which is advantageous to the formation of a homogeneous thin film. There are engineering difficulties though, and significant work needs to be done in connecting discharge parameters with thin film properties.

Chapter 4

Spectroscopic Techniques

4.1 Aim of chapter

The aim of this chapter is to provide sufficient background for the spectroscopic techniques used to probe chemical vapour deposition processes in the course of this work, and also to describe the methods used to treat the results. In particular the techniques of optical emission spectroscopy, Fourier transform infrared spectroscopy and near infrared laser diode spectroscopy are covered.

4.2 Optical emission spectroscopy

Electronic states in atoms and molecules

The Schrödinger equation, [203], is of primary importance in the field of spectroscopy. It is using this equation, and the analysis that can emerge from it, that has enabled great understanding of spectroscopy and hence atomic and molecular systems. The general form of the Schrödinger equation can be seen in equation 4.1, and is composed of the Hamiltonian (H), the wave function (Ψ) and the energy (E) of the system. The Hamiltonian is strictly speaking a mathematical operator, this means that it acts on a variable to give a result. The wave function is a vector that represents the amplitude of an electron wave, and this stems from the wave particle duality that is fundamental to quantum theory, [3].

$$H\Psi = E\Psi \tag{4.1}$$

Electrons take up specific energy levels within an atom or molecule. These energy levels are discrete, as can be seen from solutions of the Hamiltonian for electronic systems [3]. In this case the Hamiltonian is a measure of the energy of electronic states. For a many electron atom this can be seen in the equation 4.2, where h is Planck's constant, M_e is the mass of an electron and ϵ_0 is the permittivity of free space.

$$H = -\frac{h}{4\pi m_e}\sum_i \nabla_i^2 - \sum_i \frac{Ze^2}{4\pi\epsilon_0 r_i} + \sum_{i<j}\frac{e^2}{4\pi\epsilon_0 r_{ij}} \tag{4.2}$$

Solutions of this equation are used to predict the energy levels that electrons can obtain within an atom. The methods of doing so are beyond the scope of this thesis. The final term in equation 4.2 represents the repulsion between the electrons. In the case of hydrogen, this term can be removed. For an atom such as helium, which is very important in plasma processing, and more specifically plasma enhanced chemical vapour deposition, there are two valence electrons. This slightly complicates matters due to coulombic repulsion force between the two electrons.

Pictorial representation of these energy levels for a helium atom can be seen in figure 4.1. The Pauli principle dictates how the electronic levels are occupied, with no two electrons having the same set of quantum numbers. Transitions between these levels vary due to the selection rules which rise from a quantum treatment of the systems involved.

Electronic states within a molecule are a bit more complicated, owing to the bonding between the various atoms, [204]. No further treatment is required, as it would be of only slight relevance to the plasmas measured during the course of this work.

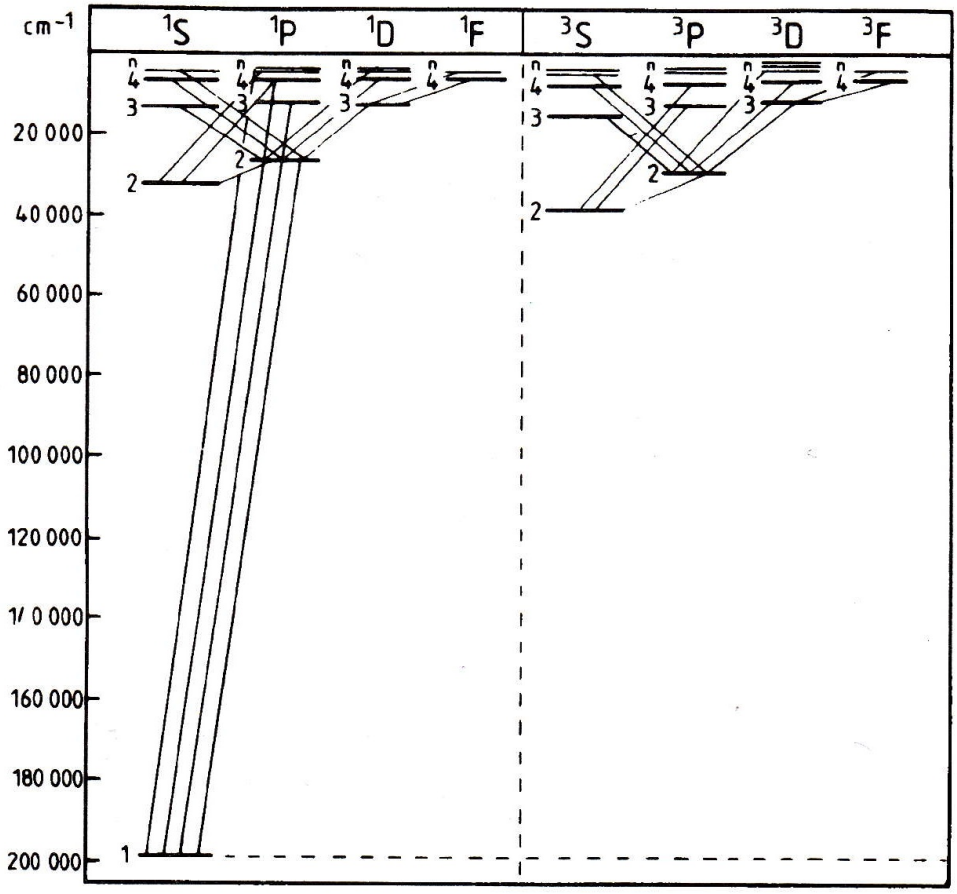

Figure 4.1: Grotrian diagram showing energy levels in atomic helium, from Modern Spectroscopy by J. M. Hollas, [3]

The Boltzmann distribution, seen in equation 4.3, can relate to the relative population of electronic levels. As can be seen in the equation, the ratio of the population, N, of one level, n, to another, m, is related to the ratio of the degeneracy, g, of the levels and the energy, E, and temperature, T.

$$\frac{N_n}{N_m} = \frac{g_n}{g_m} \exp\left(\frac{E_n - E_m}{kT}\right) \tag{4.3}$$

Excited species in plasmas

The use of optical emission spectroscopy has many applications in plasma spectroscopy, [205]. In fact, several key plasma parameters can be measured through it's use. Electron temperature, plasma density and ion and neutral densities can all be determined. The knowledge of these parameters is of great use as the parameters govern the reactions occurring within the plasma, and the rates of these reactions. Both of which are of course key in the production of thin films.

An important result in the study of plasma emission, is Saha's equation, [206], which governs ionisation equilibrium. This can be seen in equation 4.4. χ in this case is the ionisation energy; the N's refer to the density of the neutrals ($_0$), electrons ($_e$) and ions ($_i$); g the statistical weight of the particular electron level. Other terms are as defined earlier.

$$\frac{N_e N_{i,n}}{N_{0,m}} = \frac{2(2\pi mkT)^{\frac{3}{2}}}{h^3} \frac{g_{i,n}}{g_{0,m}} \exp\left(-\frac{\chi + E_n - E_m}{kT}\right) \tag{4.4}$$

The importance of Saha's equation is in the application of a Boltzmann distribution to a plasma situation. This allows for a variety of predictions to be made, however it must be remembered that these predictions are based upon an assumption of local thermal equilibrium within the plasma.

Electron transitions within a given species cause photon emissions at different wavelengths, λ_{mn}, the subscripts denoting the upper, m, and lower, n, energy levels. The Boltzmann plot method [207], which has been used for non-thermal atmospheric pressure plasmas, can be used to estimate the excitation temperature of the plasma from the relative intensities, I_{mn} of emission lines of atomic species, assuming a Boltzmann distribution of electron energy. This is calculated using equation 4.5.

$$\ln\left(\frac{I_{mn}\lambda_{mn}}{A_{mn}g_m}\right) = \ln\left(\frac{Nhc}{Z}\right) - \frac{E_m}{kT_e} \tag{4.5}$$

Where , A_{mn} is the Einstein A coefficient or transition probability between the higher and lower states, g_m is the statistical weight (or degeneracy) for the higher electron state, N is the number of atoms, h is Plancks constant, c is the speed of light, Z is the partition function for the species, E_m is the energy of the upper level and k is the Boltzmann constant. The excitation temperatures can subsequently be calculated by linear interpolation.

Another use of optical emission spectroscopy is to measure the electron density of a plasma. This is done by calculating the stark broadening of the Hβ line, [208]. Due to the low resolution of the optical emission spectrometer used for the work covered in this thesis, this measurement is not possible.

Measurement of optical emission

A typical emission spectrometer only requires some form of detection and monchromator, as the plasma provides the light source. This consists of a lens, so that light can be collected and focused on a diffraction grating or prism. The diffraction grating or prism acts to disperse the incident light by wavelength. The light is then detected by spatially arranged sensors, which are generally charge coupled device arrays.

4.3 FTIR Spectroscopy

Molecular rotation and vibration

Rotational motion of a molecule can be visualised as the molecule rotating about its axis of symmetry. Depending on the shape of the molecule, there are several different forms this rotation can take. There are also many different energy levels of rotation, which can be visualised as faster rotation. Like electronic energy levels, these energy levels are quantized, which means that molecules observe strict discrete rotational energy levels. These pure rotational transitions depend on the molecule having a permanent dipole moment [209].

Vibrational motion of a molecule can be regarded as the constituent atoms oscillating on their bonds. Again, there are several different vibrational modes, which can be visualised as the ways that the atoms can vibrate. There are also many different energy levels of vibration. Again, these energy levels are quantized, in other words there are discrete vibrational energy levels. These vibrational transitions depend on a change of dipole moment during absorption of infrared photons, [209].

The Born Oppenheimer approximation allows for the total energy of a molecule to be the summation of the electronic, vibrational and rotational energies. This also implies that all three transition types are independent of one another.

The measurement technique

Infra red spectroscopy is generally carried out by the use of Fourier transform spectroscopy. This involves the measurement of a range of frequencies simultaneously, which can be reconstructed through the use of a Fourier transform.

In order to generate a known range of frequencies, a Michelson interferometer is used, see figure 4.2. In an interferometer, light is split by means of a beamsplitter, and half is directed to a moving mirror. The two paths of light are recombined and constructively and destructively interfere with one another. An interferogram is produced, upon which a Fourier transform can be carried out which produces an infrared spectrum. It is the measurement of the inteferogram that enables the measurement of the full range of the infrared spectrum.

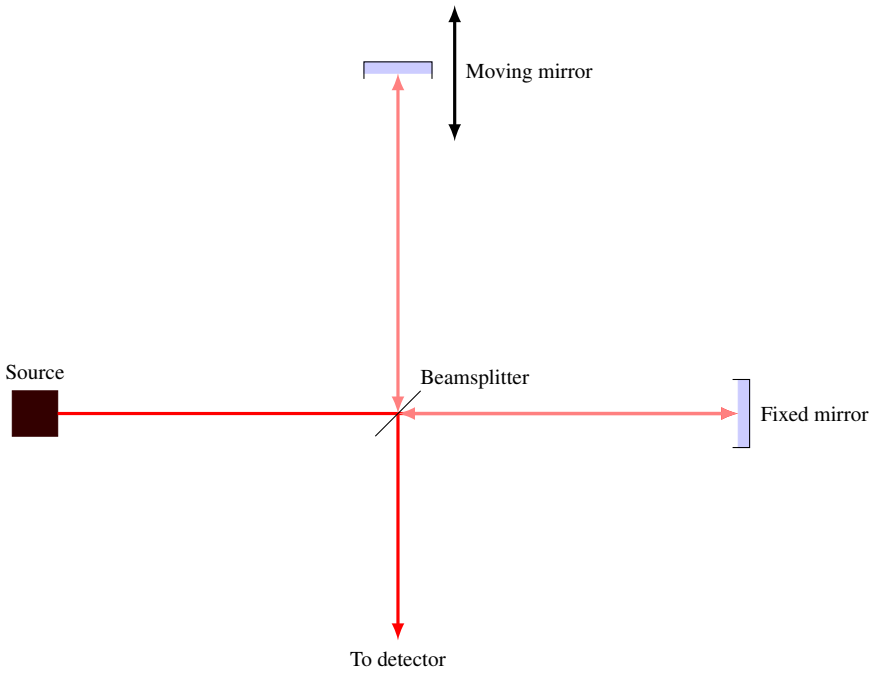

Figure 4.2: The Michelson interferometer, [4].

Previously the infra-red light had to be diffracted onto the detector through some kind of diffraction grating, similar to optical emission spectroscopy. The introduction of Fourier transform spectrometers has increased speed of acquirement of signals, and also improved the resolutions that can be achieved. The two primary advantages of Fourier transform spectrometers are known as the Fellgett and Jaquinot advantages, [210].

The Fellgett advantage relates to the signal to noise ratio that can be achieved. In a conventional scanning spectrometer, each resolution element is observed for only a

fraction of the scanning time. Fellgett's advantage occurs in Fourier transform spectra because signals from all resolution elements are detected all the time, [210]. This results in the multiplex advantage where the signal to noise ratio of spectra taken with the same resolution and the same measurement time is $n^{0.5}$ times greater for an FT instrument than that obtained on the grating instrument, where n is the number of resolution elements, [210]. This is a large advantage over traditional dispersive methods.

The Jaquinot advantage is that as there is no dispersive element in the spectrometer cutting down the energy of the light outputted from the source, then all light gathered from the source can be used to measure a given sample. This implies that greater amount of light is detected at the detector, and so there is a significant gain in the signal to noise ratio as a result.

Treatment of results

Concentrations can be derived from recorded spectra with the use of calibrated spectra, generally provided by Pacific Northwest [211] or NIST. The calculation procedure is an application of the Beer Lambert law established in the subsequent section, and uses the integration area of the absorption peaks. This area is then compared to that of the calibrated spectra, and with the knowledge of the path length a concentration can be extracted.

It is also possible to produce a set of calibration spectra, where a pure chemical is measured at several known concentrations. This requires several repetitions of each experimental condition to ensure accuracy.

4.4 The Beer Lambert Law

The use of light to identify and measure chemical species has a long history. Underpinning this use is the Beer Lambert law, which enables much to be calculated from the measurements. The Beer Lambert law, [212], is shown in equation 4.6, with symbols defined in figure 4.3:

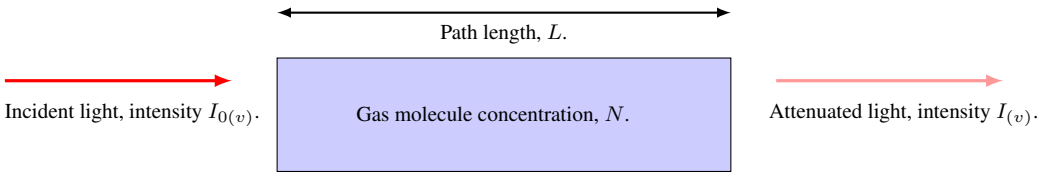

Figure 4.3: Beer Lambert law symbols.

$$\ln\left(\frac{I_{0(v)}}{I_{(v)}}\right) = \sigma N L \tag{4.6}$$

σ is defined as the absorption cross-section at a given wavenumber, v. The units of σ are cm^2 molecule^{-1}, and N are molecules. Spectra can be reported in other formats, such as absorbance (A), absorptance (Ab) and transmission (Tr), and these can be seen in equations 4.7 through 4.9.

$$A = \log\left(\frac{I_{0(v)}}{I_{(v)}}\right) \tag{4.7}$$

$$Ab = \frac{(I_{0(v)} - I_{(v)})}{I_{0(v)}} \tag{4.8}$$

$$Tr = \frac{I_{(v)}}{I_{0(v)}} \tag{4.9}$$

Concentrations of specific species can be calculated in many different units, mole fraction (x) for example. This is calculated using the ideal gas law seen in equation 4.10,

with N_a being Avogadro's number, T the gas sample temperature, P the gas pressure and R being the gas constant.

$$x = \frac{NRT}{PN_a} \tag{4.10}$$

It is now important to examine the absorption coefficient, [213], further. The absorption coefficient represents the extent to which a chemical species absorbs light, and is represented by equation 4.11.

$$\sigma = Sg(v - v_0) \tag{4.11}$$

Where S represents the linestrength of a particular spectral band, and has units cm molecule^{-1}. $g(v - v_0)$ is the lineshape function, units cm, and is normalised as seen in equation 4.12.

$$\int_{-\infty}^{\infty} g(v - v_0)\, dx = 1 \tag{4.12}$$

The line shape function takes into account a range of effects on the wavelength distribution of the light emitted. One such effect is natural line broadening which is always present, but is much more evident at higher pressures [213] where interactions between molecules are a lot more common. Collisions and interactions between molecules lead to a considerable variation in their absorption of incident light. This means that the spectral feature will be spread out across the wavelength leading to a Lorentzian line shape function, mathematically represented in equation 4.13

$$g(v - v_0) = \left(\frac{1}{\pi}\right) \frac{\gamma_s}{(v - v_0)^2 + \gamma_s^2} \tag{4.13}$$

Where γ_s is the half width at half maximum for a given spectral feature. Generally this value is found from databases such as Hitran [214] and is given at standard temperature (T_0) and pressure (P_0) for a particular chemical species. The effect of collisions between molecules will change at different temperatures and pressures. To correct for this collisional line broadening, equation 4.14 can be used [213].

$$\gamma_s = \gamma_{n0} \left(\frac{P}{P_0}\right) \left(\frac{T_0}{T}\right)^{\frac{1}{2}} \tag{4.14}$$

For lower pressures, Doppler broadening is more dominant, [213]. This effect is down to the thermal motion of the chemical species leading to blue and red shifts of the light emitted or absorbed by them [206]. The effect is commonly known as the Doppler effect, hence Doppler broadening. The distribution of speeds in a gas can be described by the Maxwell distribution, [215], and so a Gaussian line shape function is used, as represented in equation 4.15.

$$g(v - v_0) = \left(\frac{1}{\gamma_D}\right) \left(\frac{\ln 2}{\pi}\right)^{\frac{1}{2}} \exp\left(\frac{-(v - v_0)^2 \ln 2}{\gamma_D^2}\right) \tag{4.15}$$

Where γ_D is calculated as in equation 4.16.

$$\gamma_D = \left(\frac{V_0}{c}\right) \left(\frac{2kT \ln 2}{m}\right)^{\frac{1}{2}} \tag{4.16}$$

In equation 4.16, k is the Boltzmann constant, c is the speed of light and m is the mass of a molecule.

The Voigt profile is developed for situations where combinations of line broadening effects occur. In particular this tends to be in measurement situations below atmospheric pressure, but above the pressure at which Doppler broadening dominates. The Voigt profile is the result of a convolution of the Lorentzian and Gaussian profiles and is evaluated in equation 4.17.

$$g(v - v_0)\, dx = \int_{-\infty}^{\infty} \frac{e^{-t^2}}{(x+t)^2 - y^2} dt \tag{4.17}$$

Where x, y and t are evaluated in equations 4.18 through 4.20, $v*$ is the adjusted wavenumber due to the movement of the moving species.

$$x = \frac{(v - v_0)\,(\ln 2)^{\frac{1}{2}}}{\gamma_D} \tag{4.18}$$

$$y = \frac{\gamma_L\,(\ln 2)^{\frac{1}{2}}}{\gamma_D} \tag{4.19}$$

$$t = \frac{(v * -v_0)\,(\ln 2)^{\frac{1}{2}}}{\gamma_D} \tag{4.20}$$

Now, it is evident that due to the error function in equation 4.17, the integral can not be solved analytically. The presence of the positive and negative infinities also complicates numerical solutions. A common technique that is used to calculate the Voigt profile are adaptations of Gaussian quadrature, as expanded in the following: [216], [217], [218], [219]. Equation 4.21 illustrates the method, where t_j and w_j are the roots and weights of a polynomial expansion of the function $W\,(t)$ to $N - 1$.

$$\int_a^b W\,(t)\, f\,(t) \approx \sum_{j=0}^{N-1} w_j f\,(t_j) \tag{4.21}$$

The most commonly used technique is Gaussian-Hermite quadrature, which is useful for the computation of the Voigt profile, as can be seen in equation 4.22. This process is carried out with the coefficients $(t - j)$ and weights (w_j) of the Hermite polynomial, the form of which is represented by the recurrence relation seen in equation 4.23, [220].

$$\int_{-\infty}^{\infty} e^{-t^2} f(t) \approx \sum_{j=0}^{N-1} w_j f(t_j) \tag{4.22}$$

$$h_{j+1} = 2xH_j - 2jH_{j-1} \tag{4.23}$$

A comparison between the three lineshapes for a hydrogen chloride spectral feature at 5739.26 cm^{-1} is provided in figure 4.4. The line labelled "Broadening at Atmospheric Pressure" is simulated at atmospheric pressure using a Lorentzian lineshape. The line labelled "Doppler Broadening" is simulated at a pressure of 0.1 atmospheres using a Gaussian lineshape. A Voigt lineshape is used to simulate the line labelled "Intermediary Broadening", which is simulated at 0.5 atmospheres.

For the purposes of the majority of work presented in this thesis, where the processes investigated are at atmospheric pressure, the use of a Lorentzian lineshape will suffice for the analysis of spectra.

The line strength of a particular transition is temperature dependant. This is due to the way energy is distributed within molecules, and a more in depth analysis is presented in subsequent chapters.

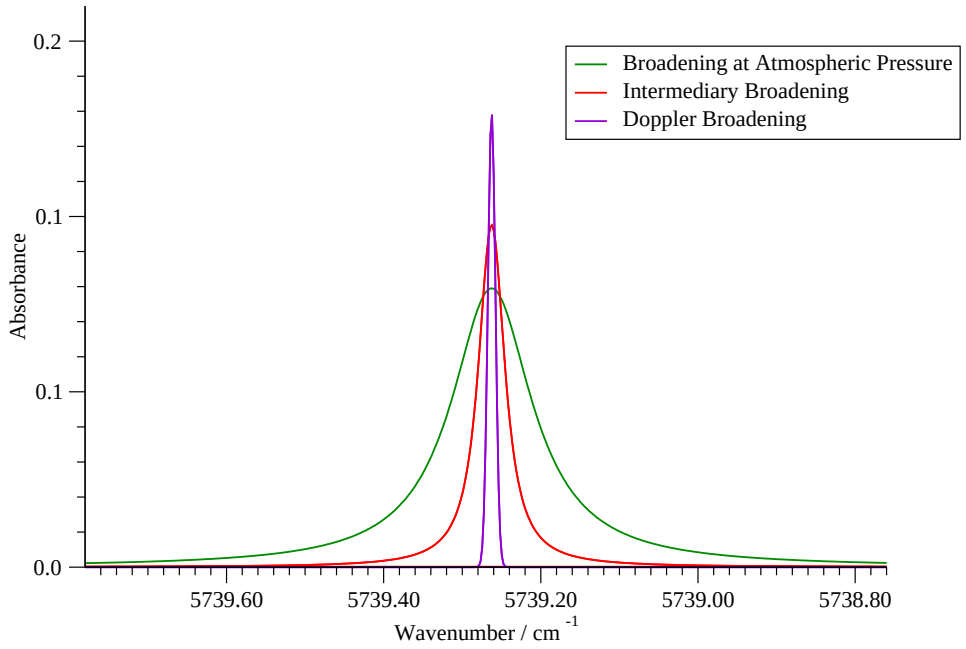

Figure 4.4: Hydrogen chloride spectral feature simulated for 500 ppm hydrogen chloride in nitrogen at atmospheric pressure and room temperature, measured over a path length of 100 cm.

Fitting routines

Once a spectrum has been recorded through the use of various spectroscopic techniques, relevant information requires extraction. Non linear least squares fits are generally used to analyse recorded spectra, especially for the calculation of concentrations of chemical species. A commonly used algorithm for non linear least squares fits is the Levenberg-Marquardt method which is employed by both the excel and Microcal Origin software packages, but others such as Chang and Shaw can be used[219]. The spectra are at present analysed using the Origin package which relies on a Levenberg-Marquardt algorithm.

The Levenberg-Marquardt algorithm, [221], is a combination of the Newton method

and Taylor series methods of fitting parameters, [220]. In the case of the spectral features recorded by the laser diode spectroscopy technique outlined in the next section, a Lorentzian line shape is fitted to the spectra. The Levenberg-Marquardt algorithm minimises the squared error between the lineshape, and the recorded data. With all measurement parameters known, it is then possible to extract an average concentration from the fit parameters. Hence the technique's usefulness.

4.5 Laser diode spectroscopy

Laser is an acronym that stands for **L**ight **A**mplification by **S**timulated **E**mission of **R**adiation, [222]. Original work was carried out with microwaves in the early 1950s, [223], but the principles for shorter wavelengths are the same, and were in fact applied to infrared and visible light several years later, [224]. The basic operating principles are briefly treated here.

Stimulated emission occurs by the action of a photon on an electron, causing that electron to drop to a lower energy level. In doing so a second photon with the same wavelength, phase, polarization and direction of movement as the original photon is created, [225]. Within a laser a material is used that has it's electrons continually raised to an excited electronic state. While the electron transitions are occurring, emission and absorption of photons occurs, as well as stimulated emission. Once the number of electrons in a higher electronic state is higher than that of the lower, ground state, population inversion has occurred. This implies that stimulated emission is the dominant process, and the number of photons are effectively amplified. Generally this process occurs within a reflective, encased chamber, known as a resonant optical cavity. Due to the stimulated emission, the light that is produced is highly coherent, and at a fixed wavelength.

Coherent light at a fixed wavelength that can be directed is of great use in spectroscopy, where direct line of site measurements can be used to build up spatial profiles of various species. The laser spectroscopy technique also has a high signal to noise ratio, due to the coherence and power of the light being measured.

The lasers used for the work presented in this thesis are diode lasers. Laser diodes use a solid state medium as the material that is excited. These materials are made up of a thin semiconducting layer (generally grown by a chemical vapour deposition process) on the surface of a crystal wafer. These layers are, for the most part, p-n junction semiconductors. A current is passed across the crystal to induce electron and hole mobility across the semiconducting region. These holes and electrons recombine, and in doing so spontaneous emission occurs, which induces stimulated emission.

The current can be changed to control the wavelength of the laser light, [213]. The temperature is changed by passing different levels of current through the diode, which in turn modulates the wavelength the laser operates at. The current can be increased, such that the wavelength of the laser increases, and this method can be used to sweep the wavelength of the laser over one absorption peak. A suitable detector needs to be used in conjunction with adequate data collection.

Typically, detection of the laser is carried out using a photodiode. Again, these devices rely on semiconductors. A photon incident on the photodiode will cause electron and hole generation in the semiconductor, inducing a current to flow. The magnitude of the current is proportional to the intensity of the light incident on the photodiode. The timing of the signal from the photodiode is synchronised with that of the current sweeping through the laser diode, and is calibrated such that the wavelength can be known. A wave-meter is generally used to calibrate the position of the laser.

Tuneable laser diodes have a high potential for spectroscopy, [226]. They can be used

to investigate one spectral feature and of course they have the advantage that they can be used to spatially and temporally resolve concentration profiles. They are also able to detect concentrations of chemicals to parts per million levels and less, with a low signal to noise ratio.

There are a few disadvantages with the technique, a major one is to do with the limited spectral range of the laser. Typically it is only possible to examine one spectral feature, although new developments are improving upon this limitation, [142]. It should also be clear that the magnitude absorption peak measured is dependent upon the temperature and pressure of the medium measured, so this information is essential for the interpretation of results. Any concentration derived is also an average concentration along the line of sight, and this should be taken account of during interpretation.

The use of laser diode spectroscopy has potential to provide *in situ* concentration measurements of a particular species within a chemical vapour deposition process, and as such, can be used to both infer and verify models of the reactor.

Chapter 5

Chemometric techniques

Chemometric techniques are used for multivariate processes, which can produce large data sets. The techniques are applied to attempt to get understanding of the complexity, and to try and identify key variables and correlations between a variety of measurements. The use of experimental design, or parametric modelling, has been used to investigate multivariate processes. Principal components analysis can be used to try and investigate correlations within large datasets where patterns are not immediately obvious.

5.1 Use of chemometrics in chemical vapour deposition processes

The use of chemometric techniques to analyse and enhance understanding of chemical vapour deposition processes has been limited at best, with application to plasma enhanced chemical vapour deposition at atmospheric pressure non-existent. This is surprising, as chemometrics can be used to analyse multivariate processes in a methodical manner, with an optimum amount of experimentation. Chemical vapour deposition at atmospheric pressure is an inherently multivariate process, and so the use of chemometrics in the form of experimental design seems a good fit.

There has been some use of experimental design in low pressure plasma processing, with deposition, surface treatment, and etching being investigated parametrically. Previous use of the experimental design methodology will be briefly discussed here.

The deposition of diamond-like carbon using plasma enhanced chemical vapour deposition has been studied using a four factor experimental design, [227]. This work identified the importance of process gas dilution on the hardness of the films produced, a key property of diamond like carbon films. The importance of other factors were also identified, showing the importance of the experimental design approach in improving thin film deposition processes. Where this work perhaps falls down, is in the lack of inclusion of other process measurements which would perhaps help with identification of the mechanism behind the formation of harder films.

Fluorocarbon film deposition by radio frequency plasma has been profiled through the use of an experimental design methodology, [228]. The methodology was used to examine the response of the process to identify the important parameters for the growth rate of the films. In addition the response of the refractive index was examined. The work succeeded in identification of the important factors, but lack of measurements again meant that underlying mechanisms could not be identified.

The surface modification of polycarbonate surfaces using radio frequency plasmas has also been studied using experimental design methodology, [229]. A statistical model was fitted to the surface energy results, and this was then used to further optimise the surface treatment process.

Etching is a similar process to deposition, and involves similar mechanisms. At the very least it is definitely as complex as the film deposition process. The etching of polysilicon, [230], has been studied with an experimental design methodology. Models were subsequently fitted to the results for several plasma parameters, as well as the etch rate. The methodology was used with optimisation of process parameters as the aim, which was amply met.

More recently, the response surface methodology has seen further use in the etching

of silicon wafers, [231], similar to that in the semiconductor industries. The work was carried out using *in situ* optical monitoring verified with *ex situ* measurements of the silica wafers. The work was successful in its goal of improving process characterisation, and this is in line with the aims of the work in this thesis.

Principal components analysis has seen even less use. The assessment of the key properties for high temperature superconductivity perhaps one of the few instances of the techniques use for analysing chemical vapour deposition, [232]. This work involved the gathering of several datasets from the literature on superconducting films deposited by chemical vapour deposition. Principal components analysis was then applied to this information, to establish whether there was any underlying structure to the data. This was achieved, highlighting the usefulness of principal components analysis.

In summation, there is some use of chemometric techniques applied to chemical vapour deposition and similar processes. This use is limited though. On the occasions where they have been used, they have proved effective in improvement of processes or in a deeper understanding of the process. In terms of process optimisation, the economic worth of such techniques is obvious.

5.2 Experimental design

In chemical vapour deposition there are a wide range of variables that can be controlled, however it is not always evident what effects these control variables have on the films produced, as the variables can effect each other strongly. For example, in any given deposition, the combination of the total flow rate and the concentration of precursor can combine to have an unknown effect on the growth rate of a film. Standard experiments would only look at one of these variables in isolation from the other, and this approach

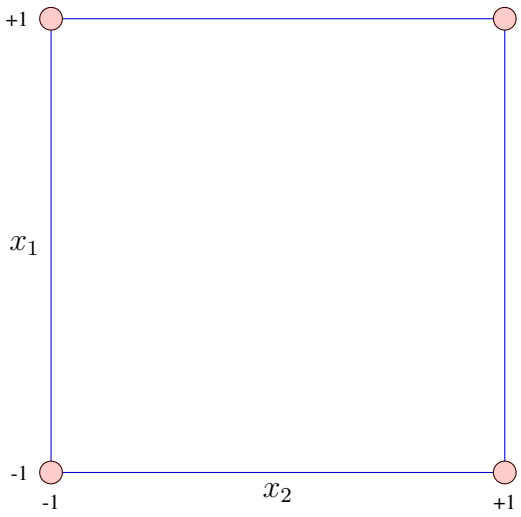

Figure 5.1: Simple experimental design.

tends to be typical across a wide variety of groups investigating various chemical vapour deposition processes. There is a more efficient way of investigating such processes.

Take the case of two factors or control variables, how best to design an experiment to maximise the information derived from it? In figure 5.1, a simple two variable design is presented, with the red circles representing experiments. A design matrix, $\mathbf{D}$, can be established from this design, and this can be seen in table 5.1. This design allows us to model the results to a simple linear equation as presented in equation 5.1 ($\hat{y}$ being the data set model) using multiple linear regression. A matrix of coefficients, $\mathbf{b}$, are calculated by taking the inverse of the design matrix, $\mathbf{D^{-1}}$, and multiplying the experimental results, $\mathbf{y}$, by it. This method is represented in equation 5.2. From just these four experiments it is possible to examine how the two investigated variables affect the measured results by examining the magnitude of the related coefficient. Evidently, it is also possible to see how they combine together to affect the results.

$$\hat{y} = b_0 + b_1 x_1 + b_2 x_2 + b_{12} x_1 x_2 \tag{5.1}$$

x_0	x_1	x_2	x_1x_2
1	1	0	0
1	1	1	1
1	0	0	0
1	0	1	0

Table 5.1: Design matrix for simple two variable experimental design.

$$\mathbf{b} = \mathbf{D^{-1}}.\mathbf{y} \tag{5.2}$$

Of course chemical vapour deposition is a more complex process with more variables and more complex interactions between them. Therefore, a more in depth experimental design is required. Before this can be established, it is perhaps prudent to examine how best to maximise the information gathered, and to do this in a reliable manner. As a model is being fitted to the experimental results, there will be the issue of degrees of freedom, (D_f) [233], [234]. The degrees of freedom, in statistical terms, is the number of values that can vary for a given result to remain true. In the experimental design illustrated in figure 5.1, four experiments (N) are used to fit a four parameter (V) model (equation 5.1). The degrees of freedom are calculated using the expression in equation 5.3, and we can see that for this system it is zero. Reducing the number of parameters, or increasing the number of experiments would raise the degrees of freedom.

$$D_f = N - V \tag{5.3}$$

At this point, some discussion of the experimental error is necessary. This simple experimental design that has been established has no way of checking for this. Replication of experimental points can provide this information on experimental error, [235]. Replication of experimental points (R) also has some bearing on the degrees of freedom, and

this can be seen in equation 5.4.

$$D_f = N - V - R \tag{5.4}$$

With the increase of degrees of freedom of the experimental design, it is possible to apply a range of statistical tests to the fitted models and the data that they are fitted to. These statistical tests can give a wealth of information about the measured processes. For a more in depth description, refer to subsequent sections on the Student's t-test and the F-test.

There are several methods for extending an experimental design [236]. A fractional factorial can be used, which involves two experiments for two factors (four experiments for three variables) and allows for a linear model to be plotted. This type of design is extremely useful for an initial investigation as it involves the minimal number of experiments. For a more in depth study, as presented in this thesis, it is not rigorous enough in identifying higher order effects. A star design is another type of design that incorporates three levels of the chosen variable. This allows the squared terms of a given model to be investigated. This is, again, not rigorous enough for chemical vapour deposition investigations, which requires investigation of the combined effects of the variables.

The extended experimental design can be provided by using a central composite experimental design with three factors, [236], this is illustrated in figure 5.2. The design matrix for such a design can be seen in table 5.2. It is a combination of a full factorial design and a star design with replication at the centre of the examined process window. This design has been chosen as it provides both an efficient means to study both the higher order effects of the variables being investigated, and to assess the repeatability of the process. The codings of low (-1), medium (0) and high (+1) enable the second order and interaction effects of a chemical vapour deposition process to be investigated. Equation

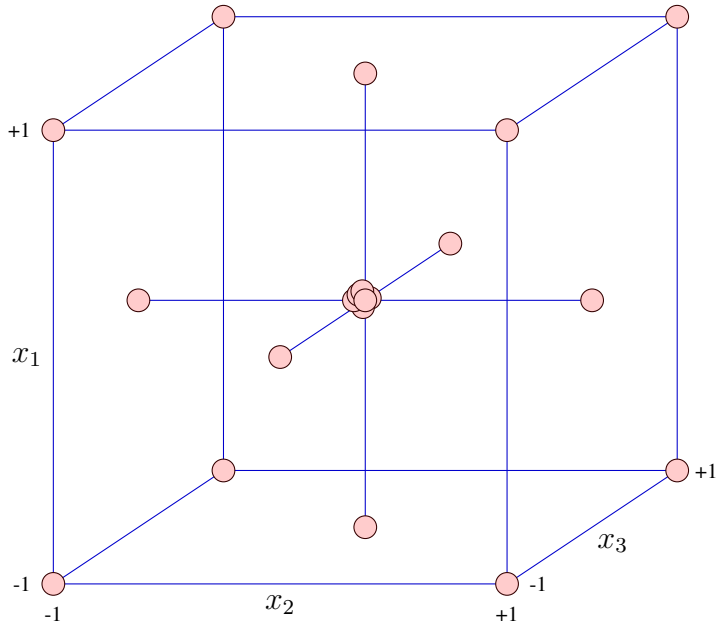

Figure 5.2: Central composite design.

5.5 shows the form of the statistical model fitted to experimental results from a central composite design.

$$\hat{y} = b_0 + b_1x_1 + b_2x_2 + b_3x_3 + b_{11}x_1^2 + b_{22}x_2^2 + b_{33}x_3^2 + b_{12}x_1x_2 + b_{13}x_1x_3 + b_{23}x_2x_3 \quad (5.5)$$

The coefficients are calculated by taking design matrix, D, and multiplying the experimental results by the pseudo-inverse. This is done by multiplying the design matrix with the transpose of the design matrix, D' and can be seen in equation 5.6.

$$\mathbf{b} = (\mathbf{D'}.\mathbf{D})^{-\mathbf{1}}.\mathbf{D'}.\mathbf{y} \quad (5.6)$$

Number	x_0	x_1	x_2	x_3	x_1^2	x_2^2	x_3^2	x_1x_2	x_1x_3	x_2x_3
1	1	-1	-1	-1	1	1	1	1	1	1
2	1	-1	-1	1	1	1	1	1	-1	-1
3	1	-1	1	-1	1	1	1	-1	1	-1
4	1	-1	1	1	1	1	1	1	1	1
5	1	-1	0	0	1	0	0	0	0	0
6	1	0	-1	0	0	1	0	0	0	0
7	1	0	0	-1	0	0	1	0	0	0
8	1	0	0	0	0	0	0	0	0	0
9	1	0	0	1	0	0	1	0	0	0
10	1	0	1	0	0	1	0	0	0	0
11	1	1	-1	-1	1	1	1	-1	-1	1
12	1	1	-1	1	1	1	1	-1	1	-1
13	1	1	0	0	1	0	0	0	0	0
14	1	1	1	-1	1	1	1	1	-1	-1
15	1	1	1	1	1	1	1	1	1	1
16	1	0	0	0	0	0	0	0	0	0
17	1	0	0	0	0	0	0	0	0	0
18	1	0	0	0	0	0	0	0	0	0
19	1	0	0	0	0	0	0	0	0	0
20	1	0	0	0	0	0	0	0	0	0

Table 5.2: Design matrix for central composite experimental design.

Student's t-test

The Student's t-test can then be used to analyse the importance, or influence, of each of the factors, [236]. In other words, to examine whether the variable effects on the model is greater than the experimental error. This is undergone by taking the initial step to calculate the pseudo matrix, the result of which is labelled $\mathbf{T}$ and can be seen in equation 5.7. This produces a square matrix, with the diagonal elements being the variance (var) of each coefficient.

$$\mathbf{T} = (\mathbf{D}'.\mathbf{D})^{-\mathbf{1}} \tag{5.7}$$

The mean error sum of squares (err_m) is also calculated. The t ratio, t_{rat}, for each coefficient can then be calculated as seen in equation 5.8. These t ratios are then used to obtain the statistical significance of each coefficient by applying a two tailed t-distribution. A significance higher than 95 % indicates that the coefficient is important, as this indicates a low chance that the correlation is due to coincidence.

$$t_{rat} = \frac{b}{\sqrt{err_m var}} \tag{5.8}$$

The results of the t-test for each coefficient of the model can be used to refine and improve the model. This is done in conjunction with the F-test, and is discussed in the next section.

The F test

The F test is another test that is used to calculate the goodness of fit of a model, given a certain replicate error. The F ratio (F_{rat}) is the ratio of the mean square lack of fit (S_{lof}) to the replicate error (S_{rep}) calculated. This is then analysed against a one tailed F-distribution, again needing a significance of 95 % to indicate good repeatability and a good fit of the model.

$$F_{rat} = \frac{S_{lof}}{S_{rep}} \tag{5.9}$$

The combination of the t and F tests can be used to check a good fit of the model to the experimental data. This is done by assessment of the result of the t-tests. If coefficients are found to be insignificant on the model using this test, they are removed, and a new model is fitted to the data. The result of the F-test should improve, especially in cases where the model has too many parameters. This process could take several iterations, with the goal being a more robust model which is statistically significant compared to the experimental error.

Response surfaces

Once the model has been fitted and statistically tested, interpretation and subsequent process optimisation is required. This can be carried out in two ways. The first is by displaying the model as a series of response surfaces. Secondly the model can be differentiated to calculate optimum conditions for a given measured quantity.

Visualisation is achieved by fixing one of the three control variables, whilst plotting the other two. The resultant two dimensional plot can be referred to as a response surface.

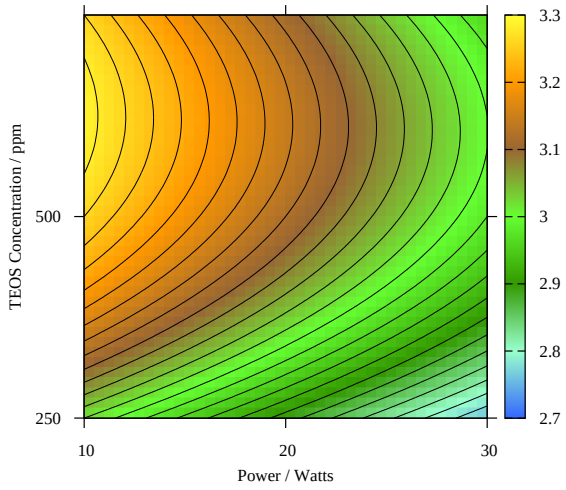

Figure 5.3: Response surface for Mohs hardness, with oxygen concentration fixed at 0.1 %.

These response surfaces can be analysed to identify the optimum conditions for a film property, and to evaluate the effects of the control variables on the measured property.

An example response surface can be seen in figure 5.3, which has been adapted from results published in reference [237], and this represents the Mohs hardness of a silica film produced from a plasma enhanced chemical vapour deposition process. This response surface has been produced with the oxygen concentration fixed at 0.1 %, and so it allows for evaluation of the effects of the other two process variables on the Mohs hardness of the film produced. Subsequently, this means that the response surfaces are interpolations of five data points, however the repetitions at the central point of the response surface serve to validate the overall response surface. In this case the optimum conditions for film hardness are at a higher precursor concentration and low deposited power. Increasing the power tends to reduce the hardness of the films produced, whilst increasing the precursor concentration increases the hardness.

5.3 Principal components analysis

Principal components analysis is a method for breaking down large data sets into several principal components, which, when plotted against each other, can reveal connections and correlations underlying the data. The principal components are vectors of numbers that are orthogonal to the data set (**X**) and each other, and are defined as in equation 5.10.

$$\mathbf{X} = \mathbf{S.L} + \mathbf{E} \tag{5.10}$$

S and **L** are the scores and loadings, and consist of vectors corresponding to the principal components. In rows in the case of the loadings, and in columns in the case of the scores. The matrix **E** is the error of the abstract model from the data.

Commonly data has to be preprocessed before being reduced to its principal components. There are three common ways of doing this. Mean centering involves calculating the mean for each column and subtracting this from each of its elements. An adaptation of this is dividing through by the population standard deviation of the column as well, and this is known as standardisation. Row scaling is the final technique, and this involves the scaling of the rows to a constant value.

The NIPALS algorithm, [238], is used to identify principal components, one vector at a time. Typically the column of the data set matrix with the highest sum of squares is selected. This is the first estimate of the scores vector, $\hat{\mathbf{s}}$, of the first principal component. The loadings vector of the principal component, ${}^{u}\hat{\mathbf{l}}$ is calculated as in equation 5.11.

$${}^{u}\hat{\mathbf{l}} = \frac{\hat{\mathbf{s}}'.\mathbf{X}}{\sum \hat{s}^2} \tag{5.11}$$

The loadings vector is then normalised to gain $\hat{\mathbf{l}}$, as can be seen in equation 5.12.

$$\hat{\mathbf{l}} = \frac{{}^{u}\hat{\mathbf{l}}}{\sqrt{\sum^{u} \hat{l}^2}} \tag{5.12}$$

A new scores vector, ${}^{n}\hat{\mathbf{s}}$, is calculated as shown in equation 5.13.

$${}^{n}\hat{\mathbf{s}} = \mathbf{X}.\hat{\mathbf{l}}' \tag{5.13}$$

The sum of squares of the new scores vector is checked with the sum of squares of the old scores vector. If this difference is reasonably small, the scores and loadings vector has been calculated for the first principal component, otherwise a new loadings vector is calculated from equation 5.11 and the procedure is repeated. If the first principal component has been found, the residual data set matrix is calculated as in equation 5.14.

$${}^{r}\mathbf{X} = \mathbf{X} - \mathbf{s}.\mathbf{l} \tag{5.14}$$

The residual data set matrix is then used to calculate subsequent principal components by repeating the above procedure.

Singular value decomposition is another method that can be used to calculate principal components, and this identifies all the principal components simultaneously. This has the advantage that many algorithms have been written to perform singular value decomposition, and maths packages such as Matlab have the method as a standard function. For large datasets however, there would be a large number of principal components produced, and so the processing time would be quite long.

The method decomposes a matrix into two sets of eigenvectors and its singular values, [239]. The eigenvectors can then be used to calculate the scores and vectors of the

principal components. The NIPALS method is used for principal components analysis in this thesis.

An important factor in principal components analysis is the estimation of how much of the dataset is modelled by a given principal component. This is done by calculating the eigenvalue, g_a, [236], of each principal component, as shown in equation 5.15. The sum of the eigenvalues of all principal components is exactly the same as the sum of the squared values of the original preprocessed dataset. Thus, the percentage of the data modelled by each principal component can be estimated, as seen in equation 5.16.

$$g_a = \sum_{i=1}^{I} s_{ia}^2 \tag{5.15}$$

$$V_a = 100 \frac{g_a}{\sum_{i=1}^{I} \sum_{j=1}^{J} x_{ij}^2} \tag{5.16}$$

The aim of principal components analysis is not necessarily to provide a firm physical connection for the data. It is instead a way to simplify large, multivariate datasets, and reduce them to an easily explorable set of numbers. It can perhaps be described as numerical modelling of data. The aim of principal component analysis as used in this work is to try to reduce the large datasets that will be forthcoming from the various techniques used to investigate chemical vapour deposition, and to contrast and compare between them.

In the case of data presented for this thesis, plots of both scores and loadings will be presented. Comparison of these plots should provide an additional way of interpreting the data collected in various investigations of chemical vapour deposition processes. The scores plot indicates can be used to identify similar data points from large sets of data. Similar data points will tend to cluster together. This is useful in the case of spectra,

where the large amounts of data can be reduced to a smaller scores plot, that can be used to identify similar spectral fingerprints within data sets. Loadings plots can be useful in characterising the differences between datasets, and also in the analysis of spectra where absorption peaks of different species overlap.

5.4 Summary

Two primary chemometrics techniques have been presented in this chapter. Their previous use in a variety of film and surface applications have also been presented, so as to highlight the usefulness of these techniques for both investigation of chemical vapour deposition and optimisation of chemical vapour deposition processes.

An experimental design methodology will be used to investigate the multivariate process of chemical vapour deposition. This will enable a variety of response surfaces to be produced, which can be used to enhance understanding of the process. In addition the technique can also show the way towards optimisation of the process.

In the series of investigations performed, a large number of data sets will be produced. These data sets can be explored using principal components analysis.

Chapter 6

Spatial concentration measurements during the thermal chemical vapour deposition of tin oxide films

Results from this chapter have been published, [240].

6.1 Tin oxide films

Tin oxide thin films are conductive and very transparent to visible light, leading to their use in the manufacture of solar cells, [5] and flat screen displays, [241]. They are part of a group of materials referred to as transparent conductive oxides. Hence the deposition of tin oxide films is of increasing economic significance as economic and political pressures drive the energy industries to move away from traditional petrochemical methods of power generation. Tin oxide films can also be used as low emissivity coatings for glass windows, as they reflect infra red light, [241], improving the heating efficiency of buildings using this glass. Tin oxide acts as a heterogeneous oxidation catalyst, and has seen use in car exhausts to reduce pollution, [241].

The focus of the process examined in this work is the production of tin oxide thin films, as a step in the manufacture of solar cells, [242]. The tin oxide, or some other transparent conductive oxide layer covers a silicon layer. The transparent conductive oxide is typically 750 nanometers to one micron thick, whilst the silicon layer is usually about 300 nanometers thick. The silicon is coated by a low pressure plasma enhanced chemical vapour deposition process onto the tin oxide layer. This silicon layer absorbs photons from incident sunlight, and in doing so generates an electron-hole pair. This

electron-hole pair generation is the mechanism by which electricity is generated. Beneath the silicon layer is a conductive contact, both this and the transparent conductive oxide layer act as charge collectors in the solar cell. A diagram is presented in figure 6.1.

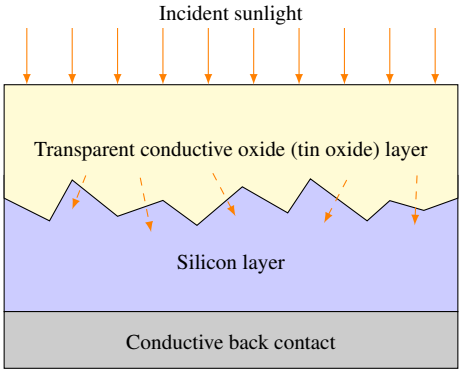

Figure 6.1: Diagram of the layers in a solar cell, [5].

A high degree of transparency, typically 80 % or more, is required for the tin oxide films, whilst still maintaining conductivity across the surface. A large degree of roughness is also required at the surface, so that when the silicon layer is present, light is scattered into it efficiently. Thermal chemical vapour deposition at atmospheric pressure provides a transparent, conductive tin oxide layer with the requisite roughness. To increase the conductivity of this layer, the tin oxide is doped with fluorine, [5].

The driving force in tin oxide deposition is to bring the costs down during deposition at atmospheric pressure. This can be achieved by further improving the reactors used within this process. Significant work, [243], [244], has been done in analysing the atmospheric pressure process, with less emphasis being placed on the methodology to make reactor improvements. The key factors to improve, by improvement of the reactor, are the thin film growth rates and the film properties outlined previously.

As discussed in previous chapters, one way to analyse a reactor could be by examining the chemistry occurring at multiple points. This would enable analysis of the gas flows and chemical reactions, identifying areas of inhomogeneity. It is perhaps prudent then to

Precursor	By-products	References
Tin tetrachloride (plasma) ($SnCl_4$)	Chlorine, (Cl_2),	[246]
Tin tetrachloride ($SnCl_4$)	Hydrogen chloride, chlorine (HCl), (Cl_2)	[247], [248], [140], [249], [250]
Tetramethyl tin ($(CH_3)_4Sn$)	Formaldehyde (CH_2O)	[248], [17], [251]
Dimethyltin dichloride ($(CH_3)_2SnCl_2$)	Methane, chlorine, hydrogen chloride (CH_4), (Cl_2), (HCl)	[252]
Monobutyltin trichloride ($C_4H_9SnCl_3$)	Ethylene, hydrogen chloride (C_2H_4), (HCl)	[253], [5], [254], [255]

Table 6.1: Tin oxide precursors and their associated by-products.

examine the typical chemistries used in the deposition of tin oxide films. Common precursors, [245], are tin tetrachloride, tetramethyl tin, dimethyltin dichloride and monobutyltin trichloride. Oxygen and water are used to provide the oxygen for the tin oxide, [5]. Previously investigated chemistries are presented in table 6.1, with the associated gaseous by-products identified.

Dimethyltin dichloride, tetramethyltin and monobutyltin trichloride commonly undergo an overall reaction with oxygen in the gas phase to form tin oxide films. The precursors thermally decompose in the gas phase with the methyl groups breaking off first, [252]. This is due to the tin carbon bond being much weaker than the tin chlorine bond, [5]. A high amount of radicals are predicted in the gas phase, leading to potentially high growth rates. Tin dichloride radicals oxidise forming the intermediates that adsorb onto the substrate surface.

In comparison, tin tetrachloride adsorbs onto the surface of a substrate before reacting with oxygen, [250], or water, [5], in a Langmuir Hinshelwood type mechanism. In many cases hydrogen chloride is evolved as a by-product that diffuses to the gas phase.

Previous work has been carried out in measuring the hydrogen chloride evolved during

the deposition of tin oxide from tin tetrachloride, [140]. The next step is to build a spatially resolved map of by-product production in the reaction zone, preferentially in two dimensions. Hydrogen chloride is produced in the majority of the tin oxide deposition chemistries, and so it will remain the measured species for the purposes of this chapter.

Tin oxide deposition aims and objectives

The primary aim of this part of the work is to show the use of near infrared laser diode spectroscopy in the characterisation of an atmospheric pressure chemical vapour deposition reactor during the deposition of tin oxide thin films. The chapter also provides an introduction to the chemical vapour deposition process at atmospheric pressure.

The use of the laser diode based measurement technique allows for the objective of building up a two dimensionally resolved profile of hydrogen chloride. This can be subsequently used to examine the process, and inform process design.

6.2 Methodology

Experimental set up

The dual flow reactor system illustrated in figure 6.2 was used. Gas enters the reaction zone top down, and is evacuated from the deposition zone by exhausts which are labelled on the schematic of the underside of the coating head presented in figure 6.3. The heated substrate holder can move to enable continuous coating, but this was not done for these experiments. Total gas flows were set to two standard litres per minute, composed of 20 % oxygen, 5000 ppm of monobutyltintrichloride, flash evaporated water and the remainder nitrogen. The gas lines were heated to 200 °C, and the substrate heater to 600 °C. The gas

is assumed to be perfectly mixed in a mixing chamber prior to entry to the reaction zone. The coating head is located 2.5 millimetres above the surface of the substrate. Coatings were deposited over one minute on one millimetre thick borosilicate glass.

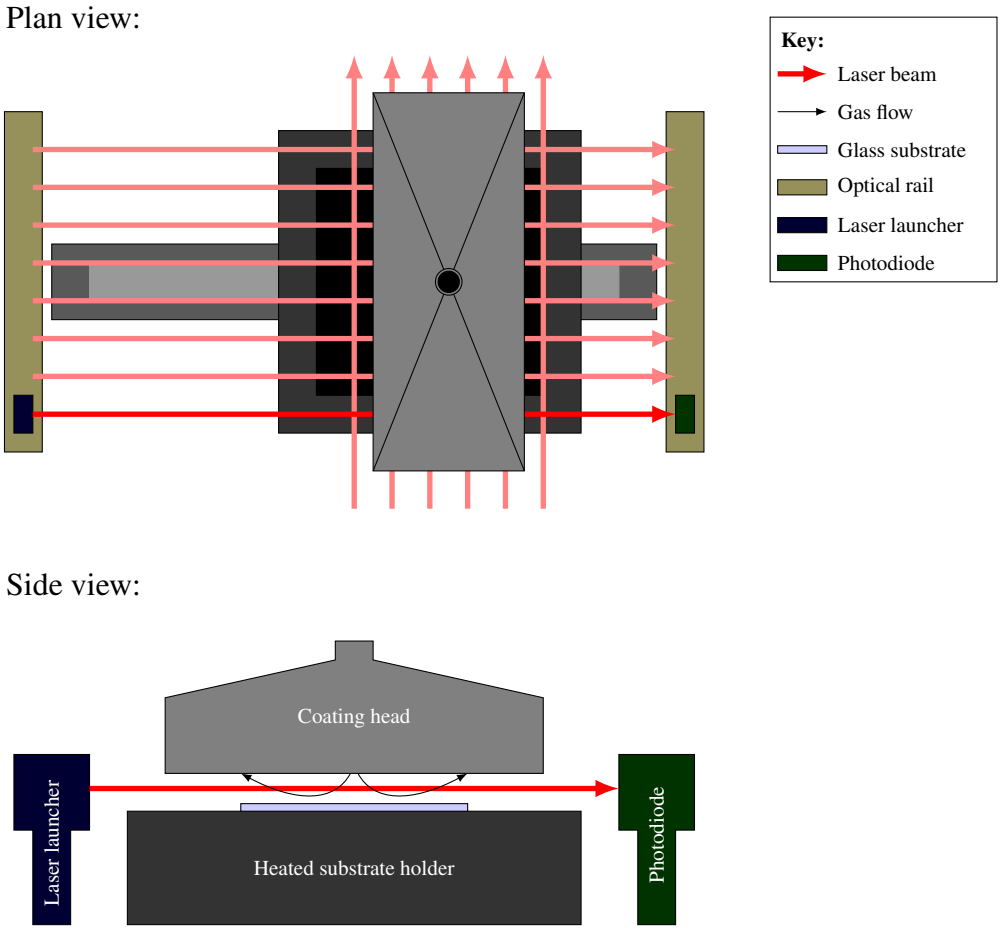

Figure 6.2: Side and plan views of the studied thermal chemical vapour deposition reactor, with laser measurements indicated by red lines.

Inlet system and mass balance

A necessary feature of chemical vapour deposition systems is the inlet system. It is important to examine the system, and describe how to set the flow rates. A process diagram of the inlet system can be seen in figure 6.4. Flowing into the reactor is oxygen, which is marked as O; nitrogen, which is split into a bypass stream, B, and precursor

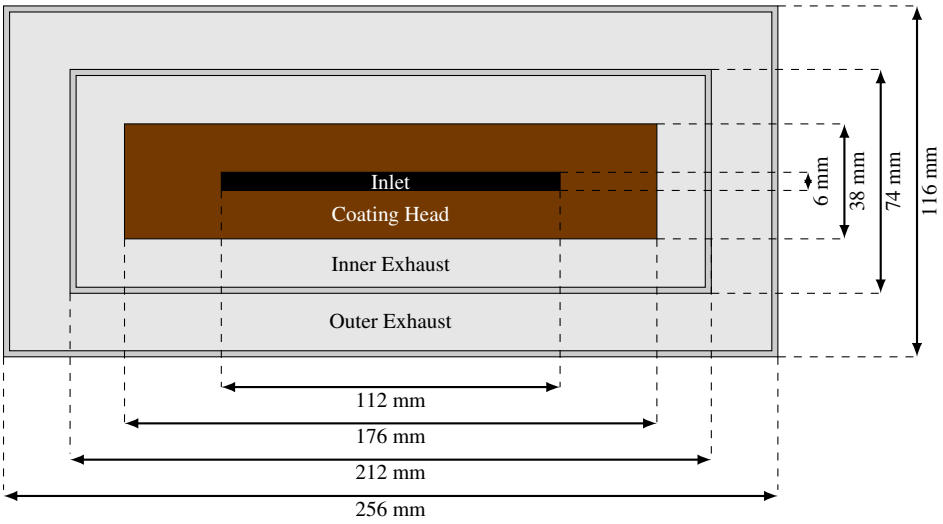

Figure 6.3: Dual flow thermal coating head schematic.

stream, M; these streams meet just prior to the reactor in stream T. The bypass, oxygen and precursor streams are all controlled by some type of flow controller.

The various streams have flow rates that can be controlled to give a desired concentration of precursor and oxidant in the reactor. The precursor stream picks up precursor in the bubbler, the amount that is picked up is controlled by the vapour pressure of the precursor, which is a function of the temperature. It is necessary to perform a mass balance over the system, so that the relevant flow rates and temperatures can be calculated for a given concentration of precursor.

It is necessary to establish that the flow rate into the reactor is the total of the flow rates of the oxygen, bypass and precursor streams. This is presented in equation 6.1.

$$T = B + O + M_1 \tag{6.1}$$

There are three different chemicals that enter the reactor, these are oxygen, nitrogen and the precursor, which is monobutyltin trichloride. The bypass stream is pure nitrogen, and the oxygen stream is pure oxygen. In order to set the oxygen to a specific mole

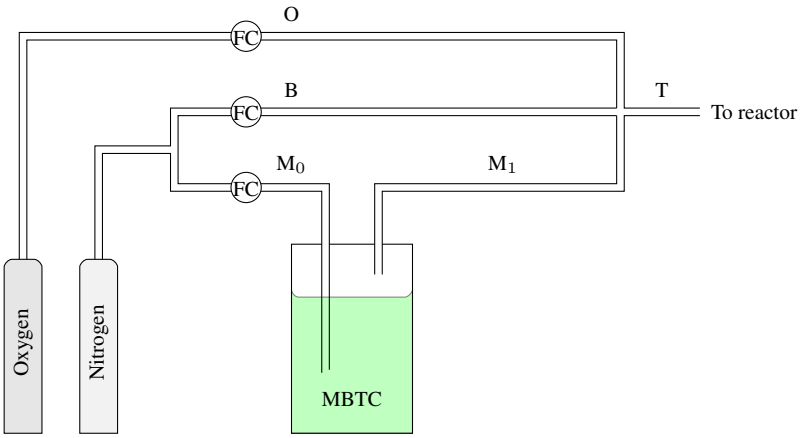

Figure 6.4: Process diagram of inlet system for the thermal chemical vapour deposition reactor. The water inlet is left out, so as to simplify explanation of calculation of concentrations.

fraction, y_{O_2}, equation 6.2 is used.

$$y_{O_2} = \frac{O}{T} \tag{6.2}$$

It is not quite so simple for the case of the calculation of the concentration of precursor, y_{MBTC}, entering the reactor. Monobutyltin trichloride is present in the precursor stream at a concentration y_i, therefore it is possible to say that y_{MBTC} can be calculated by way of equation 6.3.

$$y_{MBTC} = \frac{y_i M_1}{T} \tag{6.3}$$

The concentration of MBTC in stream P_1 is unknown. In order to calculate it, a combination of Dalton's and Raoult's law is used which governs the relationship between concentrations in gases and liquids, and partial pressures, and it's application can be seen in equation 6.4. In this equation, x_i is the concentration of the precursor in the liquid. This assumed to be pure, so it can be set to unity. P_i is the partial pressure of MBTC in

Precursor	A	B	C	Units	Reference
DDS	7.14	1328	241.05	mmHg, °C	[256]
MBTC	9.1	3070	0	mmHg, K	[257]
TEOS	16.78	3942.79	219.35	mmHg, °C	[258]

Table 6.2: Antoine coefficients for precursors used in this thesis.

the gas phase, and P is the total pressure of the gas phase.

$$y_i = \frac{x_i P_i}{P} \tag{6.4}$$

The use of the Antoine equation is required to calculate the partial pressure of MBTC in the gas phase, and this relates the vapour pressure exerted by a liquid to the liquids temperature, T. In this case, the vapour pressure can be said to be equivalent to the partial pressure of MBTC in the vapour phase. The Antoine equation is presented in equation 6.5. Antoine equation coefficients for the chemicals used throughout this thesis are presented in table 6.2.

$$\lg P_i = A + \frac{B}{C + T} \tag{6.5}$$

Near infra-red laser diode spectroscopy

As previously stated, monobutyltin trichloride breaks down into several intermediary species in the gas phase. One of the by-products of these chemical reactions is hydrogen chloride, and it is this hydrogen chloride that can be measured to give a spatial concentration profile.

The near infrared laser spectrometer used for this work was provided by TDL Sensors.

It consists of a near infra red laser diode tuned across the R(3) rotational line of the first vibrational overtone of hydrogen chloride at 1742 nanometres. The beam is columnated into an optical fibre, which can then be used to arrange the laser beam in the correct position and align it with the detector. The detector is an InGaAs photodiode. Measurements were taken both parallel and perpendicular to the direction of the gas flow, as is indicated in figure 6.2. The beam was fixed two millimetres above the surface of the substrate. Measurements made parallel to the direction of gas flow were taken every ten mm across the length of the coating head. Measurements made perpendicular to the direction of gas flow were taken every five millimetres across the width of the coating head. Measurements were taken after 50 seconds of deposition time. In addition measurements were made every 0.5 millimetres above the surface of the substrate at the 40 mm position perpendicular to the gas flow. Due to time constraints connected with the chemical vapour deposition apparatus being measured, experimental points were not repeated.

6.3 Results

Interpretation of results

Presented in figure 6.5 is the raw laser data, which is presented in transmission. A fifth order polynomial is fitted to the baseline using the Microcal Origin software, and this is represented in figure 6.5 by the red line. This baseline is subsequently used to convert the spectra from transmission into absorbance. The converted spectra can be seen in figure 6.6. Also seen in figure 6.6 is the Lorentzian line shape fitted by means of Origin's Levenberg-Marquardt method of non-linear curve fitting. The integrated absorbance can be extracted accordingly, as established from the Beer-Lambert law outlined in equation 4.6. Details of the measured absorption feature from the Hitran database, [214], can be

Position / (cm^{-1})	Linestrength / (cm^{-1} / molecule cm^{-2})	Line width / (cm^{-1})
5739.2626	1.160×10^{-20}	0.0624

Table 6.3: Hydrogen chloride spectral feature parameters.

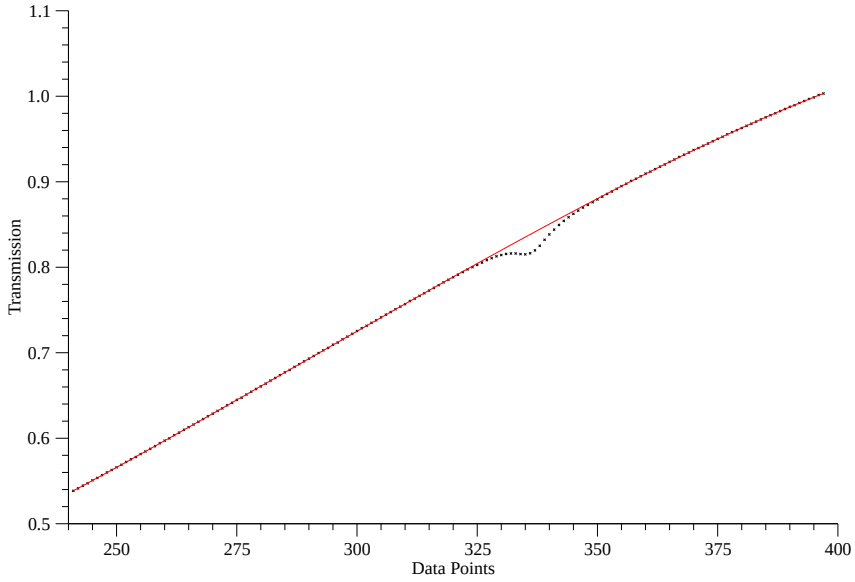

Figure 6.5: Example of raw data recorded by the near infra red laser diode spectrometer, showing a baseline (red line) being fitted to the raw data (dotted black line).

seen in table 6.3.

It has been established in the previous chapter that linestrength varies with temperature, in the case of these measurements the temperature can be anywhere between 200 and 600 °C. The linestrength of the hydrogen chloride spectral feature at these temperatures is 8.1 $\times$ 10^{-21} and 6.5 $\times$ 10^{-21} cm^{-1} / molecule cm^{-2} respectively. It is clear that the linestrength changes significantly with a temperature difference of around 400 K, which is the temperature range in this situation. This would indicate that without a temperature profile of the reaction zone, the concentrations can not be extracted from the data. The integrated absorbance is indicative of the concentration however, and firm conclusions can be drawn.

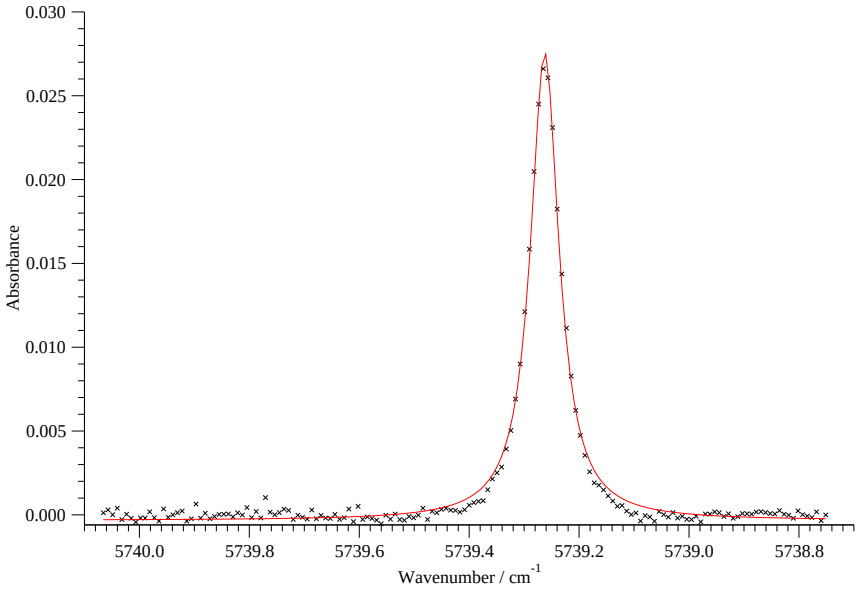

Figure 6.6: Example of Lorentzian lineshape fitted to the measured R(3) hydrogen chloride spectral feature at 5739.3 cm^{-1}.

Discussion

Presented in figure 6.7 is the integrated absorbance of the hydrogen chloride spectral feature as a function of the height of the laser beam above the substrate. These measurements were recorded perpendicular to the flow of gas in the reaction zone. This measurement shows that the trend of the spectral feature is to decrease with the height above the substrate. This is perhaps due to two complimentary reasons. Firstly there is a faster generation of hydrogen chloride closer to the substrate due to the increased temperature, therefore there is increased absorbance of the laser light due to the increased concentration. Secondly, the higher temperature closer to the substrate would cause an increase in the line strength of the hydrogen chloride spectral feature. These two effects lead to an increased absorbance closer to the substrate surface.

Results presented in figure 6.8 represent the measurements taken parallel to the flow of gas in the reaction zone. It must be noted that the flow rate is too high for the flow

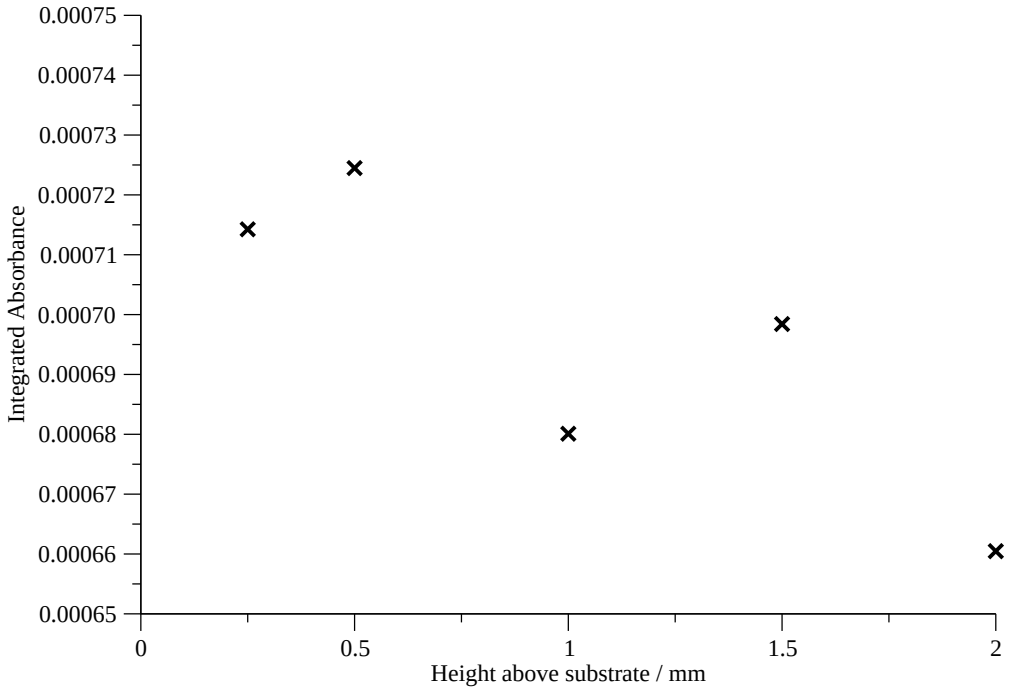

Figure 6.7: Integrated absorbance against spatial position above glass substrate.

to be strictly laminar. Assuming a relatively uniform temperature in the coating region measured, there is a degree of inhomogeneity in the absorbance of the hydrogen chloride feature. In particular there is a marked increase of the measurements at the centre of the coating head. This could suggest that there is more hydrogen chloride generated at the centre of the reaction zone, perhaps due to either poor gas mixing or temperature inhomogeneity. Another possibility will be discussed in a subsequent appraisal of both sets of results. This measurement technique is powerful in mapping the uniformity of reactions within a reactor. Figure 6.8 also indicates that both the inner and outer exhausts of the coating hood are redundant in this orientation, as the HCl is at zero at these points.

Figure 6.9 represents measurements of the hydrogen chloride absorption feature taken perpendicular to the flow of the gas. This measurement can provide information on the length of the reaction zone, and thus assist in further adaptations of the reactor design. Again, a uniform temperature profile is assumed for the measurements. Figure 6.9 indicates low concentrations of hydrogen chloride at the gas inlet to the reaction zone, approximately 60 to 70 millimetres on the x-axis. This indicates that the precursor is undergoing initial reactions at the inlet, producing hydrogen chloride. However, as the measurements are taken over the coating head, two increases in the absorbance of the hydrogen chloride peak can be seen. The concentration of hydrogen chloride in these two regions increases due to the gas flow, and hydrogen chloride generation in this region. The concentration decreases at the inner exhaust, due to the exhaust extracting the by-products from the reaction zone. The majority of the gas flow in this direction is clearly taken up by the first exhaust, with the second exhaust removing a much lesser amount of by-products.

Looking at figures 6.8 and 6.9 in combination, some evaluation of the by-product production in two dimensions can be made. Previously mentioned in the discussion about figure 6.8 was the higher region of hydrogen chloride absorbance in the centre of the measurement region. Comparing this with figure 6.9, there is perhaps some further indication

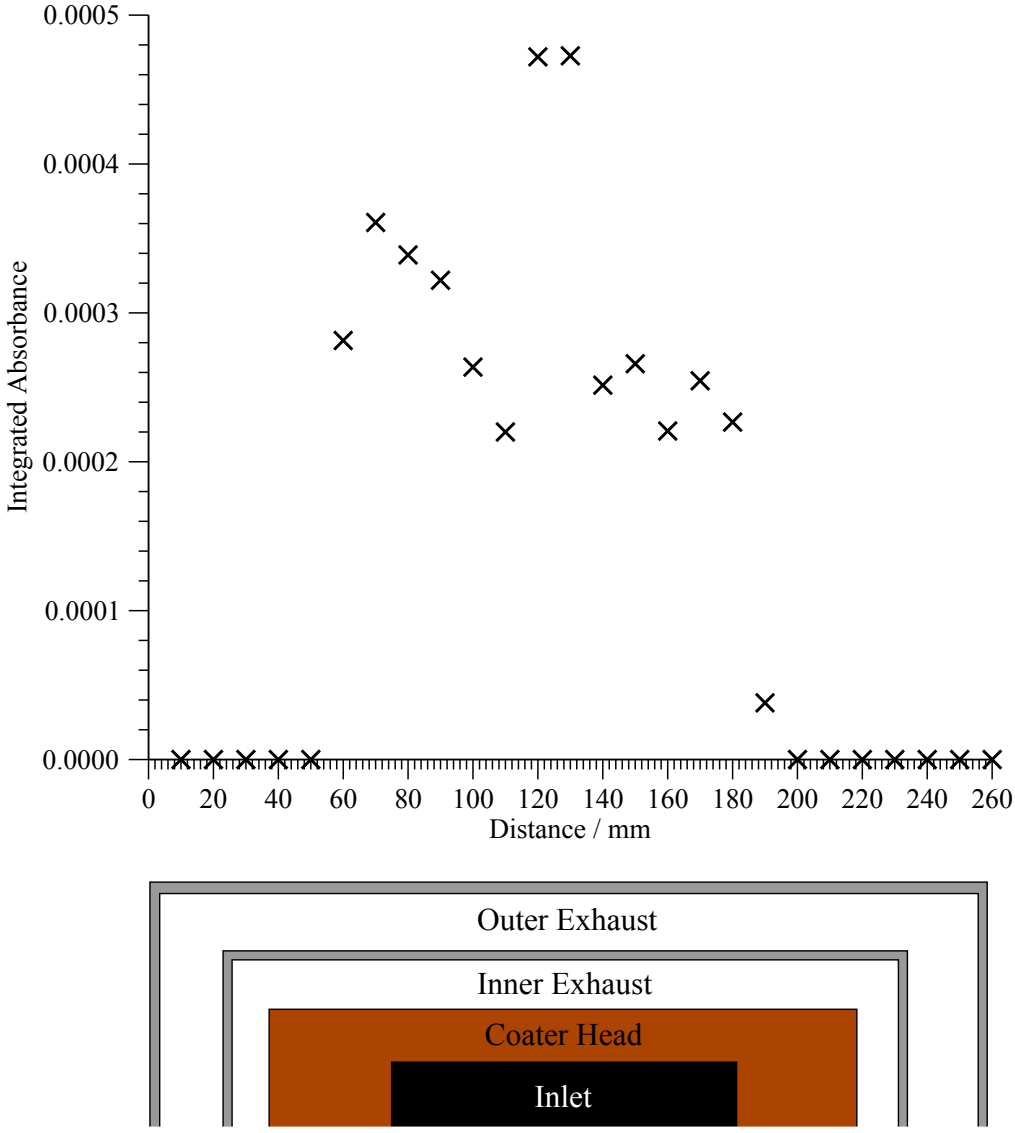

Figure 6.8: Integrated absorbance against spatial position parallel to gas flow. Presented with a scale schematic of the coating head.

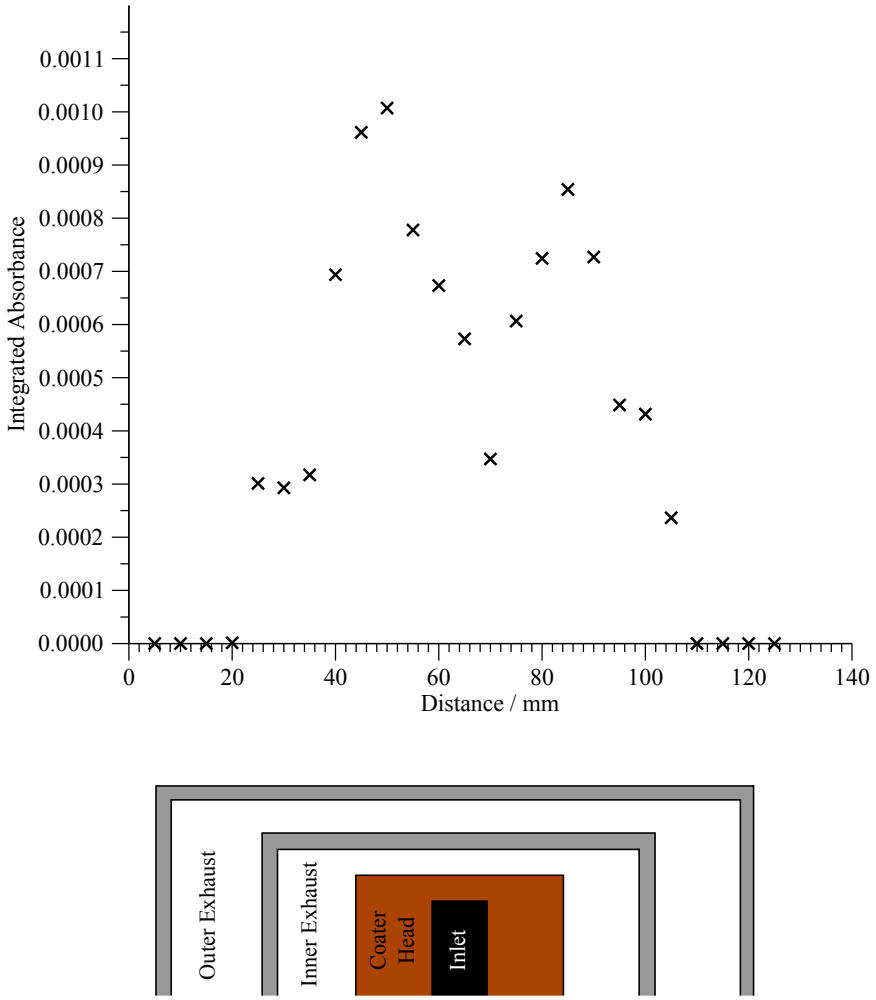

Figure 6.9: Integrated absorbance against spatial position perpendicular to gas flow. Presented with a scale schematic of the coating head.

as to what this aberrant maximum is due to. The shape of figure 6.9 is understandable, and makes sense considering the design of the process. When figure 6.8 is taken into account, there is a source of hydrogen chloride that needs to be explained. This could be due to a zone in the centre of the coating head that has less flow, perhaps due to issues with the exhaust, and so the hydrogen chloride flows out further in this region. Therefore there is a central part of the gas region that has a greater amount of hydrogen chloride in it that is picked up by the line of sight measurement.

The three results presented here show a by-product based approach for characterising the reaction zone of an atmospheric pressure chemical vapour deposition reactor. In particular they have shown inhomogeneity of the reaction zone parallel to the gas flow through it. They have also indicated that for the most part, the outer exhaust of the coating head is redundant. This perhaps indicating some way forward in term of economy of subsequent reactor designs.

6.4 Conclusions

This is the first time such measurements have been undertaken on an atmospheric pressure chemical vapour deposition reactor. The aim of this chapter was to apply near infrared laser diode spectroscopy to the thermal chemical vapour deposition of tin oxide. This has been realised, with the successful objective of a two dimensionally resolved profile of hydrogen chloride showing this. These preliminary spatial measurements of gas phase species in the atmospheric pressure chemical vapour deposition of tin oxide deposition have already proven useful in improvements to both coater head configuration and design. The identification of the redundancy of large amounts of the exhaust design has strong positive implications for the use of a reduced coating head, with the subsequent economic advantages that this would provide.

Further work should be directed towards modifying the spectrometer so that it can be used to measure at several points simultaneously, preferably in several different geometrical arrangements. In addition, some kind of scan recorder needs to be integrated into the instrument software, so as to examine temporal aspects of hydrogen chloride generation.

Away from practical matters, additional work should be done in advancing towards tomographical reconstruction of the reaction area, similar to work that has been carried out using diode lasers in combustion engines, [259]. These results, with suitable treatment, could better identify reaction hotspots. The subsequent improvements on film uniformity would be invaluable.

Chapter 7

Chemometric investigation of the plasma enhanced chemical vapour deposition of silica films from tetraethylorthosilicate

Parts of this chapter have been published [260].

7.1 Introduction

The use of atmospheric pressure plasmas, [188], to initiate chemical vapour deposition, [166] is of great interest due to the low thermal temperatures that growth can be achieved at, and the increased growth rates that are possible. There are critical issues however, in that the process design and control methodologies are still in the initial stages of research. This chapter presents a methodology for studying the process in depth.

There is a long history of silica films deposited by chemical vapour deposition, and they have widespread use, from dielectric layers in the semiconductor industry, [261], [262], [35], to corrosion protection layers, [263]. Common silica precursors can be seen in table 7.1. Tetraethylorthosilicate (TEOS) is one of the most common precursors for silica deposition [264]. There are limited studies made of the kinetics of silica deposition from TEOS in atmospheric pressure plasma systems, though there are many studies for thermal chemical vapour deposition [265]. In addition there are a wide range of parameters that can govern film properties which also require further investigation.

For TEOS deposition in low pressure discharges, the process gas is usually pure oxy-

Precursor	Chemical Formula	References
Tetraethylorthosilicate	$(C_2H_5)_4SiO_4$	[261], [264], [266], [267], [268], [269], [270], [271], [272]
Hexamethyldisiloxane	$(CH_3)_6Si_2O$	[34], [273], [274], [263], [275]
Allyltrimethylsilane	$C_3H_5(CH_3)_3Si$	[276]
Dichlorodimethylsilane	$Cl_2(CH_3)_2Si$	[237]
Divinyltetramethyldisiloxane	$(C_2H_2)_2(CH_3)_4Si_2O$	[277]

Table 7.1: Silica precursors used for atmospheric pressure chemical vapour deposition.

gen, [272]. However, at atmospheric pressure, this causes more problems as oxygen requires an increasing breakdown voltage for a plasma to initiate, and the stability criteria change. Commonly helium is used instead, but this has associated high running cost issues. Oxygen still needs to be introduced to the plasma for harder films and higher growth rates, [278]. A key parameter then, is the oxygen to TEOS ratio, [265], which has been investigated for its effects on films grown in lower pressure discharges, [261], [272]. In the case of the low pressure discharge, intermediates to silica film deposition are formed in the gas phase, and adsorb onto the surface. Here the intermediates react with oxygen radicals from the gas phase, [268].

The use of chemometrics, [230], as established in the previous chapter, allows for a large amount of information to be built up about the process, [279] and the rapid investigation of multiple variables. For this work chemometric techniques, in particular experimental design and response surface analysis, have been used to study the plasma enhanced chemical vapour deposition of silica films from TEOS. Using a combination of on line and in situ spectroscopic techniques, a large range of information can be built up about the PECVD process, potentially increasing knowledge of the chemistry occuring, and identifying the ideal processing conditions within the selected parameter space.

Aims and Objectives for investigation into plasma enhanced silica deposition from TEOS

The aim of this work is to intensively study the atmospheric pressure plasma enhanced chemical vapour deposition of silica from TEOS, and to identify the optimum processing conditions whilst using a range of spectroscopic techniques to interrogate the chemistry occurring. The objective is to use an experimental design methodology to provide the ”backbone” of this investigation. This enables a rigorous methodology to be established, by which the parameters measured can be linked. In particular, the correlation of the gas phase measurements with the thin film properties.

7.2 Methodology

Reactor Details

Experiments were carried out using a dual flow plasma enhanced chemical vapour deposition reactor system illustrated in figure 7.1, coating on a moving float glass substrate. The dual flow indicates that the process gas enters at one inlet, and is then evacuated at two exhausts. The plasma is generated by dielectric barrier discharge in helium, and is in the glow discharge regime. There are two different dielectrics located 4.5 mm apart, and are made of polyaryletheretherketone and quartz. The reactor is supplied by an audio power amplifier (Crown XLS 602) feeding into a custom made ferrite cored transformer (Amethyst Designs Limited). Secondary voltage and current measurements were performed with a Tektronix 1000 to 1 voltage probe and an inductive Pearson 411 current monitor respectively . The total flow rate was set at 4 standard litres per minute (slm), with helium being used to transport 500 ppm of 99.5 % purity TEOS, whilst oxygen flow

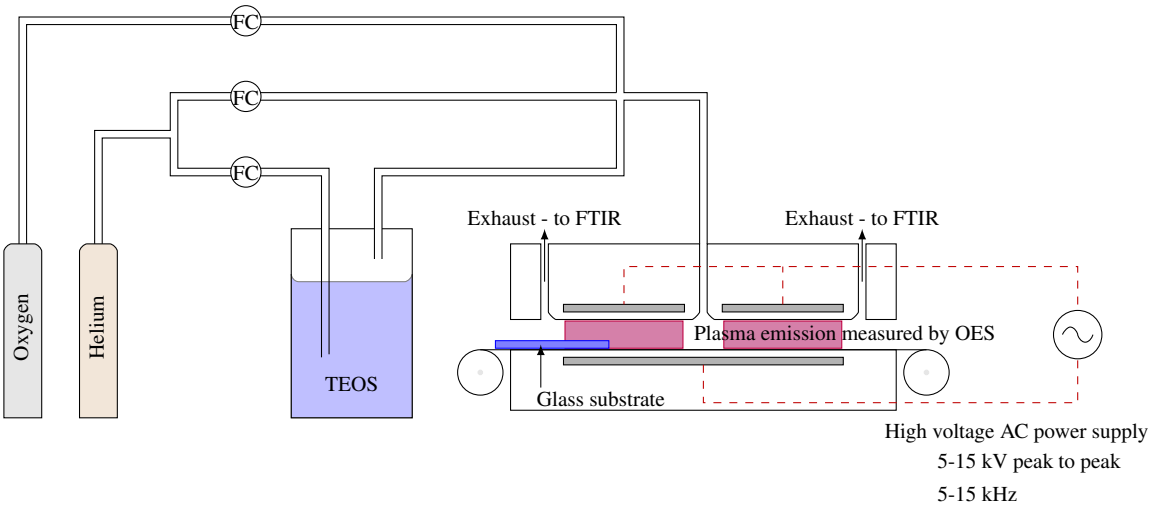

Figure 7.1: Process schematic for plasma enhanced chemical vapour deposition of silica films from tetraethylorthosilicate (TEOS) at atmospheric pressure.

rates were varied for the experiments. MKS 247 mass flow controllers were used to set individual flow rates, and the TEOS was regulated in a temperature controlled bubbler. The float glass substrates are 90 by 220 mm and are 3 mm thick. All experiments were carried out at 293 K.

Chemometric Studies

All measurements were carried out using a central composite experimental design with three factors, [236], this is illustrated in figure 7.2. This design was chosen as it provides both an efficient means to study both the higher order effects of the variables being investigated, and to assess the repeatability of the process. The codings of low (-1), medium (0) and high (+1) enable the second order and interaction effects to be investigated. Table 7.2 shows the variables investigated for this work. Secondary voltage and frequency were chosen to investigate the effect of the plasma parameters on the films produced, whereas the TEOS:O_2 ratio is a key parameter in silica deposition, [272], this also follows from initial work that has been carried out, [237]. All measurements were

Coding	Voltage (x_1) / kV	TEOS:O_2 ratio (x_2)	Frequency (x_3) / kV
-1	8	1:1	5
0	10	1:10	10
1	12	1:100	15

Table 7.2: Variables investigated for the PECVD of silica from TEOS

then fitted to a second order polynomial to represent the non-linear effects of the measured variables as seen in equation 7.1.

$$\hat{y} = b_0 + b_1x_1 + b_2x_2 + b_3x_3 + b_{11}x_1^2 + b_{22}x_2^2 + b_{33}x_3^2 + b_{12}x_1x_2 + b_{13}x_1x_3 + b_{23}x_2x_3 \quad (7.1)$$

The influence of each factor was studied using the Student's t-test, [236] , which takes into account the error between the experimental data and the model, and the degrees of freedom (ten in the case of the central composite design). A confidence level greater than 95 % indicates that the factor plays a statistically significant part in the model. The models were also tested with the F-test, [236] to ensure that they fitted well to the data. These tests take into account the replicates at the central point of the design, and the variation of the model from the experimental results to test the validity of the model. A confidence level greater than 95 % indicates that the model is a good fit. The models were then used to generate a response surface, [227] for the various measurements, and where relevant correlated with other measurements to provide insight into the PE-CVD process.

Spectroscopic techniques

Several spectroscopic techniques were used to investigate the plasma whilst deposition was occurring. Optical emission spectroscopy was used to identify the excited species. An

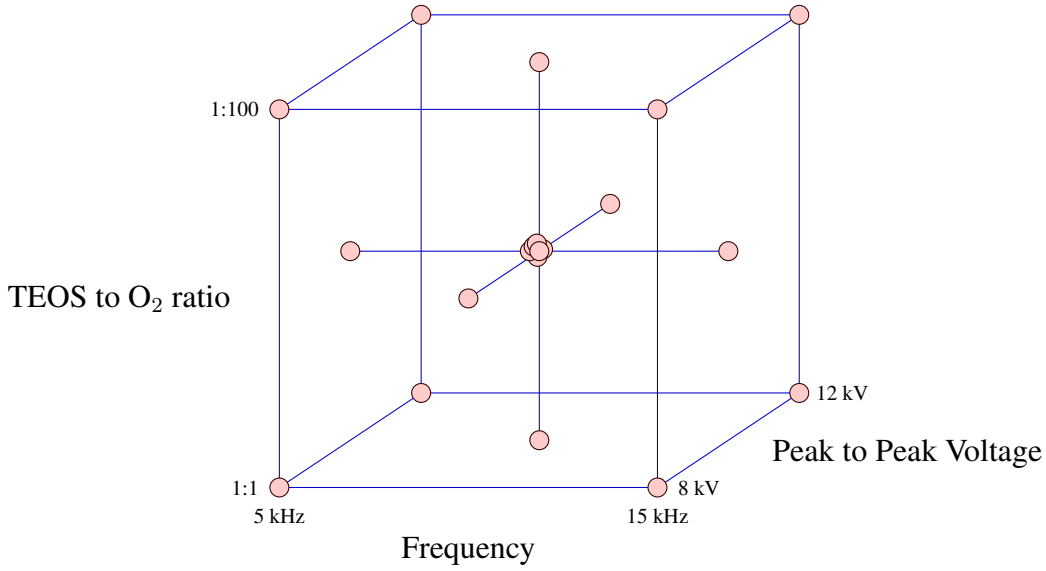

Figure 7.2: Central composite design for investigation of plasma enhanced chemical vapour deposition of silica from TEOS at atmospheric pressure.

Ocean Optics USB2000 UV-visible spectrometer with 2 nm resolution across a spectral range of 200 to 800 nm was used for this work. The spectral response of the spectrometer will vary due to the nature of the CCD array used within the spectrometer. This will have some effect on any processing of the recorded spectra.

FTIR absorption spectroscopy has been used to identify the by-products of the PE-CVD process, and to calculate their concentrations, [162]. This is achieved through the use of standard spectra, [211], except in the case of TEOS where a set of calibration spectra has been produced as there are no standard spectra. It was also used to calculate the decomposition of the precursor. Measurements were carried out on a Bruker Equinox 55 FTIR spectrometer using an MCT detector. All spectra were recorded at a resolution of 2 cm^{-1} across 500 to 4000 cm^{-1}. Gases flowed through a multipass cell 50 cm downstream of the reactor. The multipass cell was produced by Specac and has a White-type mirror arrangement with an optical pathlength of 5.3 m.

Film measurements

Several film measurements were also performed, and these were contact angle, refractive index, film absorption coefficient, film hardness and film thickness measurements. The thickness of each of the films was measured using a Dektak3 ST surface profiler to measure the difference in height between a masked off section of glass and the film. The rate of glass movement through the reactor was used to calculate the average growth rates from this data.

Film hardness was measured with a custom built scratch tester that has been calibrated with standardized materials. Scratches were made on the surface of the film, the width of which can be used to calculate the hardness. Both Mohs and absolute hardness of the films were calculated from these scratches, but as they are different measures of the same thing, Mohs hardness is reported in these results.

Water contact angles were measured using drops of distilled water on the films surface recorded with a model VCB-3512T Sanyo B/W CCD camera. The pictures of the droplets were subsequently analysed using Camtel FTA32 video software to calculate the contact angle.

An **nkd** ultraviolet-visible spectrometer was used to take spectra of the films surface. The transmittance and reflectance of the films were recorded across the spectrum. Fits to these spectra allow the refractive index and absorption coefficient of the films to be calculated.

A ThermoNicolet Avatar 360 ESP spectrometer with a diamond ATR crystal attachment was used to perform ATR FTIR spectroscopy on the films. The spectra were recorded between 400 and 4000 cm^{-1} at a resolution of 2 cm^{-1}. This allows the film composition to be investigated.

Species	λ_{mn} (nm)	A_{mn} (s^{-1})	g_m	E_m (eV)	Intensity (A.U.)
He I	587.56	2.94×10^7	3	23.074	1.63
He I	667.82	6.38×10^7	3	23.074	4.08
He I	706.52	1.54×10^7	5	22.718	22.06
He I	728.14	1.81×10^7	3	22.920	1.89

Table 7.3: Helium lines used for Boltzmann plot, [8], with example intensities from experimental condition one.

7.3 Results

Optical emission spectroscopy results

An example optical emission spectra can be seen in figure 7.3, with the main peaks being labelled. The molecular nitrogen lines, [280], that can be seen are due to the reactor being open to the atmosphere, permitting back diffusion of nitrogen into the reactor. The helium lines used for the Boltzmann plot are also indicated, and details of the lines used for the calculation are included in table 7.3. The relative spectral response of the spectrometer over 587-728 nm was not known and so the intensities of the helium lines in this region could not be corrected. This will cause an error in the values of the calculated excitation temperatures, but this does not affect comparisons of estimated temperatures obtained when different experimental conditions were investigated. A subsequent Boltzmann plot is included in figure 7.4, further calculations of the excitation temperature are made by least squares calculations. Also of interest in the emission spectrum is an emission line for atomic oxygen at 777 nm, as this indicates that various oxygen species are active in the chemistry of this system.

The optical emission data has been used to calculate the excitation temperature and this has been fitted to a second order polynomial model. The initial values for the coefficients are presented in table 7.4, as well as the t-test results by way of an example.

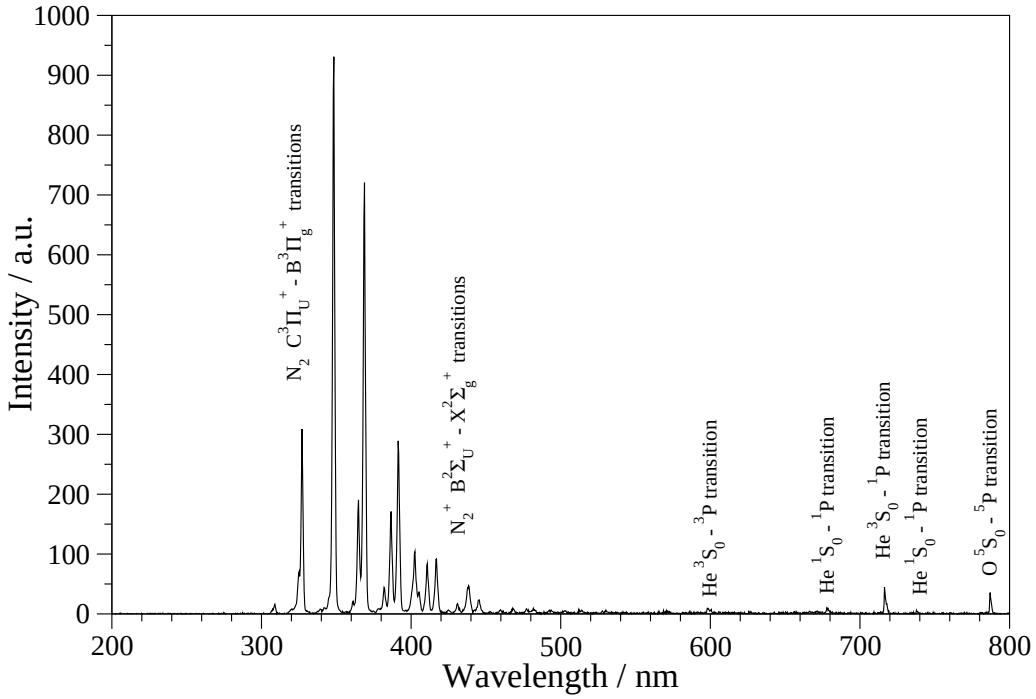

Figure 7.3: Optical emission spectrum of helium plasma containing 500 ppm of TEOS and 5000 ppm of O_2. The plasma was generated at 10 kHz with a peak to peak voltage of 12 kV.

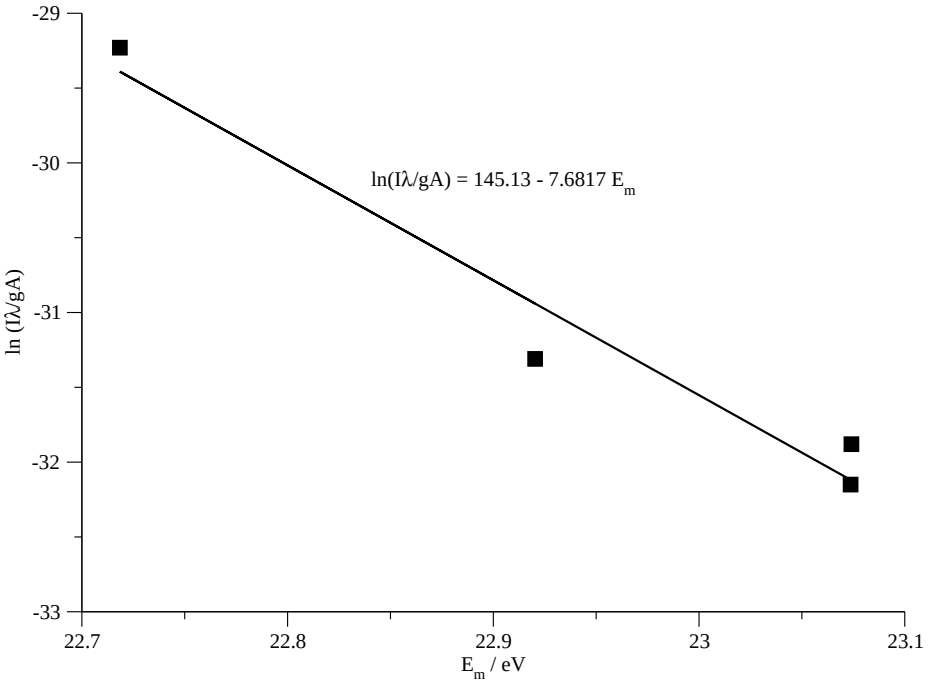

Figure 7.4: Example Boltzmann plot for experimental condition 1.

This model had an F-test result of 95.00 %. Examining the t-test results, it is evident that only a few of the coefficients are significant. As such, coefficients for a new model were calculated, this is presented in table 7.5.

The new model has an F-test score of 97.25 %, which shows that it is statistically significant. Response surfaces calculated from this model can be seen in figures 7.5 to 7.7.

The surface responses in figures 7.5 and 7.7 indicate that the excitation temperature is largely dependent on the components of the gas, and not the frequency that the plasma is generated at. The model suggests that the excitation temperature is also independent of the voltage. This would suggest that the power input into the plasma is responsible for the degree of ionisation of the gas, but not strongly responsible for the energy of the free electrons. Figure 7.6, the excitation temperature response surface at fixed oxygen

Coefficient	Value	Influence (%)
b_0	2391.52	100
b_1	143.99	77.05
b_2	1505.66	100
b_3	-75.39	48.20
b_{11}	-61.79	22.07
b_{22}	981.07	99.90
b_{33}	0.67	0.24
b_{12}	4.94	3.05
b_{13}	-217.78	88.59
b_{23}	-113.67	61.25

Table 7.4: Initital TEOS excitation temperature model coefficients.

Coefficient	Value	Influence (%)
b_0	2379.30	100
b_1	143.99	82.89
b_2	1505.66	100
b_{22}	944.40	100
b_{13}	-217.78	92.59
b_{23}	-113.67	67.76

Table 7.5: TEOS excitation temperature model coefficients for the new model.

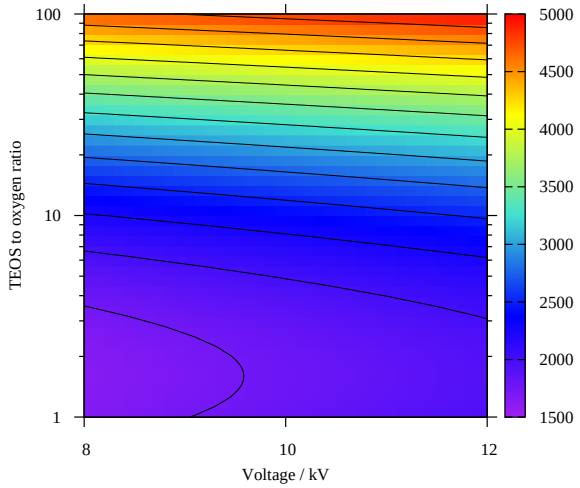

Figure 7.5: Response surface for excitation temperature (in Kelvin), with frequency fixed at 10 kHz.

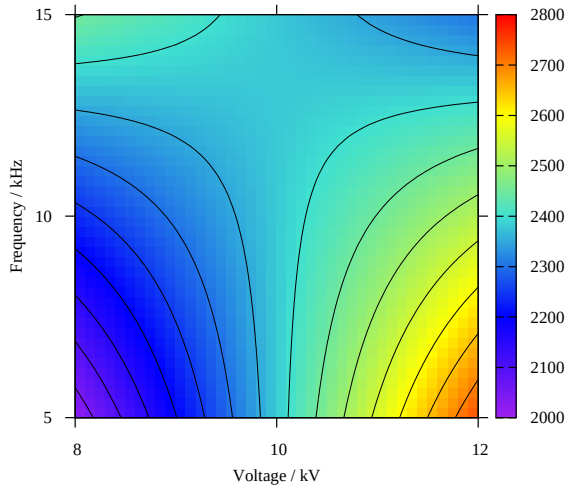

Figure 7.6: Response surface for excitation temperature (in Kelvin), with TEOS to oxygen ratio fixed at 10.

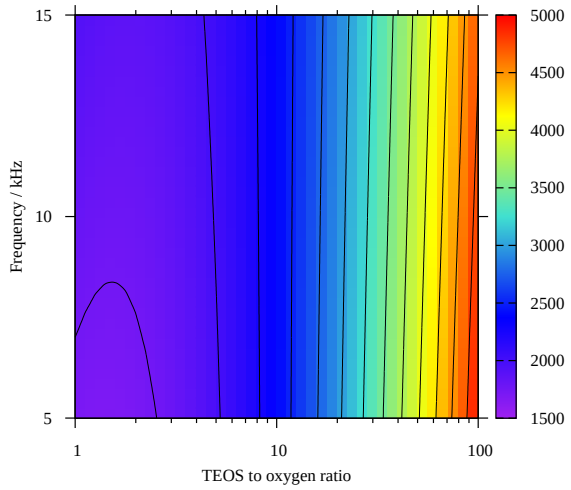

Figure 7.7: Response surface for excitation temperature (in Kelvin), with peak to peak voltage fixed at 10 kV.

concentration, supports this view, as the variation of excitation temperature is very small for the response surface. There is a region at low frequency and high voltage that is slightly higher, and this could be due to changes in the concentration of plasma species present in this operating region.

FTIR spectroscopy results

Figure 7.8 shows an FTIR spectra of 500 ppm of TEOS in helium recorded at a resolution of 2 cm^{-1}. Peaks have been assigned to the relevent molecular vibrations, [281]. Figure 7.9 shows an FTIR spectra of the exhaust of the PECVD reactor that has been supplied with 500 ppm of TEOS and 5000 ppm of O_2. The plasma was generated at 10 kHz with a peak to peak voltage of 12 kV. The breakdown species have been identified on the figure. The presence of acetaldehyde (merged with another peak at approximately

Species	Band start (cm^{-1})	Band end (cm^{-1})
TEOS	2850	3060
Carbon dioxide	2283	2393
Carbon monoxide	2045	2144
Acetaldehyde	2654.8	2851.6
Nitrous Oxide	2224.5	2263.7

Table 7.6: By-product species and their associated infrared spectral bands used for calculation of concentration.

1800 cm^{-1}) suggests that the chemistry for PECVD is similar to that of TEOS reacted with ozone in a traditional thermal CVD process, [282]:

$$Si(OC_2H_5)_4(g) + O_3(g) \rightarrow Si(OC_2H_5)_3OH(g) + CH_3CHO(g) + O_2(g) \quad (7.2)$$

$$Si(OC_2H_5)_4(g) + O \rightarrow Si(OC_2H_5)_3OH(g) + CH_3CHO(g) \quad (7.3)$$

The carbon monoxide and carbon dioxide in figure 7.9 being products of the acetaldehyde's reactions with various oxygen species. Nitrous oxide can also be detected and this is largely due to nitrogen present from the surrounding atmosphere, and as has already been established molecular nitrogen ions and atomic oxygen are present to react and form nitrous oxide.

The FTIR spectra for each experiment can be used to extract the concentration for each relevant by-product. The wavenumber range of the integrated peaks are presented in table 7.6 for each by-product. In the case of acetaldehyde, where the most intense peaks overlap with other peaks, other peaks have been used, and these peaks are indicated in table 7.6. The areas calculated are then compared to areas calculated from known standard spectra,

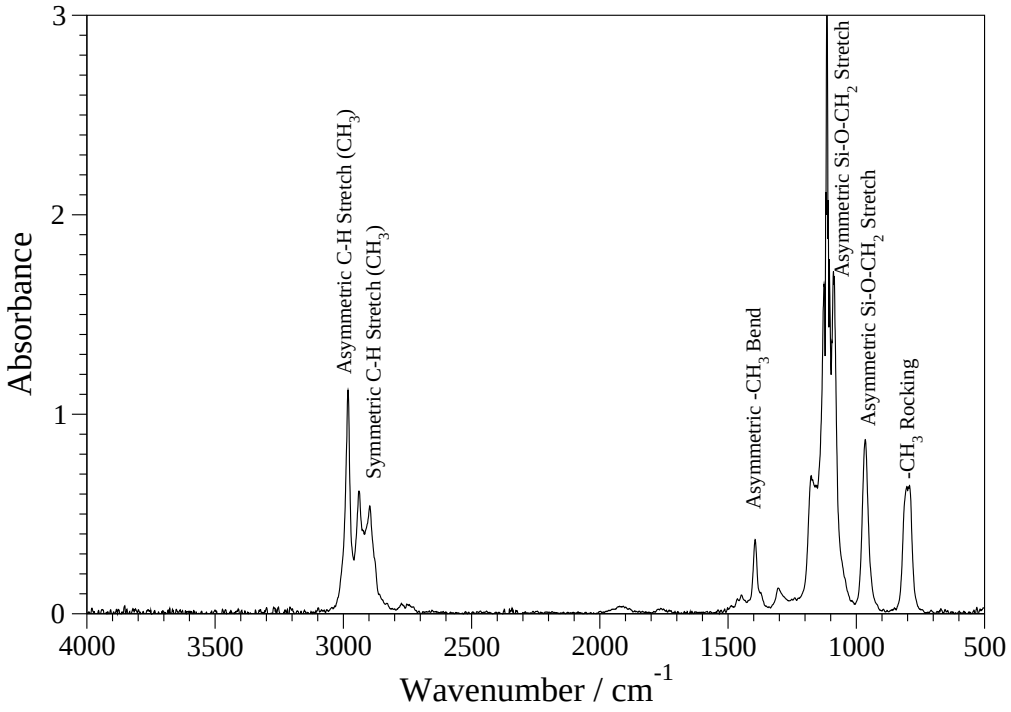

Figure 7.8: FTIR spectra of gases sampled before PECVD reactor recorded at a resolution of 2 cm^{-1}. It represents 500 ppm of TEOS.

[211], and the Beer Lambert Law (Equation 4.6) is applied to extract the concentrations from the integrated areas.

The concentrations extracted for each experiment were then fitted to chemometric models as explained in the previous chapter. The t-test and f-tests were then used to improve the model, and highlight the important variables. The f-test results for the models were above the 95 % level of statistical significance. Response surfaces for acetaldehyde (figure 7.10), carbon monoxide (figure 7.11) and carbon dioxide (figure 7.12) can be seen, the frequency is fixed at 10 kHz for all three.

Immediately it is obvious that the production of both carbon monoxide and carbon dioxide increase with oxygen concentration. In contrast acetaldehyde tends to a maximum level of production with increasing oxygen addition, and then decreases. Acetaldehyde is a major byproduct of the chemical vapour deposition of silica as indicated in equations

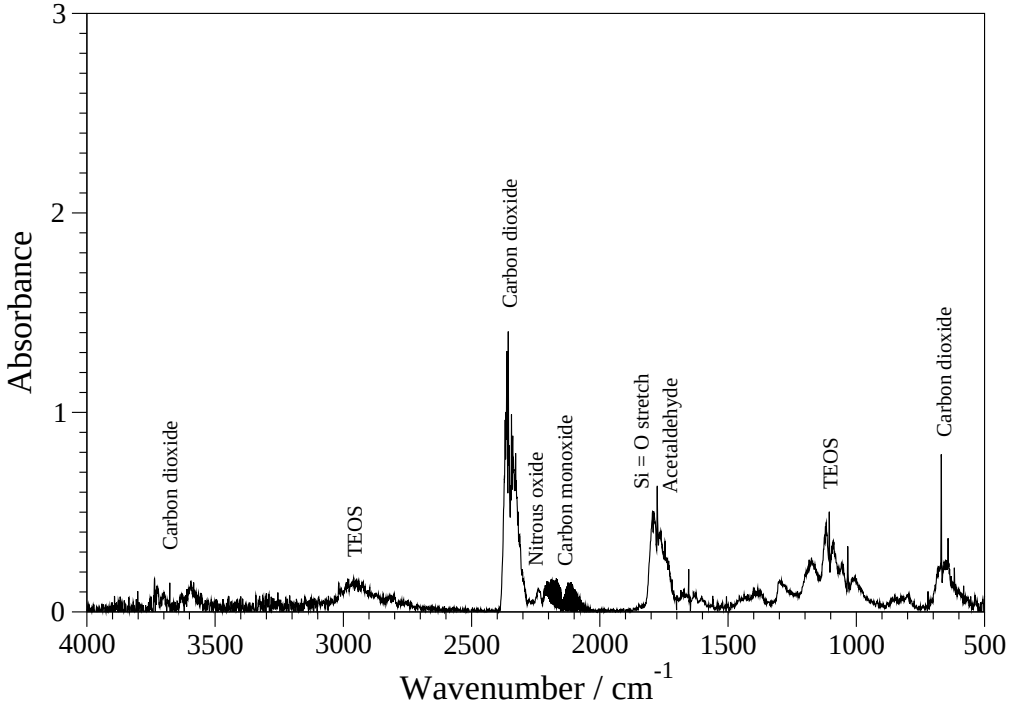

Figure 7.9: FTIR spectra of reactor exhaust from a plasma generated at 10 kHz with a peak to peak voltage of 10 kV, containing 500 ppm TEOS and 5000 ppm of oxygen. Recorded at a resolution of 2 cm^{-1}

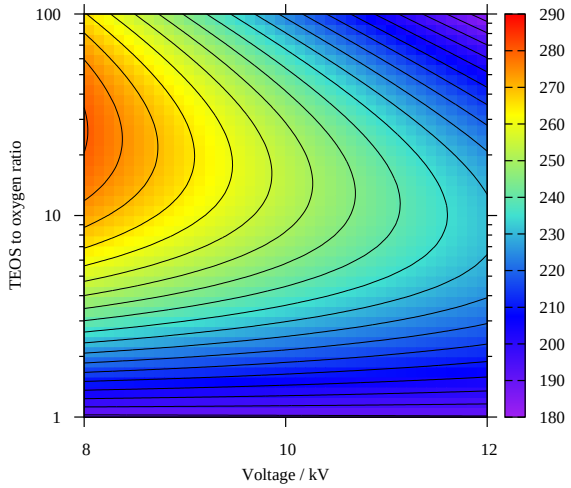

Figure 7.10: Response surface for acetaldehyde formation (in parts per million). Frequency fixed at 10 kHz

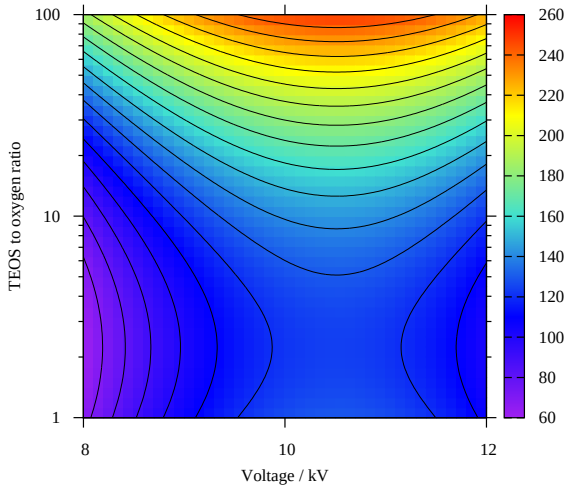

Figure 7.11: Response surface for carbon monoxide formation (in parts per million). Frequency fixed at 10 kHz

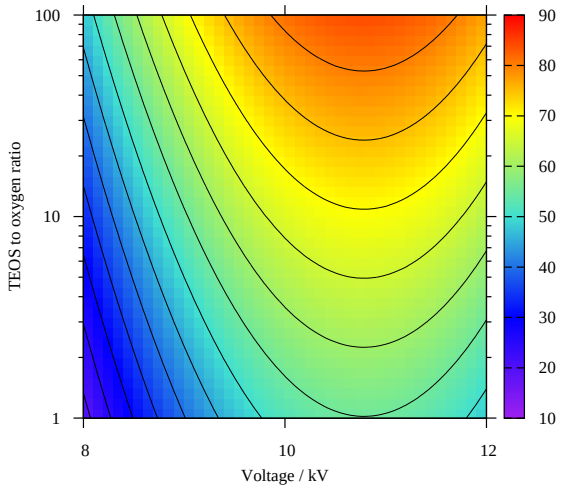

Figure 7.12: Response surface for carbon dioxide formation (in parts per million). Frequency fixed at 10 kHz

7.2 and 7.3. This also indicates that there is a maximum point beyond which acetaldehyde starts to increasingly react with oxygen species in the plasma. This would imply that the kinetics of the process are such that the reaction rate of acetaldehyde with oxygen species is far greater than the rate of formation of acetaldehyde at higher oxygen concentrations. This would also signify that the rate of formation of intermediary silanol species illustrated in equations 7.2 and 7.3 would be equally slow, meaning that the deposition rate would be less than the rate of formation of carbon dioxide and carbon monoxide. The levels of carbon dioxide would likely increase if even more oxygen was added, and the carbon monoxide would decrease.

The effect of voltage on the formation of the by-products can also be seen from the response surfaces in figures 7.10 to 7.12. Acetaldehyde formation shows a flat response to the voltage at lower oxygen concentrations, demonstrating that the reaction rate is relatively independent of the degree of ionisation of the plasma. At higher oxygen concen-

trations however, the voltage starts to have a greater effect, perhaps due to the generation of active oxygen species being highly affected by the density of the plasma. The carbon dioxide and carbon monoxide show a similar response to the driving voltage, in that they show a maximum formation at a peak to peak voltage of around 10 kV. This is possibly due to the oxygen species present at this plasma density.

The precursor decomposition (D_p) can also be calculated from the use of both the initial and final FTIR spectra for each experiment. This is done by calculation of the concentration of precursor before (C_{p0}) and after (C_p), and then using the equation set out in equation 7.4.

$$D_p = 100\frac{C_p}{C_{p0}} \tag{7.4}$$

Response surfaces for the TEOS decomposition are presented in figures 7.13 to 7.15, where the F-test shows a goodness of fit for the model of 95.21 %. The maximum decomposition occurs at high voltage and both low and high TEOS:O_2 ratios, implying that the higher order and interactions between variables are more important in the usage of TEOS in the PECVD process. This is in line with the t-test results. The voltage has a direct bearing on the power consumed by the plasma, so it is expected that more TEOS decomposition would occur with a higher voltage across the plasma. Figure 7.14, the response surface for fixed oxygen concentration, supports this supposition further as it shows higher destruction at higher voltages. The frequency is also of interest, as figures 7.14 and 7.15 show greater TEOS destruction occurs at higher frequency. This is perhaps due to a more rapid, repeated generation of more reactive species at higher frequencies.

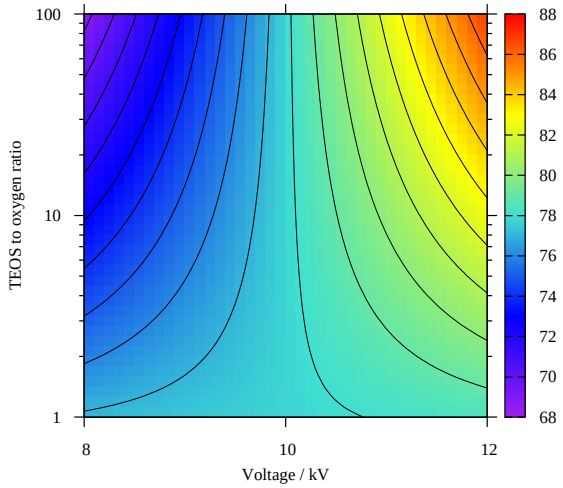

Figure 7.13: Response surface for TEOS decomposition (as a percentage), with frequency fixed at 10 kHz.

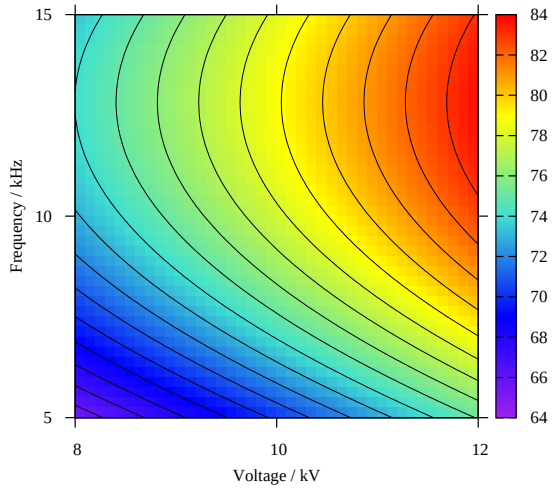

Figure 7.14: Response surface for TEOS decomposition (as a percentage), with TEOS to oxygen ratio fixed at 10.

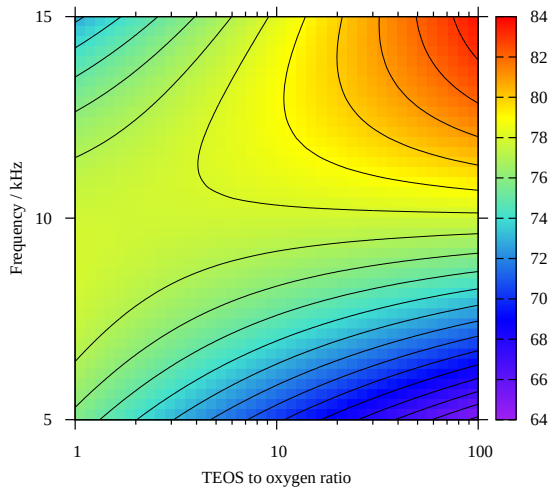

Figure 7.15: Response surface for TEOS decomposition (as a percentage), with peak to peak voltage fixed at 10 kV.

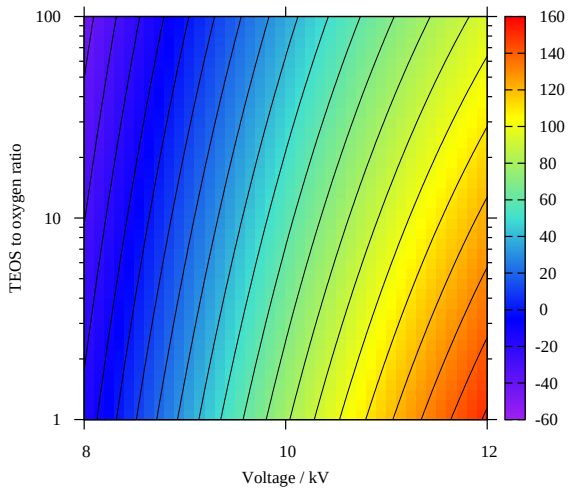

Figure 7.16: Response surface for power (in watts), with frequency fixed at 10 kHz.

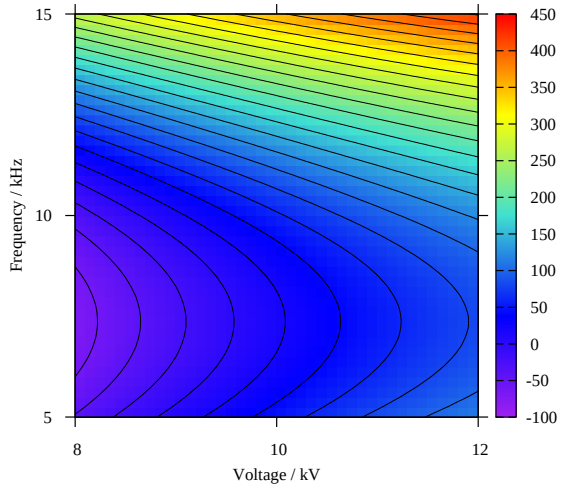

Figure 7.17: Response surface for power (in watts), with TEOS to oxygen ratio fixed at 10.

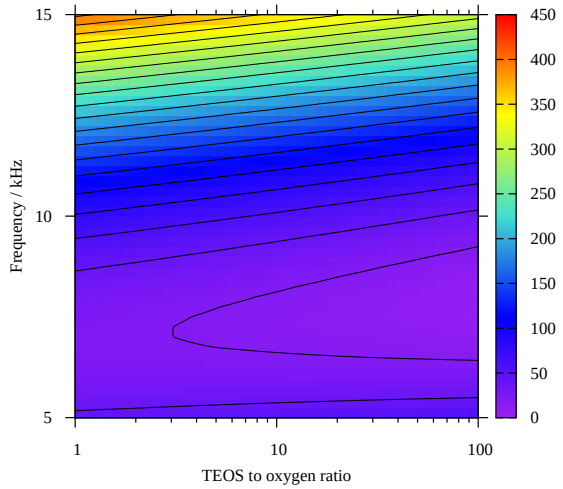

Figure 7.18: Response surface for power (in watts), with peak to peak voltage fixed at 10 kV.

Electrical results

The response surfaces produced for the power results can be seen in figures 7.16 to 7.18. Figures 7.16 and 7.17 show the expected relationship of the power with applied voltage across the cell, as voltage increases, the power increases. The frequency shows a more interesting relationship with the measured power, and this is a quadratic one, with a definite peak at the lower end of the frequency range investigated (around seven kilohertz). The quadratic relationship relates to the underlying chemometric model incorporating a square term. This relationship of power with frequency can be seen in figures 7.17 and 7.18. This relationship is due to the resonance of the power supply and plasma circuit affecting the amount of power that can be coupled into the plasma. The TEOS to oxygen ratio is also of interest, as the plasma requires differing amounts of power depending on its constituent gases. Even so, the effect of the oxygen concentration is not especially strong.

Thin film results

The thickness of the films produced varied between 40 and 120 nm. Film results have also been fitted to second order polynomials. F-tests tend to be greater than 95 %, indicating a good statistical fit of the model. Example surface responses for the growth rate of the films can be seen in figures 7.19 to 7.21, the F-test result for the model is 99.99 %. The replicates of the growth rate varied by about 4 nm / minute, as can be seen in table A.4, whilst the response surfaces vary by at least 18 nm / minute. The growth rate is important, as it governs how fast a particular process can operate. It is also an indicator of the kinetics of the process, as it is essentially the rate of formation of product.

Figure 7.19 shows that the growth rate decreases to a minimum and then increases with increasing oxygen. This would indicate that at a certain point diffusion of precursor

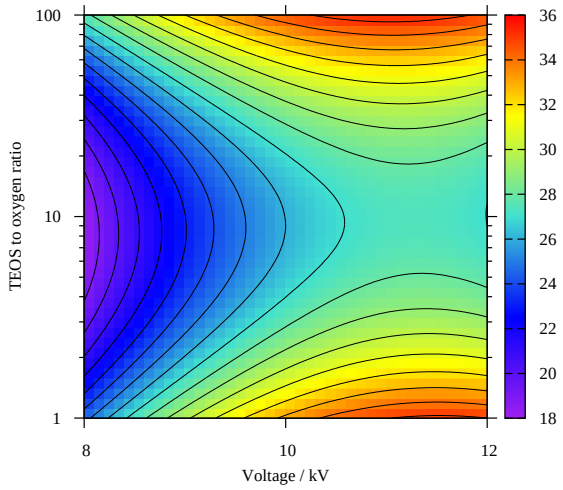

Figure 7.19: Response surface for growth rate (in nanometres per minute), with frequency fixed at 10 kHz.

molecules to the point of film growth is limited by their reaction with oxygen. However with increasing oxygen, the rate of precursor molecule production is increased and a more likely reaction of oxygen species with acetaldehyde occurs, which is corroborated by the response surface for acetaldehyde production shown in figure 7.10. Also notable is the increase of growth rate with voltage, this could either be due to increasing intermediary formation in the gas phase, or the effect of electric fields on the film formation at the surface.

Figure 7.20 is the growth rate response surface for a fixed TEOS to oxygen ratio. The growth rate tends to increase with both increases in voltage and in frequency, showing that the power supply circuit has some bearing on the overall growth rate. Whether this is due to chemistry in the gas phase or the electric fields effecting the film formation requires further investigation.

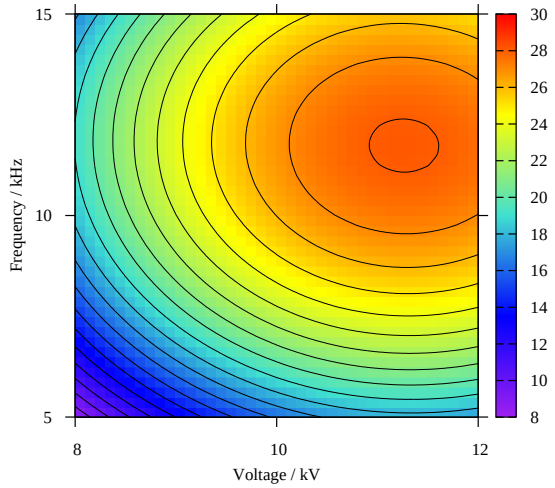

Figure 7.20: Response surface for growth rate (in nanometres per minute), with TEOS to oxygen ratio fixed at 10.

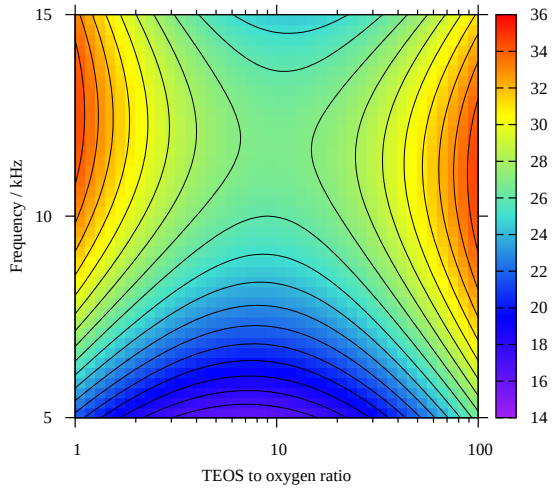

Figure 7.21: Response surface for growth rate (in nanometres per minute), with peak to peak voltage fixed at 10 kV.

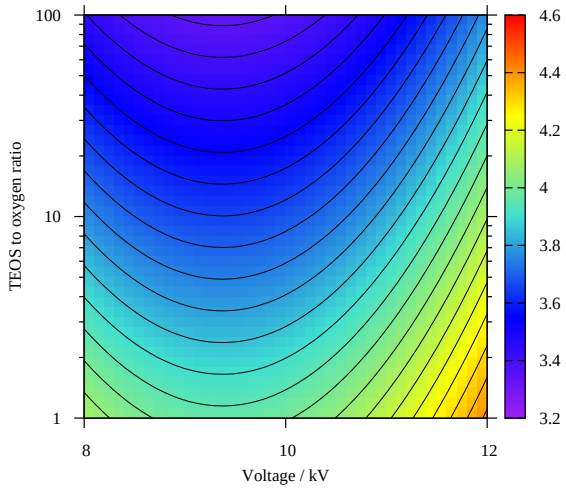

Figure 7.22: Response surface for Mohs hardness, with frequency fixed at 10 kHz.

Figure 7.21 represents the response surface for growth rate at a fixed voltage. An increase and a decrease in the oxygen levels increases the growth rate. Over a certain threshold the growth rate decreases with increasing oxygen, perhaps due to the previous suggestions of non film producing reactions increasingly dominating.

The Mohs hardness is an indicator of the quality of the film, and measures how resistant they are to physical wear. The response surfaces for the Mohs hardness statistical model are presented in figures 7.22 to 7.24. The F-test result for the model is 96.42 %.

The Mohs hardness response surface shown in figure 7.22, which is at a fixed frequency, shows a decrease in hardness with added oxygen content. As the growth rate increases, the films being formed are less dense, leading to less hard films.

In the case of the fixed oxygen concentration response surface for Mohs hardness, seen in figure 7.23, both frequency and voltage show effects on the hardness of the films

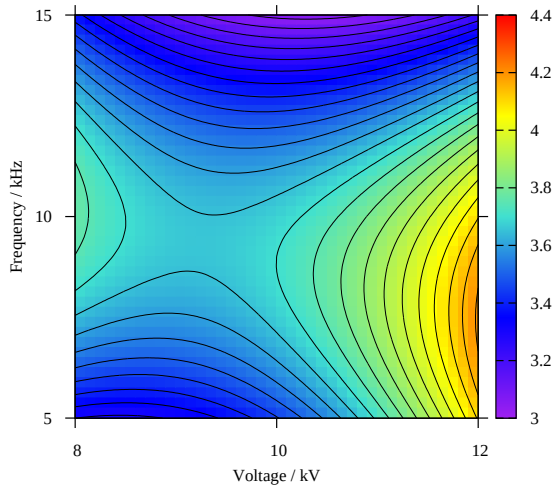

Figure 7.23: Response surface for Mohs hardness, with TEOS to oxygen ratio fixed at 10.

produced. The harder films are produced at higher voltages, perhaps indicating some effect of higher electric fields on the growth mechanism. The effect of the frequency is still significant, and shows that there is a definite sweet spot of frequency for harder films to be produced. This is probably due to several reasons, connected with the growth mechanism, and the deposited plasma power.

The fixed voltage response surface for Mohs hardness is shown in figure 7.24. This response surface indicates a decrease in hardness with oxygen concentration, similar to that shown in figure 7.22. This would further indicate that the faster the growth rate, the less dense and hard the film produced. An intuitive conclusion.

The measured water contact angles were also fitted to the statistical model shown in equation 7.1. The response surfaces for the model can be seen in figures 7.25 to 7.27. The F-test result for the model was approximately 95 %, which shows that it is statistically significant.

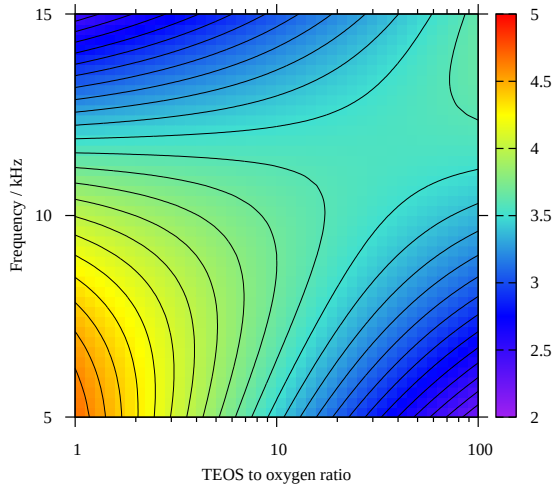

Figure 7.24: Response surface for Mohs hardness, with peak to peak voltage fixed at 10 kV.

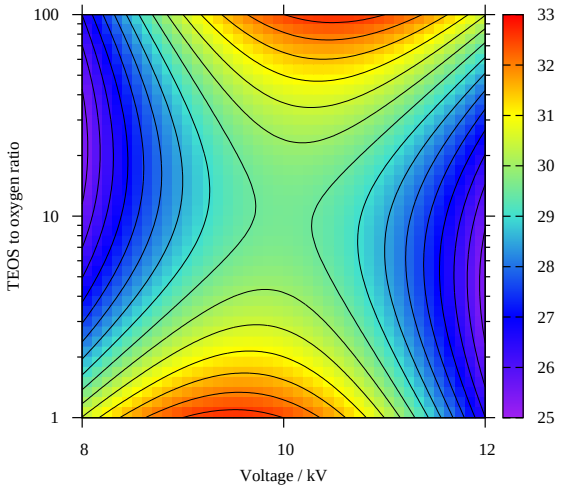

Figure 7.25: Response surface for contact angle (in degrees), with frequency fixed at 10 kHz.

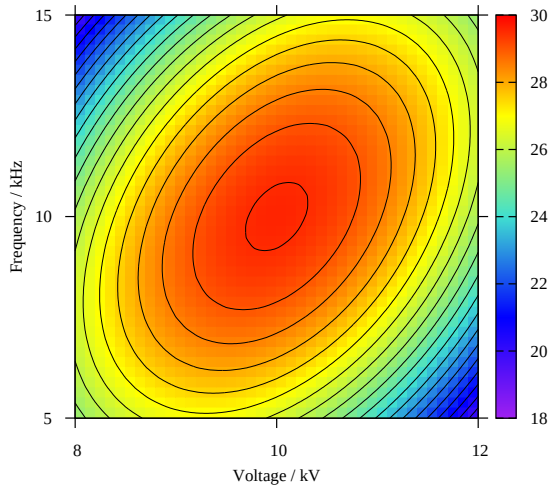

Figure 7.26: Response surface for contact angle (in degrees), with TEOS to oxygen ratio fixed at 10.

The contact angle response surface shown in figure 7.25, which is at a fixed frequency. indicates that the squares of the variables and the variable interaction terms of the model are key. This would imply that the contact angle of the films grown is highly dependent on the plasma conditions, in particular the voltage driving the plasma. The effect of the plasma conditions on the growth of silica does have a marked effect on the surface morphology of the films, and this bears further investigation to identify what is the underlying cause.

In the case of figure 7.26, the response surface for contact angle at fixed oxygen concentration, the maximum contact angle occurs at the mid point of both voltage and frequency. In addition to the wider variation of the contact angle shown in figure 7.26, this would seem to indicate that the power supply and electric field have a marked effect on the surface of the film.

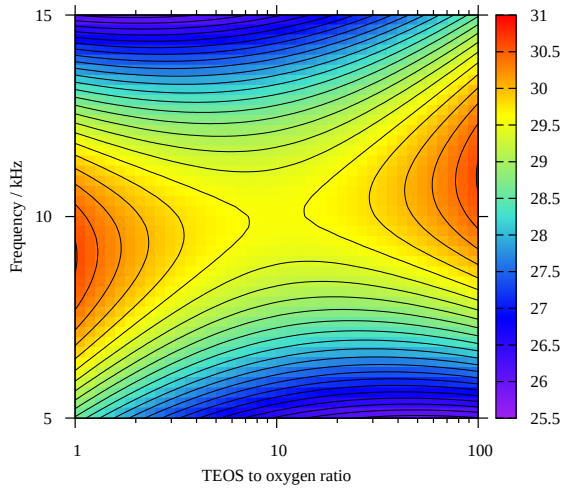

Figure 7.27: Response surface for contact angle (in degrees), with peak to peak voltage fixed at 10 kV.

The fixed voltage response surface for contact angle shows the smallest variation across its parameter space. This is shown in figure 7.27. This would suggest that the voltage is the most important parameter in governing the contact angle of a given plasma deposited silica film. In turn this would suggest that the electric field applied affects the way in which the film forms.

Optical measurements of the films showed that there was not too much variation of the refractive index and absorption coefficient between samples. Models were still fitted however, for both the refractive index of the film, and the absorption coefficient. The F-test results for these models were both greater than 95 %. The voltage and frequency were found to have the greatest impact on the refractive index, and this can be seen in figure 7.28, the response surface for refractive index with fixed oxygen concentration. Otherwise the process variables did not seem to play a role in the optical properties of the films grown.

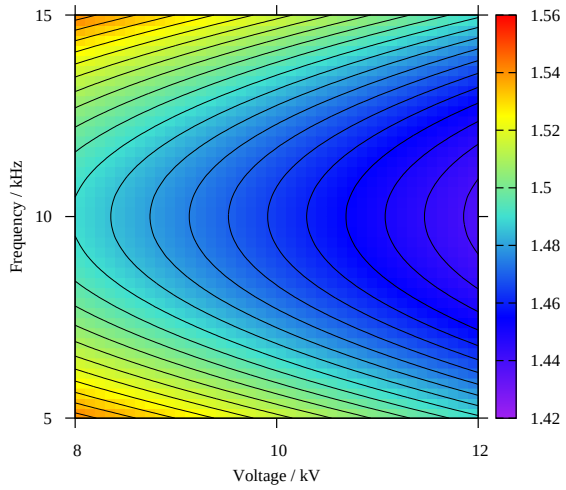

Figure 7.28: Response surface for refractive index, with TEOS to oxygen ratio fixed at 10.

The film response surfaces presented so far represent a guide to optimum processing conditions. It is possible to analyse them with the aim of optimising a particular film property. In the case of Mohs hardness, a low frequency and oxygen concentration in combination with a high voltage produces a harder film. In the case of water contact angle, it is not so easy to classify the optimum. This depends on the end use of the film, and so for hydrophilic films a lower contact angle is better. Referring back to the response surfaces, there are a multitude of processing conditions where this is the case. The refractive index is relatively independent of the processing conditions. Whatever properties are required of the film, the growth rate response surface is useful from a processing perspective, as they can be used to benchmark the process, and identify the conditions for fastest growth rate.

Figure 7.29 represents an ATR-FTIR spectrum of the silica film grown during experiment ten, it is presented in transmission as this is the standard for FTIR spectra of solids.

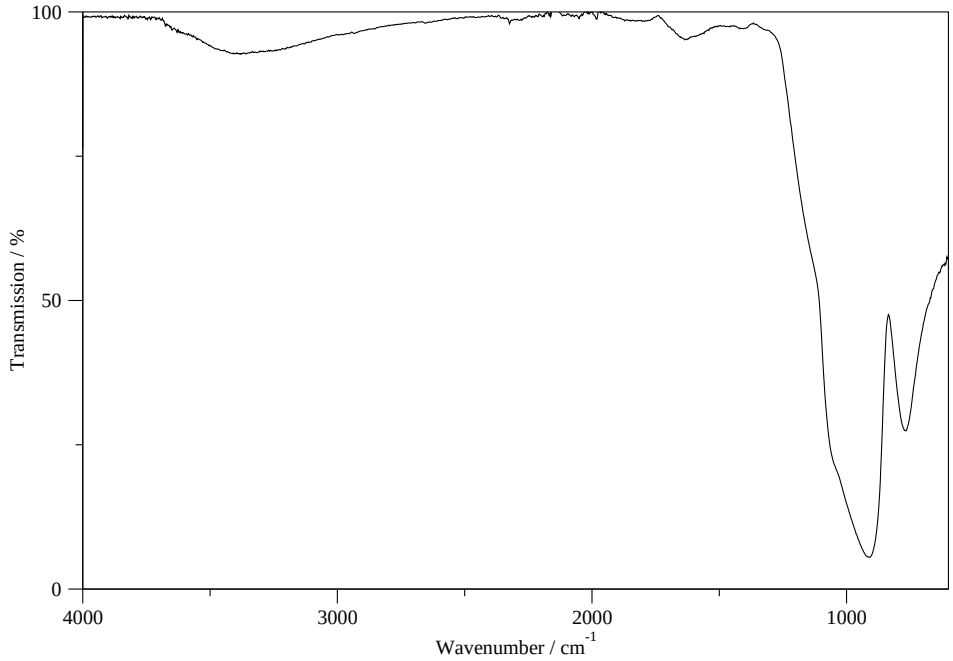

Figure 7.29: ATR-FTIR spectrum for silica thin film grown from 500 ppm TEOS, 0.01 % oxygen in a helium plasma generated at ten kilovolts peak to peak and ten kilohertz.

The peaks that can be seen are indicative of silica films, as seen in [283] and [277].

Principal components analysis

Prior to all principal components analysis, the data was arranged and labelled as described in table 7.7. Principal components analysis has been carried out for the collective interpreted data. This consists of the thin film results, electrical results and excitation temperature. In addition, any large datasets, such as the optical emission data, had principal components analysis carried out on them. All data has been row scaled to one, so as to ensure a firm basis for comparison.

The data matrix for the interpreted data was standardised as detailed in chapter five, before principal components analysis was carried out. This was due to the wide variation in the values of the data described in the dataset. The percentage modelled by the data is

Number	Experiment number	Voltage$_{pk-pk}$	TEOS:O2	Frequency
		x_1	x_2	x_3
1	1	-1	-1	-1
2	16	-1	-1	1
3	17	-1	0	0
4	7	-1	1	-1
5	5	-1	1	1
6	3	0	-1	0
7	13	0	0	-1
8	2	0	0	0
9	8	0	0	0
10	10	0	0	0
11	15	0	0	0
12	18	0	0	0
13	20	0	0	0
14	11	0	0	1
15	19	0	1	0
16	14	1	-1	-1
17	9	1	-1	1
18	12	1	0	0
19	6	1	1	-1
20	4	1	1	1

Table 7.7: Experimental labels for subsequent principal component analysis.

Principal component	Eigenvalue	Percentage modelled	Cumulative percentage
1	69.88	30.65	30.65
2	39.10	17.15	47.80
3	42.52	18.65	66.45
4	29.25	12.83	79.27
5	21.99	9.64	88.92
6	10.57	4.64	93.55
7	6.66	2.92	96.48
8	4.74	2.08	98.56
9	1.46	0.64	99.20
10	0.93	0.41	99.61

Table 7.8: Eigenvalues and percentage modelled of the first ten principal components of the interpreted data.

presented in table 7.8, this shows that the first seven principal components are significant in modelling the data. Included in figures 7.31, 7.32 and 7.33 are the scores plots for the first four principal components of the results data, which models about 80 % of the overall dataset. Figure 7.30 represents the loadings plots for the first four principal components.

From figure 7.30, it is evident that the different principal components represent differing combinations of the interpreted data. Principal component one encompasses the power, growth rate and the results pertaining to the TEOS chemistry. Principal component two relates to the power, phase shift of the current and voltage measurements, and the refractive index of the films grown. The two hardness measurements of the thin films, and the TEOS decomposition are represented by principal component three. Finally, principal component four governs the excitation temperature and the carbon monoxide concentration in the exhaust.

The scores plot for principal components one and two displayed in figure 7.31 indicates two main clusters of data that vary in principal component one. There are two main outliers from the two clusters, and those are experiments fourteen and nineteen. Experiment fourteen was carried out at a peak to peak voltage of ten kilovolts, a TEOS to oxygen

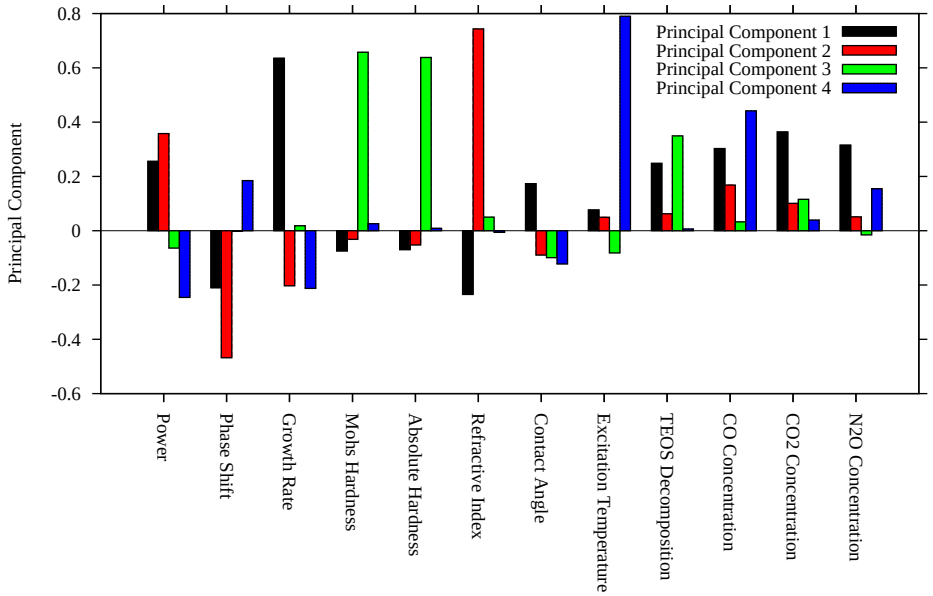

Figure 7.30: Principal component loadings plots for the first four principal components of the interpreted data. The data matrix was standardised.

ratio of one to ten, and a frequency of fifteen kilohertz. Experiment nineteen was carried out at a peak to peak voltage of twelve kilovolts, a TEOS to oxygen ratio of one to one hundred, and a frequency of five kilohertz. From the loadings plots in figure 7.30, it is established that principal component one is related to the power, growth rate, and the TEOS chemistry. This stresses the importance of treating the process as a multivariate process, as, evidenced from tables A.2, A.3 and A.4, different conditions cause similar process results. This is due to how the process parameters combine to affect the TEOS chemistry, which in turn affects the growth rate. The power will of course be affected by the voltage and driving frequency of the power supply, and the power will in turn be related to the TEOS chemistry.

There are also some outliers in terms of principal component two, these are experiments two, five, thirteen, sixteen, seventeen and nineteen. These experiments vary in the oxygen concentration and power supply frequency, indicating that these are the important variables in terms of the power and refractive index of the films produced. This would indicate that processing with higher oxygen concentrations requires less power, as indicated in table A.3, whereas higher frequencies require more power. Perhaps this is due to higher oxygen concentration plasmas being more self sustaining, requiring less overall power. The frequency dependence of the power is as a result of the resonance of the power supply circuit.

Figure 7.32, the scores plot for principal components two and three, shows less pronounced clustering of the experiments. Notable is the clustering in terms of principal component two at around minus one, with a lot more variation in principal component three being displayed. There are no real outliers in principal component three, which represents the hardness of the films produced and the decomposition of the precursor. These two variables are connected, due to the decomposition of TEOS affecting the growth rate, which in turn affects the hardness of the films produced.

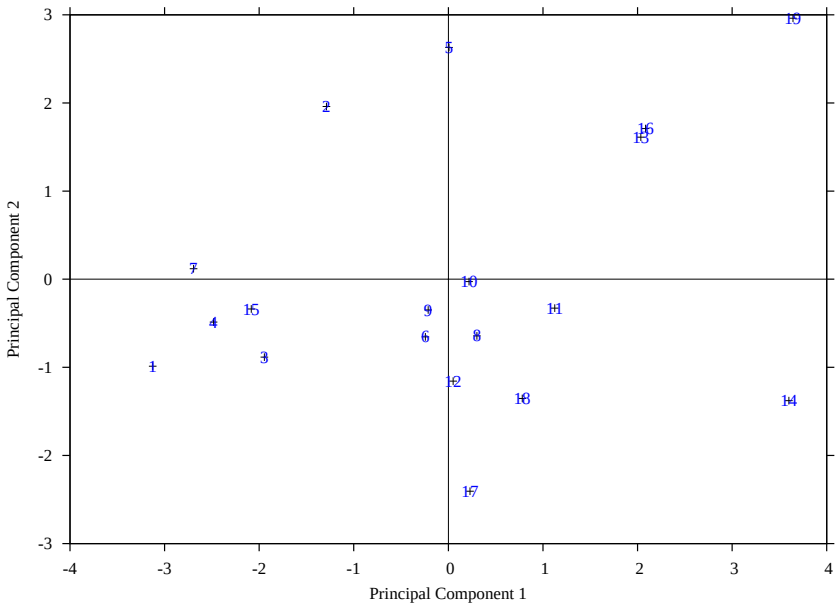

Figure 7.31: Principal component scores plot for principal components one and two of the interpreted data. The data matrix was standardised.

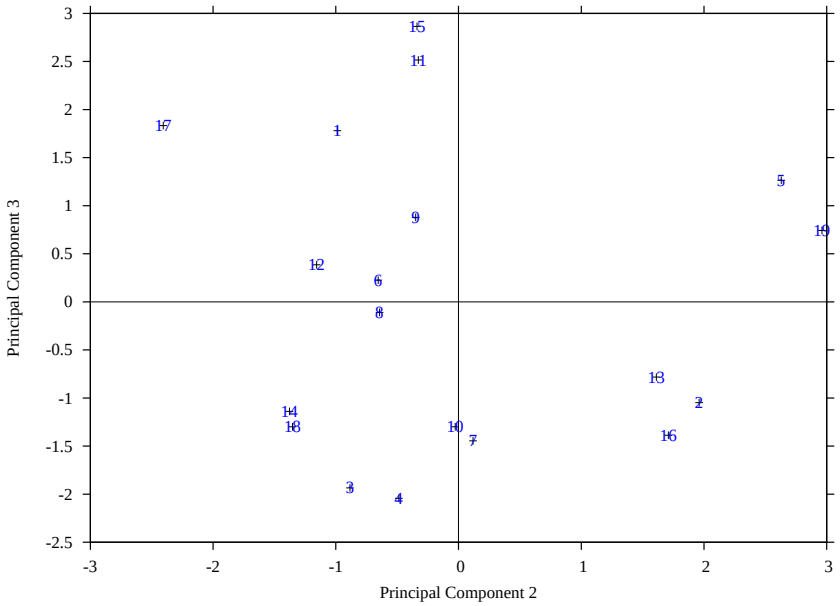

Figure 7.32: Principal component scores plot for principal components two and three of the interpreted data. The data matrix was standardised.

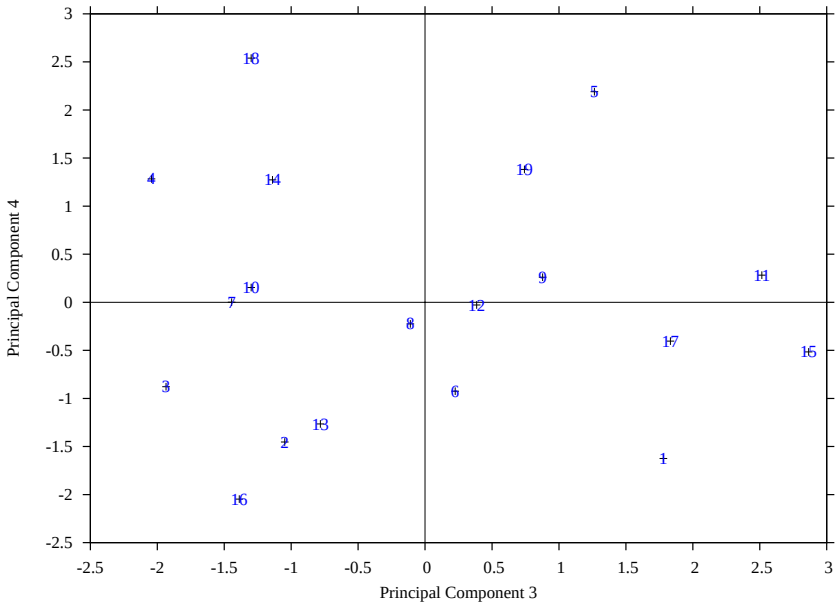

Figure 7.33: Principal component scores plot for principal components three and four of the interpreted data. The data matrix was standardised.

Principal components three and four are displayed in the scores plot on figure 7.33. There is no defined clustering that can be seen in the dataset. This would indicate that there is a lot of variation in principal component four, which, as indicated in figure 7.30, is related to the excitation temperature and the carbon monoxide concentration.

The dataset for the optical emission data was row scaled to one before principal components analysis was carried out, as the arbitrary intensity of the optical emission data is variable between experiments. The eigenvalues for the first three principal components are presented in figure 7.9, and the first three principal components model over 99 % of the dataset. Figures 7.34 and 7.37 are the scores plots for the optical emission data. Figures 7.35, 7.36 and 7.38 are the loadings plots for the first three principal components of the optical emission dataset.

The scores plot for principal components one and two, shown in figure 7.34, demon-

Principal component	Eigenvalue	Percentage modelled	Cumulative percentage
1	0.47	88.43	88.43
2	0.03	5.41	93.83
3	0.03	5.56	99.39

Table 7.9: Eigenvalues and percentage modelled of the first three principal components of the optical emission data.

strates linear clustering beneath the x-axis, with two outliers. These outliers being experiments four and five, which both consisted of low voltage and high TEOS to oxygen ratio. From the loadings plot for the second principal component, figure 7.36, it is clear that this principal component relates to the atomic emission lines from the plasma. Principal component one however, models all emission from the plasma, which can be seen from figure 7.36. Referring to table A.2, the excitation temperature for these two experiments was quite high. This would indicate that the high concentration of oxygen in the plasma provided a more electronically excited plasma, even though the driving voltage was low. The driving frequency also differentiates the two outlier experiments in terms of principal component one, which models the entire emission spectrum as seen in figure 7.36, this would indicate the frequency of the power affects the plasma chemistry of the molecular species, in addition to the atomic species. This could in part be due to coupling of the reaction kinetics being strongly affected by the frequency at which power is transferred to the plasma.

Presented in 7.37 is the scores plot for principal components two and three of the optical emission dataset. There is a similar linear clustering comparable to that seen in figure 7.34, with experiments four and five again providing outliers. Principal component three does seem to be related to the noise of the baseline, as can be seen in the loadings plot for principal component three, figure 7.38. The difference of experiments four and five is again connected to the different excitation experienced at higher oxygen concentrations in the plasma.

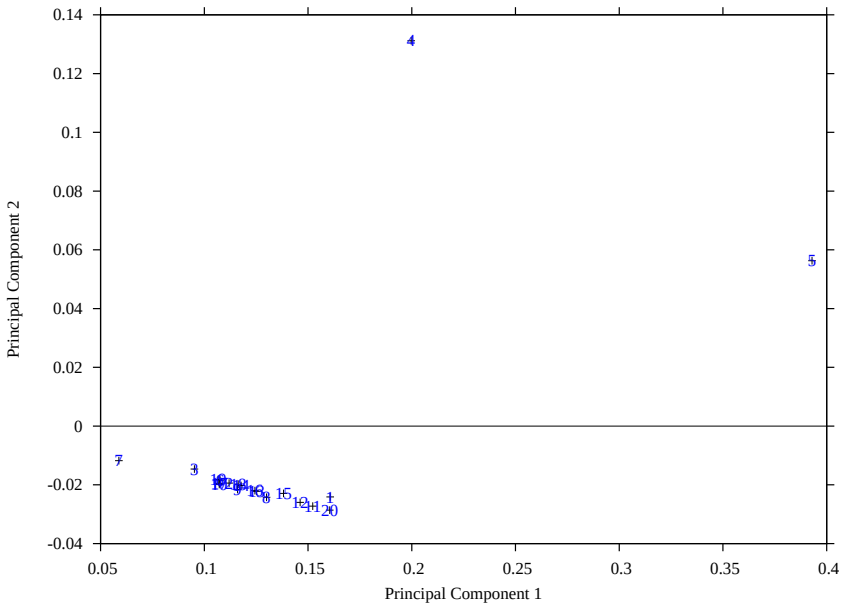

Figure 7.34: Principal component scores plot principal components one and two of the optical emission data. The data matrix was row scaled to one.

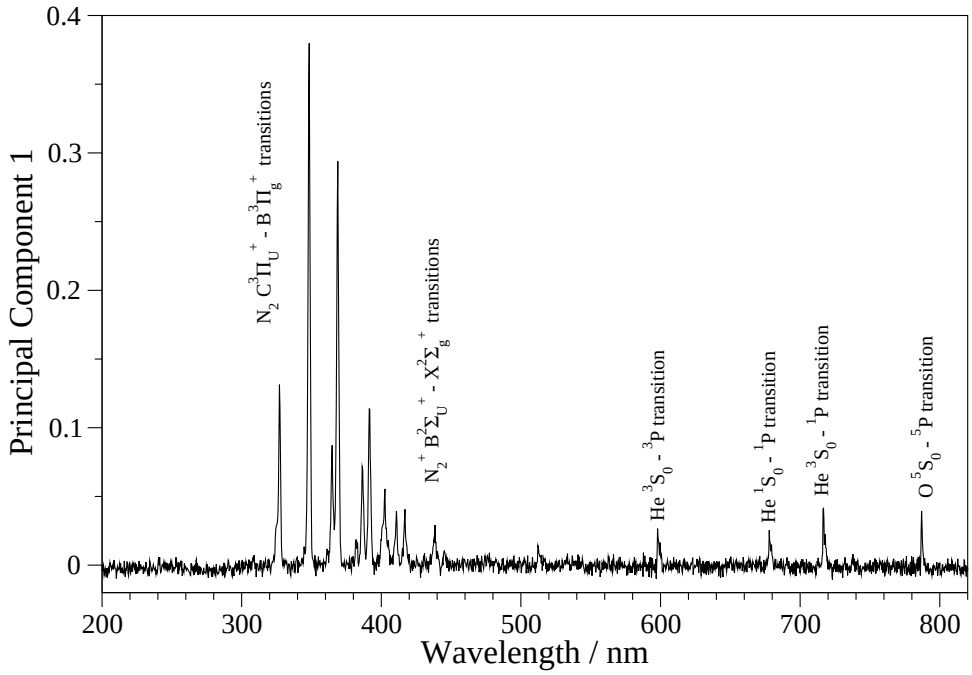

Figure 7.35: Principal component loadings plot for the principal component one of the optical emission dataset. The data matrix was row scaled to one.

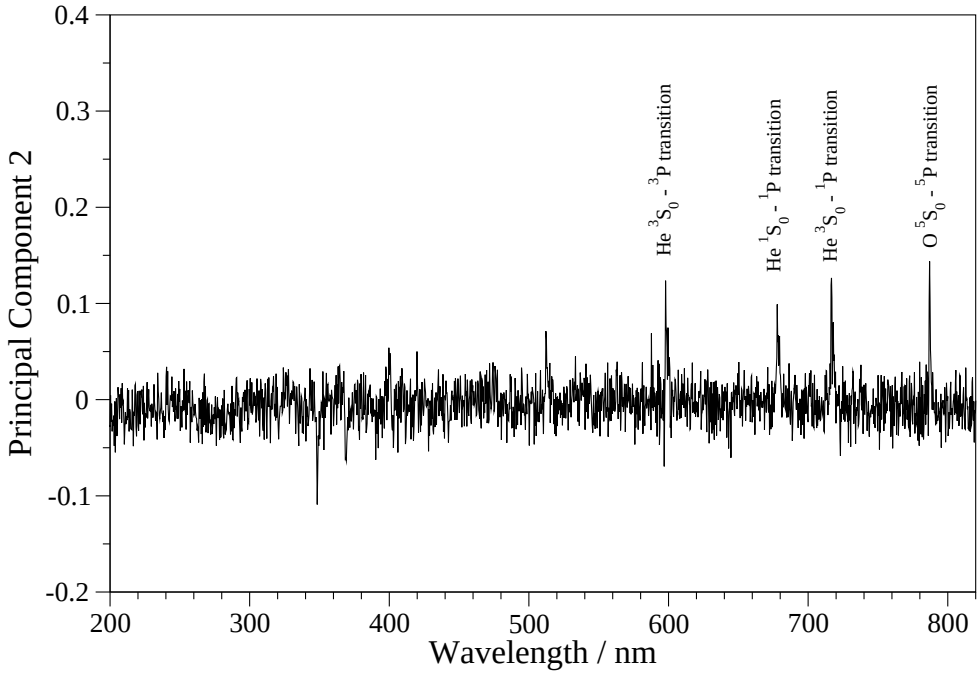

Figure 7.36: Principal component loadings plot for the principal component two of the optical emission dataset. The data matrix was row scaled to one.

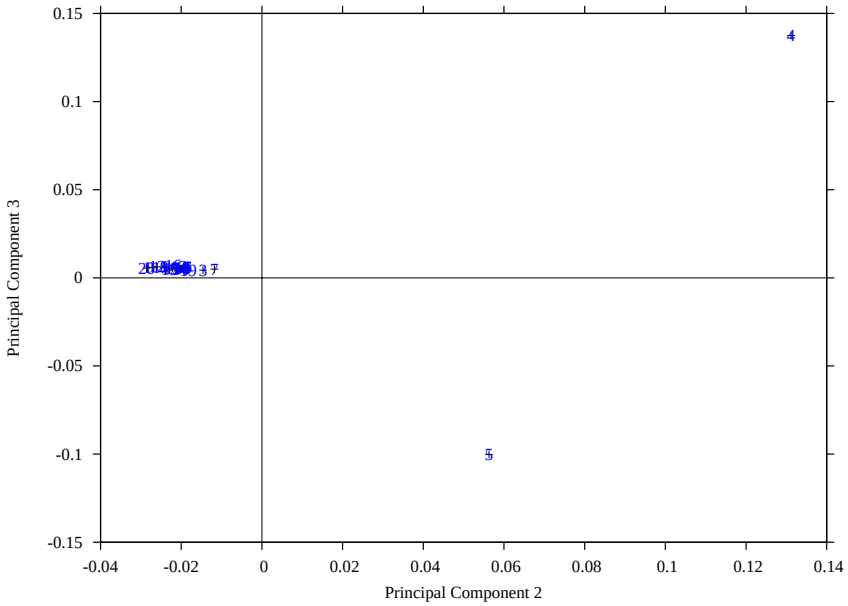

Figure 7.37: Principal component scores plot principal components two and three of the optical emission data. The data matrix was row scaled to one.

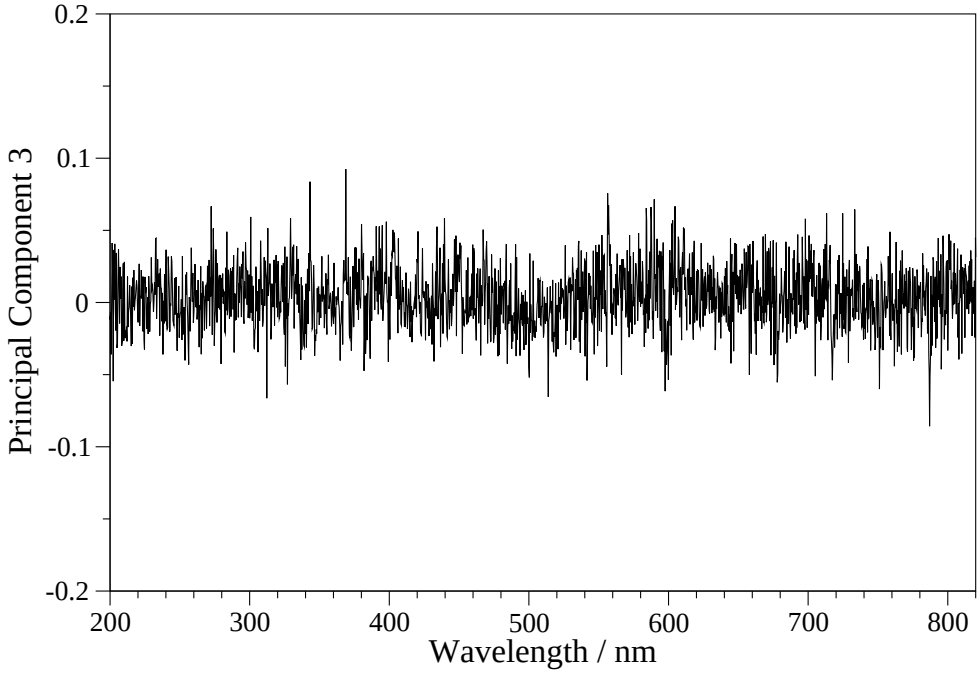

Figure 7.38: Principal component loadings plot for the principal component three of the optical emission dataset. The data matrix was row scaled to one.

Prior to the principal components analysis, mean centring was used on the FTIR dataset, so as to ensure that the FTIR spectra are compared on the same baseline. The eigenvalues of the principal components analysis are presented in table 7.10, the first four principal components modelling 80 % of the dataset. Figures 7.39, 7.42 and 7.44 are the scores plots for the first four components of the FTIR spectroscopy data. Figures 7.40, 7.41, 7.43 and 7.45 show the loadings plots for principal components one through four. The loadings plots are all dominated by carbon dioxide, due to the FTIR measurements also measuring atmospheric carbon dioxide, which fluctuated over the experimental runs.

The scores data for principal components one and two is presented in figure 7.39. There appears to be a linear relationship between principal components one and two in this case, with experiment fifteen being an outlier from this relationship. Experiment fifteen was performed at high oxygen concentration, with medium driving voltage and frequency. Examination of the loadings plots for principal components one and two in

Principal component	Eigenvalue	Percentage modelled	Cumulative percentage
1	208.30	36.85	36.85
2	121.82	21.55	58.41
3	62.79	11.11	69.52
4	61.12	10.81	80.33
5	38.69	6.84	87.18
6	10.07	1.78	88.96
7	6.67	1.18	90.14
8	8.47	1.50	91.64
9	12.65	2.24	93.88
10	6.17	1.09	94.97

Table 7.10: Eigenvalues and percentage modelled of the first ten principal components of the FTIR data.

figures 7.40 and 7.41 respectively, indicates that principal component one models the carbon dioxide and acetaldehyde by-products, whilst principal component two models the left over TEOS in the exhaust. In addition, principal component one models a feature at 1000 cm^{-1}, that does not appear in the raw spectral data, which looks to be ozone. The combination of high oxygen with medium voltage and frequency causing an aberrant point on the scores plot, implies that there is a different effect on the TEOS breakdown chemistry at these conditions, perhaps due to an increase of the amount of ozone produced in the process.

Principal components two and three are represented by the scores plot in figure 7.42. The loadings plot for principal component three shown in figure 7.43 shows the potential ozone peak at about 1000 cm^{-1}, and the acetaldehyde peak. Experiment eleven is an outlier in principal component three, and this is one of the replicate experiments. The outlier could be caused by a difference in the measured atmospheric carbon dioxide however.

The scores plot for principal components three and four of the FTIR dataset is presented in figure 7.44. The loadings plot for principal component four, figure 7.45, shows that principal component four predominantly models the acetaldehyde peak. In this in-

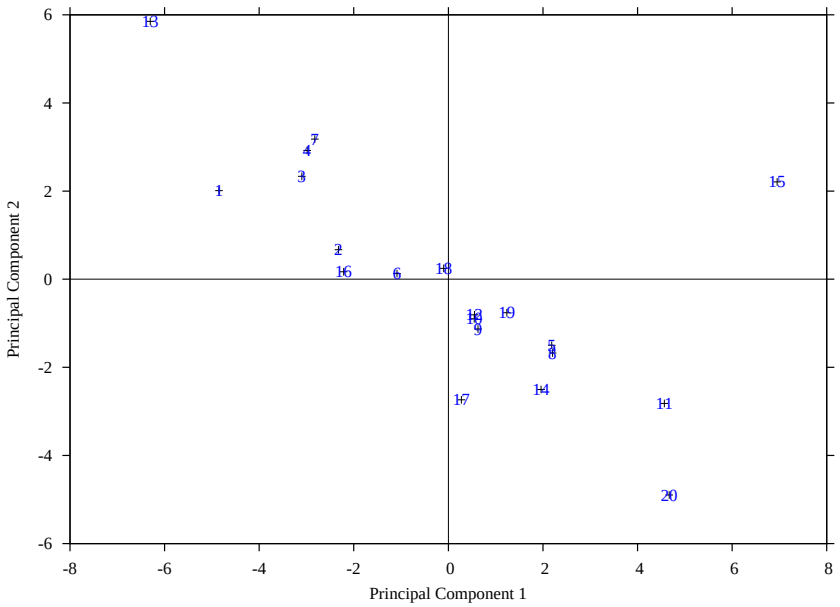

Figure 7.39: Principal component scores plot for principal components one and two of the FTIR spectroscopy data. The data matrix was standardised.

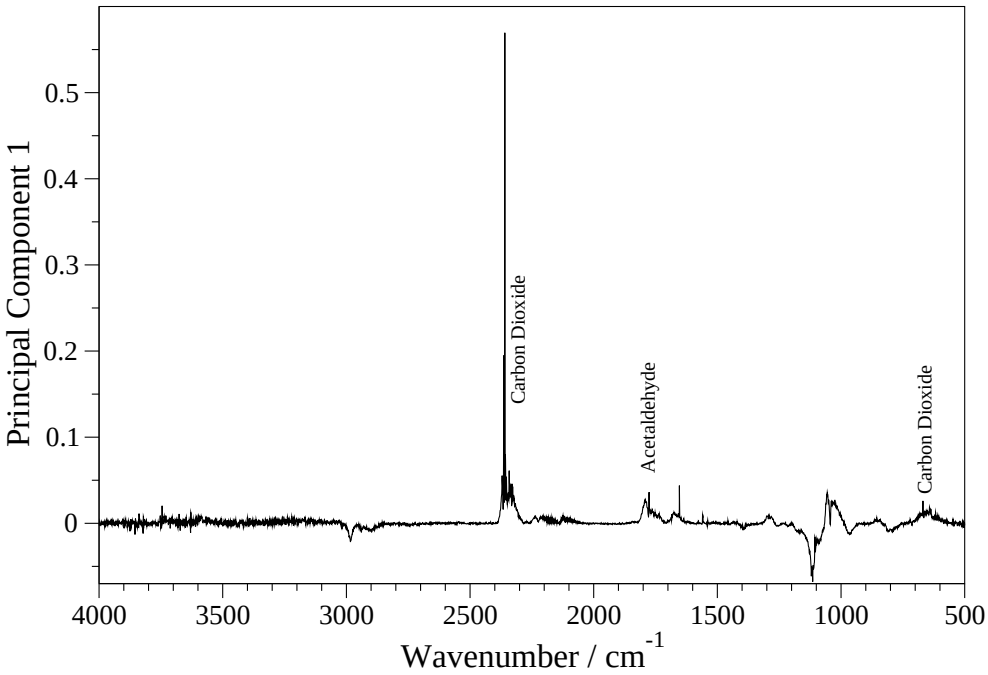

Figure 7.40: Principal component loadings plot for principal component one of the FTIR spectroscopy data. The data matrix was standardised.

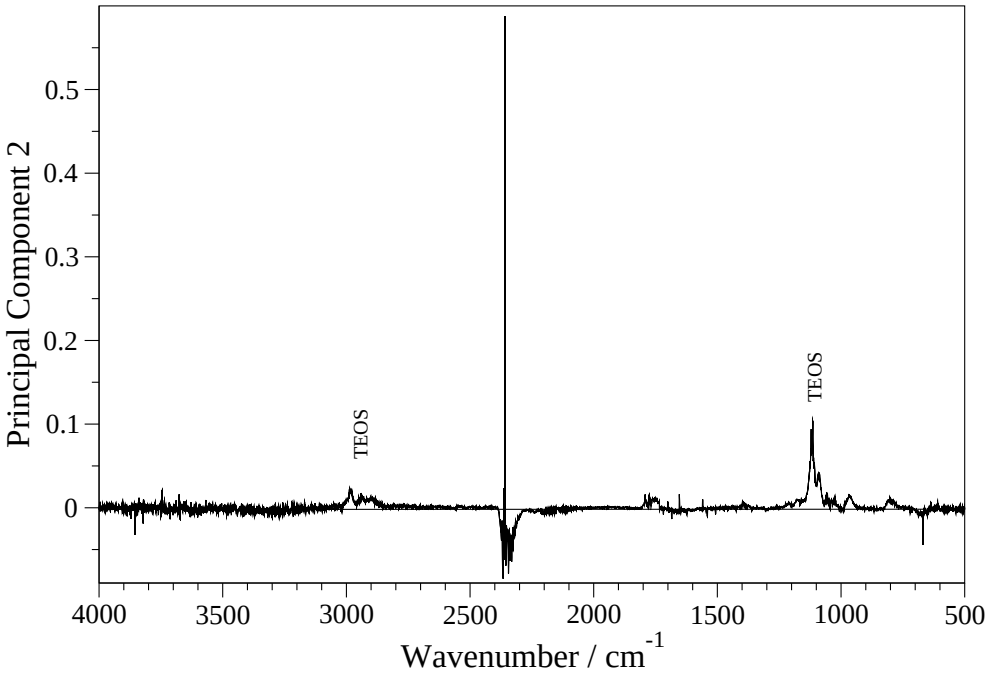

Figure 7.41: Principal component loadings plot for principal component two of the FTIR spectroscopy data. The data matrix was standardised.

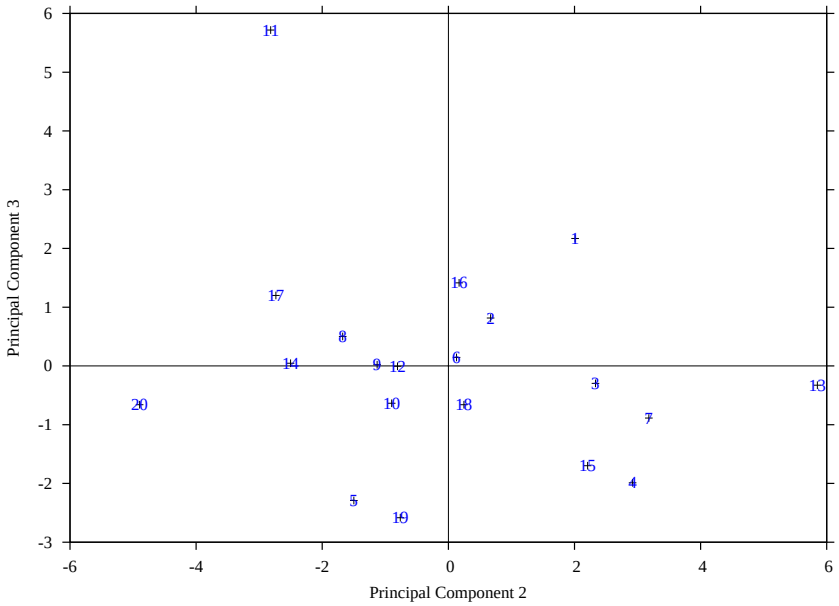

Figure 7.42: Principal component scores plot for principal components two and three of the FTIR spectroscopy data. The data matrix was standardised.

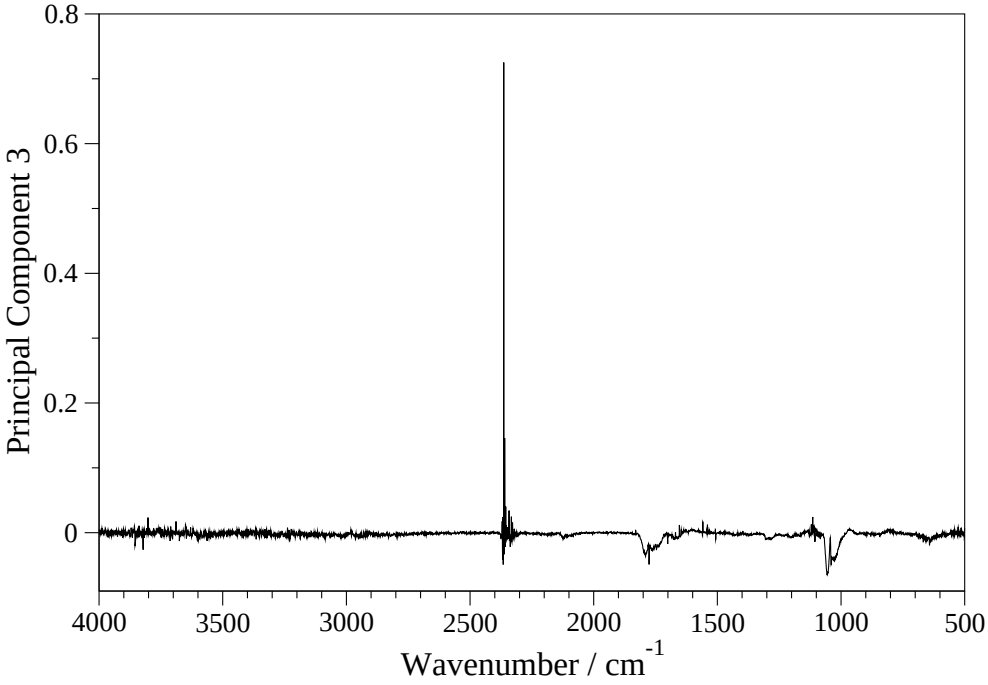

Figure 7.43: Principal component loadings plot for principal component three of the FTIR spectroscopy data. The data matrix was standardised.

stance, experiments sixteen, seventeen and one are outliers from the main clusters of data. All three experiments were performed at low frequency, indicating a frequency dependence of the acetaldehyde formation. This would be due to the kinetics of the process being heavily affected by the driving frequency of the plasma, increasing the rate of acetaldehyde production at differing frequencies.

The ATR-FTIR dataset was standardised before principal components analysis was carried out. As the spectra are very similar, standardisation will allow for the exploration of minute differences between them with principal components analysis. The eigenvalues of the first ten principal components are presented in table 7.11, the first three principal components describe just under 90 % of the dataset. Figures 7.46 and 7.49 are the scores and plots for the first three principal components of the ATR-FTIR spectroscopy data. The loadings plots for the first three principal components are presented in figures 7.47, 7.48 and 7.50.

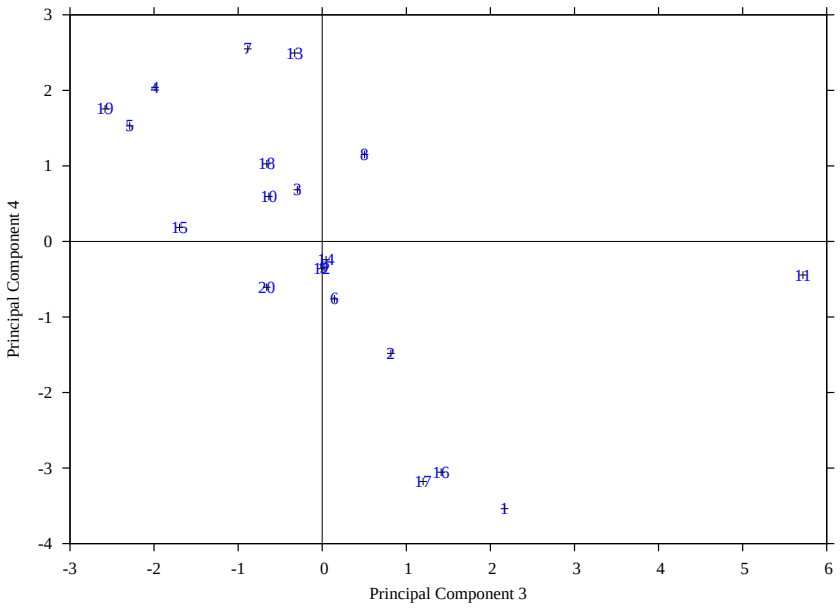

Figure 7.44: Principal component scores plot for principal components three and four of the FTIR spectroscopy data. The data matrix was standardised.

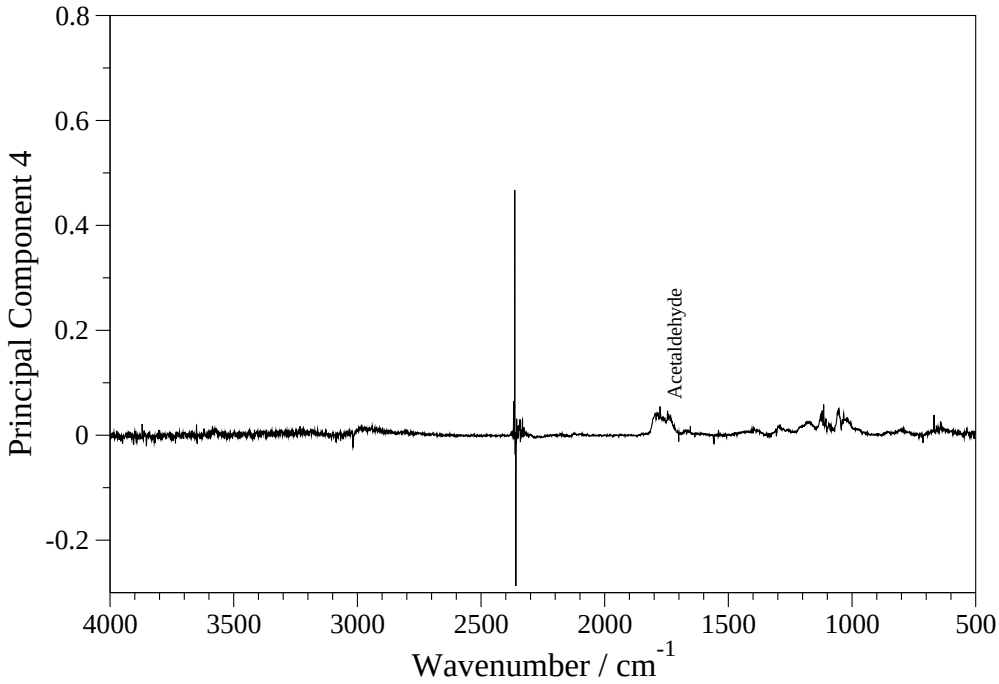

Figure 7.45: Principal component loadings plot for principal component four of the FTIR spectroscopy data. The data matrix was standardised.

Principal component	Eigenvalue	Percentage modelled	Cumulative percentage
1	8754.67	24.81	24.81
2	20330.00	57.62	82.44
3	2360.53	6.69	89.13
4	1111.65	3.15	92.28
5	266.45	0.76	93.04
6	405.34	1.15	94.19
7	308.17	0.87	95.06
8	298.58	0.85	95.19
9	148.29	0.42	96.33
10	167.71	0.48	96.80

Table 7.11: Eigenvalues and percentage modelled of the first ten principal components of the ATR FTIR data.

The scores plot for principal components one and two of the ATR-FTIR dataset shows three distinct clusters of experiments, this is shown in figure 7.46. Principal component one seems to be related to a carbon dioxide peak at 2300 cm^{-1}, indicated in the loadings plot in figure 7.47, this is most likely due to atmospheric carbon dioxide present during the measurement. Principal component one also models symmetric and asymmetric carbon hydrogen stretches at approximately 2900 cm^{-1}. Principal component two however, models a series of four peaks from 1300 to 2300 cm^{-1}, in addition to symmetric and asymmetric carbon hydrogen stretches at approximately 2900 cm^{-1}. The scores plot, figure 7.46 shows two main clusters of data in principal component two, with one large cluster in principal component one which has an outlier in experiment seventeen. Experiment two was conducted at low oxygen concentration and high voltage and frequency, which would imply that the hydrocarbon impurities in the films are strongly effected by the active oxygen species in the plasma in combination with a higher powered plasma (580 watts from table A.3).

Figure 7.49 shows the scores plot for principal components two and three of the ATR-FTIR spectroscopy data. Again, three clusters can be seen, with experiment seventeen being a notable outlier. The loading plot in figure 7.50 indicates that principal component

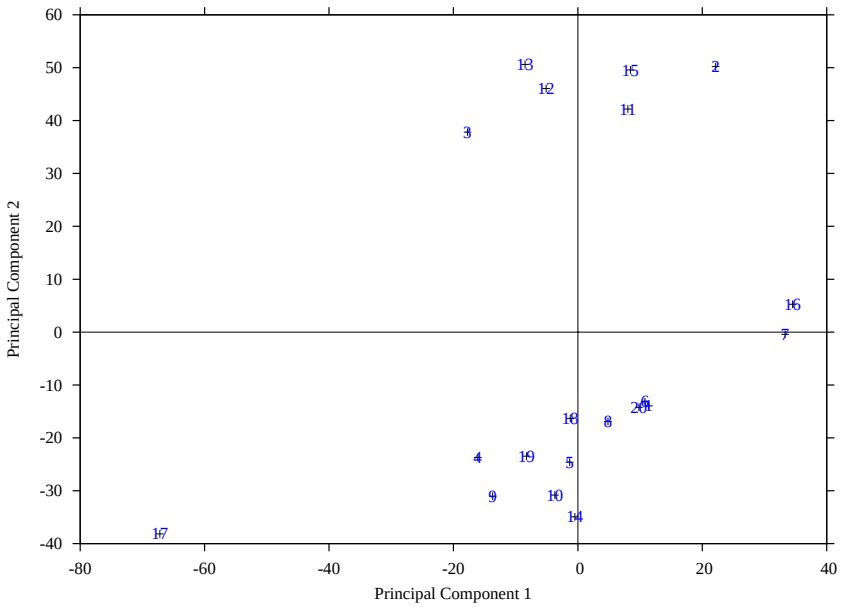

Figure 7.46: Principal component scores plot for principal components one and two of the ATR-FTIR spectroscopy data. The data matrix was standardised.

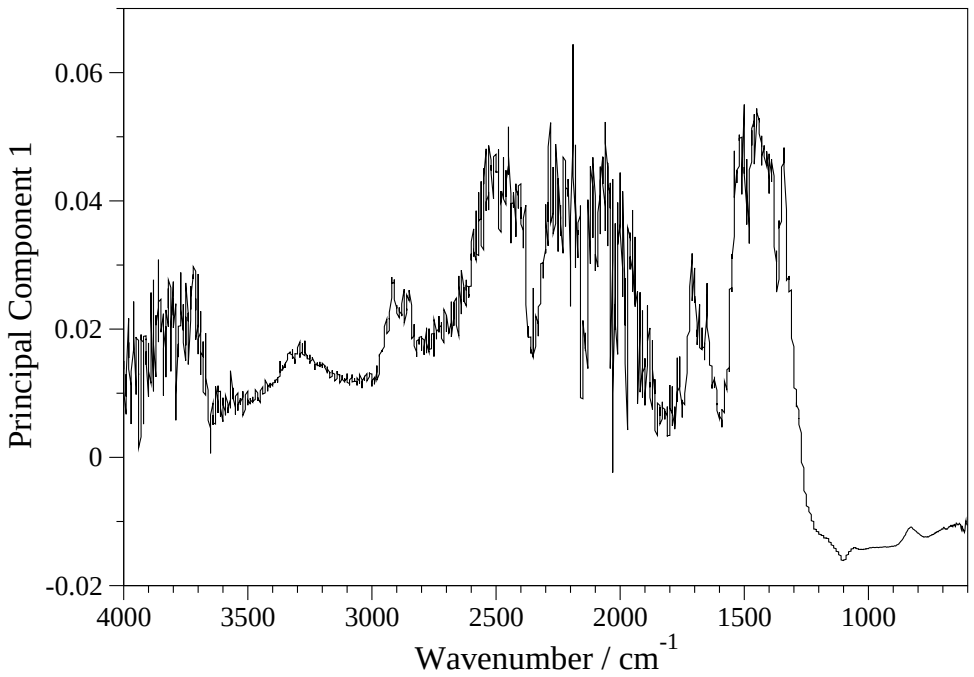

Figure 7.47: Principal component loadings plot for principal component one of the ATR-FTIR spectroscopy data. The data matrix was standardised.

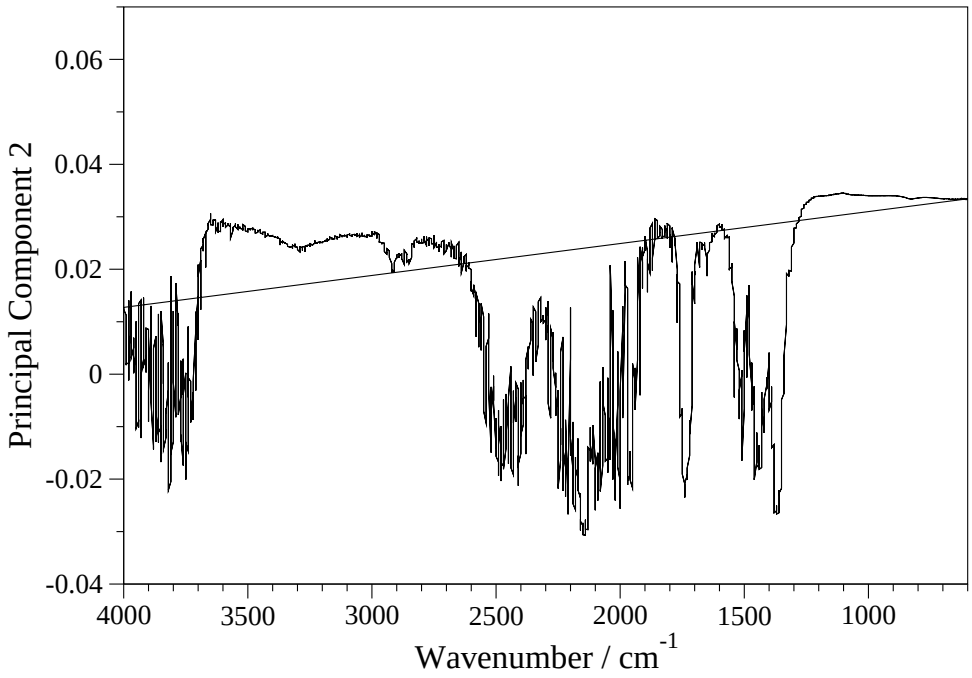

Figure 7.48: Principal component loadings plot for principal component two of the ATR-FTIR spectroscopy data. The data matrix was standardised.

three models a spectral feature from 1200 to 1500 cm^{-1}, and another at 2000 to 2200 cm^{-1}.

7.4 Conclusions

The aim of the work has been successfully met, as the optimum processing conditions for a variety of film properties have been identified for this particular process. With this information, subsequent reactor and power supply designs for the process can be tailored towards providing these conditions.

The use of FTIR spectroscopy has identified acetaldehyde as a key by-product of the TEOS based plasma enhanced chemical vapour deposition of silica films, which has so far been unreported in the literature. The optical emission spectroscopy has also highlighted

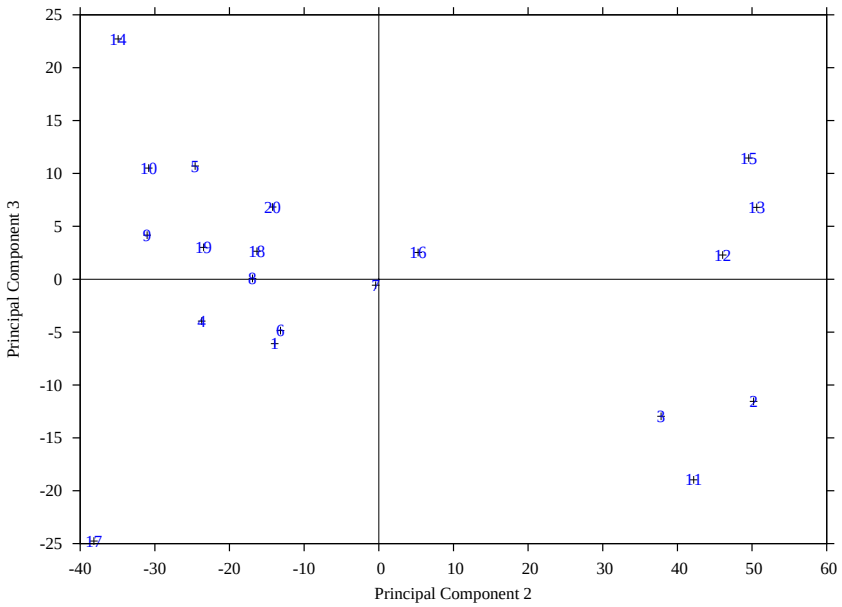

Figure 7.49: Principal component scores plot for principal components two and three of the ATR-FTIR spectroscopy data. The data matrix was standardised.

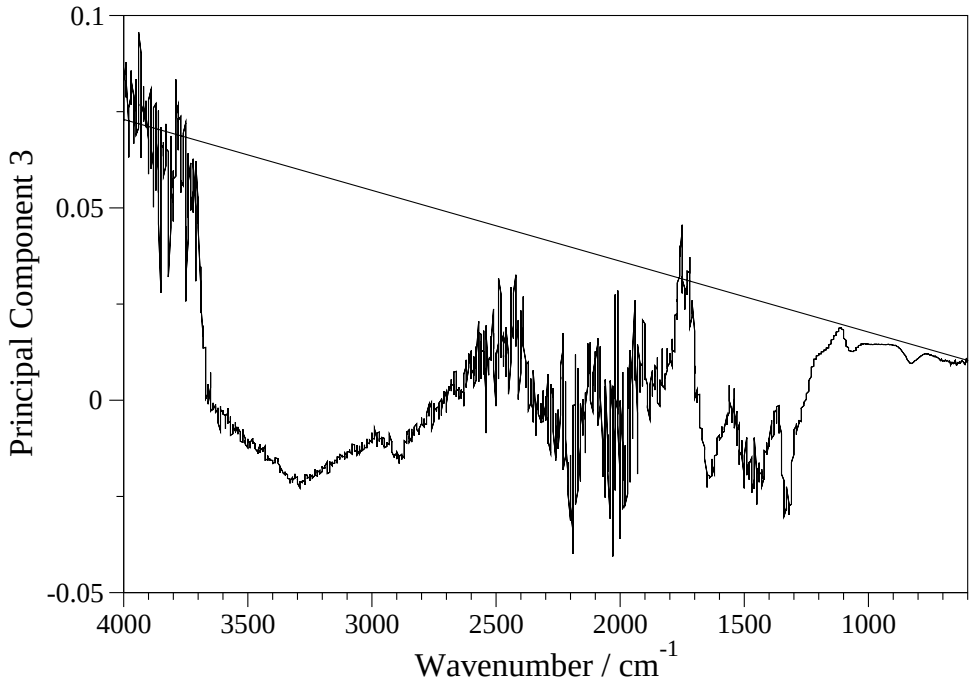

Figure 7.50: Principal component loadings plot for principal component three of the ATR-FTIR spectroscopy data. The data matrix was standardised.

the existence of reactive oxygen species in the plasma, indicating the key reactions occurring in the gas phase.

In addition the combination of the spectroscopic results with the experimental design techniques provides an insight into the chemistry of the silica deposition process. They can be used to quickly investigate the kinetics of the plasma enhanced chemical vapour deposition process, without the use of, in this case, unknown kinetic modelling schemes. In particular, the chemometric techniques have highlighted the effects of adding oxygen to the process on the formation of by-products and the film growth rates. The excitation temperature has also been shown to be highly dependent on the oxygen concentration in the gas. With their use, the rate of formation of acetaldehyde has been indicated to be less than that of carbon monoxide and carbon dioxide at higher oxygen concentrations.

This is the first time principal components analysis has been reported as being applied to the plasma enhanced chemical vapour deposition process. The principal components analysis has proven useful in identifying variations within the data sets, and the importance of the control variables on the plasma chemistry and film properties. The analysis of the interpreted data has identified links between the plasma chemistry and film properties which can be related back to the processing conditions the experiments were carried out under. The principal components analysis of the optical emission data set has identified the importance of the oxygen concentration in combination with the applied voltage on the excitation of the plasma. The principal components of the FTIR data showed that the chemistry could be broken down into distinct groups that can be controlled by the process parameters chosen. In addition, the production of ozone has been shown to occur in the process, which is a new discovery. The plasma enhanced chemical vapour deposition process is a complicated one, but it is clear from the principal components analysis that it is a controllable process.

The results produced during this work have shown that the chemometric approach is

a viable method for enhancing understanding of the plasma enhanced chemical vapour deposition process. It has proved extremely useful, given the complexity of the process, and has allowed for conclusions to be drawn about the chemistry occurring in the process. The enhanced knowledge in turn helps with improving process design and identifying key control variables, particularly with regards to the power supply.

Chapter 8

Chemometric investigation of the atmospheric pressure plasma enhanced chemical vapour deposition of silica from dichlorodimethylsilane

8.1 Introduction

The investigations in the previous chapter have been shown to be of great use in understanding the plasma enhanced chemical vapour deposition of silica from TEOS. They also provide a baseline, against which subsequent results concerning silica film deposition can be compared.

The techniques can be applied to the plasma enhanced chemical vapour deposition of silica from a new precursor. The precursor studied for the purposes of this work will be dichlorodimethylsilane (DDS). This precursor has been used previously for the low pressure chemical vapour deposition of silicon carbide films, [13]. Previous work has also been carried out by the author in coating silica thin films at atmospheric pressure using DDS as the precursor, [237].

Reasons for investigation of new precursors in chemical vapour deposition are many. They can be expensive consumables in the process, and the possibility of cheaper alternatives is always attractive when running such a process. There is also a possibility that the thin films grown from different precursors will have greatly enhanced properties. The growth rate might also be increased, providing faster processing times, or there is the possibility of using less precursor use to give an equivalent thickness of film. Finally, the

amount of unwanted atoms in the films structure could be reduced.

Comparison to an established process is important in the assessment of such precursors, and the previous chapter provides a baseline against which other precursor chemistries for silica films can be assessed.

Aims and Objectives

the aim of this work is the examination of silica films grown by plasma enhanced chemical vapour deposition from DDS at atmospheric pressure so as to examine its suitability as a precursor. This in turn will prove the feasibility of the chemometric approach.

The objective of the work presented in this chapter, is to show how the combined chemometric and spectroscopic methodology outlined in the previous chapter can be applied to the development of chemical vapour deposition processes using a relatively novel precursor. This would also highlight the use of the methodology in examining the effects of any change to the process.

8.2 Methodology

Reactor details

The reactor system used for this work is the same as the one detailed in the previous chapter. The process diagram is presented in figure 8.1. Flow rates were calculated based upon the Antoine coefficients reported in table 6.2.

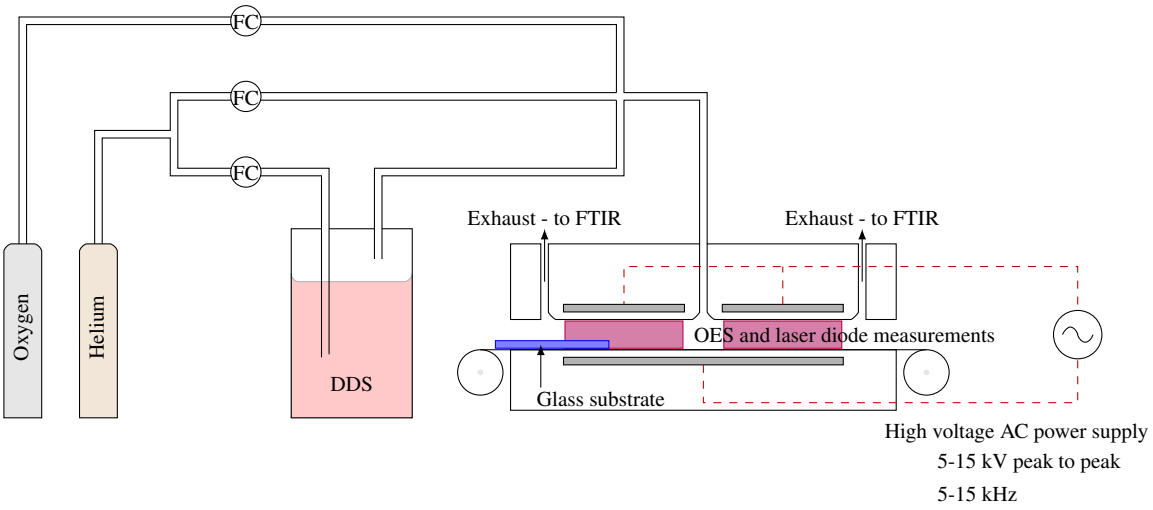

Figure 8.1: Process schematic for plasma enhanced chemical vapour deposition of silica films from dichlorodimethylsilane (DDS) at atmospheric pressure.

Spectroscopic techniques

The optical emission and FTIR spectrometers were set up the same manner as in the previous chapter.

A near infrared laser diode spectrometer was also used for this work, details of which are given in chapter four. To reiterate, the instrument consists of a near infra red laser diode tuned across the R(3) rotational line of the first vibrational overtone of hydrogen chloride at 1742 nanometres. Measurements were taken every other pass of the substrate through the reactor, giving a total of five sequential measurements for every experimental point. The final readings are an average of two hundred scans.

Experimental design

The experimental design was set up as depicted in figure 8.2. The experimental conditions are kept equivalent to those used in the previous chapter, so as to provide a fair basis for comparison between the two sets of experiments, the codings can be seen in table 8.1.

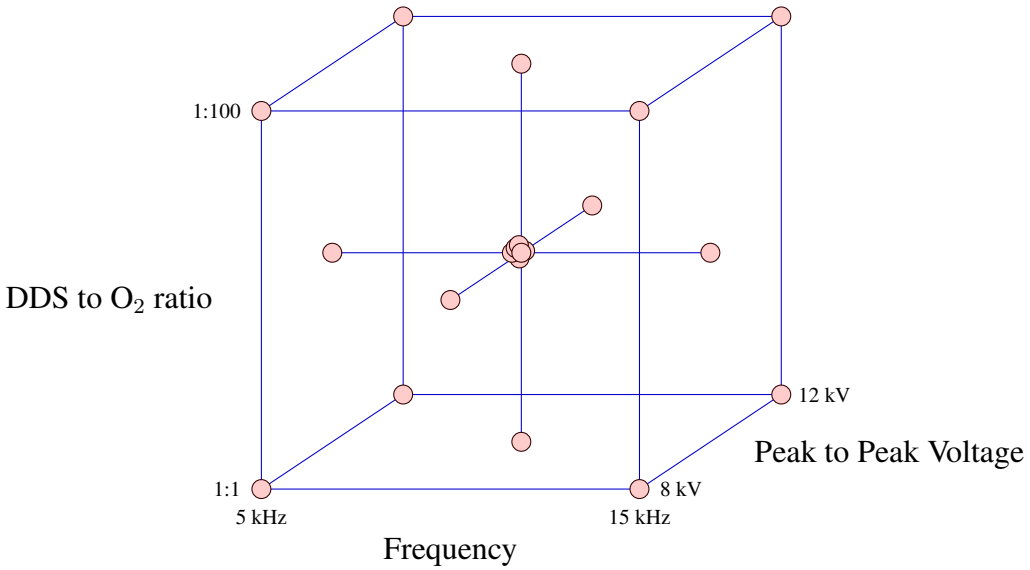

Figure 8.2: Central composite design for investigation of plasma enhanced chemical vapour deposition of silica from DDS at atmospheric pressure.

Coding	Frequency (x_1) / kHz	Frequency (x_2) / kV	DDS:O_2 ratio (x_3)
-1	8	1:1	5
0	10	1:10	10
1	12	1:100	15

Table 8.1: Variables investigated for the plasma enhanced chemical vapour deposition of silica from DDS.

Thin Film Measurements

The same measurement techniques were made on the silica films produced for this work as those detailed in chapter seven.

8.3 Results and discussion

Optical emission results

An example optical emission spectrum from these set of experiments can be seen in figure 8.3, with emission lines labelled. Similarities with figure 7.3 can be seen as regards to the excited species present. The spectrum as a whole however, is more intense. The nitrogen is present due to atmospheric air back diffusing into the reactor, which is also the reason it was present in the emission spectra recorded during the TEOS experiments.

The excitation temperatures were calculated for each experiment, and a model fitted as in the previous chapter. The emission lines for the calculations are presented in table 7.3. The F-test result for the excitation temperature statistical model is 99.67 %. The response surface plots for excitation temperature can be seen in figures 8.4 to 8.6. Compared to the TEOS results for excitation temperature seen in figures 7.5 to 7.7, the excitation temperatures are considerably higher on average. The relationships between the control variables and the excitation temperature show slight differences, but fundamentally remain the same.

In figure 8.4, the excitation temperature response surface, where frequency has been fixed, is presented. Similar to figure 7.5, the excitation temperature shows a quadratic increase with increasing oxygen. The voltage, however, plays more of a role. This could be due to the chemistry of this process being more dependent upon the power, which is

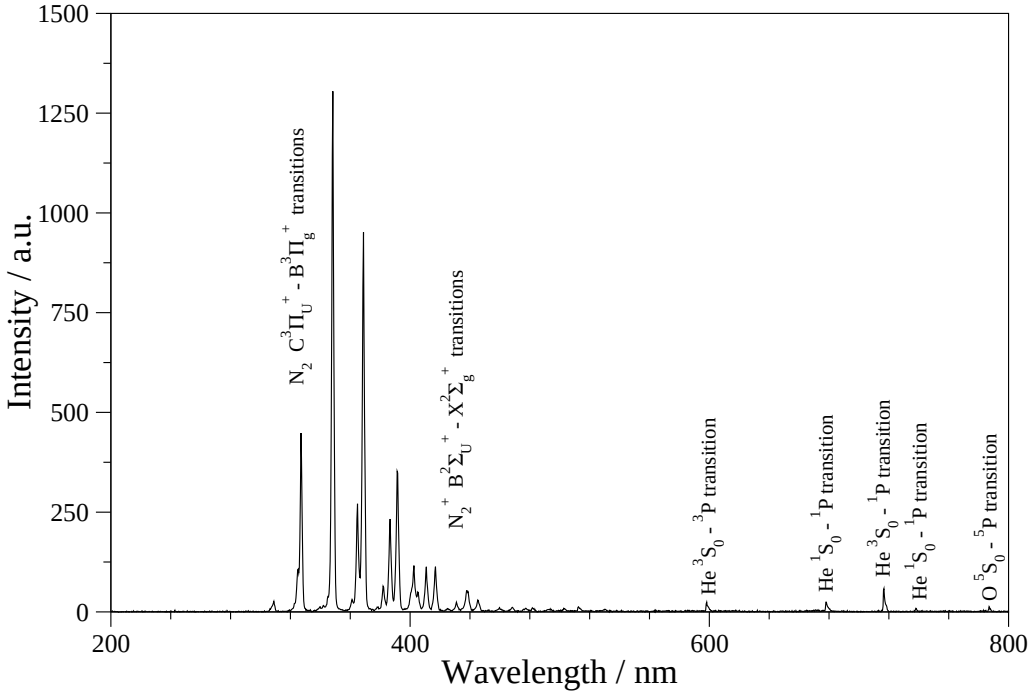

Figure 8.3: Optical emission spectrum of helium plasma containing 500 ppm of DDS and 5000 ppm of O_2. The plasma was generated at 10 kHz with a peak to peak voltage of 10 kV.

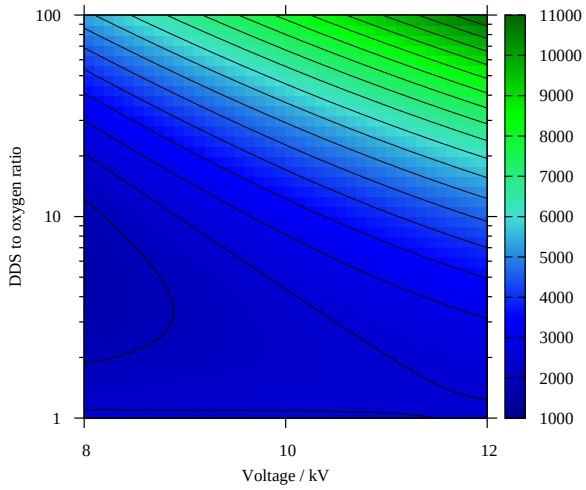

Figure 8.4: Response surface for excitation temperature (in Kelvin), with frequency has been fixed at 10 kHz.

voltage dependent, than with the TEOS process.

Comparing figures 8.5 and 7.6, which are the response surfaces for excitation temperature for DDS and TEOS respectively, both having the oxygen level as the fixed quantity, it is evident that the excitation temperature of the plasma containing DDS is more dependent upon the power supplied to the plasma than with the TEOS process. The voltage has the largest effect on the excitation temperature, again implying that the DDS chemistry is more dependent upon the power and electric field sustaining the plasma.

Figure 8.6 again shows some similarity to the equivalent figure for TEOS, figure 7.7. The precursor to oxygen ratio is the most important control variable for the excitation temperature in both sets of results, however the supply frequency has a lesser effect on the excitation temperature in the DDS chemistry.

With both sets of results, it is clear that the precursor to oxygen ratio is the most

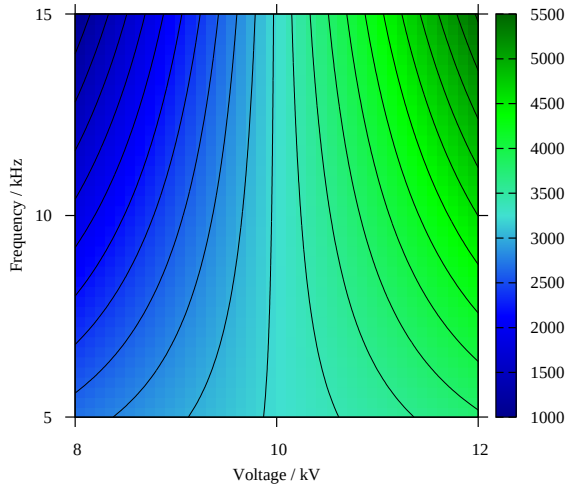

Figure 8.5: Response surface for excitation temperature (in Kelvin), with DDS to oxygen ratio fixed at 10.

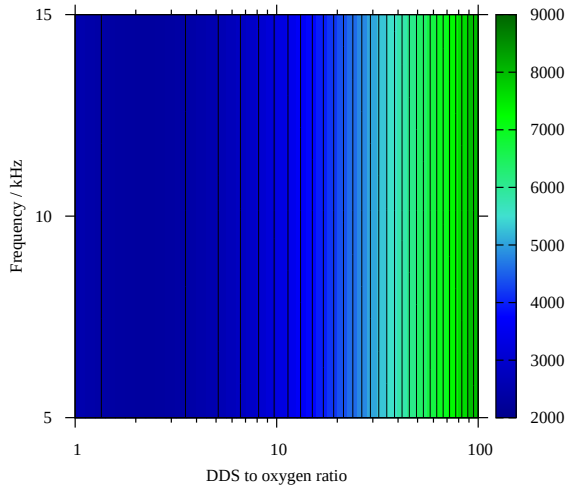

Figure 8.6: Response surface for excitation temperature (in Kelvin), with peak to peak voltage fixed at 10 kV.

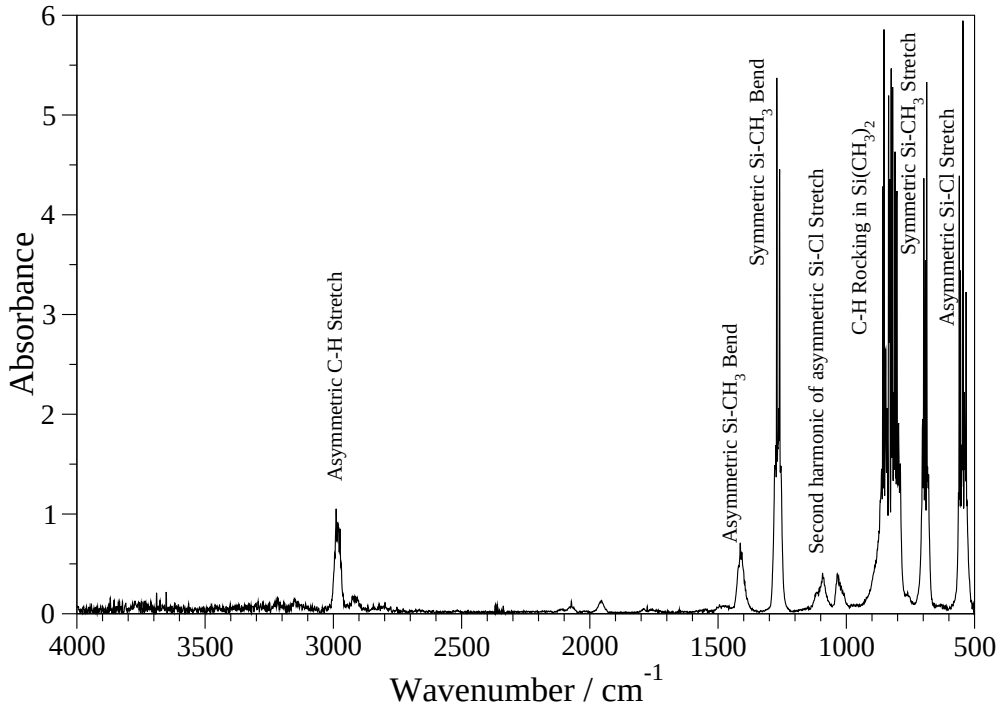

Figure 8.7: FTIR spectra of gases sampled before PECVD reactor recorded at a resolution of 2 cm^{-1}. It represents 500 ppm of DDS in helium.

important factor in controlling the excitation temperature. In other words, the concentrations of chemical species within the plasma determine how excited the electrons get. This corresponds with known plasma theory, [174]. The larger effect of the voltage on the excitation temperature in the case of the DDS chemistry implies that smaller variations of the electric field can play more of a role in the plasma chemistry of DDS than they do in the plasma chemistry of TEOS.

FTIR results

An FTIR spectrum of DDS can be seen in figure 8.7, some spectral features are labelled, and molecular vibrations have been assigned, [281]. DDS absorbs very strongly in the infra-red region of the spectrum.

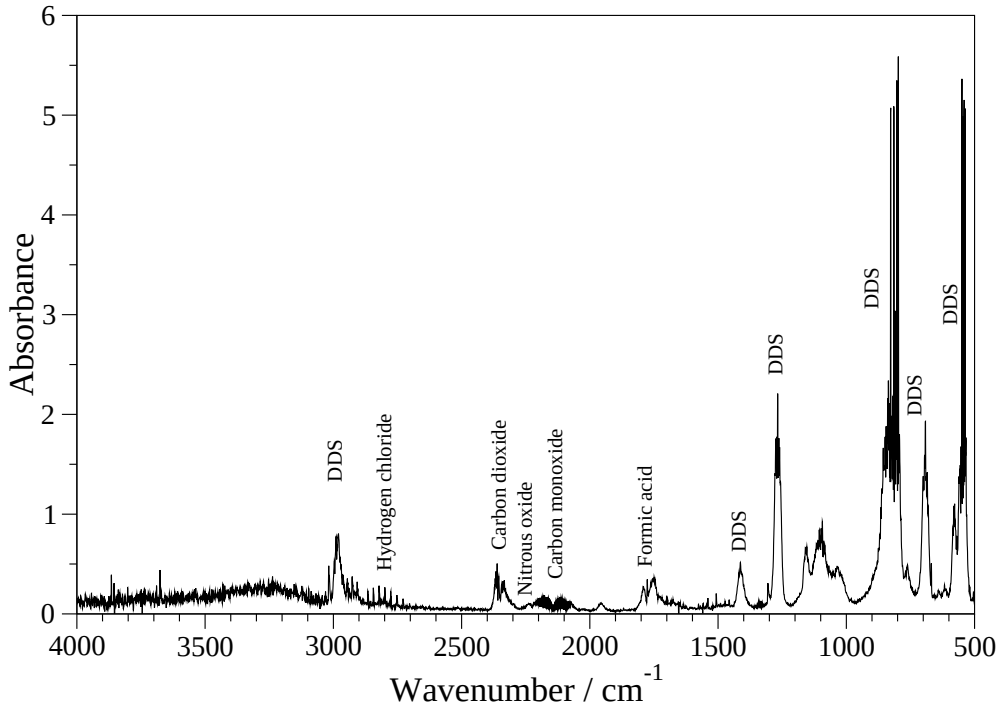

Figure 8.8: FTIR spectra of reactor exhaust from a plasma generated at 10 kHz with a peak to peak voltage of 10 kV, containing 500 ppm DDS and 5000 ppm of oxygen. Recorded at a resolution of 2 cm^{-1}

Species	Band start (cm^{-1})	Band end (cm^{-1})
DDS	2945.86	3012.14
Carbon dioxide	2289.1	2391.5
Carbon monoxide	2042	2144.5
Formic acid	1704.6	1819.1
Hydrogen chloride	2710.9	2879.6
Nitrous oxide	2224.5	2263.7

Table 8.2: By-product species and their associated infrared spectral bands used for calculation of concentration.

An FTIR spectrum of reactor exhaust can be seen in figure 8.8. Key by-products are labelled on the spectrum. These are carbon monoxide, carbon dioxide, hydrogen chloride and formic acid. A potential overall reaction for the process is suggested in equation 8.1. The formic acid subsequently reacts with the various oxygen species to form the carbon monoxide and carbon dioxide. As in the TEOS experiments, nitrous oxide is present. The reason for this is the same, nitrogen impurities in the reactor form nitrous oxide in the plasma chemistry. The results have been further analysed so as to calculate the final concentrations of the various gaseous by-products. As in the TEOS results, chemometric models have been fitted for all relevant species.

$$SiCl_2(CH_3)_2(g) + 3O_2(g) \rightarrow SiO_2(s) + 2CH_2O_2(g) + 2HCl(g) \tag{8.1}$$

Response surfaces for formic acid formation can be seen in figures 8.9 to 8.11. The F-test result for the model is 100 %. The formic acid is a direct by-product of the decomposition of DDS, and the variations of it's concentration have potential to be informative of the chemistry of the process.

Figure 8.9 is the response surface for formic acid formation in the case where the frequency is fixed. In this case the formation of the formic acid shows a quite linear response to both the input voltage and the DDS to oxygen ratio, increasing with both.

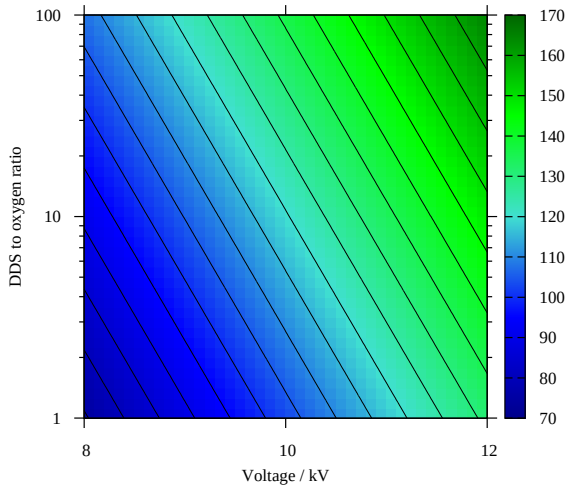

Figure 8.9: Response surface for formic acid formation (in parts per million). Frequency fixed at 10 kHz

The formation of formic acid shows a stronger dependence on the voltage, implying that the electric field has a strong effect on the plasma chemistry of DDS.

The fixed oxygen concentration response surface for formic acid formation is presented in figure 8.10. Both the voltage and frequency have a bearing on the formic acid production, with maximised production occurring at about ten kilohertz. Again, increasing voltage tends to increase formic acid production, however it could also be acting to suppress subsequent reactions of formic acid with oxygen.

In figure 8.11 is the response surface for formic acid production at a fixed voltage. The maximum concentration reached in this response surface is less than the previous two, additional evidence for the effect of electric field on the formic acid formation. A frequency of about ten kilohertz is where the maximum formic acid production occurs, whilst increasing oxygen concentration keeps increasing the formic acid formation.

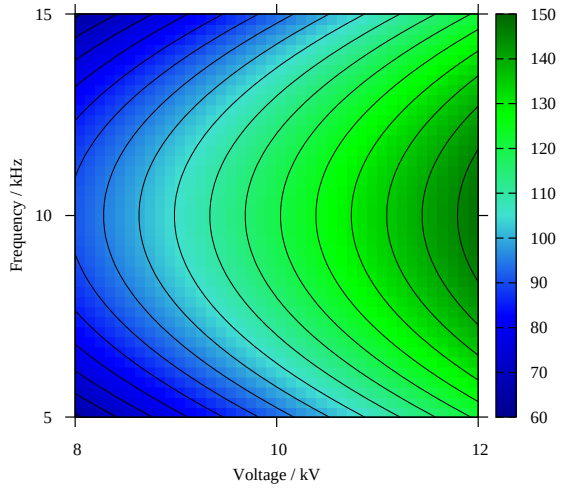

Figure 8.10: Response surface for formic acid formation (in parts per million), with DDS to oxygen ratio fixed at 10.

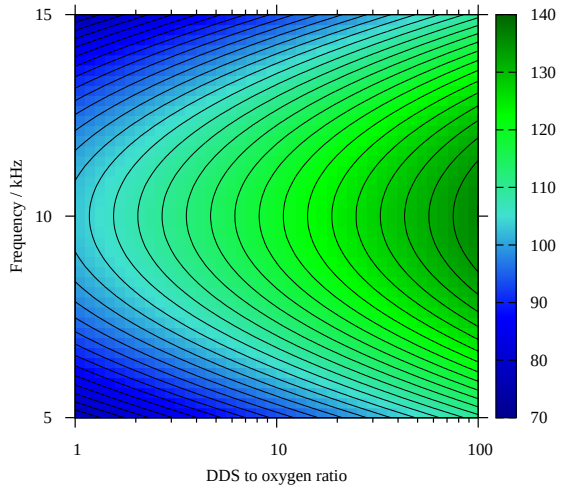

Figure 8.11: Response surface for formic acid formation (in parts per million), with voltage fixed at 10 kV.

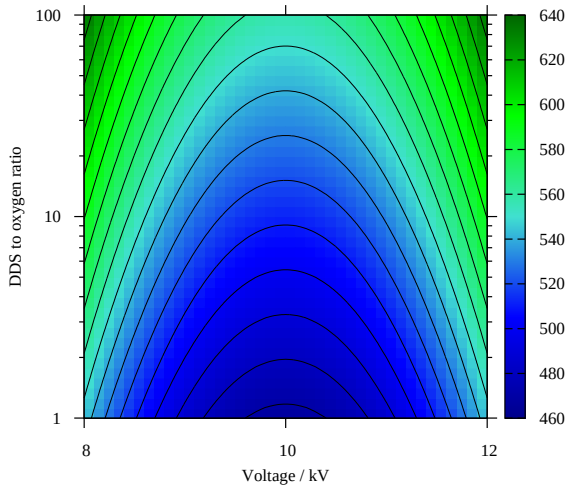

Figure 8.12: Response surface for hydrogen chloride formation (in parts per million). Frequency fixed at 10 kHz

Response surfaces for hydrogen chloride formation can be seen in figures 8.12 to 8.14. The F-test result for the model is 95.45 %. Hydrogen chloride is another direct by-product of the DDS decomposition. It is possible that there is no further significant reaction of this by-product within the plasma, as the concentration of hydrogen chloride produced tends to be quite high. This possibility is contradicted by the *in situ* measurements of hydrogen chloride presented later in this chapter.

Figure 8.12 shows the response surface for hydrogen chloride formation, at a fixed frequency. There is a trend towards more hydrogen chloride production with increased oxygen content in the plasma, perhaps due to the effect of active oxygen species within the plasma. The voltage has a different effect however, with hydrogen chloride production decreasing at higher voltages.

In figure 8.13, is the response surface for hydrogen chloride production at fixed oxygen

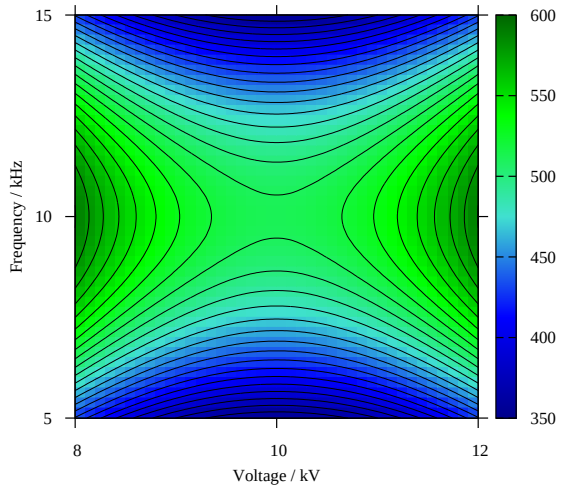

Figure 8.13: Response surface for hydrogen chloride formation (in parts per million), with TEOS to oxygen ratio fixed at 10.

concentration. The interaction between the voltage and frequency is clearly important in governing the production of hydrogen chloride, with production maximised at around ten kilohertz. There is also a tendency exhibited in both figures 8.12 and 8.13 for the voltage to not be as important a factor in governing hydrogen chloride production.

Figure 8.14 represents the response surface for hydrogen chloride formation at a fixed voltage. The amount of hydrogen chloride produced tends to increase with oxygen concentration in the plasma, similar to figure 8.12. This further supports the assertion that oxygen species play a role in the chemistry of DDS.

Response surfaces for carbon monoxide formation can be seen in figures 8.15 to 8.17. The F-test for the model is 96.96 %. There is about a 100 ppm variation in carbon monoxide production across the process window. It is probable that the carbon monoxide is produced due to formic acid reacting with active oxygen species.

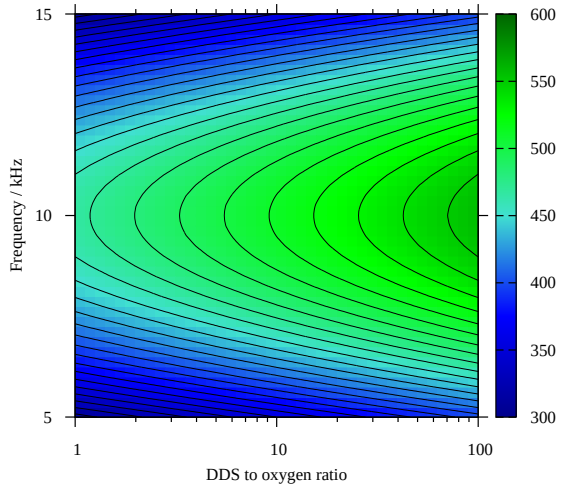

Figure 8.14: Response surface for hydrogen chloride formation (in parts per million), with peak to peak voltage fixed at 10 kV.

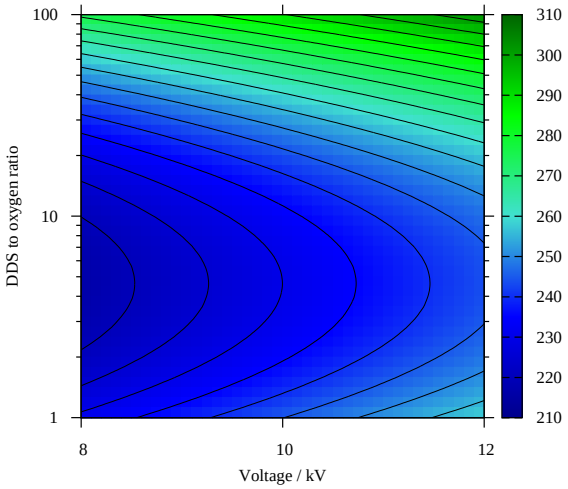

Figure 8.15: Response surface for carbon monoxide formation (in parts per million). Frequency fixed at 10 kHz

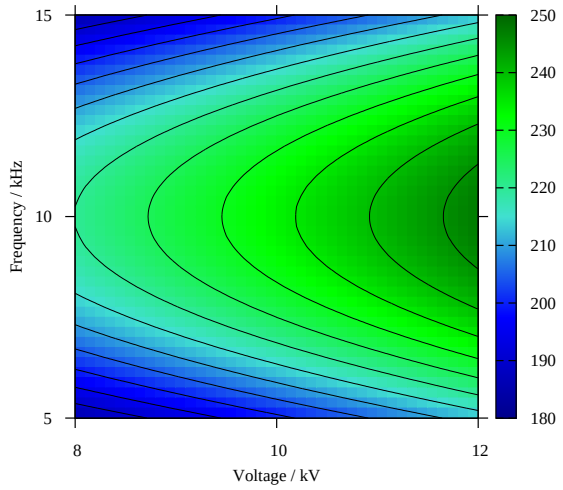

Figure 8.16: Response surface for carbon monoxide formation (in parts per million), with TEOS to oxygen ratio fixed at 10.

Comparing figures 8.15 and 7.11, the response surfaces for carbon monoxide production from the DDS and TEOS processes respectively, it is clear that the mechanism for carbon monoxide production in the two processes has some similarities. The oxygen concentration plays a role in both processes, as does the voltage. In the case of the DDS chemistry however, the voltage has a slightly more significant effect on the carbon monoxide produced compared to the TEOS chemistry. The oxygen species within the plasma control the formation of carbon monoxide from formic acid much more strongly than the voltage does however.

The response surface for carbon monoxide production at fixed oxygen concentration can be seen in figure 8.16. All factors play some role in the carbon monoxide production, but the power supply frequency is the most significant. There is maximum production of carbon monoxide at about 10 kHz.

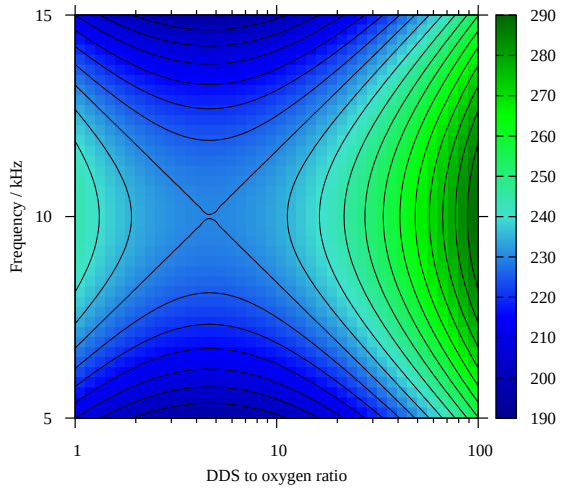

Figure 8.17: Response surface for carbon monoxide formation (in parts per million), with voltage fixed at 10 kV.

Figure 8.17 presents the voltage fixed response surface for carbon monoxide production. The oxygen concentration is the strongest factor in this case, but the frequency is also very important too. This is perhaps due to the production of active oxygen species changing at different frequencies.

Response surfaces for carbon dioxide formation can be seen in figures 8.18 to 8.20. The F-test for the model is 99.98 %. Like carbon monoxide, carbon dioxide production in this plasma chemistry is likely to be due to reaction of formic acid with oxygen species.

The response surface for carbon dioxide at a fixed frequency is presented in figure 8.18. Of immediate importance is the fact that the oxygen concentration does not play a role in the formation of the carbon dioxide, whereas the voltage quite strongly does. Compared with the equivalent response surface for the TEOS process, figure 7.12, it is apparent that there is some difference. The concentrations in both cases are not very

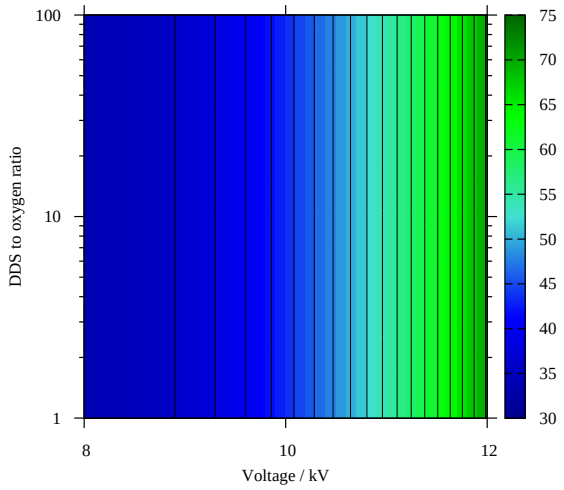

Figure 8.18: Response surface for carbon dioxide formation (in parts per million). Frequency fixed at 10 kHz

high either. It is possible that the mechanism for carbon dioxide production in the DDS chemistry is not due to formic acid's reaction with oxygen species in the plasma, but rather something else.

Figure 8.19 shows the fixed oxygen concentration response surface for carbon dioxide production. The voltage applied is the strongest factor in the production of carbon dioxide, suggesting the strength of the electric field sustaining the plasma has a strong effect. The frequency has a lesser effect, but still plays a role.

The fixed voltage response surface for carbon dioxide production is seen in figure 8.20. Again, the oxygen concentration plays no role, and the frequency is dominant. A key observation is that the overall concentration is less than in the other two cases, reinforcing the supposition that the electric field strength is key in carbon dioxide production.

Response surfaces for DDS decomposition can be seen in figures 8.21 to 8.23. The

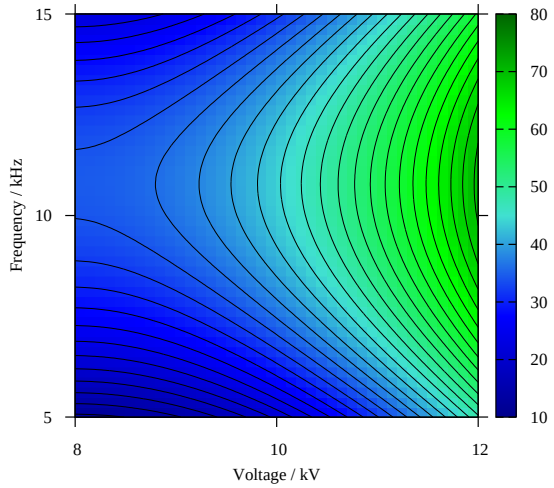

Figure 8.19: Response surface for carbon dioxide formation (in parts per million), with TEOS to oxygen ratio fixed at 10.

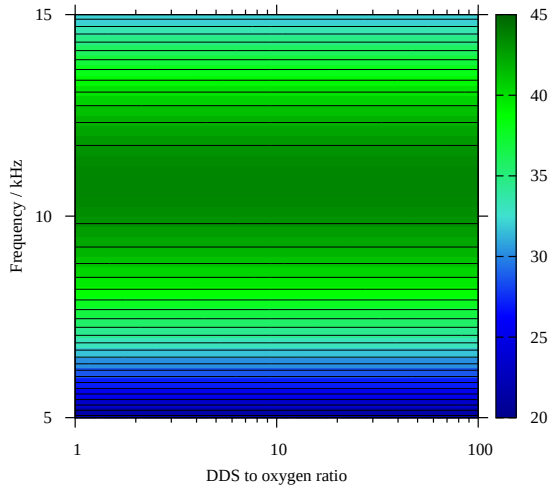

Figure 8.20: Response surface for carbon dioxide formation (in parts per million), with voltage fixed at 10 kV.

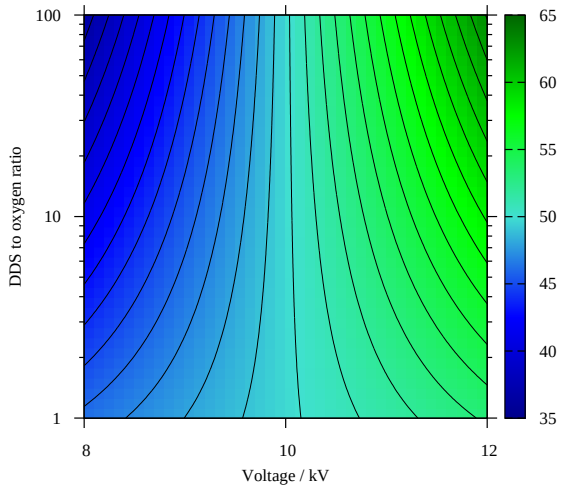

Figure 8.21: Response surface for DDS decomposition (as a percentage), with frequency fixed at 10 kHz.

goodness of fit of the model is 99.85 %. Overall, the decomposition is not as much as it was in the TEOS chemistry. This is perhaps due to the DDS molecule requiring more energy to break it down.

Figure 8.21 shows strong similarity with figure 7.13, which are the fixed frequency response surface plots for the respective precursor decomposition. Both figures indicate a strong dependence of the precursor destruction on the voltage, which would suggest that the chemistry of the precursor breakdown becomes more rapid upon the input of more power.

Again the response surfaces for precursor decomposition at a fixed oxygen concentration seen in figures 8.22 and 7.14 show remarkable similarity. There is a strong influence of the frequency upon the decomposition of precursor in both figures, with both showing a squared relationship. This indicates the importance the power supply has upon the

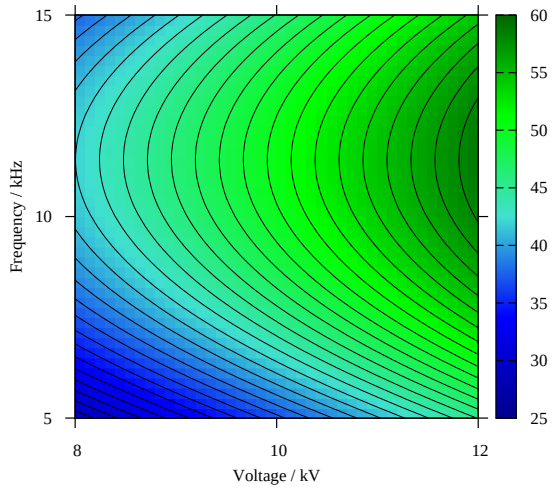

Figure 8.22: Response surface for DDS decomposition (as a percentage), with TEOS to oxygen ratio fixed at 10.

frequency.

The surface responses for precursor decomposition at fixed voltage, shown in figures 8.23 and 7.15, are quite different for DDS and TEOS chemistries however. The DDS decomposition is not influenced at all by the oxygen concentration, whereas the TEOS decomposition is. The frequency is of importance in both chemistries though, with both being affected similarly.

There is quite obviously a different chemistry to that occurring in the TEOS process. The FTIR results show this extremely well, and they also allow for commentary on the chemistry that is occurring. Comparisons of the response surfaces produced from these FTIR results with those from the TEOS experiments highlight the different effect the studied parameters have on a given process, and may highlight possibilities for decreased precursor amounts to be used to produce a given film.

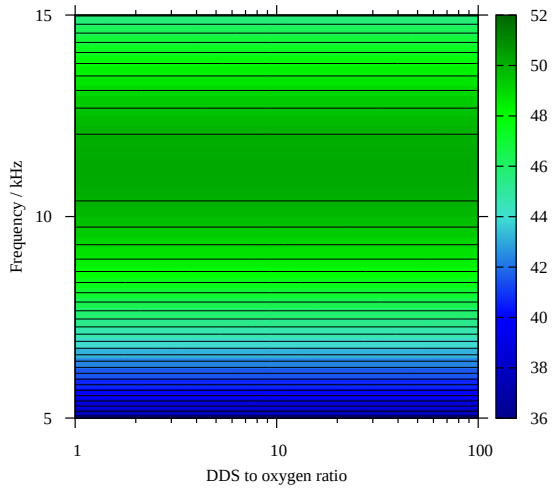

Figure 8.23: Response surface for DDS decomposition (as a percentage), with peak to peak voltage fixed at 10 kV.

Laser diode spectroscopy results

Hydrogen chloride was measured *in situ* using a near infrared laser diode spectrometer, and the results of this were fitted to a statistical model. The F-test result for which was 98.19 %. The response surfaces for this can be seen in figures 8.24 to 8.26. The results are reported as integrated absorbance due to the temperature being unknown. According to the Beer-Lambert law, this is directly proportional to the concentration.

Figure 8.24 shows the response surface for the *in situ* measurement of hydrogen chloride at a fixed frequency. From the response surface it is evident that increasing voltage tends to increase the formation of hydrogen chloride, whereas increasing oxygen concentration has a more complicated effect which combines with that of the voltage. This is dissimilar to figure 8.12 with respect to the voltage as there is a clear maximum in that case. This effect is likely due to the differing positions of the measurements in the process,

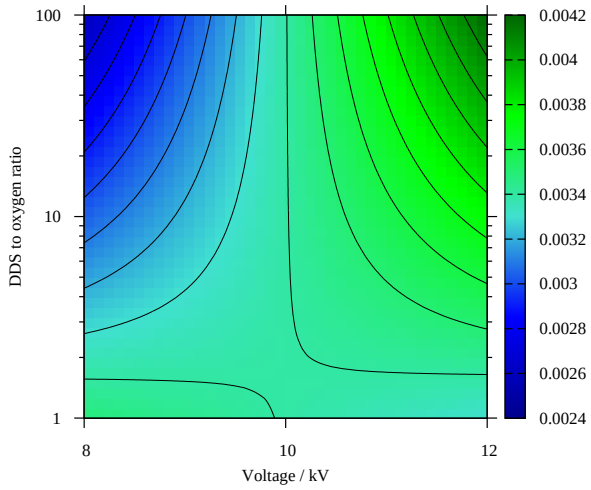

Figure 8.24: Response surface for *in situ* hydrogen chloride formation (in integrated absorbance units), with frequency fixed at 10 kHz.

and something happening to the hydrogen chloride between the *in situ* and downstream measurements. This would require further investigation.

The response surface for hydrogen chloride formation at a fixed oxygen concentration can be seen in figure 8.25. A positive linear relationship can be seen between hydrogen chloride formation and both frequency and voltage. Referring back to figure 8.22, the response surface for DDS destruction at fixed oxygen concentration, the maximum destruction can be seen at the same point where maximum hydrogen chloride formation can be seen in figure 8.25. The measurements *in situ* again show quite a difference with those measured downstream of the reactor as shown in figure 8.13.

The response surface shown in figure 8.26 is the hydrogen chloride formation at a fixed voltage. The response is linear with respect to the frequency, but the oxygen concentration has no effect. Links can be made with the DDS destruction again, shown in figure 8.23,

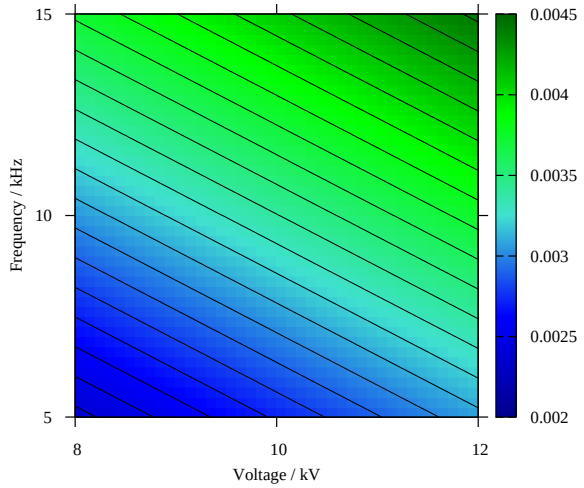

Figure 8.25: Response surface for *in situ* hydrogen chloride formation (in integrated absorbance units), with TEOS to oxygen ratio fixed at 1.

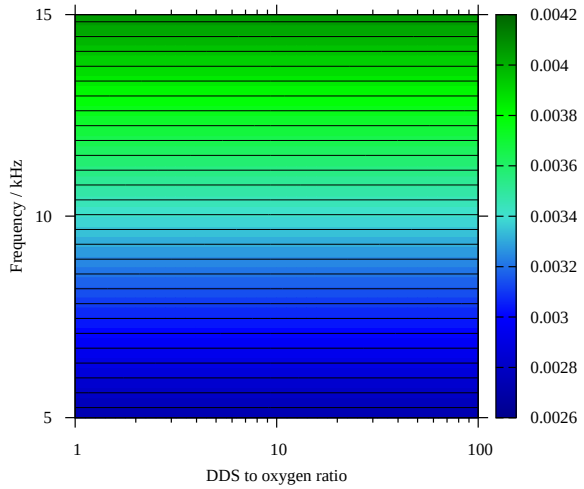

Figure 8.26: Response surface for *in situ* hydrogen chloride formation (in integrated absorbance units), with peak to peak voltage fixed at 10 kV.

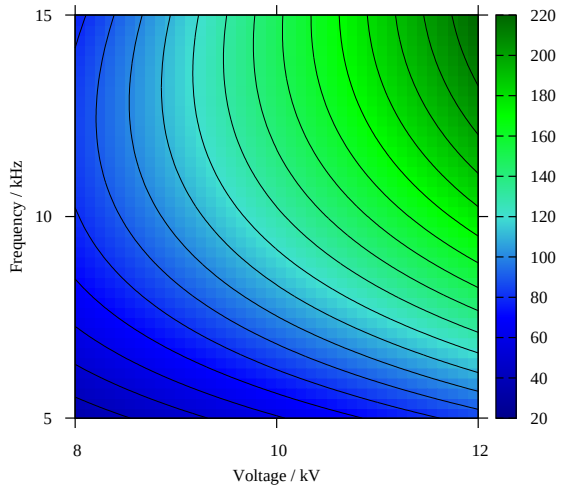

Figure 8.27: Response surface for power (in Watts), with TEOS to oxygen ratio fixed at 10.

with both maximum destruction and maximum hydrogen chloride formation occurring at higher frequencies. The discrepancy between *in situ* and downstream measurements can also be seen again when figure 8.26 is compared to figure 8.14.

These *in situ* measurements show the importance of measuring species concentration in the plasma region, as the response surfaces that have been generated are markedly different to those generated from the downstream FTIR measurements of hydrogen chloride. This would indicate some further reaction mechanism that occurs within the plasma with respect to the hydrogen chloride. With a species such as hydrogen chloride, there is a possibility of etching occurring which would use up the hydrogen chloride that is being produced.

Electrical results

The response surface for deposited power can be seen in figure 8.27. The F-test result for this model is 97.77 %. Only the one response surface is presented, as the oxygen content does not play a role in governing the power deposited in the plasma.

Comparing the deposited powers in the two processes, TEOS and DDS, the DDS process has a lower average power for equivalent processing conditions. This is an interesting result, as it indicates that a DDS based silica coating process can be run more economically than a TEOS one. Comparing figure 8.27 with the equivalent TEOS response surface, figure 7.17, there are some similarities. The power increases with voltage, as expected. There is also a quadratic (or higher order) relationship with frequency. This would indicate the resonance of the power supply is important. The effect of frequency is slightly different in the DDS process than in the TEOS one, this is due to the different chemistries occurring.

Thin film results

Response surfaces for growth rate can be seen in figures 8.28 to 8.30. The thickness of the films produced varied between 50 and 350 nm. The F-test for the model is 99.66 %. Further to the F-test result, the growth rate varied by 20 nm / minute across the replicate experiments (seen in table A.7), whilst the response surfaces vary by at least 60 nm / minute. What is quite evident, is that the growth rate tends to be about four times greater than equivalent conditions for TEOS. This is a significant result, and the implications for a silica deposition process are self evident. A possible reason for this is suggested by the FTIR results. Unlike with the TEOS chemistry, there seems to be no production of any other silicon containing compounds as a by-product. This suggests that the reaction scheme is perhaps simpler, and that there are no competing side reactions. When the DDS

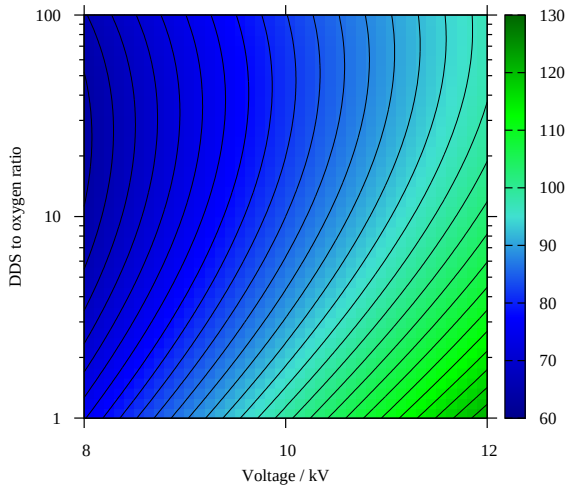

Figure 8.28: Response surface for growth rate (in nanometres per minute), with frequency fixed at 10 kHz.

reacts, it forms silica preferentially.

Figure 8.28 is the response surface for growth rate at a fixed frequency. This is quite different to the equivalent response surface for the TEOS experiments in figure 7.19. For a start, the oxygen concentration only decreases the silica production from DDS, whereas for silica production from TEOS, the oxygen concentration has a far more complicated relationship with the growth rate. The voltage is a more significant factor in the case of the growth from DDS, as we know that the voltage is also a significant factor in the DDS decomposition from figures 8.22 and 8.23, this provides further evidence for the silica formation from DDS being the preferential reaction occurring.

In figure 8.29 is the growth rate response surface for a fixed DDS to oxygen ratio. This shows a similar relationship to the response surface for TEOS, shown in figure 7.20, with both voltage and frequency increasing the growth rate of the silica films. Frequency

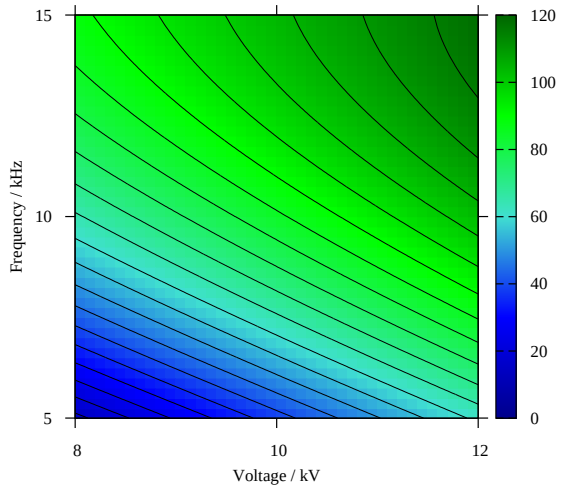

Figure 8.29: Response surface for growth rate (in nanometres per minute), with DDS to oxygen ratio fixed at 10.

is the more significant factor in this case, and in conjunction with figure 8.22 further corroborates the formation of silica being the dominating reaction in this chemistry.

Presented in figure 8.30 is the fixed voltage response surface for growth rate of the thin film. There is some similarity to figure 7.21, but the oxygen tends to retard the growth rate overall as in figure 8.28. Frequency remains a strong influence on the growth rate, suggesting that larger amounts of reactive oxygen species are produced at higher frequencies, causing the thin film growth to be faster at higher frequencies.

Response surfaces for Mohs hardness can be seen in figures 8.31 to 8.33. The F-test for the model is 98.13 %. On average, the hardness of the films produced from DDS is less than those produced from the TEOS chemistry. This is largely due to the increased growth rates of silica involved in this chemistry, leading to less dense, weaker silica films.

Figure 8.31 presents the Mohs hardness response surface for a fixed frequency. It

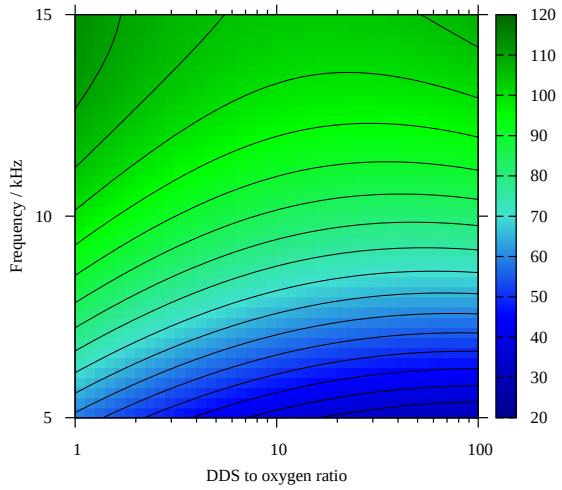

Figure 8.30: Response surface for growth rate (in nanometres per minute), with peak to peak voltage fixed at 10 kV.

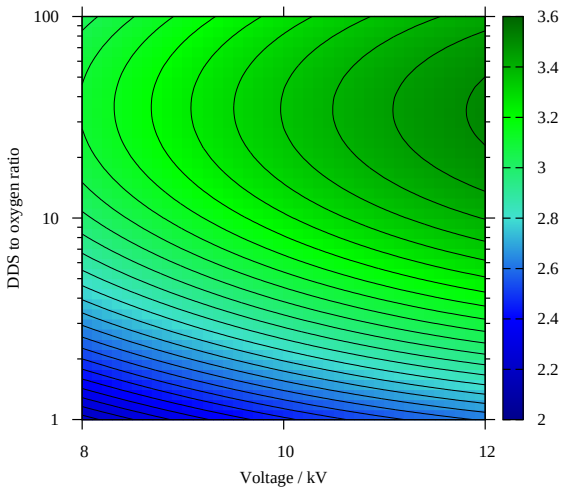

Figure 8.31: Response surface for Mohs hardness, with frequency fixed at 10 kHz.

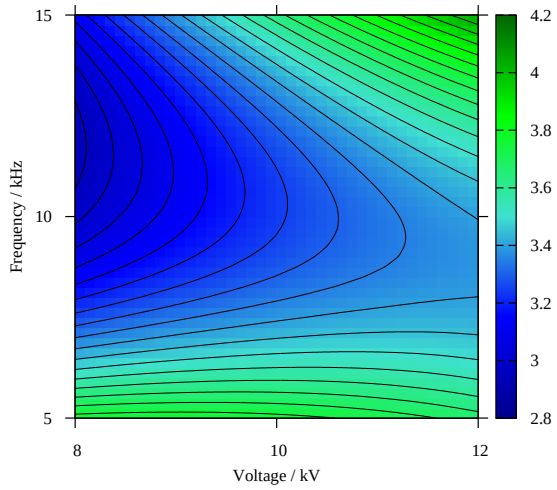

Figure 8.32: Response surface for Mohs hardness, with DDS to oxygen ratio fixed at 10.

shows a similar complicated relationship with the process variables that figure 7.22 exhibits. Both response surfaces show a maximum hardness of the film at a high oxygen concentration, however the voltage plays a different role. The different chemistry involved would suggest that the growth mechanism of the silica film has a different dependence upon the energy of the plasma for both processes.

The response surface for Mohs hardness at fixed DDS to oxygen ratio can be seen in figure 8.32. The relationship of the voltage and the frequency with the films produced is, again, a complicated one. Figure 7.23, the equivalent response surface for TEOS, shows a complicated relationship as well. This relationship is obviously dependent upon the chemistry leading to film growth. The growth rates play a role as well, and comparing figures 8.32 and 8.29, the two process regions for harder films occur when the growth rates are slow, but also when they are high. This is unusual, and a possible reason for this could be two different modes of film growth. One mode at low growth rates, that

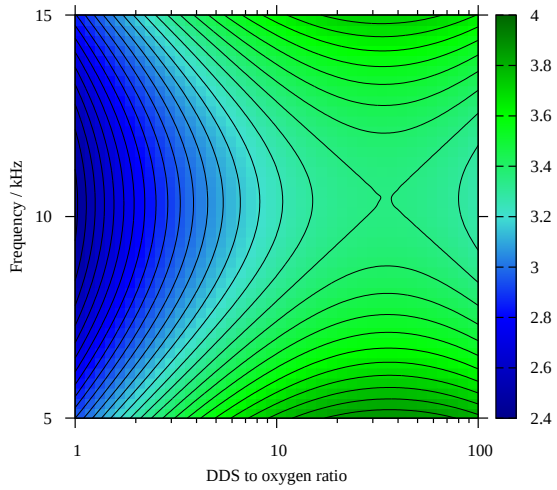

Figure 8.33: Response surface for Mohs hardness, with peak to peak voltage fixed at 10 kV.

produces a dense hard film would be expected. The other growth mode occurs at higher growth rates and this could be due to the higher power in the plasma producing more intermediaries, causing high growth rate, and also inducing denser films to grow.

In figure 8.33 is the response surface for Mohs hardness at fixed voltage. Comparison with figure 7.21 shows additional evidence for two modes of film growth. There is high hardness at both low and high growth rates.

Contact angles for the films were measured, and the results fitted to the statistical model, the F-test result for which was 99.92 %. The t-test results indicated that frequency and the voltage were the key control variables in governing the contact angle on the surface of the film. As a result of which only the response surface for the contact angle at a fixed DDS to oxygen ratio is presented in figure 8.34.

Several points can be made for the contact angle results. Firstly, the values are, in

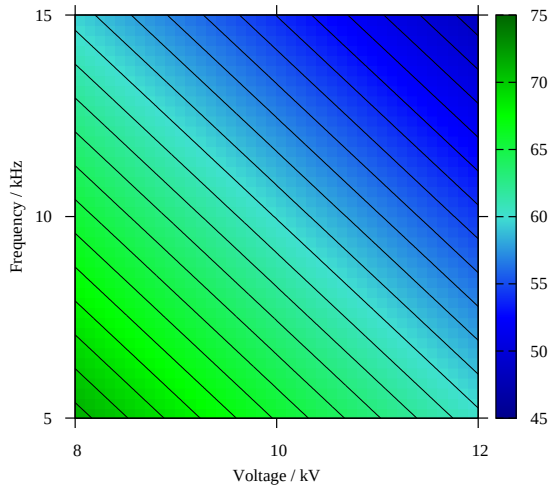

Figure 8.34: Response surface for contact angle, with DDS to oxygen ratio fixed at 10.

general, larger than the contact angles of the TEOS produced films. The range of values is also greater, covering about thirty degrees as opposed to twelve in the equivalent figure for TEOS derived films (figure 7.26). The relationship of the contact angle with the process variables is also not as complicated, being solely linear with respect to both voltage and frequency. This is a similar relationship to that of the hydrogen chloride production, presented in figure 8.25, and indicates that detection of hydrogen chloride could be used to control the contact angle of the film.

The refractive index statistical model t-test results also showed that the voltage and frequency were the only relevant variables in controlling the refractive index. The F-test result for the model was 98.96 %. The response surface for the refractive index at a fixed DDS to oxygen ratio is presented in figure 8.35.

Overall, these response surfaces give some indication as to how the process can be run to give a given quality of film. Harder films are produced at high voltage and high oxygen

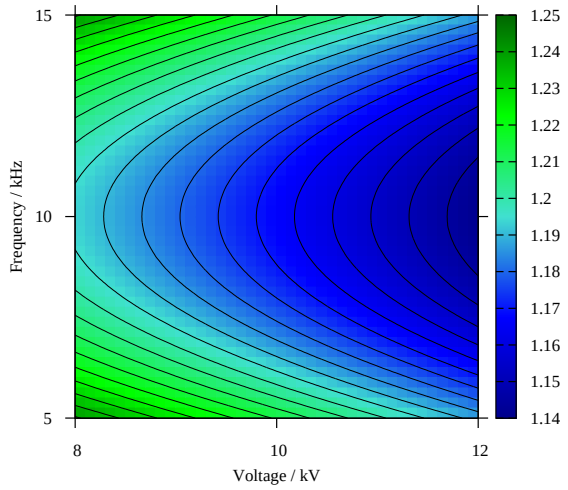

Figure 8.35: Response surface for refractive index, with DDS to oxygen ratio fixed at 10.

concentrations. More hydrophilic films, with lower contact angles, are produced at higher voltages and frequencies. The refractive index of the film, important for anti-reflective coatings, can be modified by changing the frequency and voltages as well.

An example ATR FTIR spectrum can be seen in figure 8.36, and this shows the classic traits of a silica thin film as outlined in the previous chapter.

Principal Components Analysis

The preprocessings carried out on the datasets in the following principal components analysis are exactly the same for a given dataset as in the TEOS chemometric work outlined in the previous chapter. The selection of the preprocessing methods were made for identical reasons. Experimental conditions for the labels in the scores sets are given in table 8.3

Number	Experiment number	Voltage$_{pk-pk}$	DDS:O2	Frequency
		x_1	x_2	x_3
1	1	-1	-1	-1
2	16	-1	-1	1
3	17	-1	0	0
4	7	-1	1	-1
5	5	-1	1	1
6	3	0	-1	0
7	13	0	0	-1
8	2	0	0	0
9	8	0	0	0
10	10	0	0	0
11	15	0	0	0
12	18	0	0	0
13	20	0	0	0
14	11	0	0	1
15	19	0	1	0
16	14	1	-1	-1
17	9	1	-1	1
18	12	1	0	0
19	6	1	1	-1
20	4	1	1	1

Table 8.3: Experimental labels for subsequent principal component analysis.

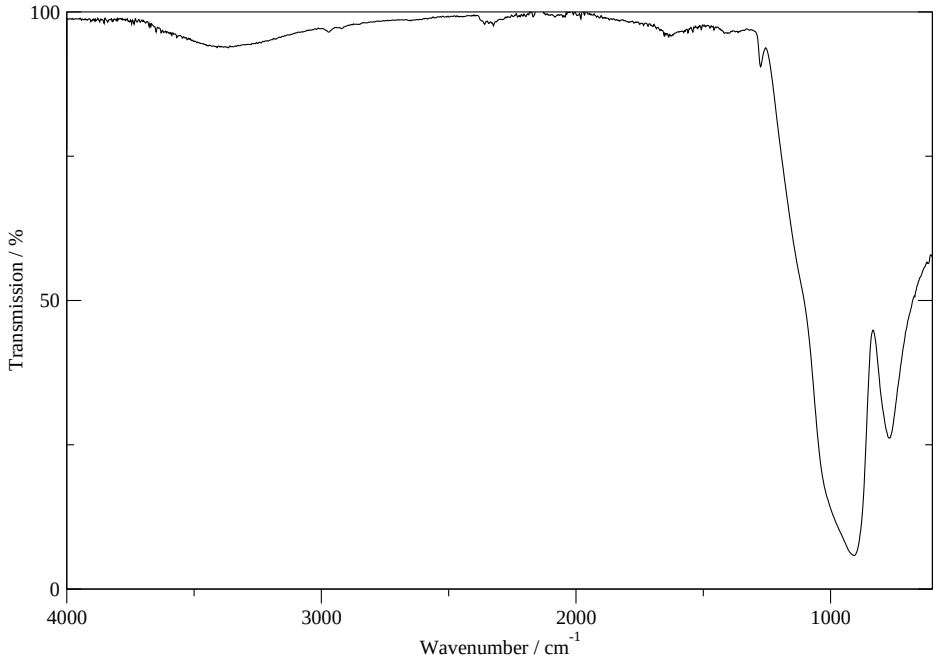

Figure 8.36: ATR-FTIR spectrum for silica thin film grown from 500 ppm DDS, 0.01 % oxygen in a helium plasma generated at ten kilovolts peak to peak and ten kilohertz.

The eigenvalues for the interpreted scores of the DDS interpreted dataset are presented in table 8.4, this indicates that approximately 80 % of the data is modelled by the first four principal components. The scores plots for the first four principal components of the interpreted results data are presented in figures 8.38, 8.39 and 8.40 respectively. The loadings plots for the first four principal components are presented in figure 8.37.

The scores plot for principal components one and two, figure 8.38, shows the majority of experiments are clustered at the origin, with seven outlying experiments. The loadings plot in 8.37 indicates that principal component one models the majority of the measured data, except for the phase shift and the refractive index of the films. In contrast, principal component two models the hardness and excitation temperature. Experiments one, four and seven are all outliers in principal component one, and were all performed at low frequency. The frequency of the power supply very strongly affects all the measured variables. Experiments four, seven and twenty are outliers in principal component

Principal component	Eigenvalue	Percentage modelled	Cumulative percentage
1	104.88	43.70	43.70
2	35.31	14.71	58.41
3	35.15	14.65	73.06
4	19.59	8.16	81.22
5	17.66	7.36	88.58
6	10.58	4.41	92.99
7	6.67	2.78	95.77
8	4.36	1.82	97.58
9	4.17	1.74	99.32
10	1.22	0.51	99.83

Table 8.4: Eigenvalues and percentage modelled of the first ten principal components of the interpreted data.

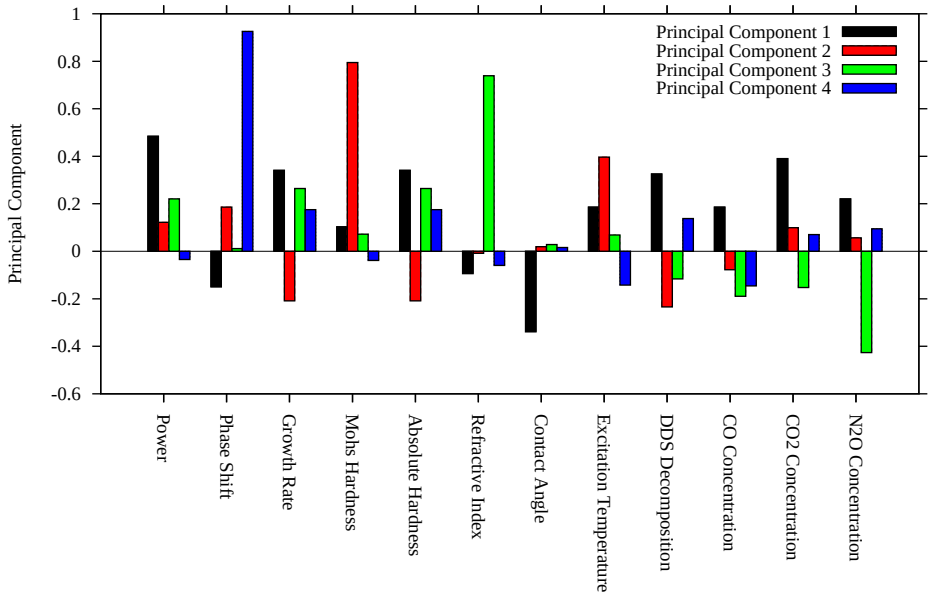

Figure 8.37: Principal component loadings plot for the interpreted results for the DDS dataset. The data matrix was standardised.

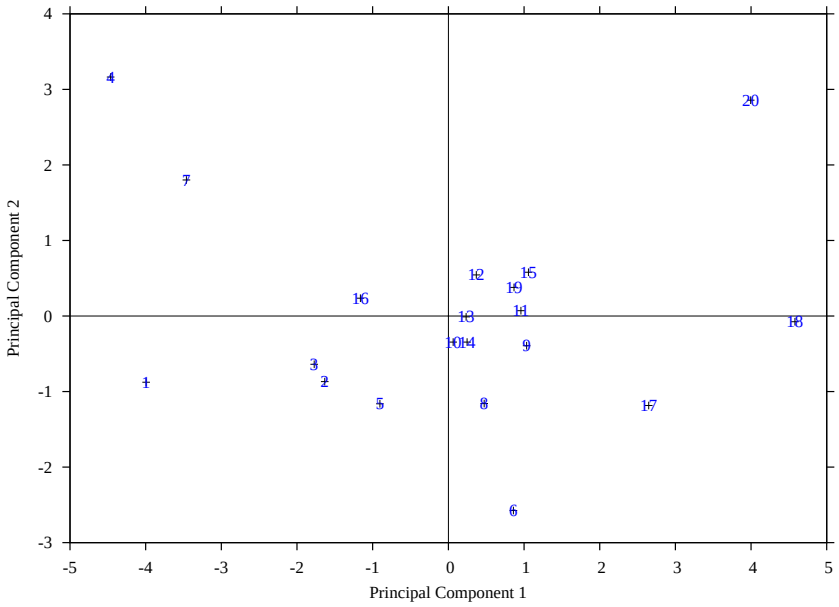

Figure 8.38: Principal component scores plot for principal components one and two of the interpreted data. The data matrix was standardised

two. Examining table A.7, the process conditions produced films with high hardness. Experiments four and twenty, the more extreme outliers, displayed higher excitation temperatures. This would perhaps indicate some effect of the excitation temperature on the hardness of the films produced. This would probably not be a direct effect, but the result of a slightly different chemistry at higher excitation temperatures.

Figure 8.39 indicates that there is also close clustering at the origin in these principal components. The loadings plot shows that principal component three predominantly models the refractive index and nitrous oxide exhaust concentration. The experiments are evenly distributed in principal component three.

The scores plot for principal components three and four shown in figure 8.40 shows a lot more dispersed arrangement of experiments. Principal component four strongly models the phase shift of the voltage and current traces in the power supply.

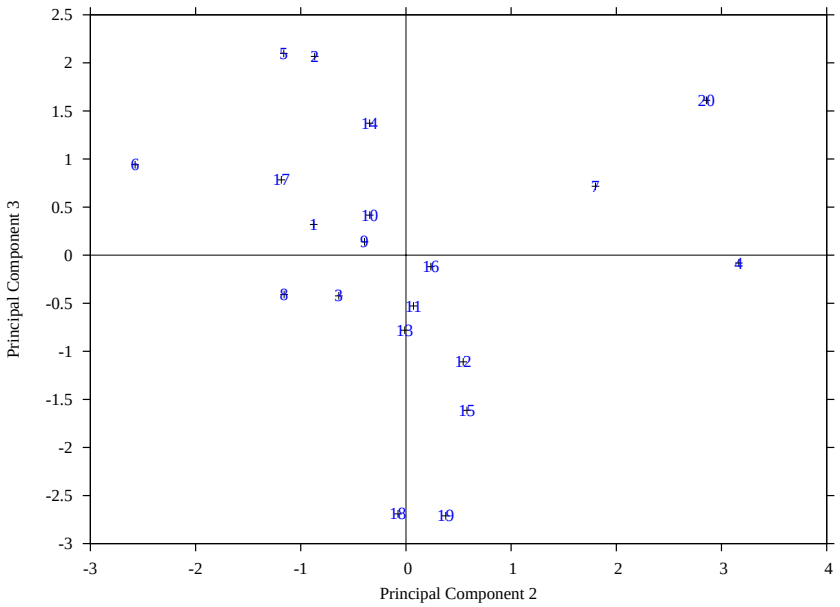

Figure 8.39: Principal component scores plot for principal components two and three of the interpreted data. The data matrix was standardised

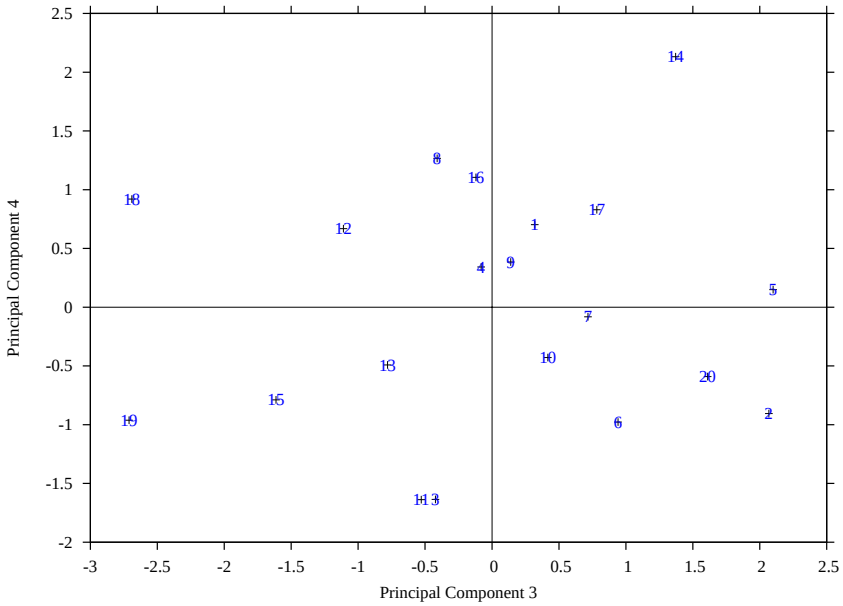

Figure 8.40: Principal component scores plot for principal components three and four of the interpreted data. The data matrix was standardised

Principal component	Eigenvalue	Percentage modelled	Cumulative percentage
1	163.92	35.03	35.03
2	109.02	23.29	58.32
3	47.45	10.14	68.46
4	39.44	8.43	76.89
5	51.10	10.92	87.81
6	27.60	5.90	93.70
7	14.36	3.07	96.77
8	5.32	1.14	97.91
9	3.96	0.85	98.76
10	2.50	0.53	99.29

Table 8.5: Eigenvalues and percentage modelled of the first ten principal components of the interpreted data for both the TEOS and DDS based experiments.

Following on from this, the datasets for both the TEOS and DDS interpreted results were combined, and principal components analysis was carried out on the combined dataset after preprocessing by standardising. Table 8.5 shows the eigenvalues for the first ten principal components, with the first five describing approximately 80 % of the dataset. Presented in figures 8.42, 8.43 and 8.44 are the scores plots of the first four principal components of the interpreted data for both the DDS and TEOS datasets. The loadings plot in figure 8.41 presents the first four principal components for this combined dataset.

The two sets of data occupy different areas of the plot in figure 8.42, with marked discontinuity between the two sets of data. The points modelling the TEOS data show closer clustering than those for the DDS data. This is possibly supporting evidence for the increased controllability of the TEOS based plasma enhanced chemical vapour deposition process. The difference between the two datasets is primarily in principal component one, which models the power, film properties and carbon monoxide. From the response surfaces it was evident that the film properties differed between the two different precursor chemistries, this might be linked to the different growth rates the two chemistries provide. Principal component two models the power, refractive index, contact angle, precursor decomposition and carbon dioxide concentration. The two datasets are roughly equally

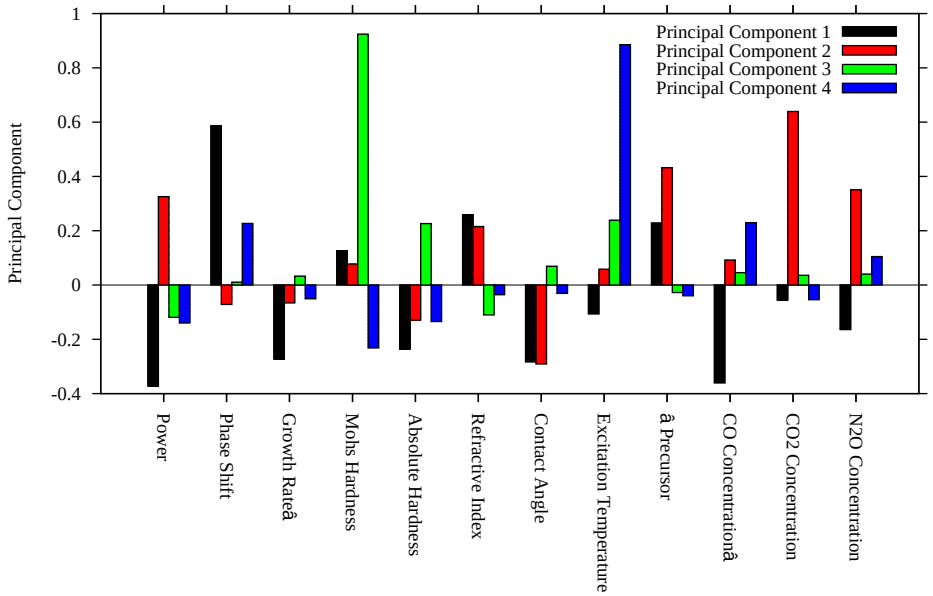

Figure 8.41: Principal component loadings plot for the combined interpreted results datasets. The data matrix was standardised.

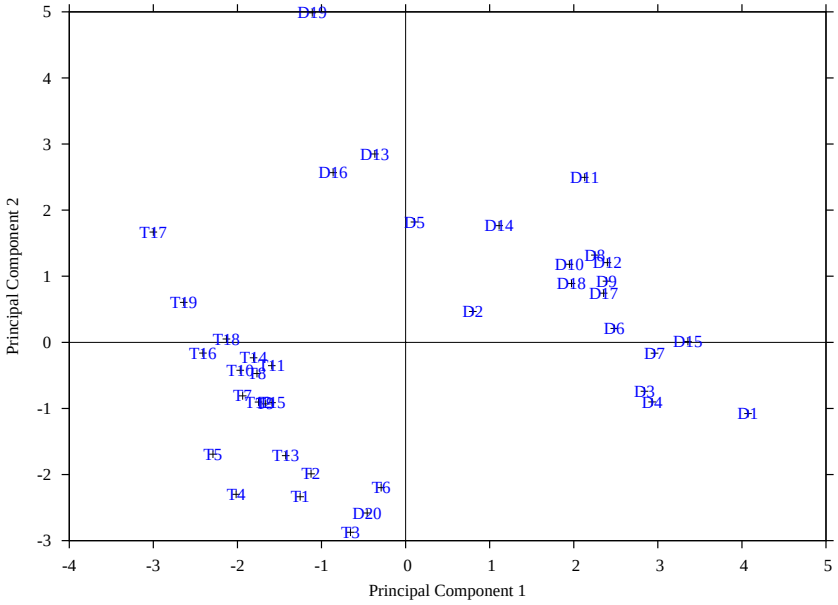

Figure 8.42: Principal component scores plot for principal components one and two of the interpreted results data for TEOS and DDS grown films. The data matrix was standardised. Points corresponding to the TEOS results are marked T, whilst those pertaining to the DDS results are marked D.

distributed in terms of principal component two.

Figure 8.43 presents the scores plots for principal components two and three of the combined interpreted data. The two datasets are merged in these two principal components. The Mohs hardness dominates principal component three, tables A.4 and A.7, show that these are in a similar range for both sets of experiments.

The scores plot for principal components three and four is presented in figure 8.44. Again, the two data sets are merged in these two principal components. Principal component four is dominated by the excitation temperature (figure 8.41), which, referring to tables A.2 and A.5, were on similar orders of magnitude for all experiments performed.

Table 8.6 represents the eigenvalues for the first three principal components of the optical emission data for the DDS dataset. Figures 8.45 and 8.48 are the scores plots for

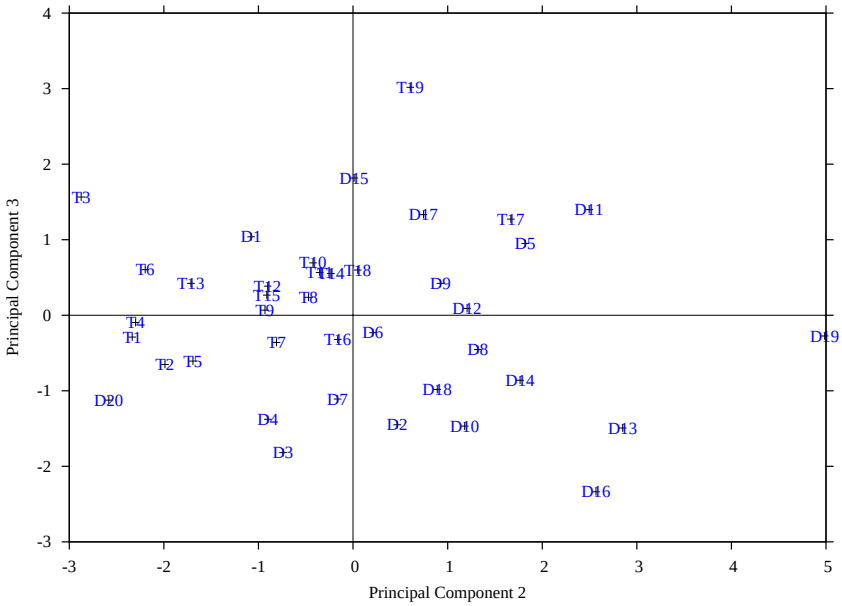

Figure 8.43: Principal component scores plot for principal components two and three of the interpreted results data for TEOS and DDS grown films. The data matrix was standardised. Points corresponding to the TEOS results are marked T, whilst those pertaining to the DDS results are marked D.

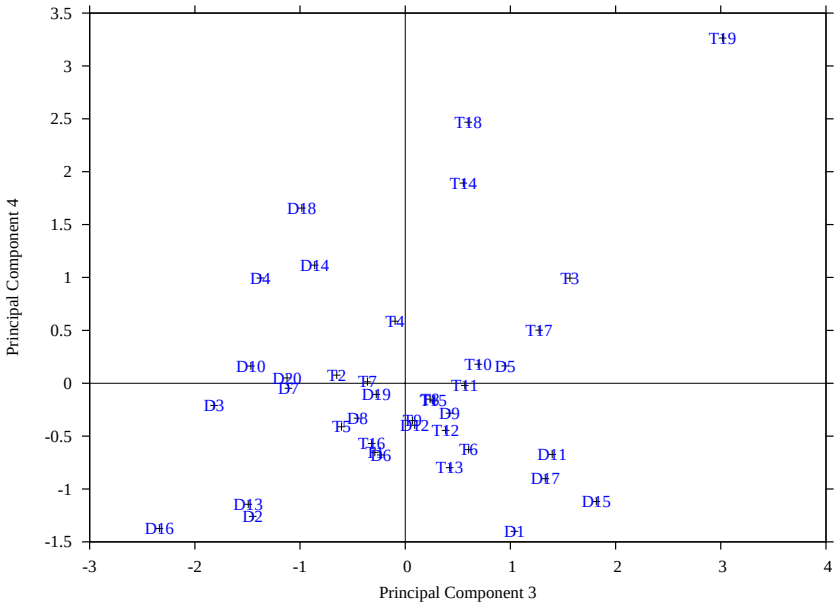

Figure 8.44: Principal component scores plot for principal components three and four of the interpreted results data for TEOS and DDS grown films. The data matrix was standardised. Points corresponding to the TEOS results are marked T, whilst those pertaining to the DDS results are marked D.

Principal component	Eigenvalue	Percentage modelled	Cumulative percentage
1	0.29	85.20	85.20
2	0.04	11.97	97.17
3	0.00	1.31	98.48

Table 8.6: Eigenvalues and percentage modelled of the first three principal components of the optical emission data.

optical emission

the first three principal components of the optical emission data. Figures 8.46, 8.47 and 8.49 are the loadings plots for the first three principal components.

Examining figures 8.45 and 8.48, strong similarities can be seen with the scores plots for the TEOS work, as seen in figures 7.34 and 7.37. This would suggest a strong similarity between the optical emission data for the two sets of experiments. The difference can be seen in the outliers, in the case of the DDS based scores plots, these are experiments four and seven. Experiment four was also an outlier in figure 7.34, but experiment seven was not, and was performed at medium voltage and DDS to oxygen ratio, with a low driving frequency. The other outlier in figure 7.34, experiment five, is also slightly distinct from the main cluster in figure 8.45. The loadings plot for principal component one, figure 8.46, shows that principal component one models the full spectrum, whereas principal component two models the atomic spectral features, as witnessed by figure 8.46.

The scores plot for principal components two and three shown in figure 8.48 shows similar clustering to 8.48, with the same outlying experiments, four and seven. Figure 8.49 shows that principal component three models one nitrogen transition and the strongest helium transition, which is different to the equivalent figure, figure 7.38, in the TEOS experiments.

The eigenvalue table for the combined OES dataset is presented in table 8.7, where it can be seen that the first three principal components model the vast majority of the data. The scores plots resulting from the principal components analysis can be seen in figures

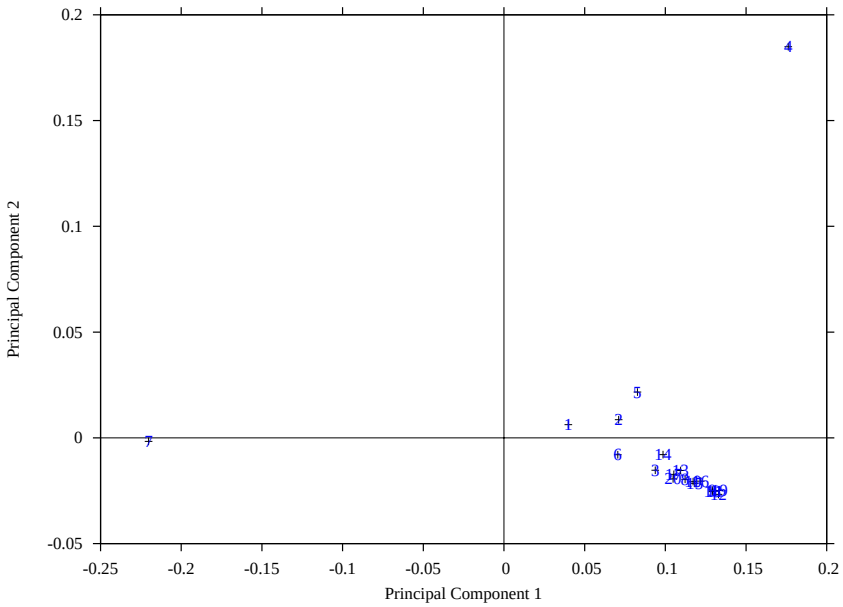

Figure 8.45: Principal component scores plot principal components one and two of the optical emission data. The data matrix was row scaled to one.

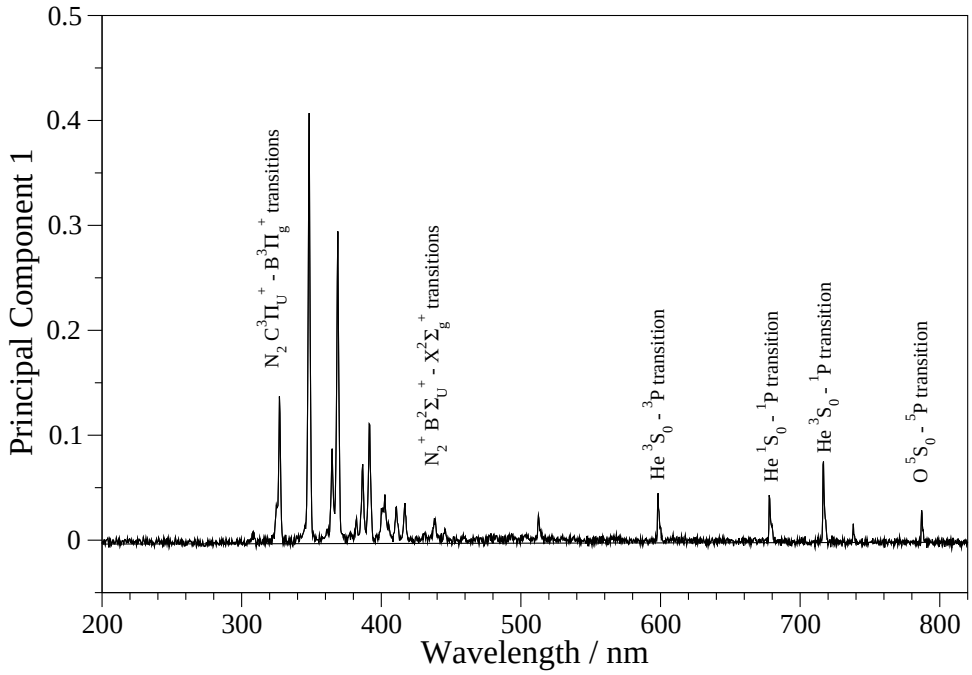

Figure 8.46: Principal component loadings plot for the principal component one of the optical emission dataset. The data matrix was row scaled to one.

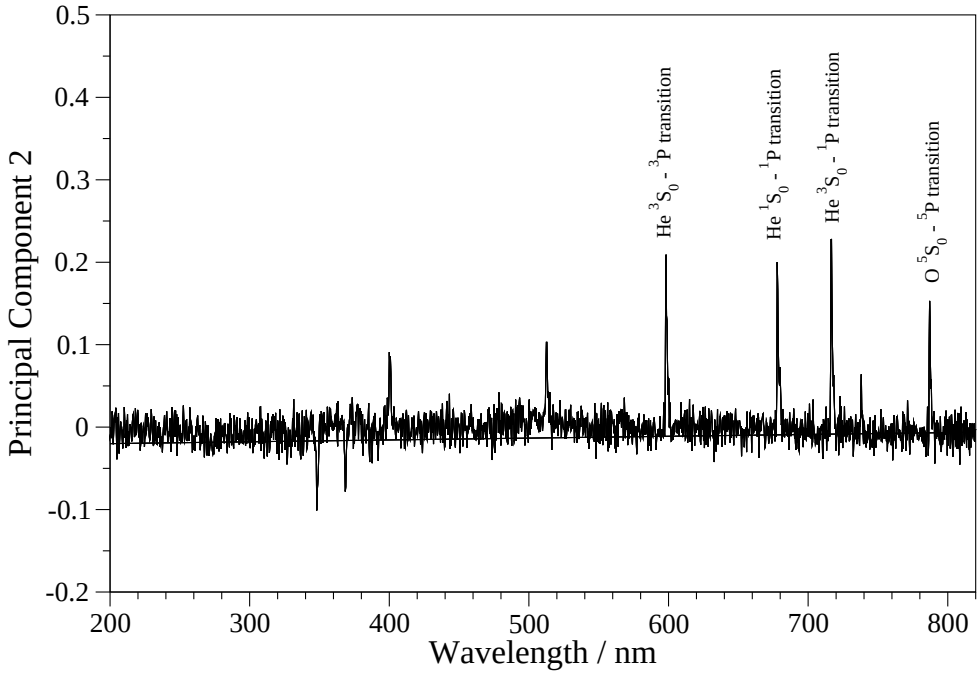

Figure 8.47: Principal component loadings plot for the principal component two of the optical emission dataset. The data matrix was row scaled to one.

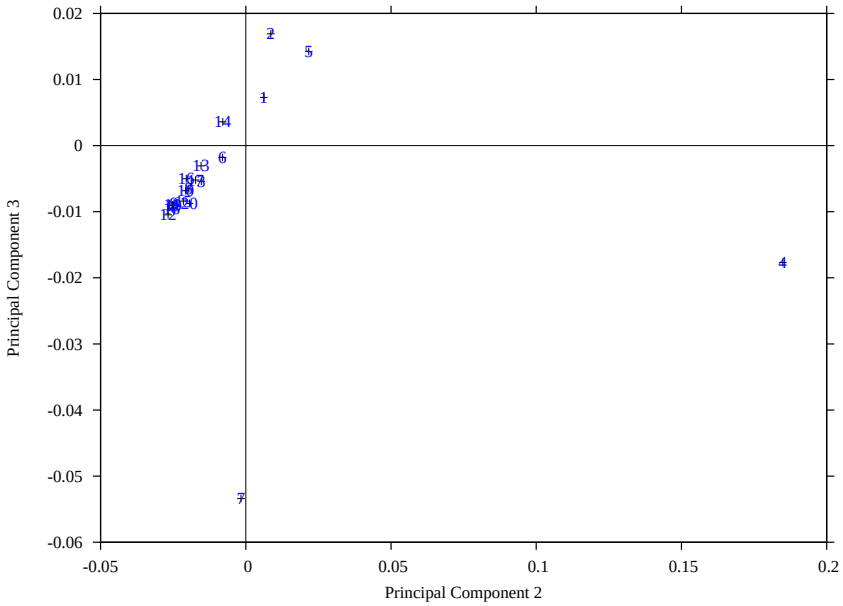

Figure 8.48: Principal component scores plot principal components two and three of the optical emission data. The data matrix was row scaled to one.

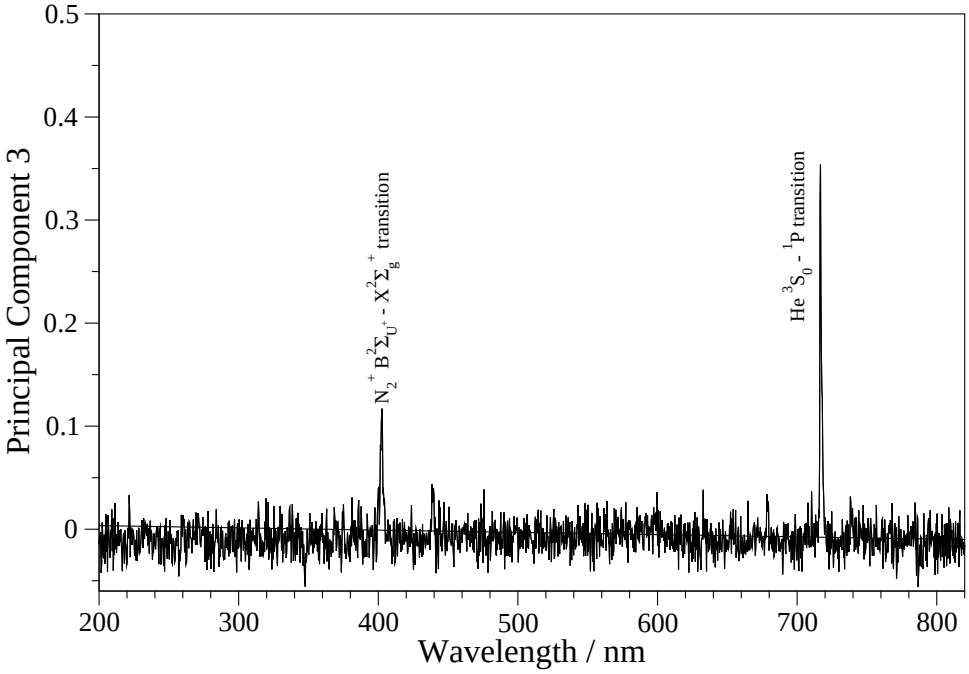

Figure 8.49: Principal component loadings plot for the principal component three of the optical emission dataset. The data matrix was row scaled to one.

Principal component	Eigenvalue	Percentage modelled	Cumulative percentage
1	0.75	86.41	86.41
2	0.05	5.51	91.92
3	0.04	4.30	96.22

Table 8.7: Eigenvalues and percentage modelled of the first three principal components of the optical emission data for both the TEOS and DDS based experiments.

8.50 and 8.53.

The scores plot for principal components one and two of the combined optical emission dataset, figure 8.50, shows that the linear clustering observed in the two separate scores plots, figures 7.34 and 8.45, is common to both sets of experiments. The outliers are also the same as in the original scores plots. This indicates that the plasma chemistry is very similar for the two sets of experiments in terms of the helium, oxygen and nitrogen. The outliers indicate that it is possible to change this fundamental chemistry, but that it is unchanged by the choice of precursor. Principal components one (figure 8.51) and

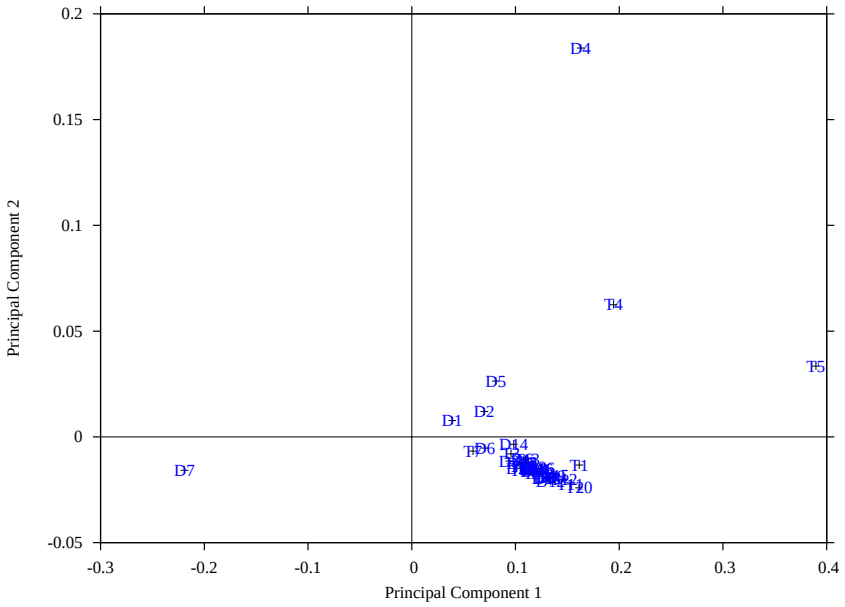

Figure 8.50: Principal component scores plot principal components one and two of the optical emission data of both the TEOS and DDS experiments. The data matrix was row scaled to one.

two (figure 8.52) also model the same spectral features as seen in the previous loadings plots.

Figure 8.53 again shows similarities to figures 7.37 and 8.45, the scores plots for principal components two and three of it's constituent datasets. Again, the same conclusions can be drawn about the plasma chemistry, that it is relatively unchanged by the choice of precursor. The loadings plot in figure 8.54 demonstrates that principal component three is dominated by the noise of the baseline.

Eigenvalues for the FTIR spectroscopy data are presented in table 8.8, which shows that the first ten principal components model only 65 % of the data. This would imply that the chemistry of this process, with regards to the precursor, is quite complicated. Scores plots for the first four principal components can be seen in figures 8.55, 8.58 and 8.60. Loadings plots for the first four principal components are shown in figures 8.56, 8.57,

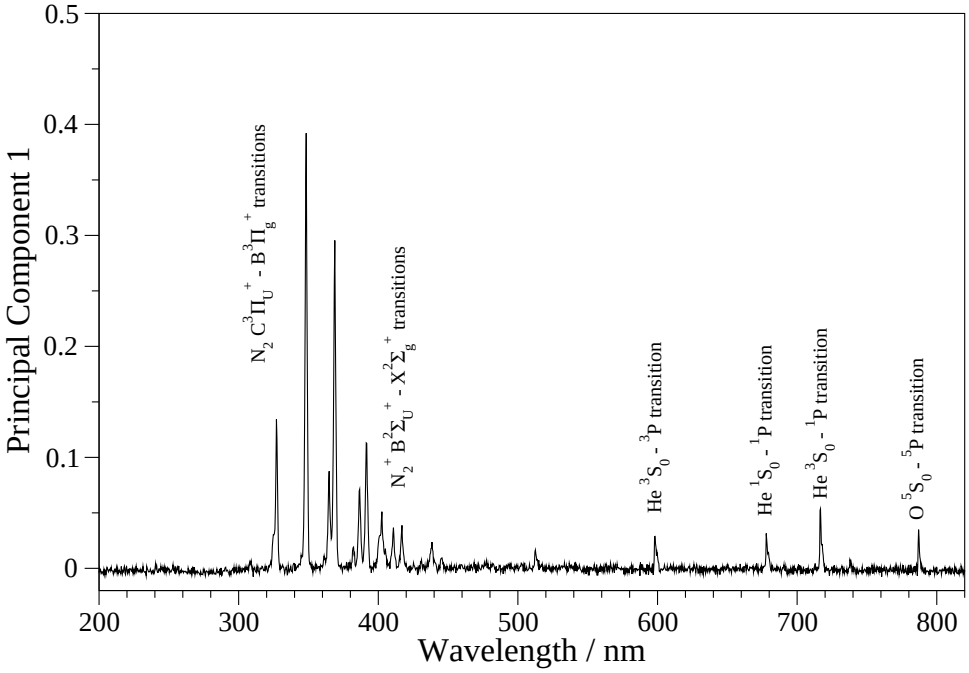

Figure 8.51: Principal component loadings plot for principal component one of the optical emission for the combined DDS and TEOS datasets. The data matrix was row scaled to one.

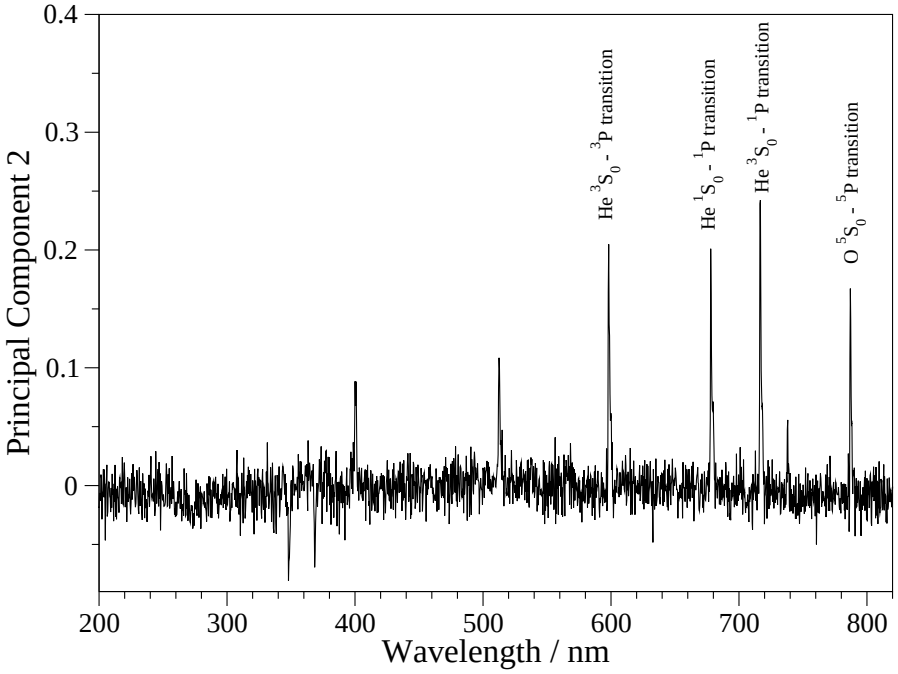

Figure 8.52: Principal component loadings plot for principal component two of the optical emission for the combined DDS and TEOS datasets. The data matrix was row scaled to one.

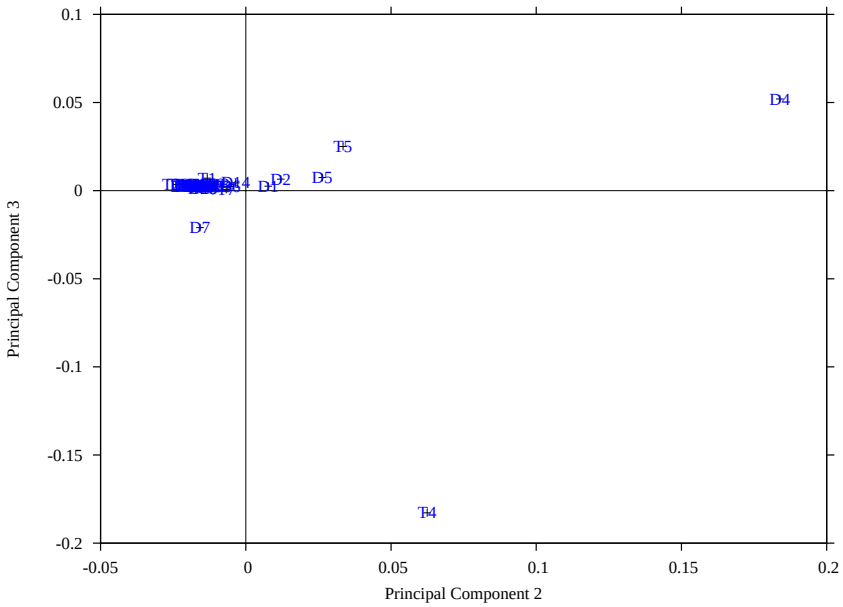

Figure 8.53: Principal component scores plot principal components two and three of the optical emission data of both the TEOS and DDS experiments. The data matrix was row scaled to one.

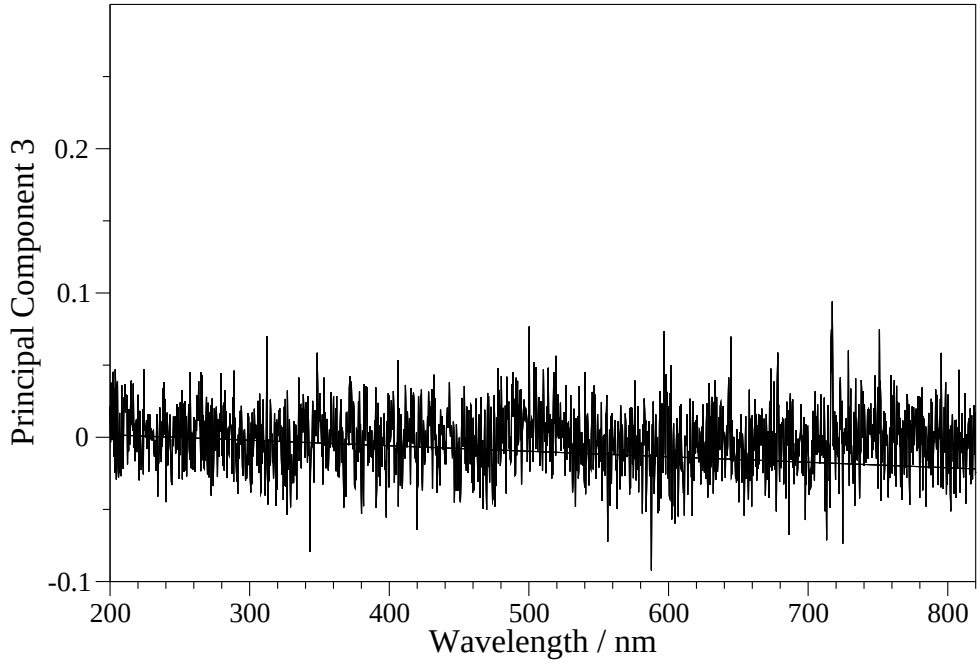

Figure 8.54: Principal component loadings plot for principal component three of the optical emission for the combined DDS and TEOS datasets. The data matrix was row scaled to one.

Principal component	Eigenvalue	Percentage modelled	Cumulative percentage
1	517.24	7.33	7.33
2	457.40	6.48	13.81
3	499.53	7.08	20.89
4	553.50	7.85	28.74
5	537.23	7.61	36.35
6	419.18	5.94	42.30
7	419.65	5.95	48.24
8	506.72	7.18	55.43
9	367.66	5.21	60.64
10	309.17	4.38	65.02

Table 8.8: Eigenvalues and percentage modelled of the first ten principal components of the FTIR data.

8.59 and 8.61.

The scores plot for principal components one and two of the FTIR spectroscopy data shown in figure 8.55 shows several clusters of experiments. The loadings plots for principal components one and two, figures 8.56 and 8.57, both show the dichlorodimethylsilane peaks. Principal component two also represents the peak at about 1000 cm^{-1}, that is extremely similar to the peak seen in principal components one (figure 7.40) and three (figure 7.43) of the TEOS FTIR principal components analysis, and looks to be ozone. There are six outliers with regards to principal component one, and five with regards to principal component two. The differences of the conditions for these outliers are varied, making any reason for their outlier nature unclear. As the two principal components are related to the DDS molecule, the differences might in some part be due to the non linear nature of the strong absorbance of this molecule.

Figure 8.58, represents the scores plot for principal components two and three of the FTIR spectroscopy data. The loadings plot for principal component three is presented in figure 8.59, and in addition to the dichlorodimethylsilane related peaks, also represents the formic acid and carbon dioxide peaks. The dichlorodimethylsilane peaks dominate

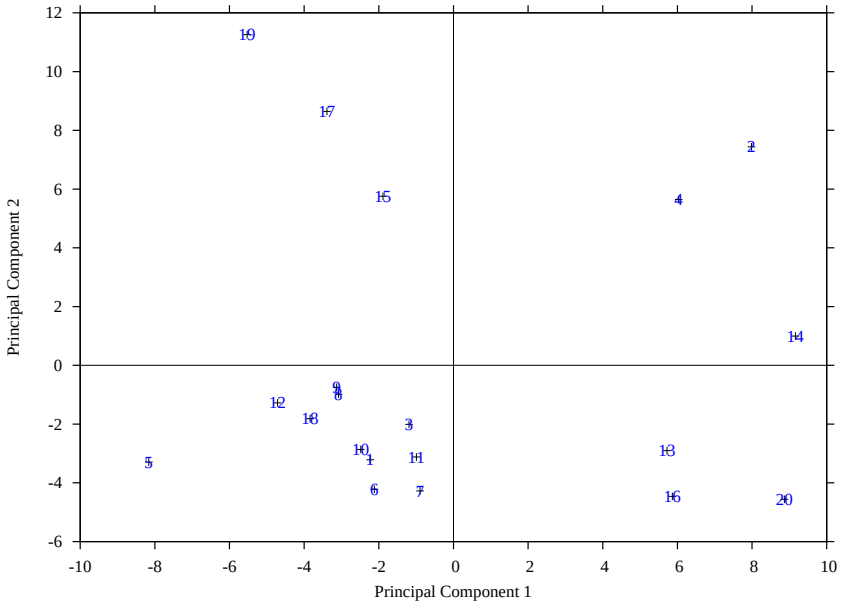

Figure 8.55: Principal component scores plot for principal components one and two of the FTIR spectroscopy data. The data matrix was standardised.

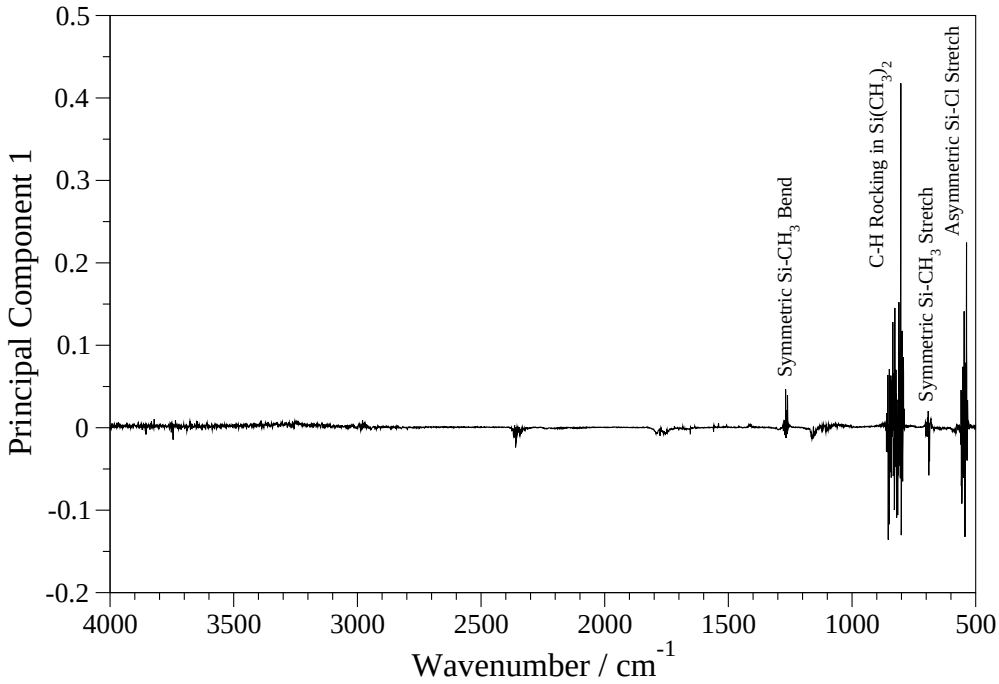

Figure 8.56: Principal component loadings plot for principal component one of the FTIR spectroscopy data. The data matrix was standardised.

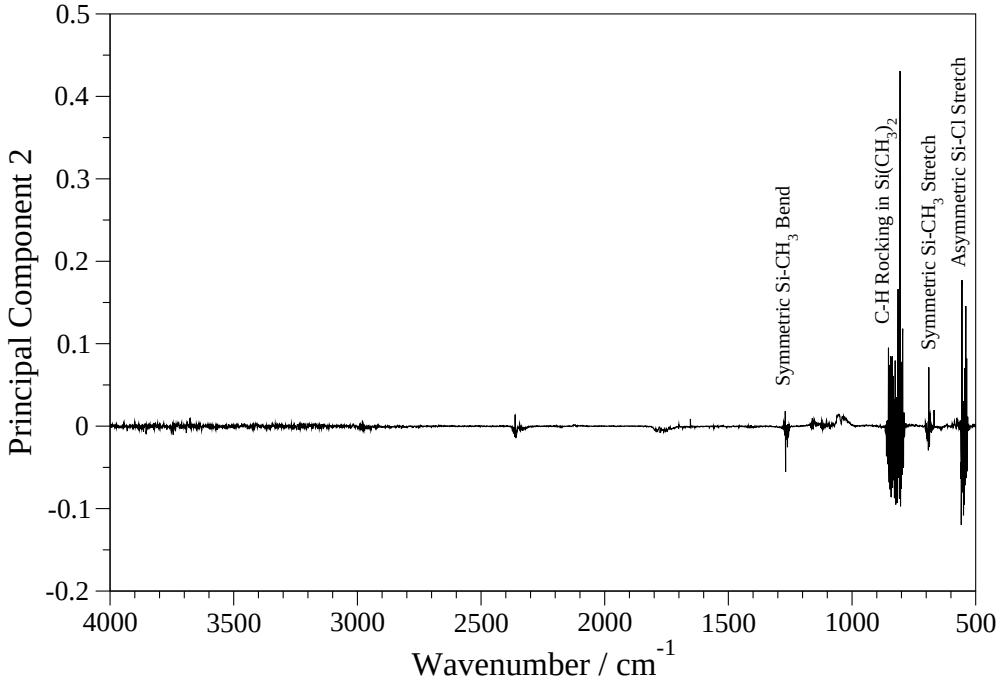

Figure 8.57: Principal component loadings plot for principal component two of the FTIR spectroscopy data. The data matrix was standardised.

again, making interpretation difficult.

The scores plot for principal components three and four, presented in figure 8.60, does not show strong clustering. Principal component four again represents the dichlorodimethylsilane, or breakdown products thereof, as shown in figure 8.61.

The eigenvalues for the principal components analysis of the combined DDS and TEOS FTIR datasets is presented in table 8.9. Again, the data matrix was standardised before principal components analysis was carried out. The first four principal components model about 70 % of the dataset.

Figure 8.62 represents the scores plot for principal components one and two of the combined FTIR dataset. This scores plot shows strong clustering of the DDS experiments. With examination of the loadings plots in figures 8.63 and 8.64, the first two principal components are definitely related to the DDS chemistry, which would explain the strong

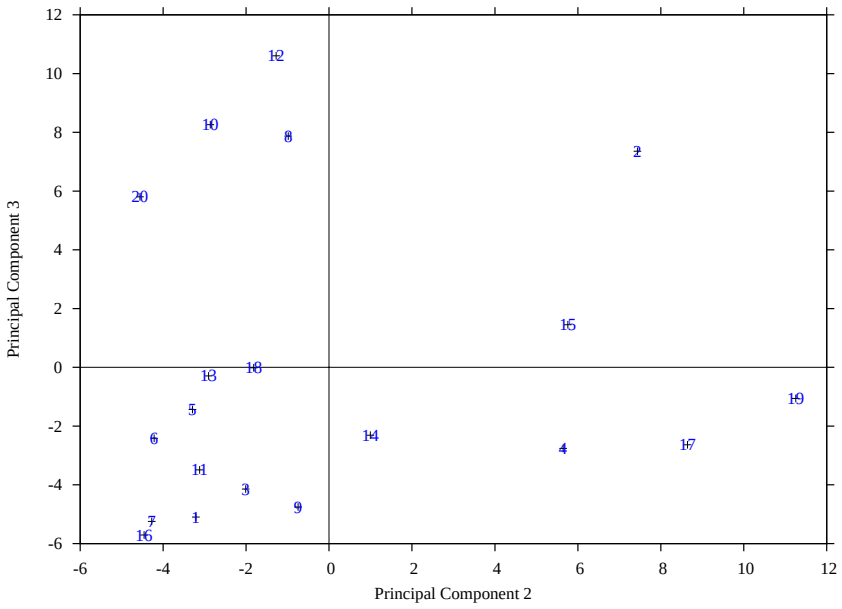

Figure 8.58: Principal component scores plot for principal components two and three of the FTIR spectroscopy data. The data matrix was standardised.

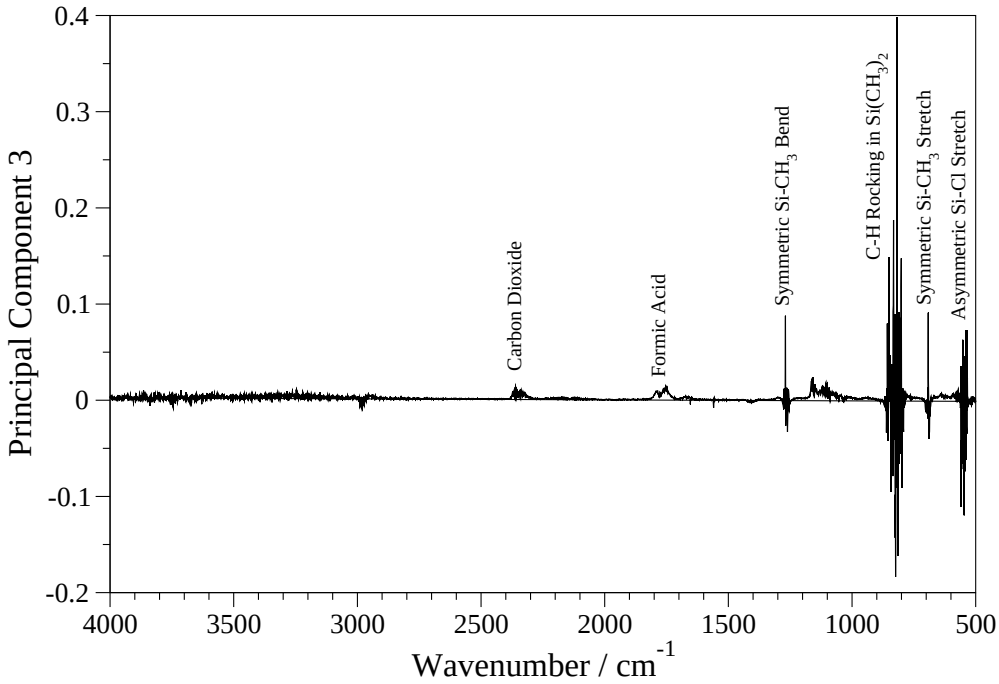

Figure 8.59: Principal component loadings plot for principal component three of the FTIR spectroscopy data. The data matrix was standardised.

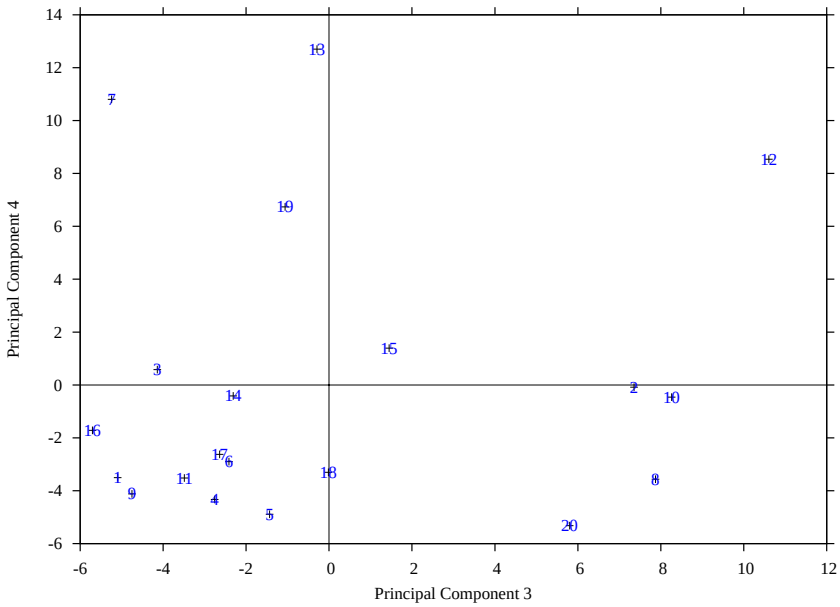

Figure 8.60: Principal component scores plot for principal components three and four of the FTIR spectroscopy data. The data matrix was standardised.

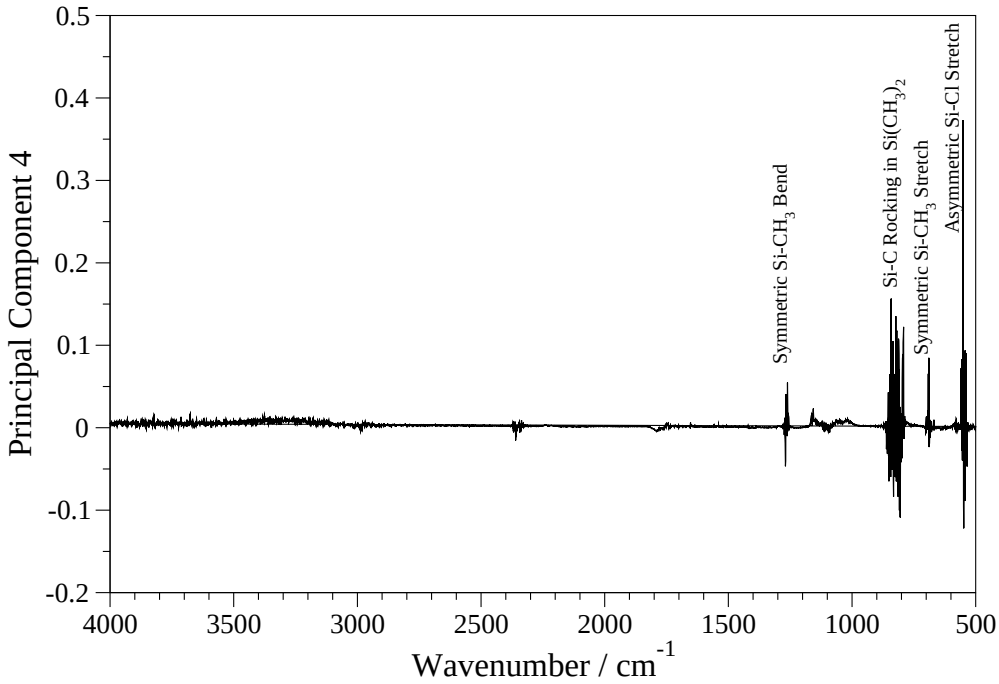

Figure 8.61: Principal component loadings plot for principal component four of the FTIR spectroscopy data. The data matrix was standardised.

Principal component	Eigenvalue	Percentage modelled	Cumulative percentage
1	11589.65	59.28	59.28
2	961.58	4.92	64.20
3	455.63	2.33	66.53
4	618.49	3.16	69.69
5	474.47	2.43	72.12
6	586.80	3.00	75.12
7	554.00	2.83	77.95
8	407.05	2.08	80.04
9	430.6	2.20	82.24
10	301.34	1.54	83.78

Table 8.9: Eigenvalues and percentage modelled of the first ten principal components of the FTIR data for both the TEOS and DDS based experiments.

clustering of the DDS experiments. Principal component one models a lot of the by-products from the DDS chemistry, whereas principal component two models the spectral features related to the DDS molecule.

The scores plot for principal components two and three of the combined FTIR dataset in figure 8.65 again shows strong clustering of the DDS experiments. The loadings plot for principal component three in figure 8.66 strongly models the DDS spectral features, and the ozone spectral feature at about 1050 cm^{-1} that is common to both the TEOS and DDS chemistry. The common species would explain why a large proportion of the TEOS experiments are clustered in the same region as the DDS experiments in terms of principal component three.

Figure 8.67 represents the scores plot for principal components three and four of the combined FTIR dataset. The DDS experiments are clustered very closely together, with the TEOS experiments not being clustered at all, the same as the previous scores plots. Figure 8.68 shows that principal component four models the DDS peaks, which would explain the close clustering of the DDS experiments in the scores plot.

The eigenvalues for the first ten principal components of the ATR-FTIR spectroscopy

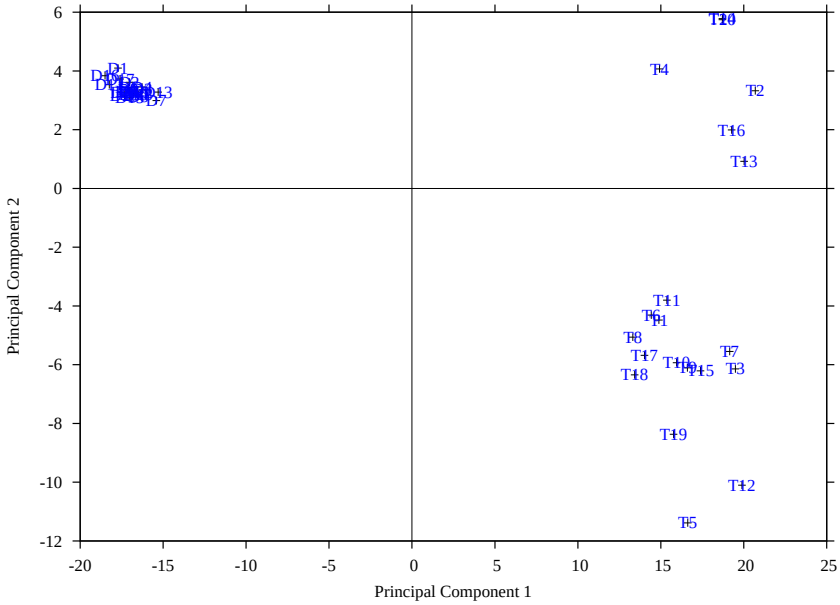

Figure 8.62: Principal component scores plot for principal components one and two of the FTIR spectroscopy data for both the TEOS and DDS experiments. The data matrix was standardised.

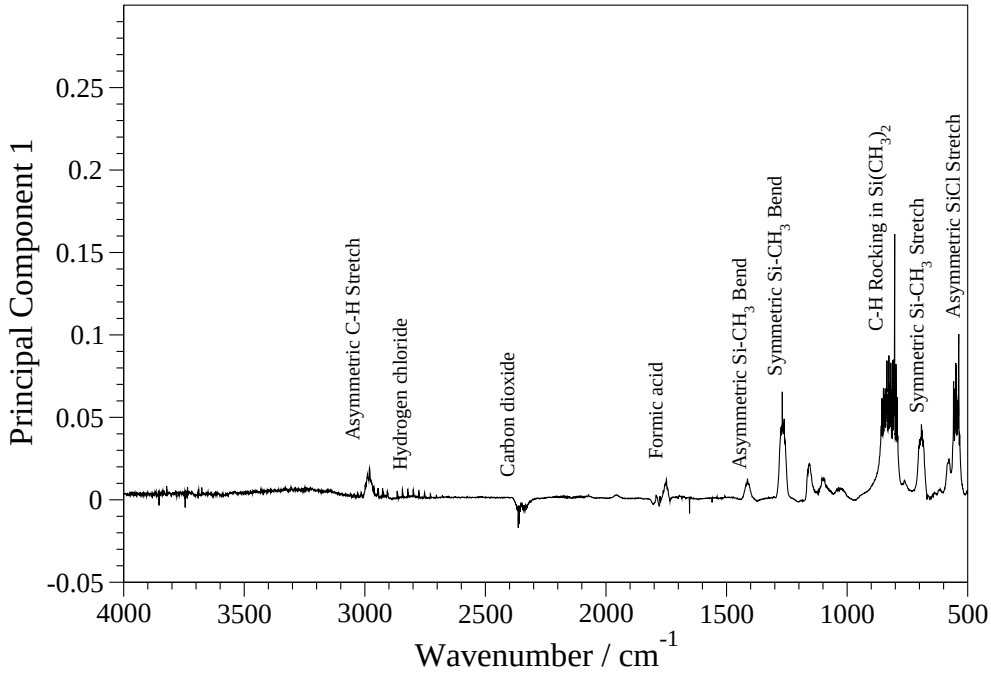

Figure 8.63: Principal component loadings plot for principal component one of the combined FTIR spectroscopy data. The data matrix was standardised.

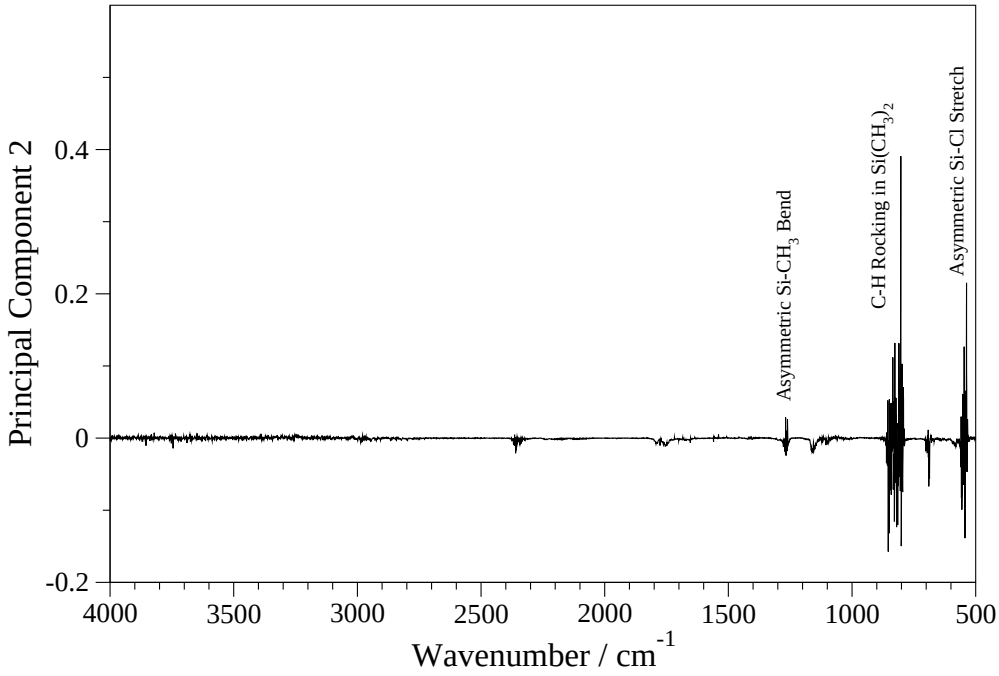

Figure 8.64: Principal component loadings plot for principal component two of the combined FTIR spectroscopy data. The data matrix was standardised.

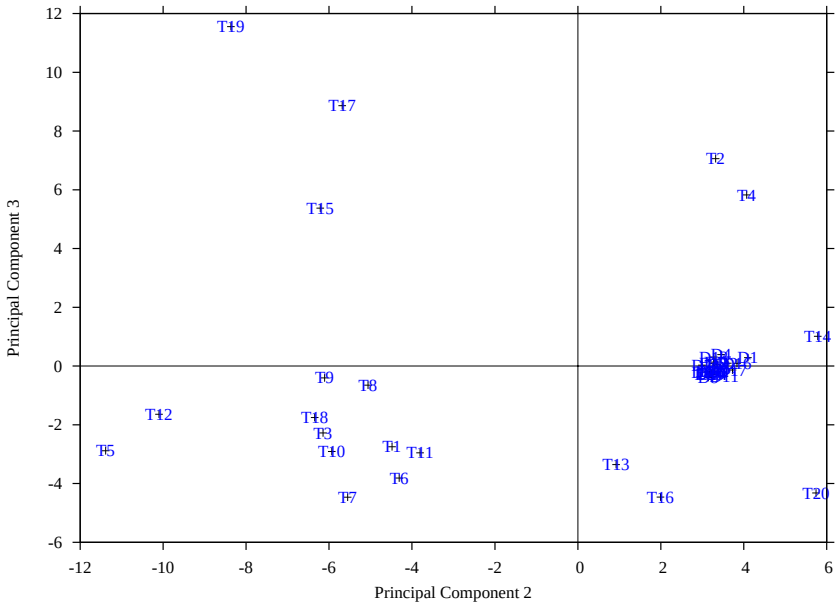

Figure 8.65: Principal component scores plot for principal components two and three of the FTIR spectroscopy data for both the TEOS and DDS experiments. The data matrix was standardised.

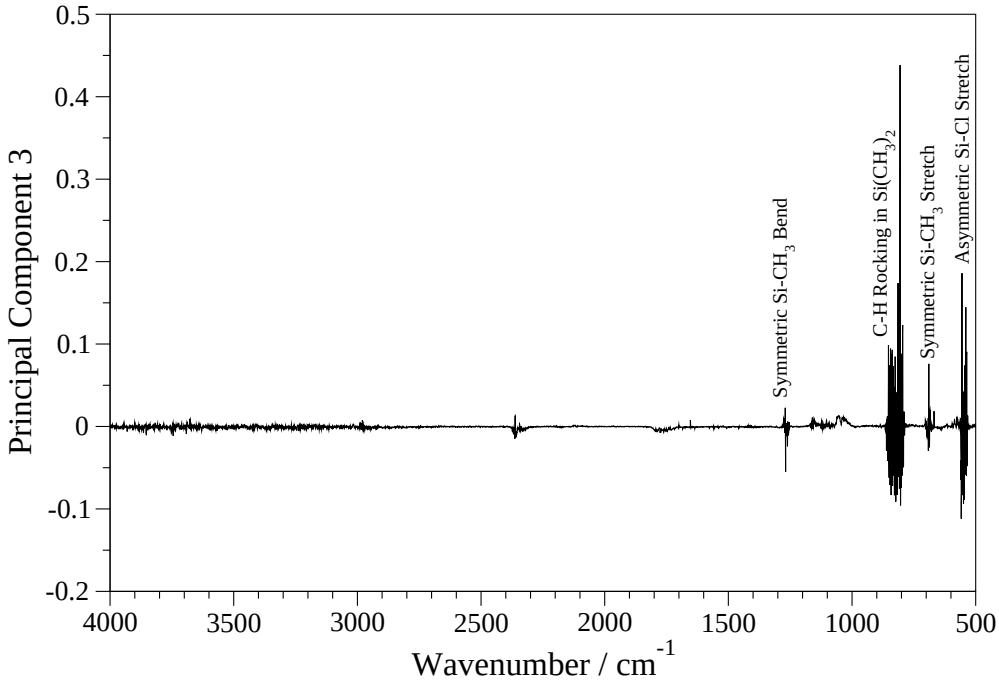

Figure 8.66: Principal component loadings plot for principal component three of the combined FTIR spectroscopy data. The data matrix was standardised.

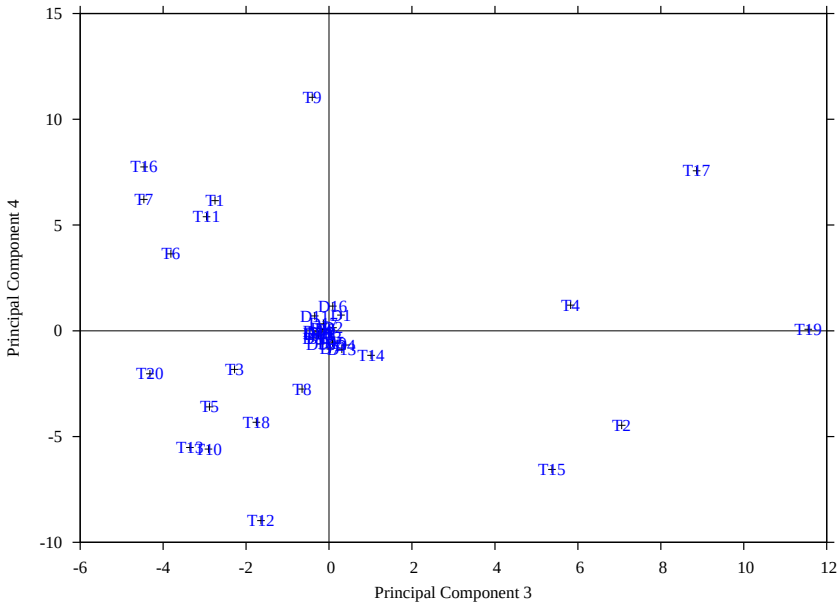

Figure 8.67: Principal component scores plot for principal components three and four of the FTIR spectroscopy data for both the TEOS and DDS experiments. The data matrix was standardised.

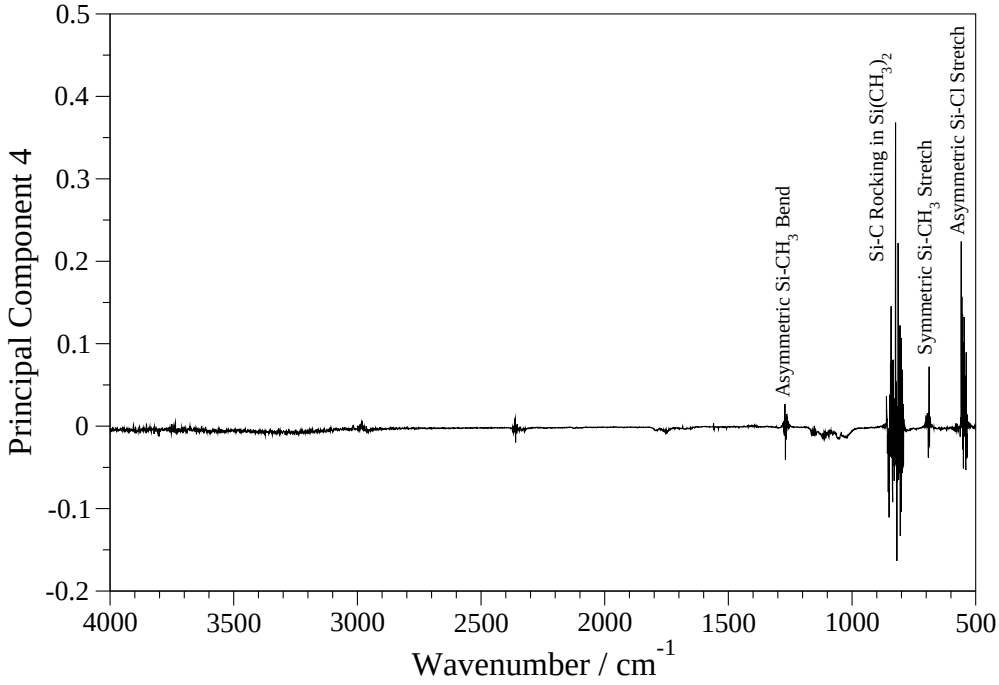

Figure 8.68: Principal component loadings plot for principal component four of the combined FTIR spectroscopy data. The data matrix was standardised.

data are provided in table 8.10 and the first three principal components model over 85 % of the dataset. The dataset was standardised before principal components analysis was carried out. Figures 8.69 and 8.72 are the scores plots for the first three principal components of the ATR-FTIR spectroscopy data. The loadings plots for the first three principal components are presented in figures 8.70, 8.71, and 8.73.

Principal components one and two are presented in the scores plot in figure 8.69, with the relevant loadings plots in figures 8.70 and 8.71. Experiment four is clearly an outlier from the main cluster in the scores plot, and this varies in principal component one. The loadings plot for principal component one indicates that it models a series of peaks from 1900 to 2600 cm^{-1}. Principal component two models a series of peaks from 1300 to 2600 cm^{-1}. Low voltage and frequency in combination with high oxygen concentration clearly has a strong effect on the film composition.

Principal component	Eigenvalue	Percentage modelled	Cumulative percentage
1	28095.63	79.64	79.64
2	1438.45	4.08	83.71
3	765.77	2.17	85.88
4	792.50	2.25	88.13
5	1098.38	3.11	91.24
6	1206.82	3.42	94.66
7	464.49	1.32	95.98
8	145.35	0.41	96.39
9	191.04	0.54	96.93
10	149.64	0.42	97.36

Table 8.10: Eigenvalues and percentage modelled of the first ten principal components of the ATR FTIR data.

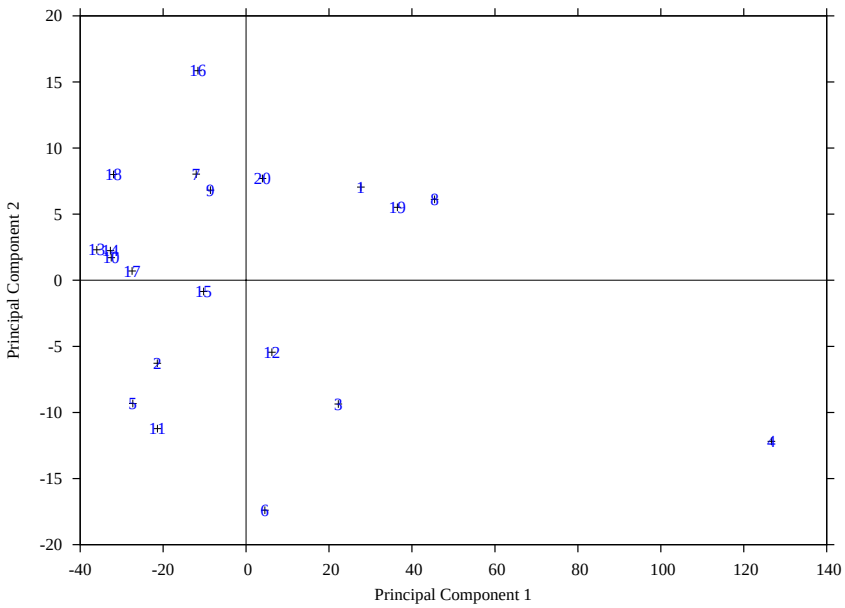

Figure 8.69: Principal component scores plot for principal components one and two of the ATR-FTIR spectroscopy data. The data matrix was standardised.

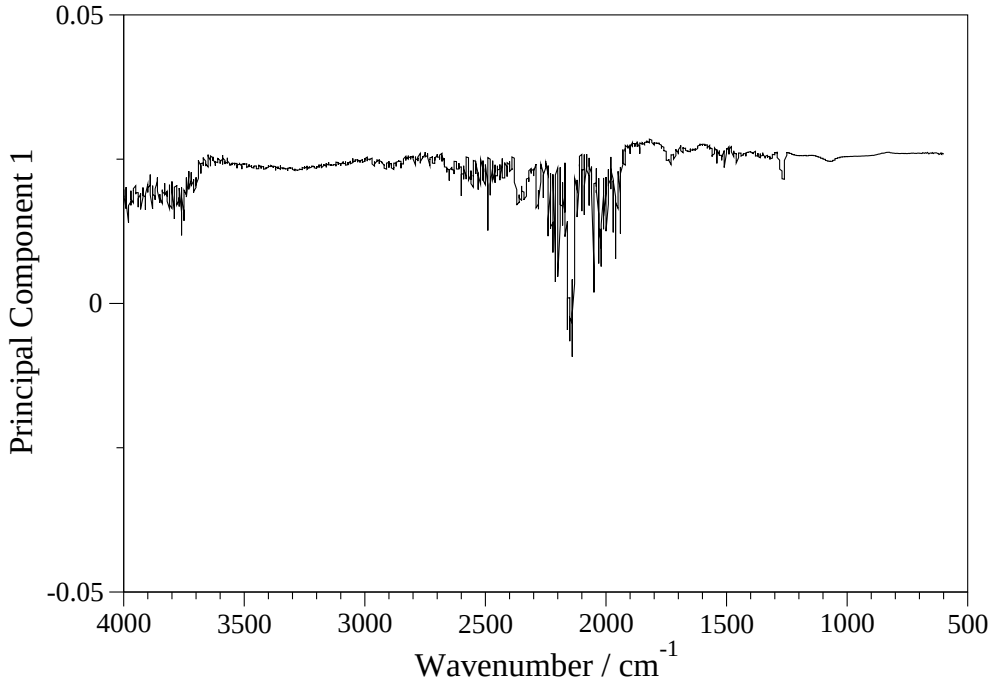

Figure 8.70: Principal component loadings plot for principal component one of the ATR-FTIR spectroscopy data. The data matrix was standardised.

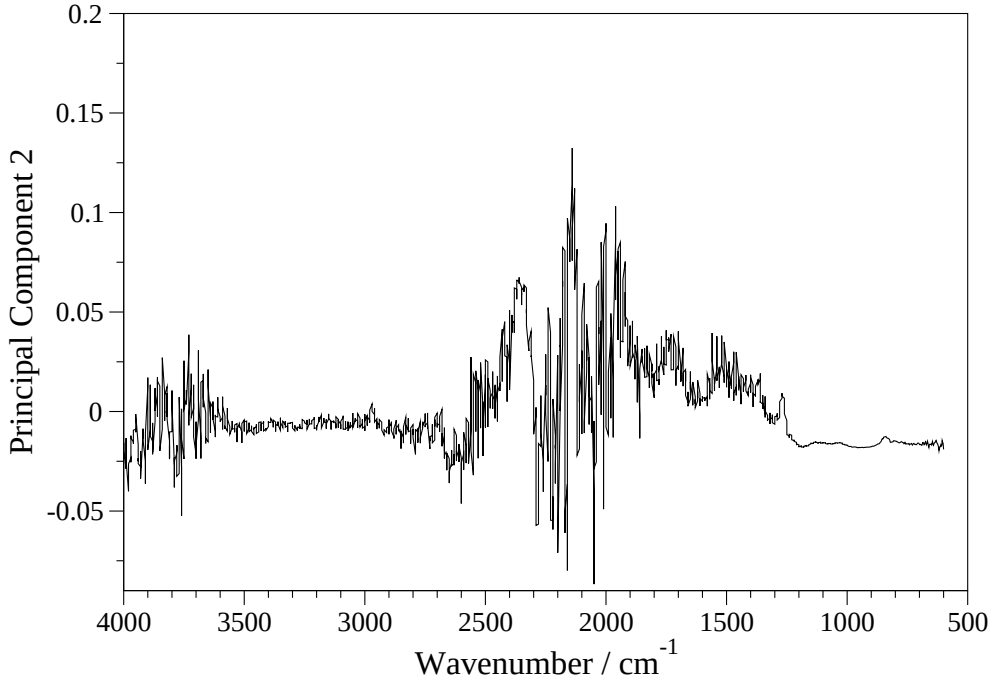

Figure 8.71: Principal component loadings plot for principal component two of the ATR-FTIR spectroscopy data. The data matrix was standardised.

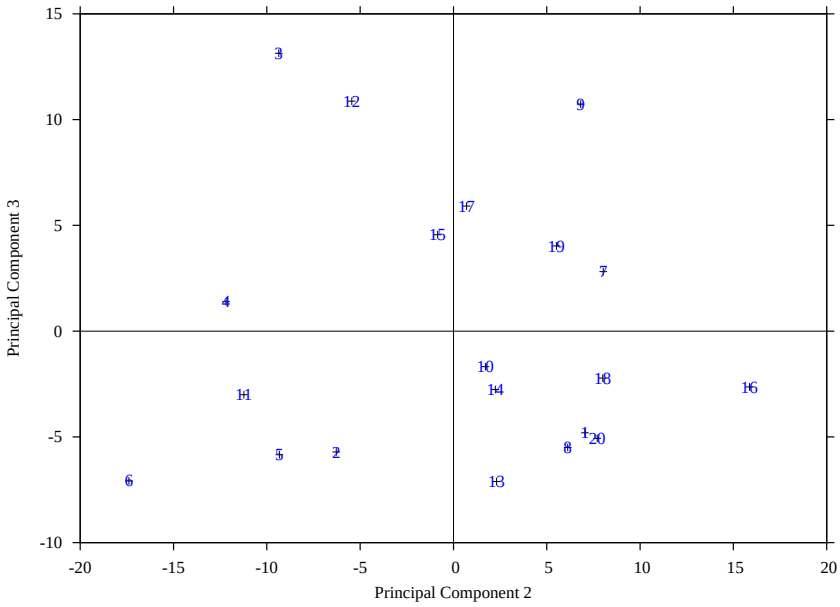

Figure 8.72: Principal component scores plot for principal components two and three of the ATR-FTIR spectroscopy data. The data matrix was standardised.

The scores plot for principal components two and three is presented in figure 8.72, whilst the loadings plot for principal component three is presented in figure 8.73. A wider range of peaks is modelled by principal component three, including symmetric and asymmetric carbon hydrogen stretches at 2900 cm^{-1}. There are no clear outliers in the scores plot, and no defined clustering.

The composition data from the TEOS experiments was then incorporated into the principal components analysis, and a table of eigenvalues is presented in table 8.11. The first three principal components model the majority of the data.

The first scores plot from the principal components analysis can be seen in figure 8.74. This represents the first and second principal components. Two distinct clusters can be seen in this plot, which perhaps indicates three subtly different silica films being produced in terms of composition. The majority of the DDS and TEOS points belong to one of

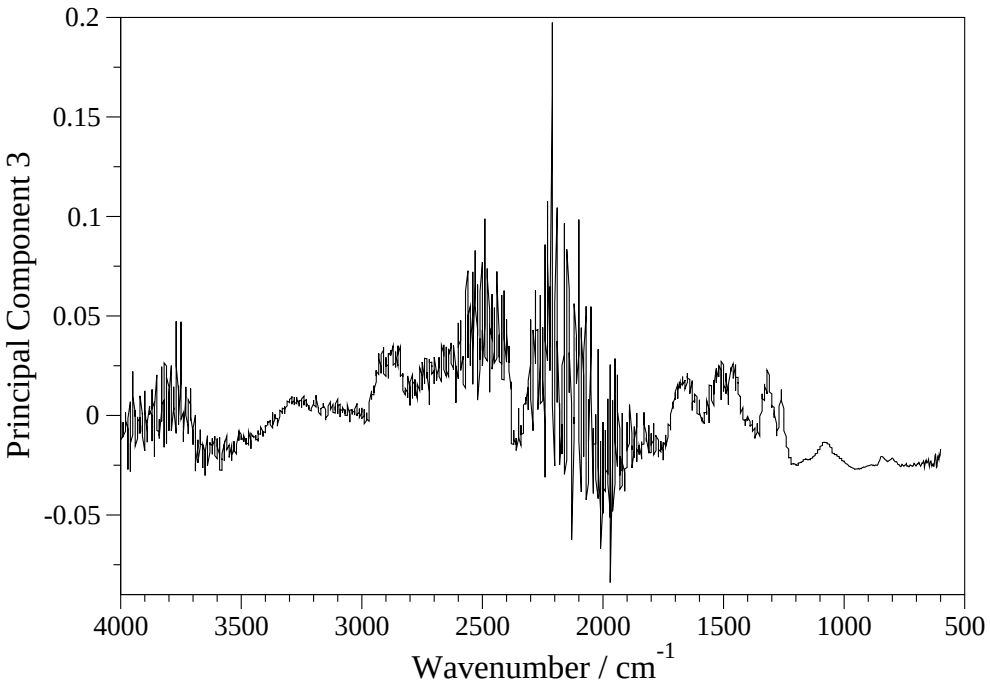

Figure 8.73: Principal component loadings plot for principal component three of the ATR-FTIR spectroscopy data. The data matrix was standardised.

Principal component	Eigenvalue	Percentage modelled	Cumulative percentage
1	36720.11	52.04	52.04
2	20682.57	29.31	81.35
3	4616.75	6.64	87.90
4	1481.37	2.10	90.00
5	847.97	1.20	91.20
6	960.86	1.36	92.56
7	1305.80	1.85	94.41
8	905.73	1.28	95.69
9	411.79	0.58	96.28
10	285.55	0.40	96.68

Table 8.11: Eigenvalues and percentage modelled of the first ten principal components of the ATR FTIR data for both the TEOS and DDS based experiments.

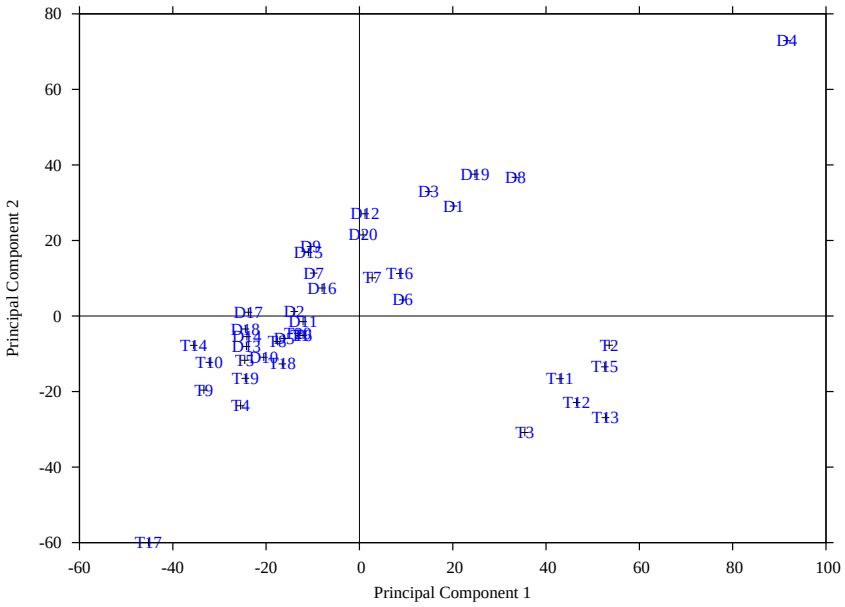

Figure 8.74: Principal component scores plot for principal components one and two of the the ATR-FTIR spectroscopy data for both TEOS and DDS films. The data matrix was standardised.

these clusters, with the other being completely comprised of TEOS experiments. There is also an outlier from the two clusters, experiment four of the DDS experiments. Principal component one (loadings plot in figure 8.75) models a series of defined peaks from 1300 to 2600 cm^{-1}, whilst principal component two models a carbon hydrogen stretch at 3000 cm^{-1} and another sharp peak at 1300 cm^{-1}.

The scores plot in figure 8.77 represents principal components two and three of the combined ATR-FTIR spectroscopy data. The loadings plot for principal component three shown in figure 8.78 shows that principal component three models carbon hydrogen stretches at 3000 cm^{-1} and peaks at 1300 cm^{-1}, 1400 cm^{-1} and 1750 cm^{-1}.

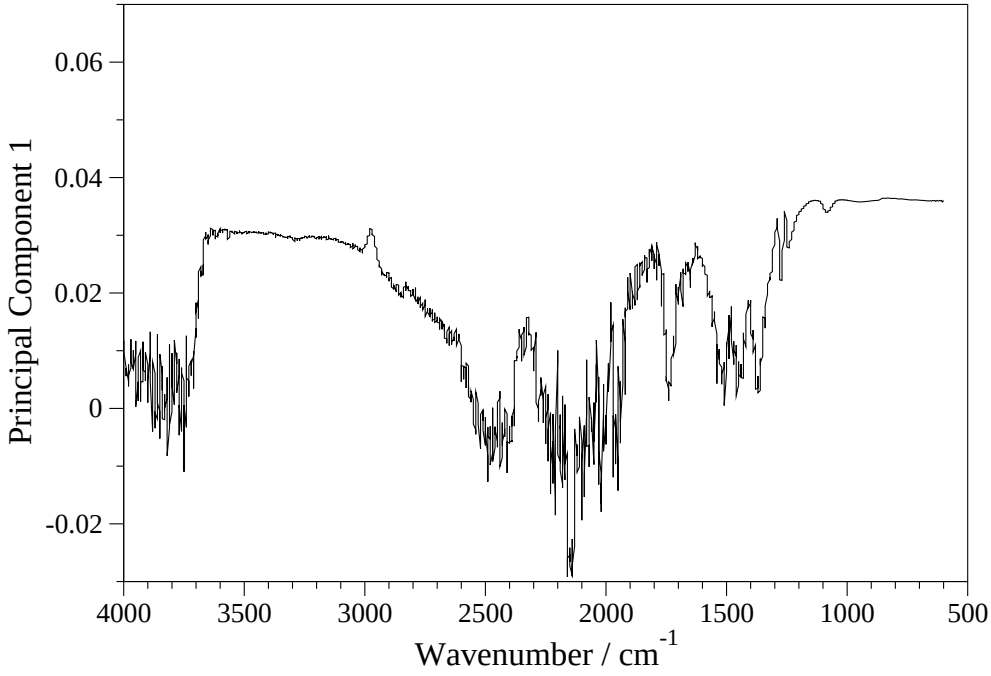

Figure 8.75: Principal component loadings plot for principal component one of the ATR-FTIR spectroscopy data for the combined DDS and TEOS datasets. The data matrix was standardised.

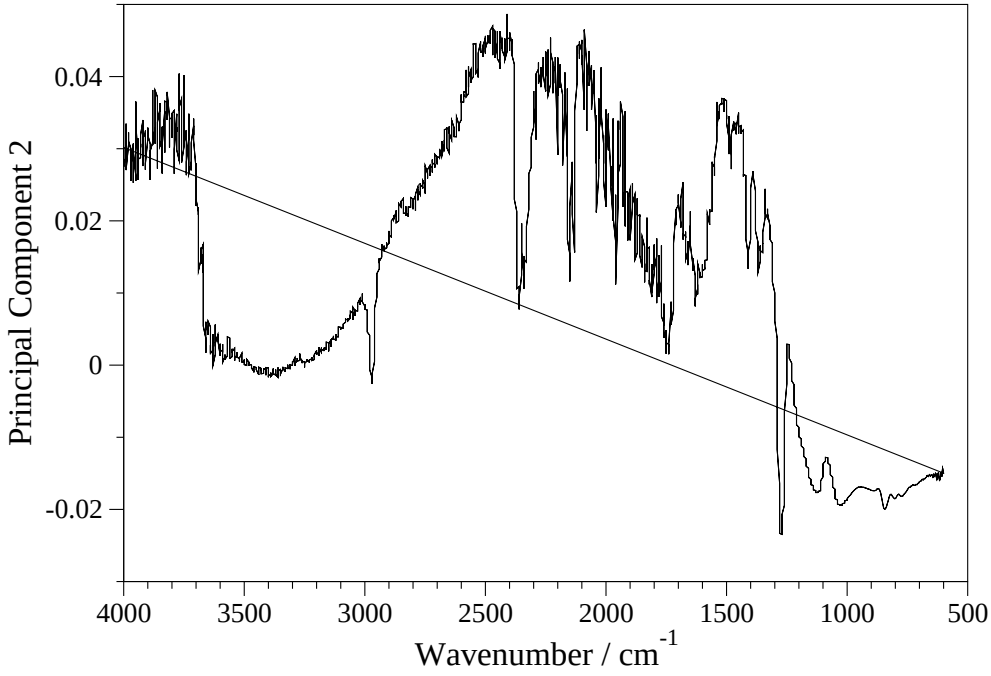

Figure 8.76: Principal component loadings plot for principal component two of the ATR-FTIR spectroscopy data for the combined DDS and TEOS datasets. The data matrix was standardised.

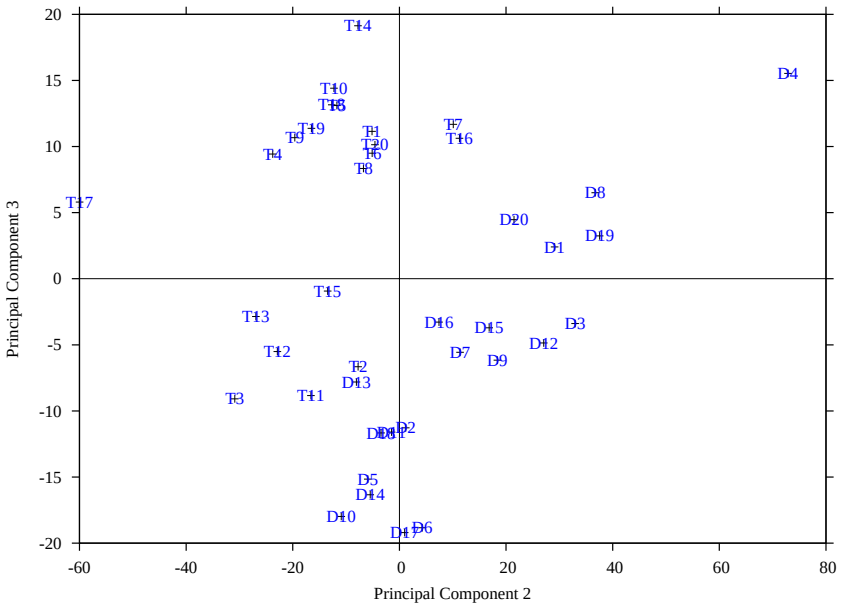

Figure 8.77: Principal component scores plot for principal components two and three of the the ATR-FTIR spectroscopy data for both TEOS and DDS films. The data matrix was standardised.

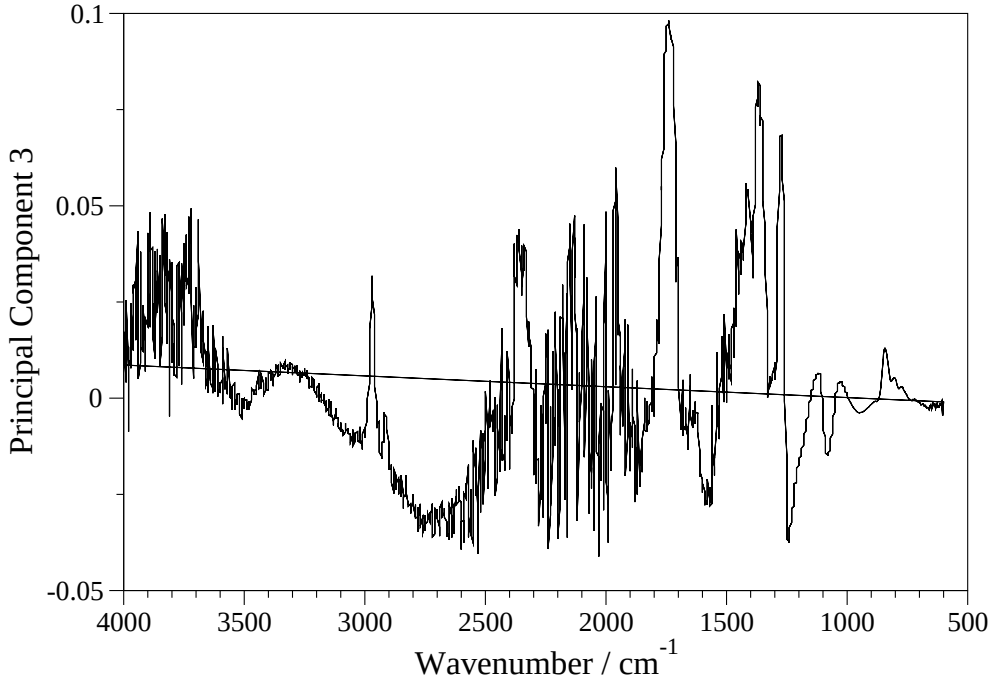

Figure 8.78: Principal component loadings plot for principal component three of the ATR-FTIR spectroscopy data for the combined DDS and TEOS datasets. The data matrix was standardised.

8.4 Conclusions

A new chemistry for silica film deposition has been examined in depth, with the previously outlined chemometric approach, thus meeting the aim of the work. In this case the work has provided an intriguing look into a new precursor chemistry for silica deposition. The results shown here demonstrate that a silica film can be grown faster, and with less power with DDS than it can be in an equivalent TEOS based process. Consequently, the objective of the work has also been met, as the combined chemometric and spectroscopic approach has been vindicated.

This is the first time that spectroscopy has been used to characterise the use of DDS in this process, and the FTIR spectrometer has allowed for an overall reaction to be hypothesised. The optical emission spectroscopy has highlighted the influence of active oxygen species, comparable to the TEOS based silica deposition process. The examination of the hydrogen chloride evolved within the process has highlighted the importance of measuring species concentration *in situ* as well as downstream of the process.

The principal components analysis shows that the process operates in a similar manner to the TEOS one, in terms of the controllability of the various measured parameters. The principal components analysis of the interpreted results showed possible links between the plasma excitation and the film hardness. The principal components analysis of the optical emission dataset was useful in the analysis of process conditions effects on the emission spectra, and the results showed strong similarities with the principal components analysis for the TEOS based results, which was corroborated with the loadings plots. The FTIR principal components analysis showed that the DDS peaks dominated, although there was some variation in the by-products between principal components. These results also demonstrated the importance of ozone in the overall chemistry of the process. The principal components analysis also showed that, although the ATR-FTIR spectroscopy data

film composition was relatively similar to the TEOS produced films, there are differences in the film composition that are worthy of further investigation.

Comparisons with the TEOS results have been useful, as the response surface results for TEOS have provided a basis for comparison of the various measured properties. The incorporation of these results into the principal components analysis also highlighted the similarities and differences between the two processes.

These results have proved useful both in validating the combined approach to the investigation of atmospheric pressure chemical vapour deposition, and in indicating the importance of examining new chemistries for the process. Further work should be directed to extending the data set by the investigation of further silica precursors.

Chapter 9

In situ studies of the chemistry of plasma enhanced chemical vapour deposition of silica

9.1 Introduction

Work in previous chapters has brought up the question of what chemistry is occurring within the plasma reactor, and how is it leading to film growth? In the case of the investigation of silica deposition from a TEOS precursor, it is apparent that active oxygen species are involved in the reaction mechanisms. It is also known that TEOS breaks down without the presence of oxygen species, [237], and that this provides another chemical mechanism for silica growth. What these mechanisms are is an area for further investigation.

As previously established in this thesis, there are two types of reactions occurring in chemical vapour deposition. These are gas phase reactions; and surface reactions. The gas phase reactions generate intermediary species which then adsorb to the surface and react, in turn forming the thin film. Of course these two types of reaction are linked, but at atmospheric pressure it is assumed that the gas phase reactions are rate limiting. In other words they control the overall formation of the thin film.

As the hypothesis is that the reactions in the gas phase are the important ones, then it is important to measure them as they are going on, *in situ*. In chapter two a range of techniques were discussed, and Fourier transform infra-red spectroscopy was identified as a key technique to carry out such an investigation. To restate, the technique allows for a wide ranging investigation of chemical species within the reactor, with the caveat

that these species are infra-red active. This is likely in the case of the break down of an organo-silicon compound such as TEOS.

Previous work using *in situ* FTIR spectroscopy has either been concerned with thermal chemical vapour deposition processes, [122], or with different plasma processes, [118]. No work has been presented in the literature concerning its use in the characterisation of the atmospheric pressure plasma enhanced chemical vapour deposition of silica films from TEOS.

In addition to the literature discussed in chapter two, some work has been carried out concerning *in situ* FTIR spectroscopy of plasma processes. One such example is concerned with the investigation of the plasma assisted oxidative conversion of methane, [284]. The use of FTIR spectroscopy enabled the identification of oxidised hydrocarbon products. The increase of these oxidised products was observed with increasing initial oxygen concentration. Nitrogen containing compounds were also identified at higher input energies. This work shows that the use of *in situ* FTIR spectroscopy has been instrumental in analysing the chemistry of methane oxidation in plasma conditions.

Time resolved FTIR spectroscopy has seen use in characterising a low pressure nitrous oxide plasma, [285]. In this study the time resolved FTIR measurements were used to both modify and validate an existing model of a discharge in nitrous oxide.

The use of this particular measurement technique in conjunction with the chemometric techniques outlined in previous chapters has not been carried out. This is surprising, as it would allow for an in depth, methodical approach to the investigation of the chemistry of plasma processes. In addition a technique such as principal components analysis would enhance the ability to identify trends across the processing conditions.

Aims and Objectives

The aim of this work is to examine the chemistry of the plasma enhanced chemical vapour deposition of silica thin films through FTIR spectroscopy. To facilitate this work, the design and construction of a plasma reactor that is both accessible for infra-red spectroscopy and is also capable of simulating a plasma enhanced chemical vapour deposition process is required.

The overall objective is to extend the chemometric methodology established in previous chapters to the *in situ* FTIR studies of a plasma enhanced chemical vapour deposition process. This objective being met will provide a solid methodology to build a robust dataset describing any given chemical vapour deposition process.

9.2 Methodology

Reactor design

The primary criterion for the design of this new reactor is to ensure spectroscopic access in the infra-red region of the spectrum. As outlined in the introduction, the use of infra-red spectroscopy allows for the measurement of infrared active molecules. Ideally an open reactor would be used, but there are health and safety issues involved with such a design, and there would also be problems with gas flow distribution. Therefore, a closed reactor with windows to allow infra-red light into and out of the reactor is required.

Potassium bromide is a suitable material for the windows, as it transmits infra-red light down to about 400 cm^{-1}. These can be glued to the reactor, forming an air tight seal. This ensures gas can flow through the reactor and directly to a suitable exhaust, reducing the risk of exposure to various chemicals.

Schematics for the reactor design can be seen in figure 9.1. The dielectric plates are made of alumina, and measure 60 by 90 millimetres. In order that spectroscopic techniques can be used that rely on spectral information into the mid infra red region, special potassium bromide crystal windows are placed perpendicular to the electrodes. The reactor support structure has been made out of teflon, partly due to it being chemically inactive, and partly due to cleaning concerns. Two teflon pieces have been machined, providing support slots for the dielectrics and holes for gas and power cables. There are then four support struts, again made out of teflon, that connect the two end pieces. These supports act to reduce the strain on the alumina plates, and ensure there is no movement. The whole support structure is encapsulated by a glass tube with an 80 mm diameter.

Electrical system

Two sets of power supplies have been used for these experiments. One power supply is a neon sign power supply, that has its input voltage modulated by a variac. This is a relatively low power supply. It is also modulated by the mains frequency of 50 Hz.

The second power supply is a home built one, similar to that used in chapters eight and nine. To reiterate, this consists of an audio amplifier fed by a signal generator. The amplifier is connected to a step up transformer, which is connected to the plasma reactor.

Inlet system

A process diagram of the inlet system is presented in figure 9.2. Flow controllers (marked as FC) are rotameters made by Porter Instruments. Piping is all quarter inch, with Swagelok fittings. The oxygen and helium cylinders are both provided by BOC. The oxygen is 99.5 % purity, whilst the helium is 99.5 % purity. Regulators on both cylinders

Side on view:

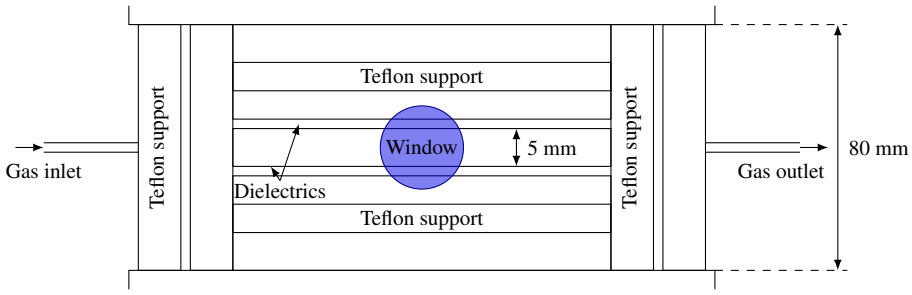

Top down view:

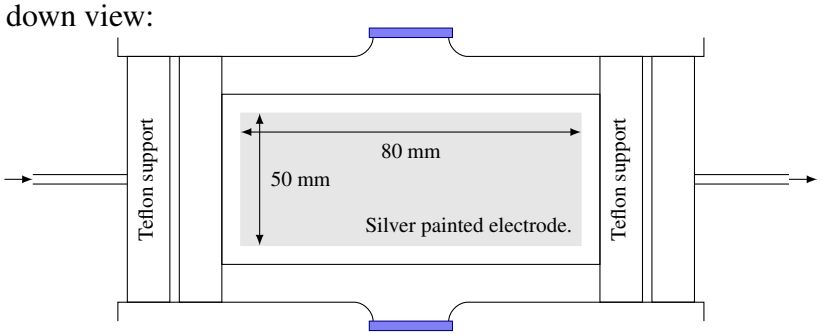

End on view:

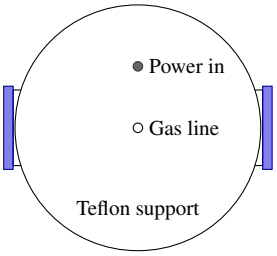

Figure 9.1: Plans of *in situ* spectroscopic reactor.

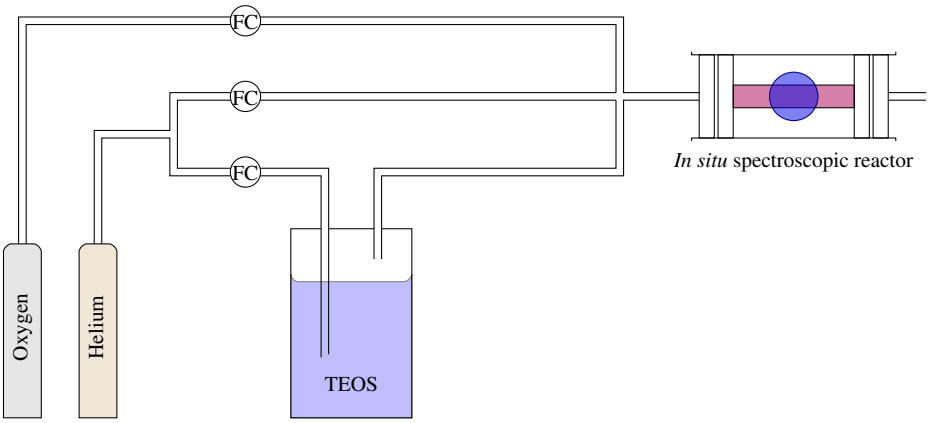

Figure 9.2: Process diagram of inlet system for *in situ* spectroscopic reactor.

are set to a pressure of one bar gauge.

Experimental design

Due to the different arrangement of the reactor and inlet system to those used in previous experiments, a different range of parameters to investigate were required. The flow rate was chosen so as to investigate the effect that residence time has on the chemistry. The oxygen concentration was examined, for similar reasons as outlined in the previous chapter on silica growth from TEOS, due to availability of flow meters however, a smaller range was chosen. Additionally, in order to investigate the chemistry occurring with no oxygen in the plasma, an oxygen concentration of zero was chosen as the low point. The voltage of the power supplied to the neon sign power supply was chosen, as this was the only way of controlling the power. The experimental design can be seen in figure 9.3, with the range of variables in table 9.1.

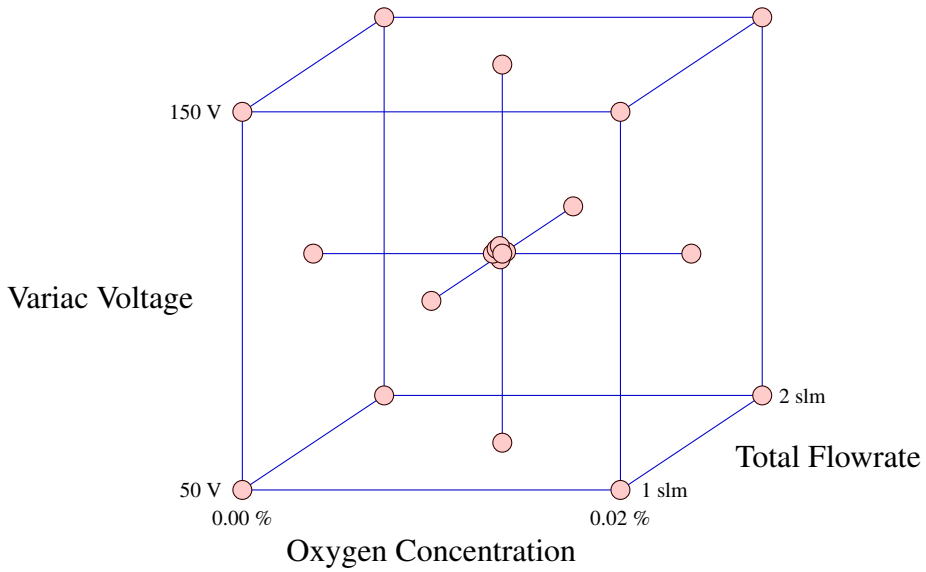

Figure 9.3: Central composite design for *in situ* investigation of TEOS decomposition in atmospheric helium plasma.

Coding	Variac Voltage (x_1) / V	Oxygen Concentration (x_2) / %	Total flow-rate (x_3) slm
-1	50	0.00	1.0
0	100	0.01	1.5
1	150	0.02	2.0

Table 9.1: Variables investigated for the *in situ* measurements of TEOS decomposition.

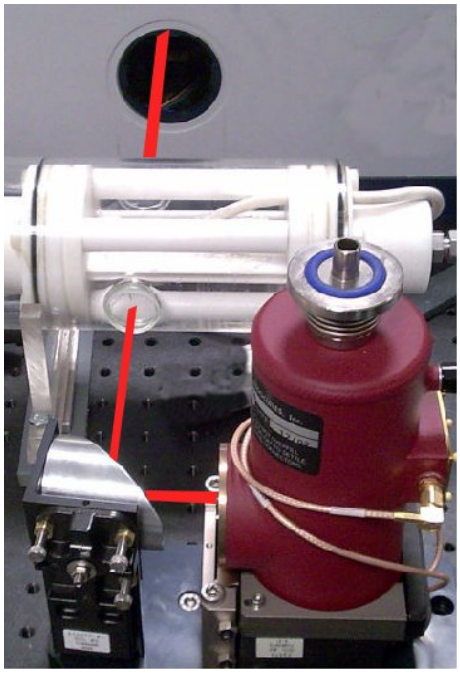

Figure 9.4: Photograph of the *in situ* reactor, with MCT detector in foreground. The red line indicates the path of the FTIR beam.

FTIR spectroscopy

The Bruker Equinox 55 FTIR spectrometer was used to make the following measurements. The FTIR beam was directed through the plasma, and detected with an external MCT detector. A photograph of the set up is presented in figure 9.4.

The resolution was set to 2 cm^{-1}, and measurements were taken over the spectral range of 400 to 4000 cm^{-1}.

Step Scan FTIR Spectroscopy

The step scan module for the Bruker Equinox 55 was used to further investigate the plasma chemistry. This module enables the chemistry to be investigated in time slices down to 5 μs. This enables the plasma chemistry to be investigated over the discharge cycle, with up to ten time slices being possible for a discharge frequency of 15 kHz.

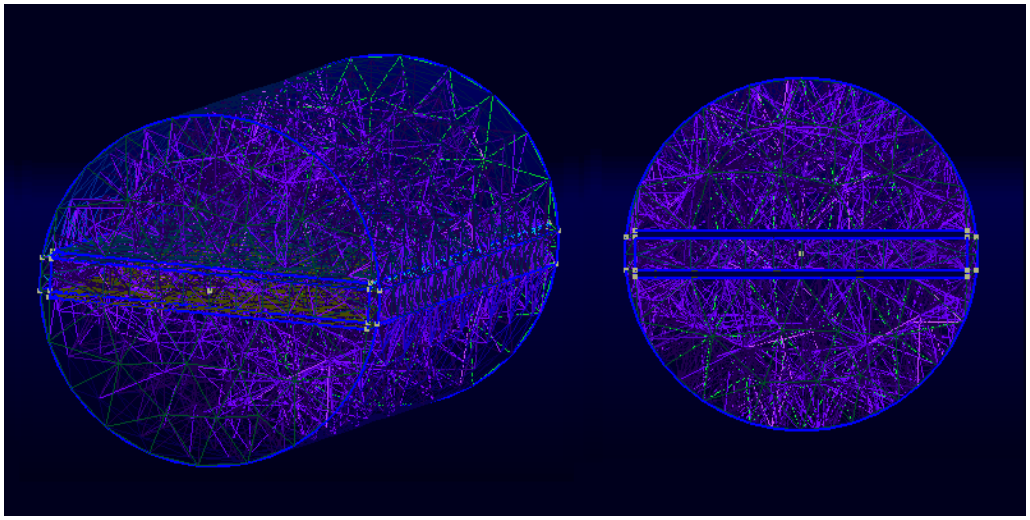

Figure 9.5: Views of the mesh used for computational fluid dynamic simulation of gas flow through reactor.

At present the neon sign power supply can not be used, as the step scan module requires a trigger to initiate the time resolved measurements. This is provided by the signal generator on the custom built power supply. The power supply is most stable at a frequency of around 15 kHz, allowing the plasma reactor to stay consistent over a long time scale. The time resolved measurements were taken at a resolution of 2 cm^{-1} over a spectral range of 400 to 4000 cm^{-1}.

9.3 Calibration of *in situ* spectroscopic reactor

CFD results

The first stage of a computational fluid dynamic model is to generate a mesh. The mesh of the spectroscopic reactor can be seen in figure 9.5. This was generated using the gmsh* program and has a characteristic length of 0.01 relative to the sizing.

The second stage was then to examine the velocity field within the reactor with helium

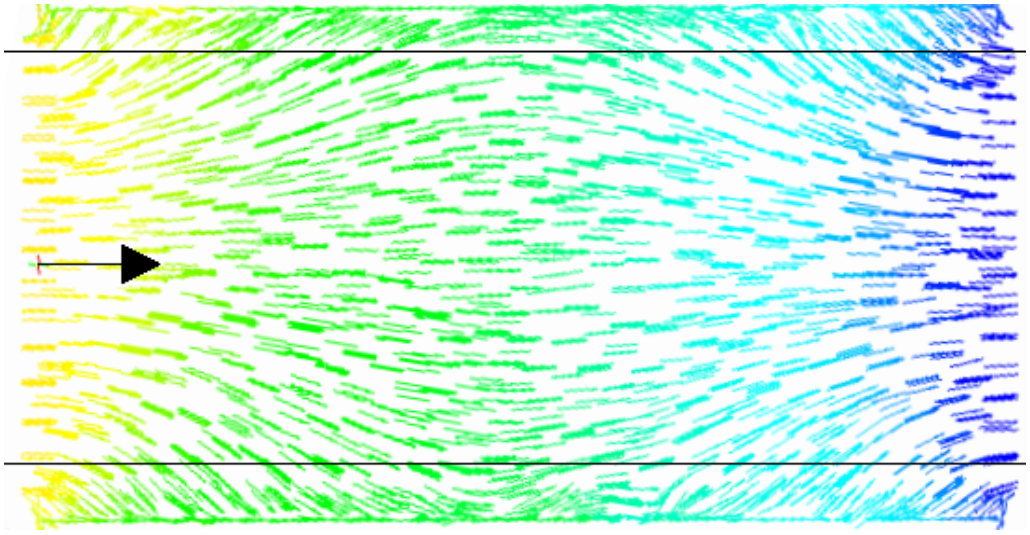

Figure 9.6: Result of computational fluid dynamic simulation of gas flow over the surface of the electrodes in the reactor. The arrow indicates direction of gas flow through the reactor.

flowing and no plasma initiated. The inlet flow was set at a reasonable value. The pressure at the inlet was set to 1 bar above atmospheric pressure, and was set to atmospheric pressure at the outlet. The velocity fields over the surface of the electrodes are described in figure 9.6. These indicate that the gas flows evenly through the plasma region, in a laminar type regime.

Electrical calibration

Some characterisation of the power supply was carried out before experiments were started. This was done by characterising the frequency response of the power supply circuit. Initially this was carried out across a resistive load of one mega Ohm. The power supply was connected across this load, and voltage measurements were taken on both the primary and secondary sides of the power supply so as to calculate the gain across the transformer. The frequency was increased incrementally, and measurements taken approximately every two kilohertz from ten to forty kilohertz. In addition, several readings were taken at higher frequencies.

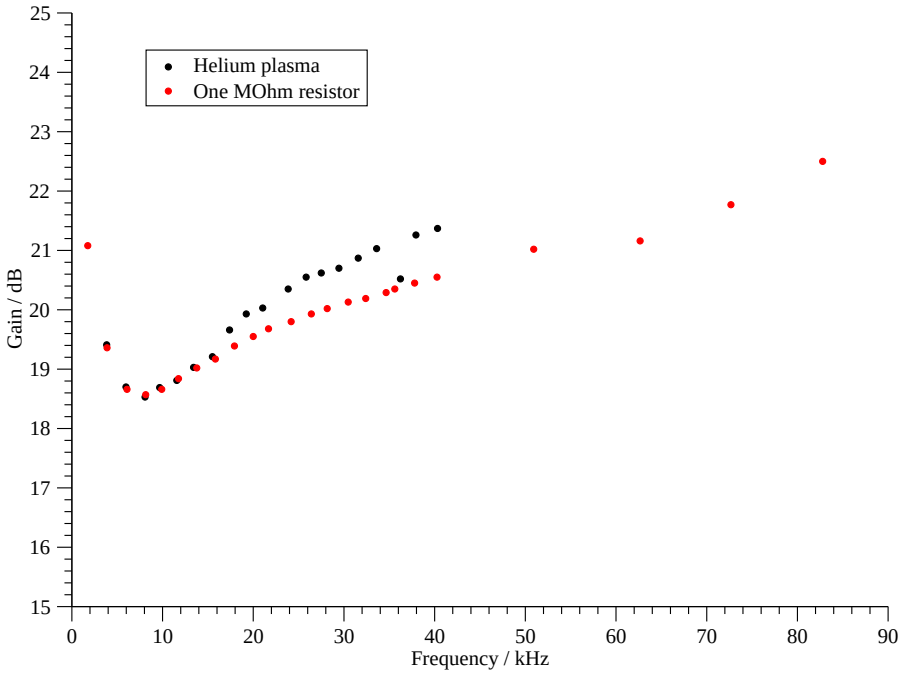

Figure 9.7: Gain against frequency for the *in situ* plasma reactor power supply across both a plasma and a dummy load.

The same procedure was carried out across the plasma reactor described in figure 9.1, striking a helium plasma. The power on the amplifier was increased until the point at which a plasma was struck, the voltage readings on the primary and secondary were then recorded. No readings were taken at frequencies higher than forty kilohertz due to excessive overheating of the audio amplifier. The comparison of the two situations are presented in figure 9.7.

It is evident from figure 9.7 that the transformer and power supply set up have a relatively flat response over a wide range of frequencies and loads. Therefore, it can be used to investigate a variety of conditions.

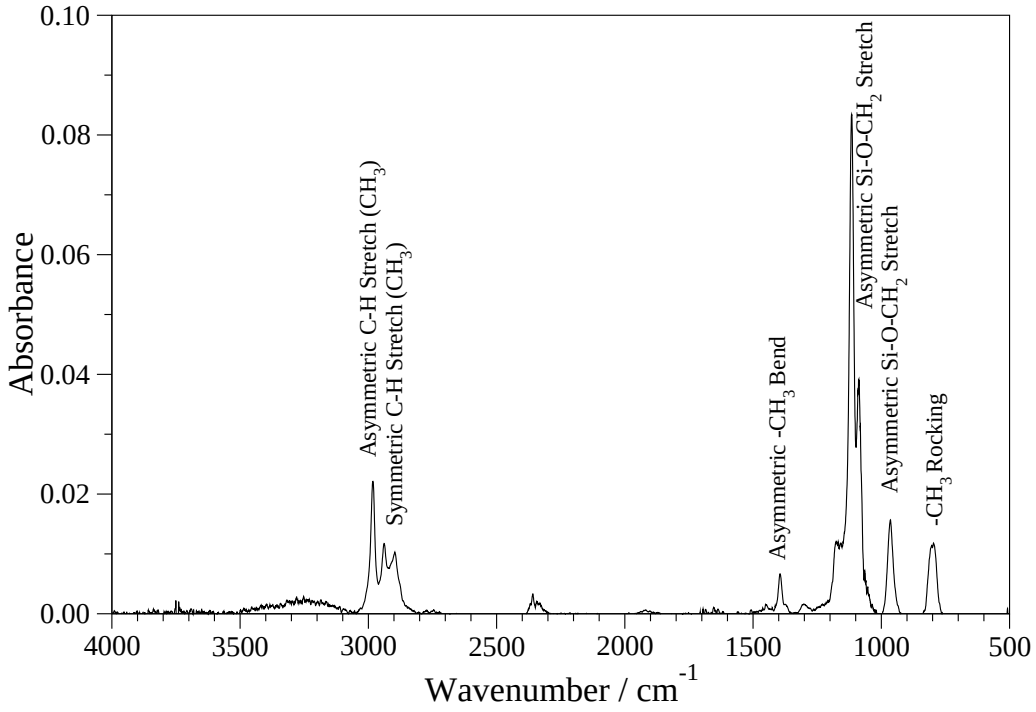

Figure 9.8: FTIR spectra of gases measured *in situ* in the plasma enhanced chemical vapour deposition reactor recorded at a resolution of 2 cm^{-1}. It represents 500 ppm of TEOS.

9.4 Results and Discussion

Spectroscopic Results

A spectrum of TEOS recorded *in situ* in the purpose built reactor can be seen in figure 9.8. The spectrum is similar to that seen in figure 7.8, with the same peaks. Figure 9.8 is presented to show the magnitude of absorbance through the reactor.

Figure 9.9 represents an FTIR spectrum recorded of a helium plasma containing 500 ppm TEOS and 500 ppm oxygen at the inlet. This is a typical FTIR spectrum of a plasma containing both TEOS and oxygen, with only intensities of various peaks changing with varying conditions. Key breakdown products and intermediaries have been identified and labelled on figure 9.9. The same species as reported in figure 7.9 can be seen, validating

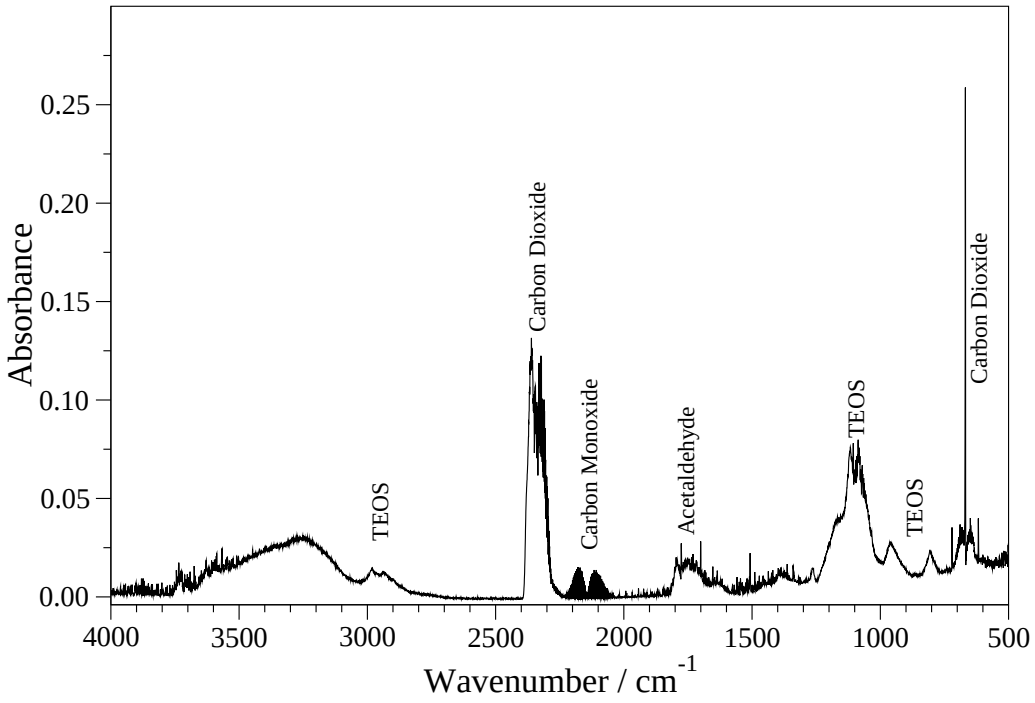

Figure 9.9: FTIR spectra of plasma measured *in situ* in the plasma enhanced chemical vapour deposition reactor recorded at a resolution of 2 cm^{-1}. The primarily helium plasma contains 500 ppm of TEOS and 0.02 % of oxygen. Chemical species are labelled.

the reactions postulated in equations 7.2 and 7.3. Ozone is active in the infrared region, however, it's characteristic stretches overlap with those of TEOS, and so it cannot be readily identified in figure 9.9.

As mentioned in the experimental design portion of the methodology of this chapter, several of the experiments had no added oxygen. The FTIR spectrum for one of these experiments can be seen in figure 9.10, which is the FTIR spectrum recorded of the plasma generated at experimental conditions of low oxygen and flow-rate and high variac voltage. A clear by-product of the process is methane, which was also seen down stream of the reactor in preliminary work that has been carried out, [237]. Minimal carbon dioxide is present, due to the oxygen poor atmosphere of the reactor. A large amount of carbon monoxide is generated however.

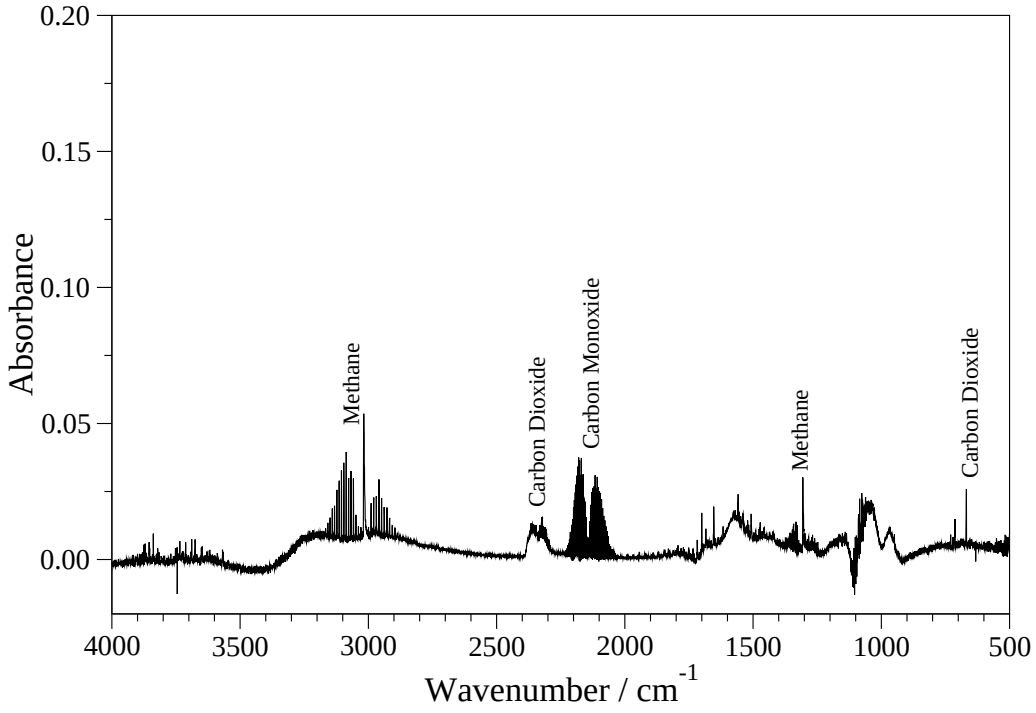

Figure 9.10: FTIR spectra of plasma measured *in situ* in the plasma enhanced chemical vapour deposition reactor recorded at a resolution of 2 cm^{-1}. The primarily helium plasma contains 500 ppm of TEOS and no oxygen. Chemical species are labelled.

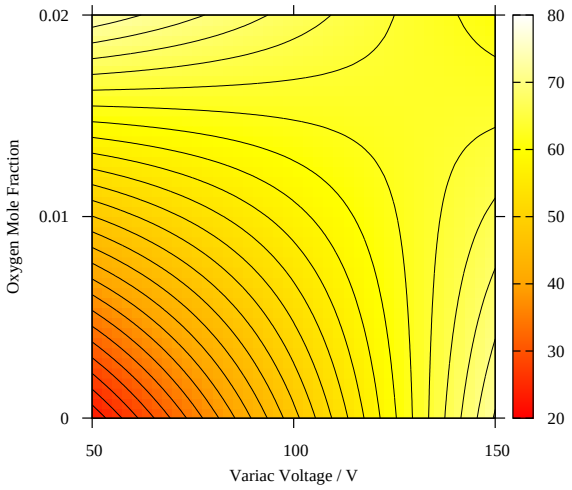

Figure 9.11: Response surface for carbon monoxide formation (in parts per million). Flow rate fixed at 1.5 slm.

In order for methane to be generated the carbon to carbon bond within the TEOS ethyl groups has to break, leaving a CH_3 radical which scavenges a hydrogen from the remaining fragment of the ethyl group. The oxygen to silicon bond connecting this fragment to the remainder of the TEOS molecule would also have to break, with the remaining hydrogen joining with the silicon atom to form triethoxysilane.

Response Surfaces

As in previous chapters the calculated concentrations of the different species were fitted to statistical models. These are now presented. Figures 9.11 to 9.13 represent the response surfaces generated from the statistical model for carbon monoxide generation in the plasma. The F-test result for the carbon monoxide model is 99.96 %.

The response surface in figure 9.11 is for carbon monoxide at a fixed flow rate. This

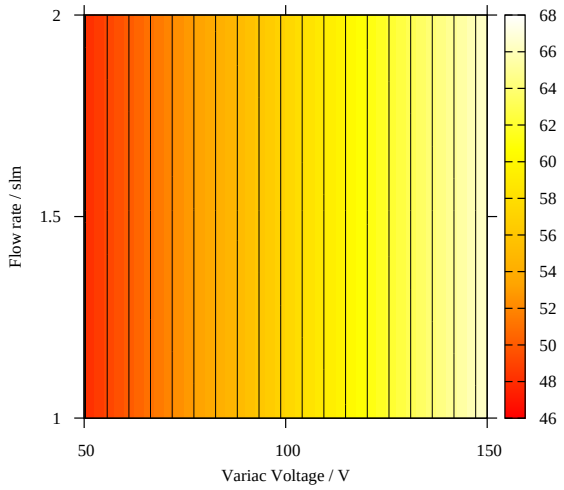

Figure 9.12: Response surface for carbon monoxide formation (in parts per million). Oxygen mole fraction fixed at 0.01.

indicates an increase in carbon monoxide formation with increasing oxygen, which is an intuitive result as more oxygen is present to form carbon monoxide. The formation also increases with voltage, again this is an intuitive result, as there is more energy in the plasma to initiate the reactions that lead to carbon monoxide formation.

Figure 9.12 is the response surface for a fixed oxygen concentration. It indicates that the flow rate has little to no effect on the carbon monoxide formation, which would indicate a relatively high reaction rate of carbon monoxide formation. The voltage shows a similar effect as previously highlighted.

The fixed voltage response surface for carbon monoxide formation is presented in figure 9.13. The flow rate has some effect, but it is combined with the oxygen concentration. This is further supporting evidence for a high reaction rate. The oxygen concentration has more effect with increasing flow rate.

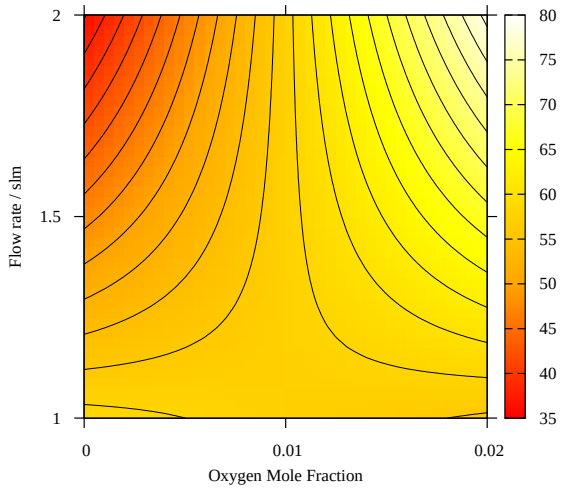

Figure 9.13: Response surface for carbon monoxide formation (in parts per million). Variac voltage fixed at 100 V.

The carbon dioxide response surfaces are presented in figures 9.14 to 9.16. The F-test result for this model was 99.85 %.

Presented in figure 9.14 is the carbon dioxide response surface at a fixed flow rate. The combination of increasing both the oxygen concentration and the voltage tends to maximise the carbon dioxide production in this case. This will be for similar reasons as outlined for the carbon monoxide above.

The response surface for carbon dioxide formation at a fixed oxygen concentration is presented in figure 9.15. There is some effect of the flow rate decreasing the carbon dioxide formation, and this is due to the high flow rate taking carbon dioxide forming species out of the reactive zone. The increase of formation with voltage, is due to the higher density of plasma species at higher powers.

Figure 9.16 is the fixed voltage response surface for carbon dioxide formation. As

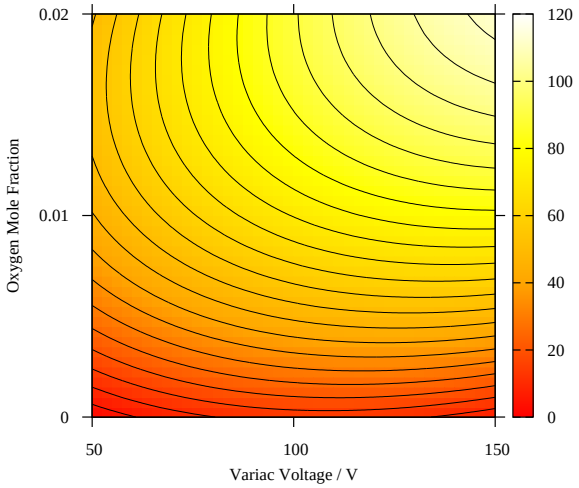

Figure 9.14: Response surface for carbon dioxide formation (in parts per million). Flow rate fixed at 1.5 slm.

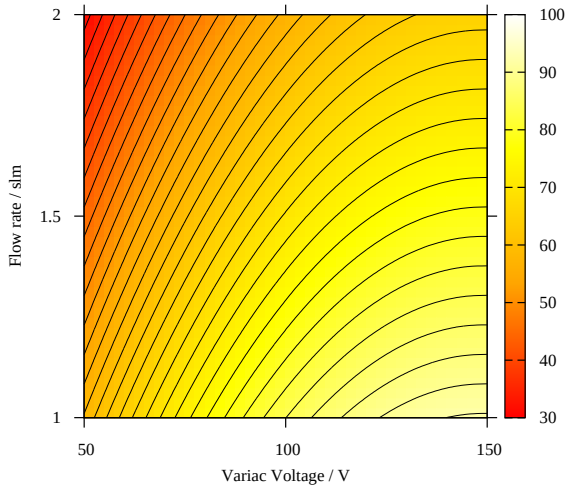

Figure 9.15: Response surface for carbon dioxide formation (in parts per million). Oxygen mole fraction fixed at 0.01.

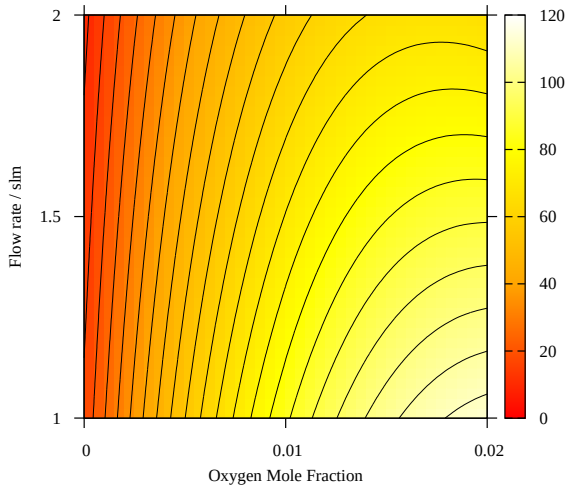

Figure 9.16: Response surface for carbon dioxide formation (in parts per million). Variac voltage fixed at 100 V.

expected, increasing the oxygen concentration increases the carbon dioxide formation. The formation is also rather insensitive to the flow rate in this instance, and this is likely due to the fast rate of carbon dioxide formation.

Due to the acetaldehyde peaks merging with other, unknown peaks on the FTIR spectra, it is not possible to form a chemometric model for the acetaldehyde formation. In addition water present in the atmosphere also obscures other smaller acetaldehyde peaks. Analysis shows that the replicate error is too great in this case, and F-test results much less than the required 95 % confidence level are returned. Therefore any response surfaces generated would not be conducive to further analysis.

Response surfaces for the methane production in the plasma are shown in figures 9.17 to 9.19. The F-test result for the chemometric model that produced these response surfaces is 99.7 %. There is no methane formation at higher oxygen concentrations, but

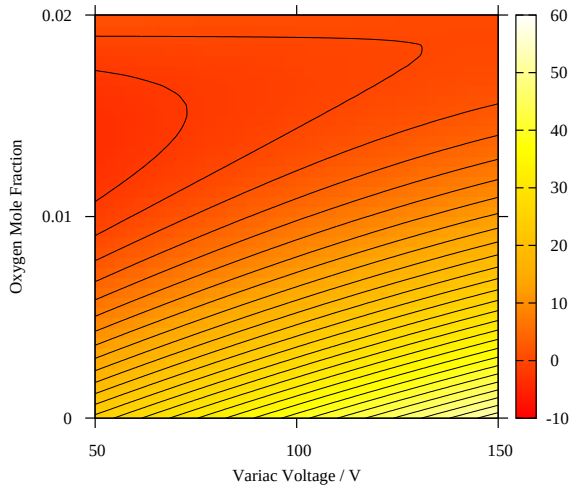

Figure 9.17: Response surface for methane formation (in parts per million). Flow rate fixed at 1.5 slm.

as the model is a second order polynomial this comes across as a negative concentration on the response surfaces.

The methane formation response surface for a fixed flow rate can be seen in figure 9.17. The voltage increases the formation of methane, as more TEOS molecules are broken down in the more chemically active plasmas produced at higher powers. Increasing the oxygen concentration reduces the methane formation as the methane has a tendency to undergo combustion reactions as it forms, subsequently forming carbon monoxide and carbon dioxide instead.

The response surface for methane formation at a fixed oxygen mole fraction of zero is presented in figure 9.18. The voltage has the strongest effect upon the carbon dioxide formation, indicating that the plasma has more reactive species at higher voltages. The flow rate increasing tends to decrease the methane formation, as there is less time for the

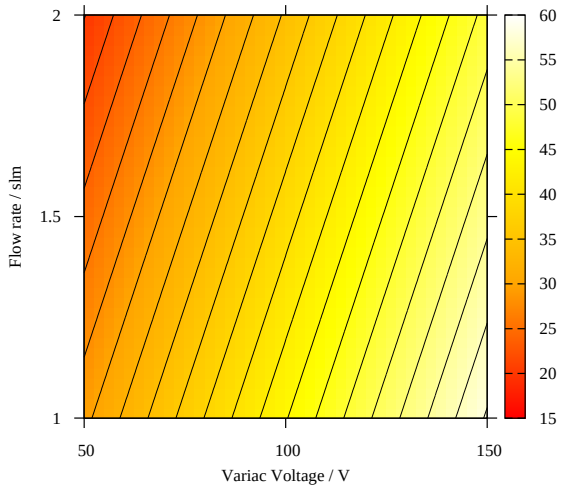

Figure 9.18: Response surface for methane formation (in parts per million). Oxygen mole fraction fixed at zero.

reaction to occur in the plasma.

The final response surface for methane formation is presented in figure 9.19, and this is calculated at a fixed voltage. The oxygen concentration has the strongest effect on the methane formation, with the highest formation occurring when there is no oxygen present. The effect of the flow rate is small compared to the oxygen concentration.

These results have shown the advantages of measuring the chemical species generated *in situ* in the plasma. In conjunction with the response surfaces, they allow for investigation of the chemistry occurring as it occurs.

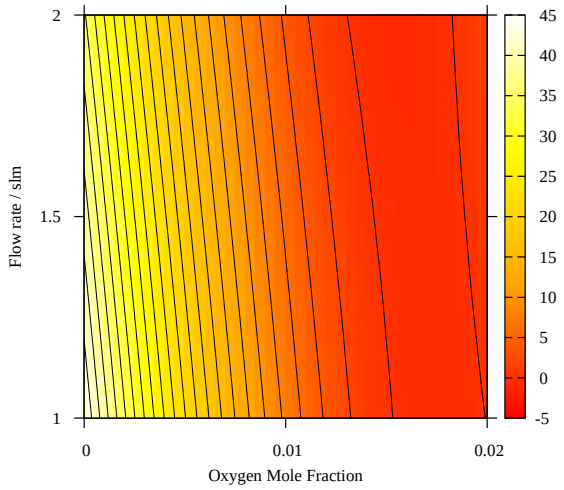

Figure 9.19: Response surface for methane formation (in parts per million). Variac voltage fixed at 100 V.

Power Results

The power supplied to the plasma differs with the neon sign power supply. It comes in the form of pulsed audio frequency alternating current. This is shown in figure 9.20.

The power response surfaces are presented in figures 9.21 to 9.23. The overall powers are less than in previous experiments, and this is due to the different power supply and smaller reactor being used. The F-test result for the statistical model is 99.22 %.

The response surface shown in figure 9.21 shows the power with the flow rate fixed at 1.5 s.lm. Voltage has the most effect on the power in the plasma, as would be expected. The oxygen concentration shows a much smaller variation, and this is due to the plasma conditions not changing greatly with the amount of oxygen being added.

Figure 9.22 represents the power response surface at a fixed oxygen concentration.

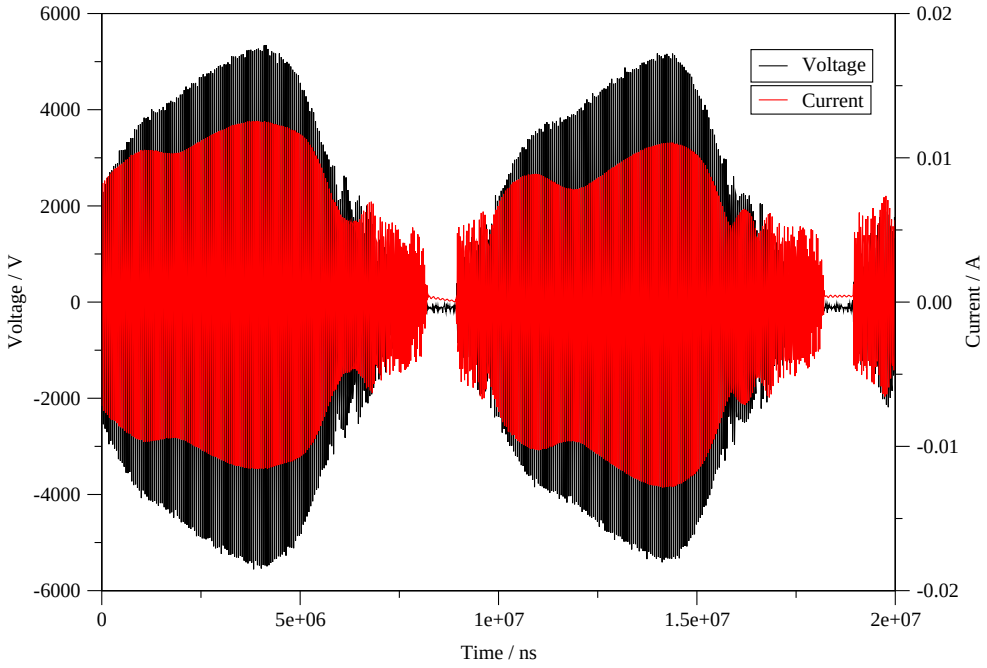

Figure 9.20: Current and voltage readings from the power supply circuit. Experimental conditions were 100 volts on the variac, 0.01 oxygen and a flow rate of 2 slm.

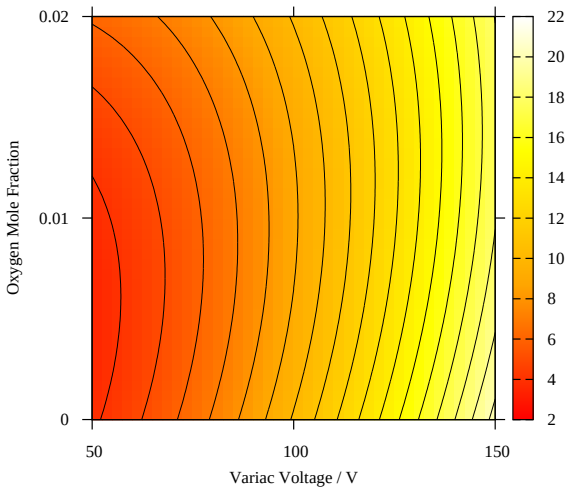

Figure 9.21: Response surface for power (in watts). Flow rate fixed at 1.5 slm.

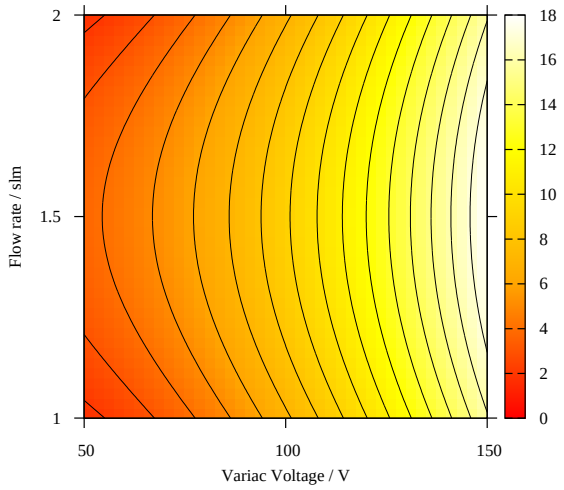

Figure 9.22: Response surface for power (in watts). Oxygen concentration fixed at 0.01 %.

Again the voltage is the most significant factor, with the flow rate being slightly more significant than the oxygen concentration was in figure 9.21. This indicates that the load on the power supply does not increase significantly with relatively small increases in flow rate.

The fixed voltage response surface is shown in figure 9.23. This response surface allows for a better examination of the effects of the flow rate and the oxygen concentration on the power. The flow rate has a squared effect on the power, with the maximum value coming at 1.5 slm. The oxygen concentration also has a squared effect on the power, but there is a minimum power at a mole fraction of 0.01.

Number	Experiment number	Variac voltage	Oxygen concentration	Flow-rate
		x_1	x_2	x_3
1	9	-1	-1	-1
2	2	-1	-1	1
3	19	-1	0	0
4	15	-1	1	-1
5	4	-1	1	1
6	17	0	-1	0
7	7	0	0	-1
8	5	0	0	0
9	10	0	0	0
10	11	0	0	0
11	14	0	0	0
12	16	0	0	0
13	20	0	0	0
14	1	0	0	1
15	18	0	1	0
16	6	1	-1	-1
17	13	1	-1	1
18	8	1	0	0
19	12	1	1	-1
20	3	1	1	1

Table 9.2: Experimental labels for subsequent principal component analysis.

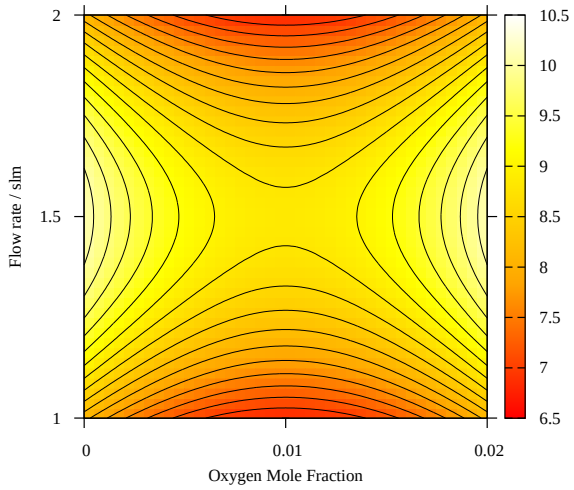

Figure 9.23: Response surface for power (in watts). Voltage fixed at 100 V.

Principal Components Analysis

Principal components analysis was carried out on the FTIR spectroscopy data, which was standardised before this occurred. Table 9.2 provides the labels for the scores plots. The eigenvalues are presented in figure 9.3, which shows that 95 % of the data is modelled by the first four principal components. Experimental labels are provided in table 9.2. The scores plots can be seen in figures 9.24, 9.27 and 9.29. The loadings plots for the first four principal components of this dataset are presented in figures 9.25, 9.26, 9.28 and 9.30.

The scores plot for principal components one and two in figure 9.24 shows no clear features, but still exhibits some close clustering, and this is comparable to that seen in figure 7.39. The loadings plot for principal component one in figure 9.25 shows that principal component one predominently models the carbon dioxide produced in the reactor. In contrast, the loadings plot for principal component two, figure 9.26, shows that principal component two models the TEOS being used up within the reactor. The variation

Principal component	Eigenvalue	Percentage modelled	Cumulative percentage
1	6.88	54.89	54.89
2	3.65	29.10	84.00
3	1.06	8.43	92.43
4	0.33	2.61	95.04
5	0.14	1.15	96.19
6	0.14	1.11	97.30
7	0.14	1.09	98.39
8	0.04	0.29	98.68
9	0.03	0.20	98.88
10	0.04	0.36	99.24

Table 9.3: Eigenvalues and percentage modelled of the first ten principal components of the FTIR data.

in principal component one seems to be related to the amount of oxygen in the process, which was shown to be linked to the carbon dioxide produced in the response surfaces. Overall, the dataset is distributed over the scores plot.

The scores plot for principal components two and three is shown in figure 9.27, whilst the loadings plot for principal component three is presented in figure 9.28. The loadings plot shows that principal component three models the infra-red peaks associated with methane, acetaldehyde and water. However, the water could be as a result of atmospheric water. Experiment two is a clear outlier in principal component three, and this is an experiment carried out with no oxygen, producing methane as a by-product.

Finally, the scores plot for principal components three and four is presented in figure 9.29, and the loadings plot for principal component four in figure 9.30. Principal component four models similar species to principal component three, these being methane, carbon dioxide and water. There is no strongly pronounced clustering in terms of principal component four.

The *in situ* results were also combined with the downstream FTIR measurements made for the work presented in chapter seven. The eigenvalues for the subsequent principal

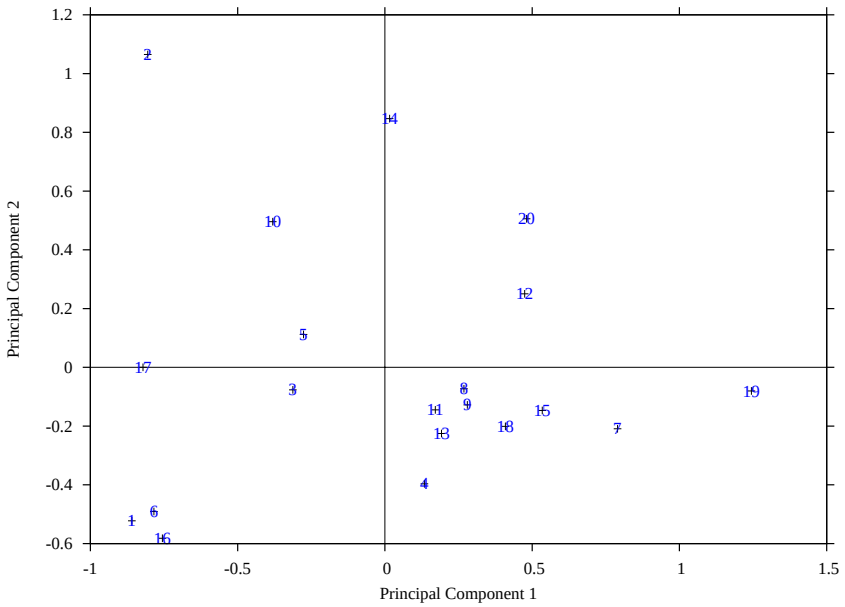

Figure 9.24: Principal component scores plot for principal components one and two of the FTIR spectroscopy data. The data matrix was standardised.

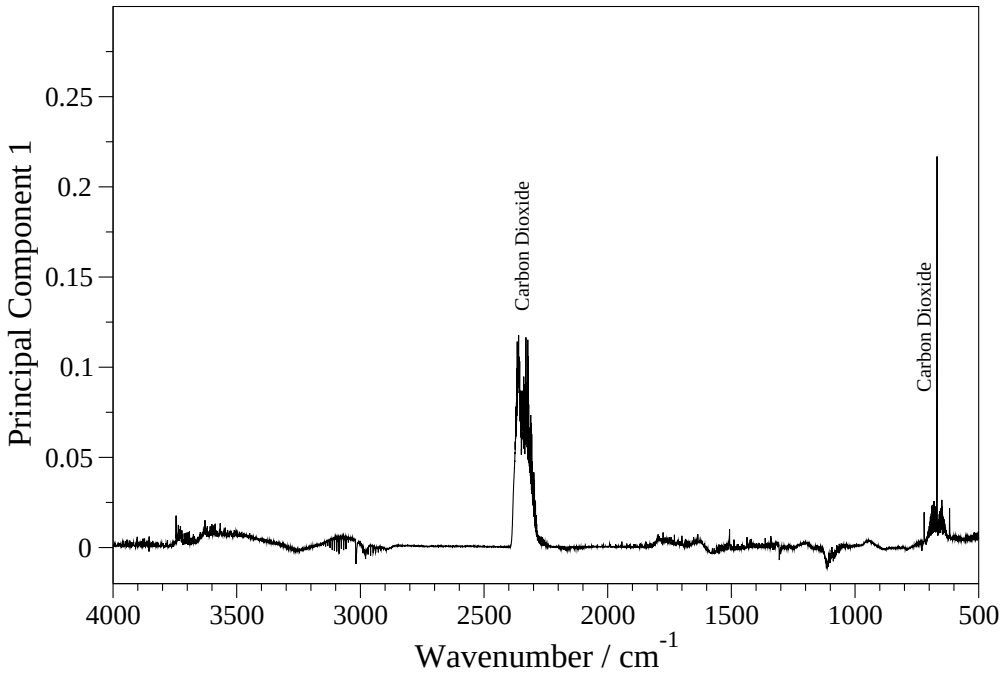

Figure 9.25: Principal component loadings plot for principal component one of the FTIR spectroscopy data. The data matrix was standardised.

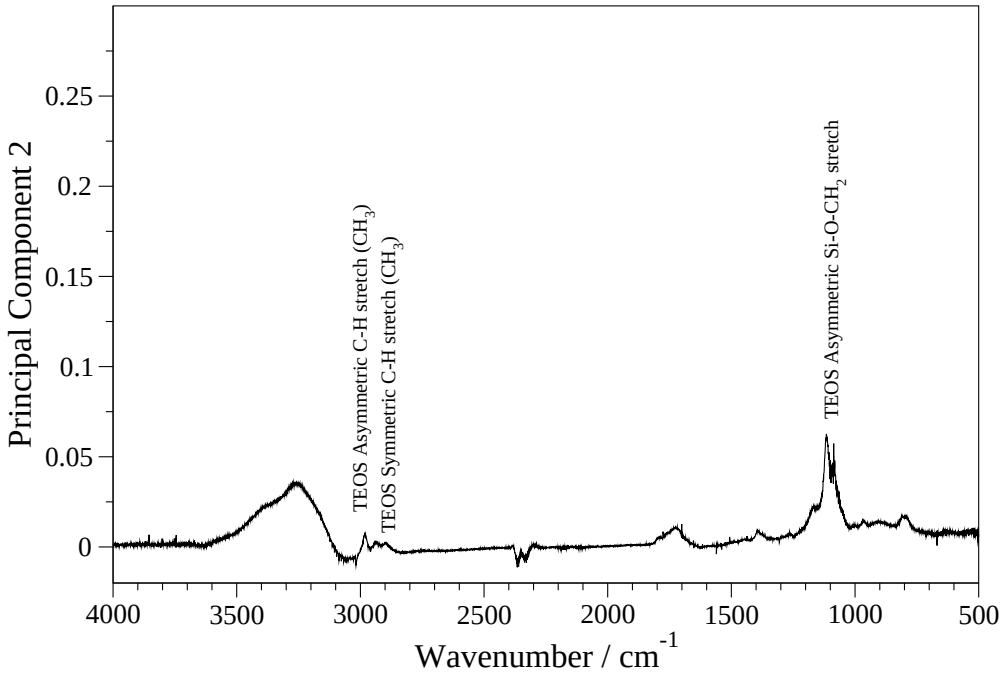

Figure 9.26: Principal component loadings plot for principal component two of the FTIR spectroscopy data. The data matrix was standardised.

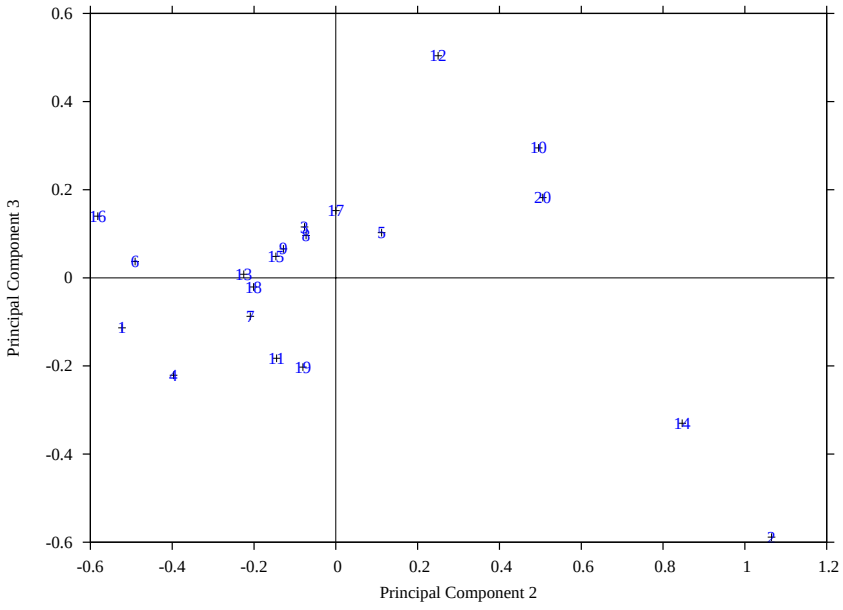

Figure 9.27: Principal component scores plot for principal components two and three of the FTIR spectroscopy data. The data matrix was standardised.

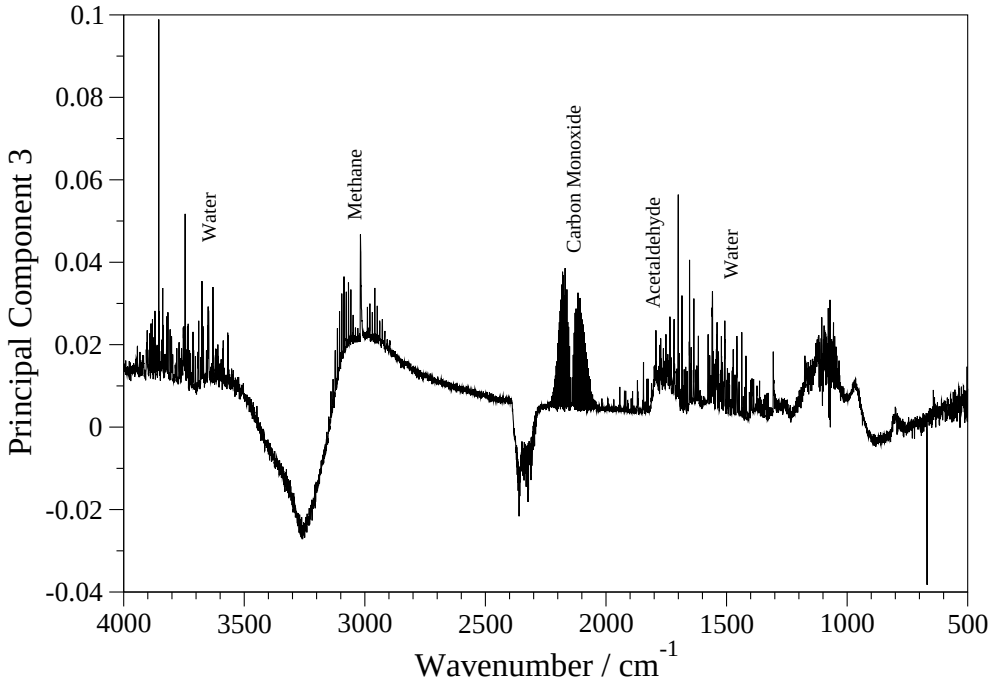

Figure 9.28: Principal component loadings plot for principal component three of the FTIR spectroscopy data. The data matrix was standardised.

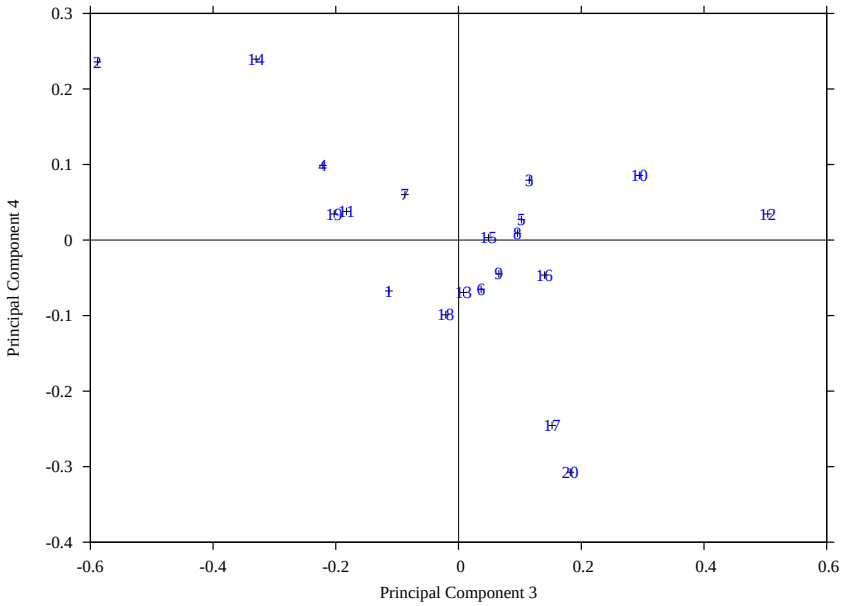

Figure 9.29: Principal component scores plot for principal components three and four of the FTIR spectroscopy data. The data matrix was standardised.

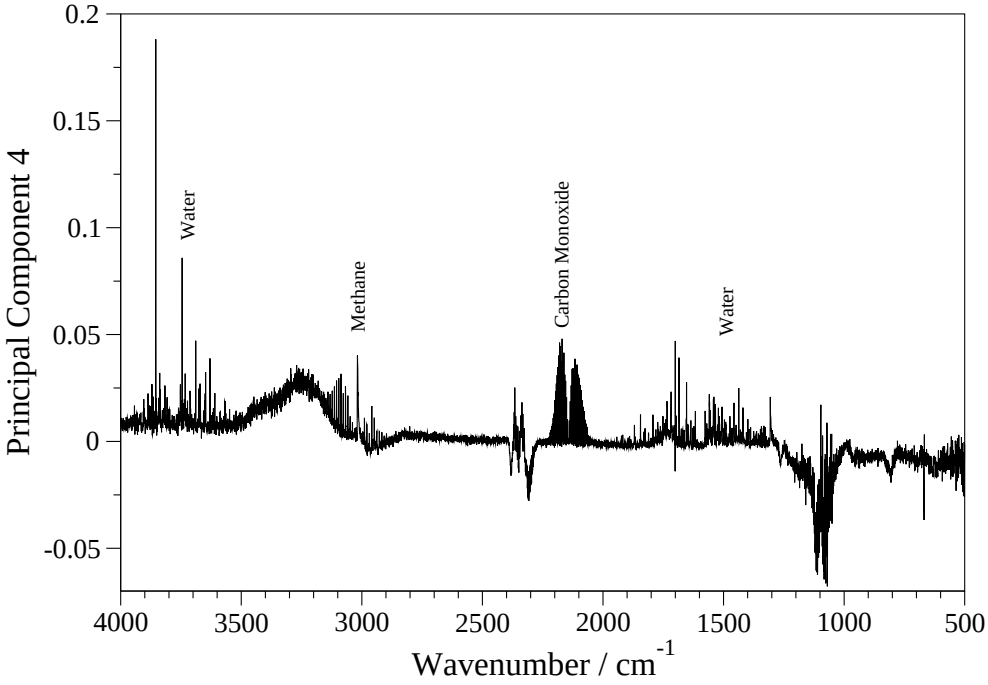

Figure 9.30: Principal component loadings plot for principal component four of the FTIR spectroscopy data. The data matrix was standardised.

components analysis is presented in table 9.4. The first four principal components govern over 90 % of the dataset.

Figure 9.31 shows the scores plot for the principal components one and two from principal component analysis carried out on both the FTIR data for the downstream measurements made in chapter eight and the *in situ* measurements collectively. There are two distinct clusters of data above and below the x-axis, that correspond to the *in situ* and downstream measurements respectively. The scores of the *in situ* measurements show closer clustering than the downstream measurements, this is likely due to the differing process variables that have been investigated in both sets of results, as well as the different reactor set ups that have been used. The loadings plots for principal components one and two are presented in figures 9.32 and 9.33 respectively. Principal component one models the carbon monoxide, carbon dioxide and acetaldehyde by-products of the process. Principal component two models the TEOS and acetaldehyde peaks.

Principal component	Eigenvalue	Percentage modelled	Cumulative percentage
1	794.17	51.16	51.16
2	466.43	30.05	81.21
3	129.99	8.37	89.58
4	38.73	2.49	92.07
5	34.47	2.22	94.29
6	12.25	0.79	95.08
7	8.03	0.52	95.60
8	7.61	0.49	96.09
9	12.43	0.80	96.89
10	3.73	0.24	97.13

Table 9.4: Eigenvalues and percentage modelled of the first ten principal components of the FTIR data for both the *in situ* and *ex situ* TEOS based experiments.

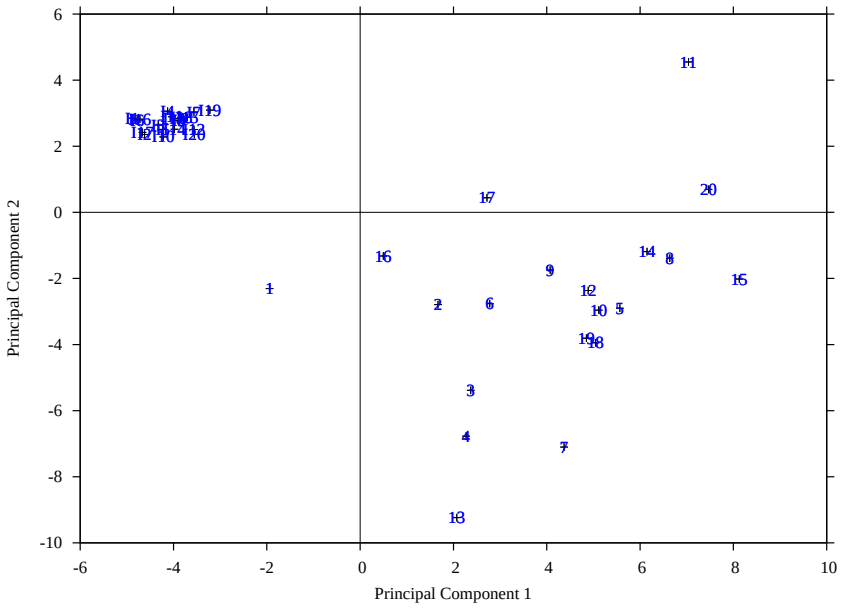

Figure 9.31: Principal component scores plot for principal components one and two of the FTIR spectroscopy data from both downstream (data from chapter eight) and *in situ* measurements. The data matrix was standardised. *In situ* experiments are labelled "I" on the figure.

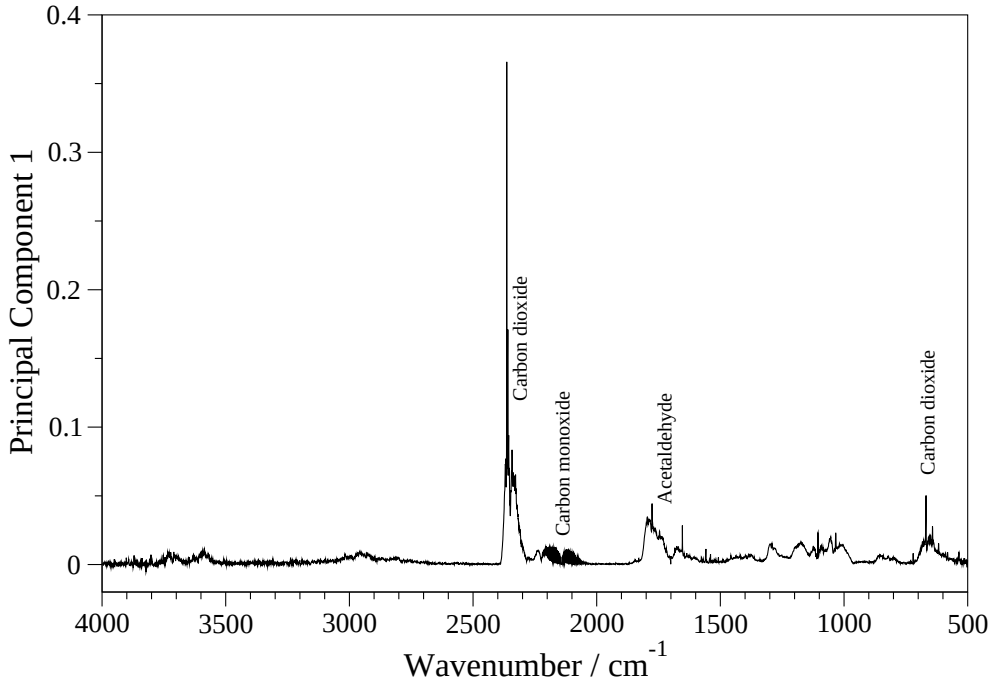

Figure 9.32: Principal component loadings plot for principal component one of the combined FTIR spectroscopy data. The data matrix was standardised.

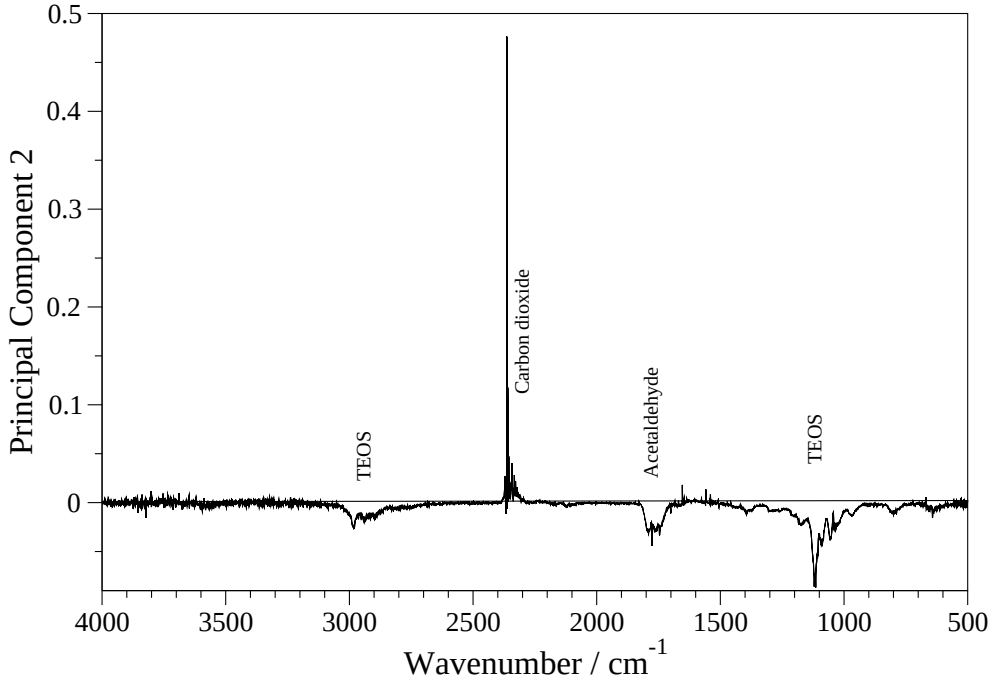

Figure 9.33: Principal component loadings plot for principal component two of the combined FTIR spectroscopy data. The data matrix was standardised.

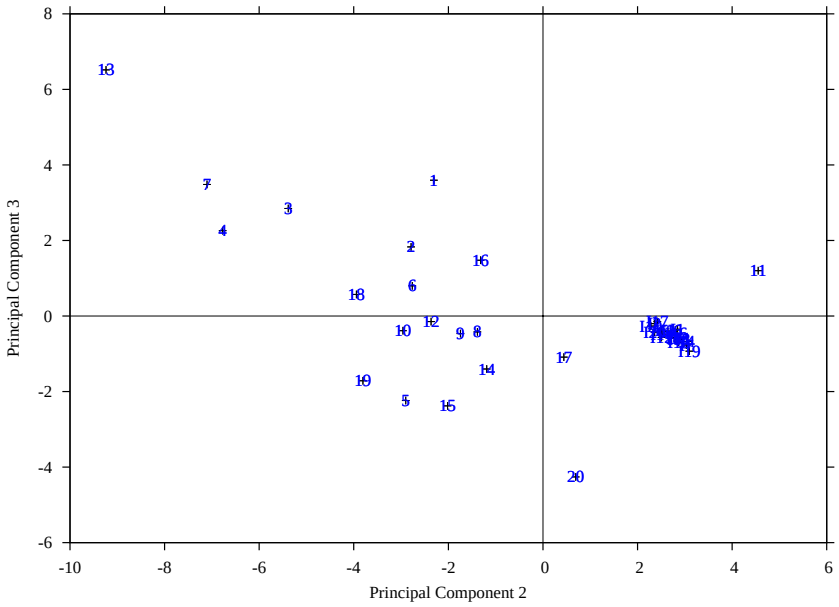

Figure 9.34: Principal component scores plot for principal components two and three of the FTIR spectroscopy data from both downstream (data from chapter eight) and *in situ* measurements. The data matrix was standardised. *In situ* experiments are labelled "I" on the figure.

Figure 9.34 represents the scores plot for principal components two and three, the loadings plot for principal component three is presented in figure 9.35. Principal component three models the TEOS peaks. Again, the close clustering of the *in situ* experiments can be seen, which is opposite to the downstream produced results.

The final scores plot, for principal components three and four, is presented in figure 9.36, whilst the loading plot for principal component four is presented in figure 9.37. The ozone peak at 1100 cm^{-1} is modelled by principal component four. This peak is clearly common to all the experiments within the principal components analysis, as they are all clustered in terms of principal component four. This is apart from experiment fifteen of the dataset presented in chapter seven. This experiment was run at high oxygen concentration, indicating the greater formation of ozone this peak represents at higher oxygen concentrations.

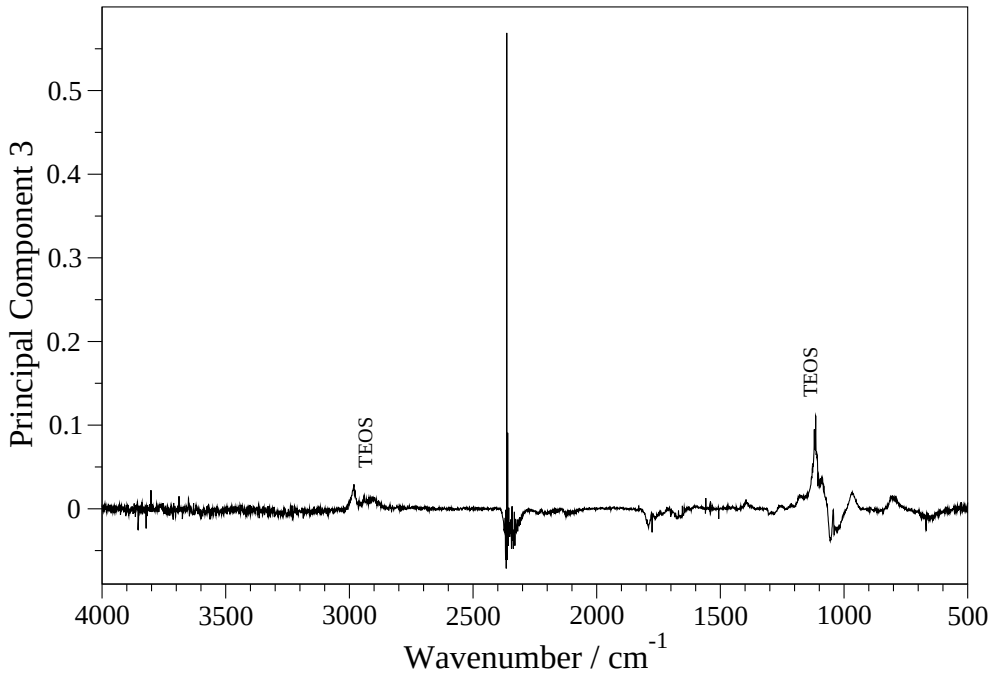

Figure 9.35: Principal component loadings plot for principal component three of the combined FTIR spectroscopy data. The data matrix was standardised.

Time Resolved FTIR Spectroscopy

Presented in figure 9.38 is a series of time resolved FTIR spectra for a helium plasma containing 0.02 % oxygen. The driving frequency for the plasma was 15 kHz. The infrared spectrum of ozone shows peaks at about 1200 cm^{-1}, and at around 2000 cm^{-1}. T his standard spectra for ozone can be seen in figure 9.39. Figure 9.38 shows slight rises in the baseline at these points, but this implies that the concentration of ozone generated is quite low. The formation of ozone at specific points in the plasma cycle has implications on the deposition of silica films by plasma enhanced chemical vapour deposition, as it has been shown that this is an important species in the process.

Figure 9.40 is a series of time resolved FTIR spectra for a helium plasma containing 1000 ppm TEOS and 0.02 % oxygen. The driving frequency for the plasma was 15 kHz, with only half the cycle being recorded. There is a peak at 2400 cm^{-1} and at 5

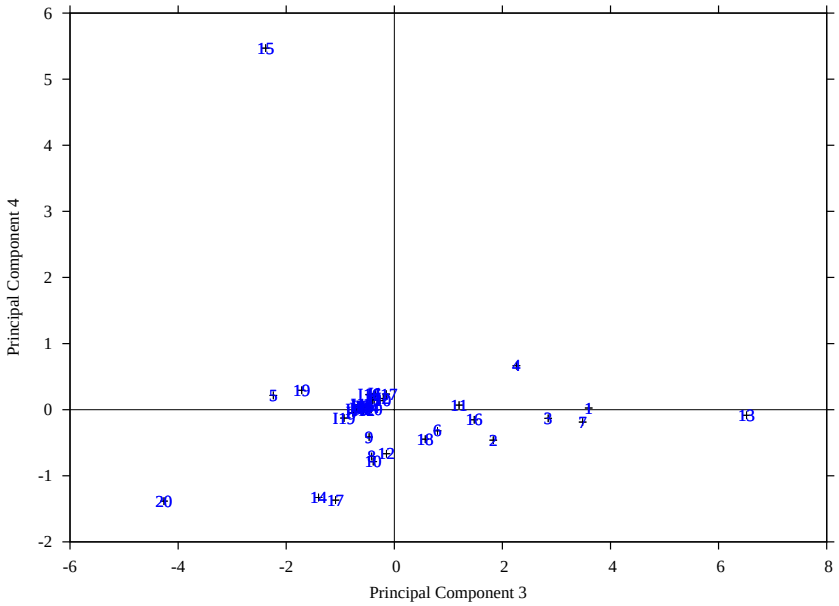

Figure 9.36: Principal component scores plot for principal components three and four of the FTIR spectroscopy data from both downstream (data from chapter eight) and *in situ* measurements. The data matrix was standardised. *In situ* experiments are labelled ”I” on the figure.

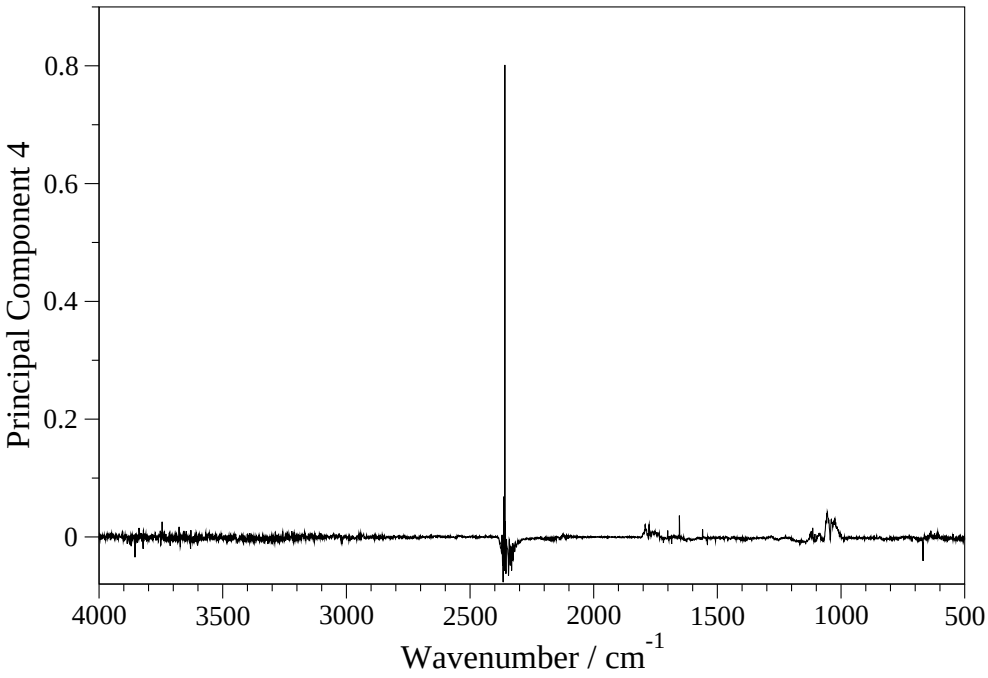

Figure 9.37: Principal component loadings plot for principal component four of the combined FTIR spectroscopy data. The data matrix was standardised.

μs and then a subsequent smaller peak at 20 μs that could correspond to carbon dioxide formation within the discharge cycle. There are also peaks that occur twice at about 3250 cm^{-1}, which don't correspond to anything in figure 9.9, and so bear further investigation.

9.5 Conclusions

The use of *in situ* FTIR has lead to further understanding of the chemistry of silica deposition from TEOS in a plasma environment, thus meeting the primary aim of this work. The construction of a plasma reactor suitable for these measurements has also been carried out. In addition the chemometric methodology has been suitably extended, with the *in situ* FTIR results forming part of an increased dataset concerning this process. This is also the first time that methane has been observed being produced in the absence of oxygen in this process.

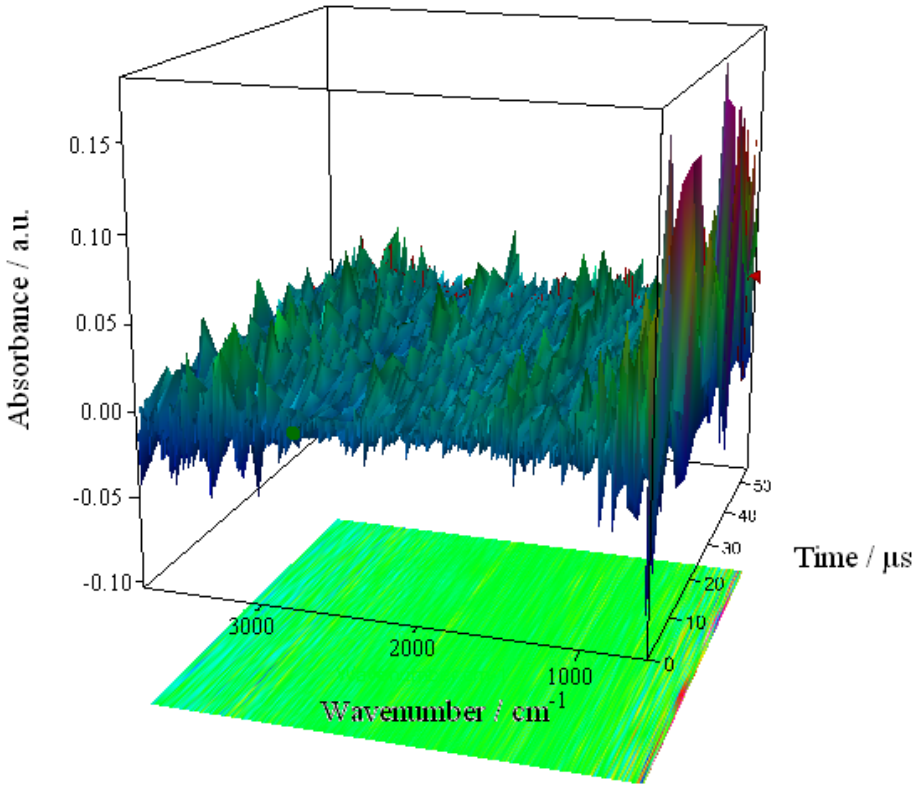

Figure 9.38: Time resolved FTIR spectra of 0.02 % oxygen in a helium plasma.

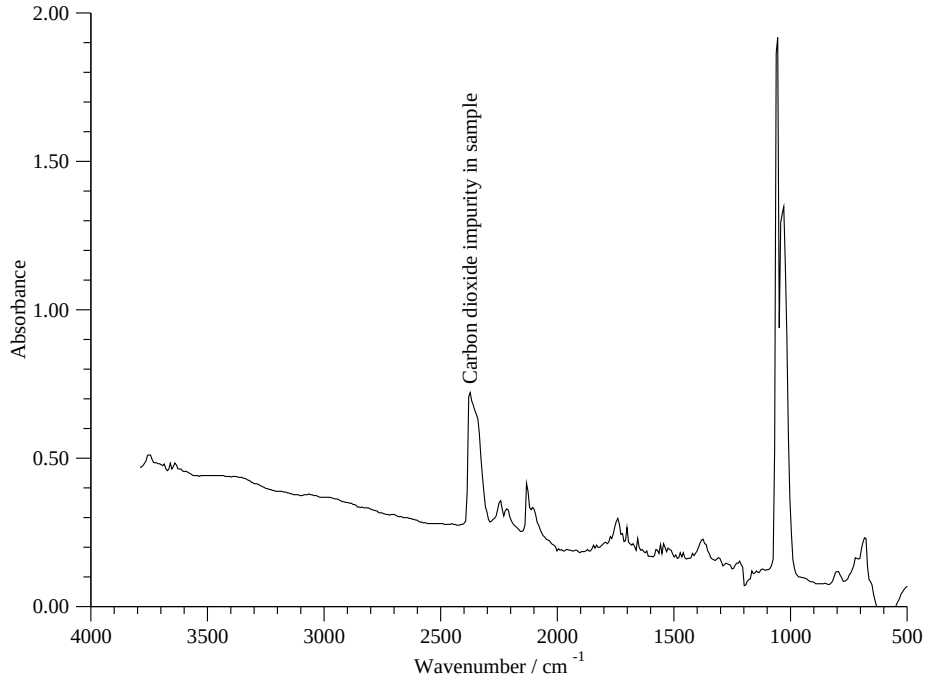

Figure 9.39: Standard infra red spectra of ozone, data from The Coblentz Society, [6].

The response surfaces have again proved useful in the characterisation of this process. They give a good representation of the effects of the process variables studied. In addition the statistical analysis helps to back the validity of this approach. The analysis of the methane response surfaces shows the strong effect of oxygen on the process, and how it breaks down the TEOS molecule.

Principal components analysis has proved useful in corroborating the important break down products from the process. The combined principal components analysis has also proved useful in characterising the measurements as either *in situ* or downstream of the process. This would indicate that there is further work to be done in trying to measure species in the plasma that are not present downstream. The further appearance of the ozone spectral feature at 1100 cm^{-1} further emphasises the importance of active oxygen species in the chemistry of silica deposition processes in plasma.

Time resolved spectroscopy is a promising technique for analysing the time depen-

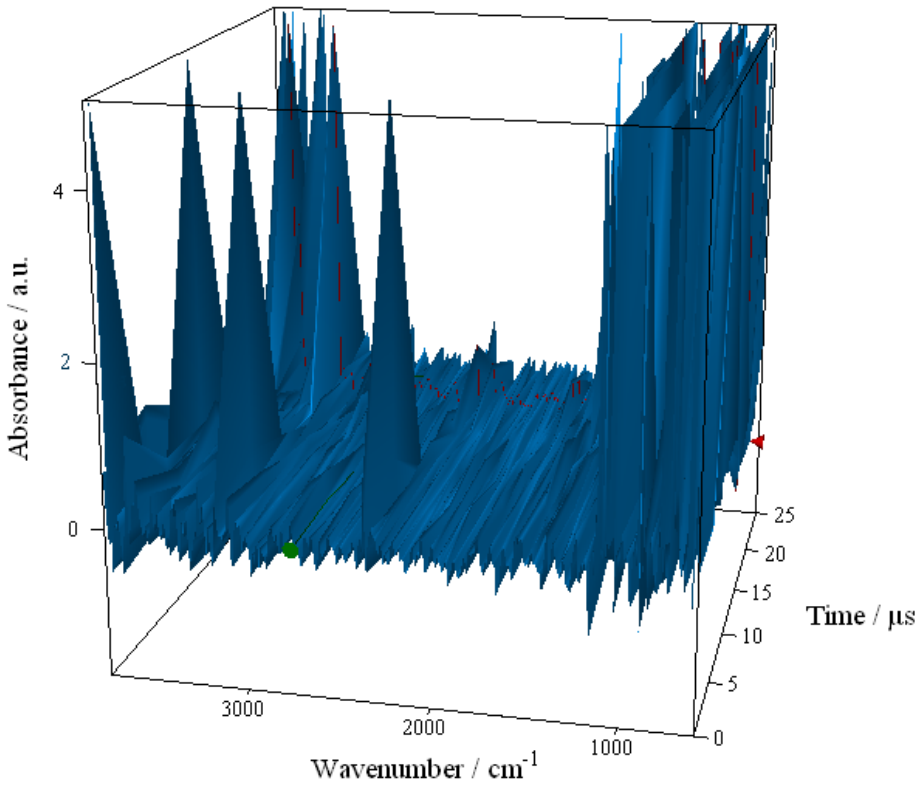

Figure 9.40: Time resolved FTIR spectra of 1000 ppm TEOS and 0.02 % oxygen in a helium plasma.

dence of the chemistry. Initial work here presents the possibility of time dependant ozone formation, that has been shown to an important species in the silica deposition process. With further work, the technique could see use in discovering and validating in depth mechanisms governing the plasma enhanced chemical vapour deposition of silica thin films.

Chapter 10

Conclusions and Further Work

10.1 Conclusions

The primary aim of this work was the development of a variety of techniques to examine the atmospheric pressure chemical vapour deposition process. This aim has been met, and has enabled the in depth examination of several processes. From a scientific perspective, much has been discovered about the chemistry of the plasma enhanced chemical vapour deposition of silica films, and the spatial mapping work has the potential to validate computational fluid dynamics models. The mapping of several process windows has also helped progress the twin aims of process optimisation and control.

Spatial mapping of the hydrogen chloride evolved during the thermal chemical vapour deposition of tin oxide films has been carried out. This work has been invaluable in identifying the reaction ”hotspots” within the reactor that would lead to film inhomogeneity. In addition the work identified the redundancy of the secondary exhaust within the coating head. This has already had significant implications for optimisation of further reactor designs. The two dimensional nature of the measurements has shown use in further understanding the process, and it is the first time that such measurements have been reported in a chemical vapour deposition process.

Extensive work has been carried out into investigating the atmospheric pressure plasma enhanced chemical vapour deposition of silica films. This work has highlighted the importance of several control variables as well as allowing for an in depth examination of the chemistry occurring during the process. The effects of the oxygen concentration, and

power supply are particularly strong on the processes studied.

The identification of active oxygen species through the use of FTIR and optical emission spectroscopy has emphasised the importance of these species in the atmospheric pressure chemical vapour deposition of silica thin films. The use of principal components analysis to support this result was an important part of the identification process. In addition, the by-products in the two processes examined have not been identified prior to the work presented in this thesis. Comparison between the *in situ* and downstream measurements of hydrogen chloride in chapter eight emphasises the importance of both measurements in the analysis of the process.

The response surfaces produced for chapters seven and eight have identified both key process variables and their subsequent effects on film properties. In particular, the effect of oxygen on growth rates of silica films, and the subsequent effect on the hardness of the films produced. Similar conclusions were made with the contact angle and refractive index.

In situ FTIR spectroscopic measurements have further enabled characterisation of the chemistry of the TEOS based silica deposition process, again verifying the importance of ozone in the overall process. The step scan FTIR spectroscopy then showed the time dependence of the ozone formation in the plasma.

Chemical vapour deposition at atmospheric pressure is a complicated process. There are a multitude of different physical and chemical mechanisms occurring, as a result of this it is hard to assign any single contributing factor to a given film property. Instead it is a combination of these factors that will lead to improved film properties and better process control, and this is what any further investigations of the subject should be concerned with.

10.2 Areas for Further Work

The work presented in this thesis represents both the development of a methodology for studying the chemical vapour deposition process, and several full investigations in their own right. The most obvious route for further work would be to extend this methodology to examine further precursors, and subsequently different thin films. An example of an important silica precursor that has potential to be examined in such a way is hexamethyldisiloxane. The combined chemometric and spectroscopic methodology could also be extended to other chemical vapour deposition processes.

The addition of tomographical measurements into the analysis of the plasma reactors could yield great benefits in improving reactor design. In addition, with suitable preparation, it could be possible to conduct such studies on quite a fast timescale. This would enable examination of the mechanisms during the plasma cycle.

It is also recommended that further work be directed towards modelling of the chemical vapour deposition process. This will help direct experiments towards validation of these models. It will also give further insight into the process as a whole, which will in turn help to improve process design and control.

Bibliography

[1] B. Chapman. *Glow Discharge Processes*. John Wiley and Sons, 1980.

[2] H-E. Wagner, R. Brandenburg, K. V. Kozlov, A. Sonnenfeld, P. Michel, and J. F. Behnke. The barrier discharge: basic properties and applications to surface treatment. *Vacuum*, 71:417–436, 2003.

[3] J. M. Hollas. *Modern Spectroscopy*. John Wiley and Sons, 1996.

[4] F. T. S. Yu and I. C. Khoo. *Principles of Optical Engineering*. John Wiley and Sons, 1990.

[5] A. M. B. van Mol, Y. Chae, A. H. McDaniel, and M. D. Allendorf. Chemical vapor deposition of tin oxide: Fundamentals and applications. *Thin Solid Films*, 502:72 – 78, 2006.

[6] A. L. Smith. *The Coblentz Society Desk Book of Infrared Spectra*, pages 1–24. The Coblentz Society: Kirkwood MO, 1982.

[7] L. Mangolini, C. Anderson, J. Heberlein, and U. Kortshagen. Effects of current limitation through the dielectric in atmospheric pressure glows in helium. *Journal of Physics D: Applied Physics*, 37:1021 – 1030h, 2004.

[8] W. C. Martin. Energy Levels and Spectrum of Neutral Helium (^{4}He I). *Journal of Research of the National Bureau of Standards*, 64a, 1960.

[9] X. Shaokui, X. Jinzhou, P. Xiaobo, and Z. Jing. Deposition of Thin Titania Films by Dielectric Barrier Discharge at Atmospheric Pressure. *Plasma Science and Technology*, 8:292 – 296, 2006.

[10] A. Mills, N. Elliot, I. P. Parkin, S. A. O'Neill, and R. J. Clark. Novel TiO_2 CVD films for semiconductor photocatalysis. *Journal of Photochemistry and Photobiology A: Chemistry*, 151:171–179, 2002.

[11] I. P. Parkin and R. G. Palgrave. Self-cleaning coatings. *Journal of Materials Chemistry*, 15:1689–1695, 2005.

[12] L. A. Brook, P. Evans, H. A. Foster, M. E. Pemble, A. Steele, D. W. Sheel, and H. M. Yates. Highly bioactive silver and silver/titania composite films grown by chemical vapour deposition. *Journal of Photochemistry and Photobiology A: Chemistry*, 187:52 – 63, 2007.

[13] T. Takeuchi, Y. Egashira, T. Osawa, and H. Komiyama. A Kinetic Study of the Chemical Vapor Deposition of Silicon Carbide from Dichlorodimethylsilane Precursors. *Journal of the Electrochemical Society*, 145:1277 – 1284, 1998.

[14] K L Choy. Chemical vapour deposition of coatings. *Progress in Materials Science*, 48:57 – 170, 2003.

[15] K. M. Gustin and R. G. Gordon. A Study Of Aluminum Oxide Thin Films Prepared By Atmospheric-Pressure Chemical Vapor Deposition From Trimethylaluminum + Oxygen And/Or Nitrous Oxide. *Journal of Electronic Materials*, 17:509–517, 1988.

[16] A. A. Bessonov, N. B. Morozova, N. V. Gelfond, P. P. Semyannikov, S. V. Trubin, Yu. V. Shevtsov, Yu.V. Shubin, and I.K. Igumenov. Dimethylgold(III) carboxylates as new precursors for gold CVD. *Surface and Coatings Technology*, 201:9099–9103, 2007.

[17] R. G. Gordon, J. Proscia, F. B. Ellis, and A. E. Delahoy. Textured tin oxide films produced by atmospheric pressure chemical vapor deposition from tetramethyltin

and their usefulness in producing light trapping in thin film amorphous silicon solar cells. *Solar Energy Materials*, 18:263–281, 1989.

[18] H .M. Yates, L.A. Brook, I. B. Ditta, P. Evans, H. A. Foster, D. W. Sheel, and A. Steele. Photo-induced self-cleaning and biocidal behaviour of titania and copper oxide multilayers. *Journal of Photochemistry and Photobiology A: Chemistry*, 197:197–205, 2008.

[19] H. M. Yates, L. A. Brook, and D. W. Sheel. Photoactive Thin Silver Films by Atmospheric Pressure CVD. *International Journal of Photoenergy*, 2008:8 pages, 2008.

[20] P.J. Wright and B. Cockayne. The organometallic chemical vapour deposition of ZnS and ZnSe at atmospheric pressure. *Journal of Crystal Growth*, 59:148–154, 1982.

[21] A. T. Hunt, W. B. Carter, and J. K. Cochran. Combustion chemical vapor deposition: A novel thin-film deposition technique. *Applied Physics Letters*, 62:266–268, 1993.

[22] M. R. Hendrick, J. M. Hampikian, and W. B. Carter. Alumina Coatings Applied via Combustion Chemical Vapor Deposition and Their Effects on the Oxidation of a Ni-Base Chromia Former. *Journal of the Electrochemical Society*, 145:3986–3984, 1998.

[23] V. S. K. G. Kelekanjeri, W. B. Carter, and J. M. Hampikian. Deposition of α-alumina via combustion chemical vapor deposition. *Thin Solid Films*, 515:1905–1911, 2006.

[24] W. B. Carter, G. W. Book, T. A. Polley, D. W. Stollberg, and J. M. Hampikian. Combustion chemical vapor deposition of CeO_2 film. *Thin Solid Films*, 347:25–30, 1999.

[25] R. M. Trommer, F. N. Souza, M. D. Lima, L. A. Santos, and C. P. Bergmann. Alternative technique for hydroxyapatite coatings. *Surface and Coatings Technology*, 201:9587–9593, 2007.

[26] M.J. Davis, G. Benito, D.W. Sheel, and M.E. Pemble. Growth of Thin Films of Molybdenum and Tungsten Oxides by Combustion CVD Using Aqueous Precursor Solutions. *Chemical Vapor Deposition*, 10:29–34, 2004.

[27] B.C. Valek and J.M. Hampikian. Silica thin films applied to Ni-20Cr alloy via combustion chemical vapor deposition. *Surface and Coatings Technology*, 94-95:13–20, 1997.

[28] H. Y. H. Chan, C. G. Takoudis, and M. J. Weaver. In-Situ Monitoring of Chemical Vapor Deposition at Ambient Pressure by Surface-Enhanced Raman Spectroscopy: Initial Growth of Tantalum(V) Oxide on Platinum. *Journal of the American Chemical Society*, 121:9219–9220, 1999.

[29] Q.-H. Wu, J. Song, and J. Li. High oxygen vacancy tin oxide synthesized by combustion chemical vapor deposition (CCVD). *Surface and Interface Analysis*, 40:1488–1492, 2008.

[30] T. A. Polley, W. B. Carter, and D. B. Poker. Deposition of zinc oxide thin films by combustion CVD. *Thin Solid Films*, 357:132–136, 1999.

[31] Z.-Y. Li, F. Xu, Q.-H. Wu, and J. Li. Zinc oxide thin film synthesized by combustion chemical vapor deposition. *Applied Surface Science*, 255:28592863, 2008.

[32] A Inspektor-Koren. Principles of plasma-activated chemical vapour deposition. *Surface and Coatings Technology*, 33:31 – 48, 1987.

[33] J. L. Hodgkinson, D. W. Sheel, H. M. Yates, and M. E. Pemble. Atmospheric Pressure Glow Discharge CVD of Al_2O_3 Thin Films. *Plasma Processes and Polymers*, 3:597–605, 2006.

[34] S. E. Alexandrov, N. McSporran, and M. L. Hitchman. Remote AP-PECVD of Silicon Dioxide Films from Hexamethyldisiloxane (HMDSO). *Chemical Vapor Deposition*, 11:481 – 490, 2005.

[35] T. P. Kasih, S i Kuroda, and H. Kubota. A Nonequilibrium, Atmospheric-Pressure Argon Plasma Torch for Deposition of Thin Silicon Dioxide Films. *Chemical Vapor Deposition*, 13:169 – 175, 2007.

[36] S. Martin, F. Massines, N. Gherardi, and C. Jimenez. Atmospheric pressure PECVD of silicon based coatings using a glow dielectric barrier discharge. *Surface and Coatings Technology*, 177 - 178:693 – 698, 2004.

[37] H. Kakiuchi, Y. Nakahama, H. Ohmi, K. Yasutake, K. Yoshii, and Y. Mori. Investigation of deposition characteristics and properties of high-rate deposited silicon nitride films prepared by atmospheric pressure plasma chemical vapor deposition. *Thin Solid Films*, 479:17 – 23, 2005.

[38] J. L. Hodgkinson, H. M. Yates, and D. W. Sheel. Low Temperature Growth of Photoactive Titania by Atmospheric Pressure Plasma. *Plasma Processes and Polymers*, 6:575–582, 2009.

[39] G. Auvert. Laser chemical vapour deposition for microelectronics. *Applied Surface Science*, 86:466–474, 1995.

[40] J. C. Oliveira, P. Paiva, M. N. Oliveira, and O. Conde. Laser-assisted CVD of boron carbide at atmospheric pressure. *Applied Surface Science*, 139:159–164, 1999.

[41] J. S. Cohan, H. Yuan, R. S. Williams, and J. I. Zink. Laser-assisted organometallic chemical vapor deposition of films of rhodium and iridium. *Applied Physics Letters*, 60:1402–1403, 1992.

[42] L. V. Koplitz, D. K. Shuh, Y.-J. Chen, R. S. Williams, and J. I. Zink. Laser-driven chemical vapor deposition of platinum at atmospheric pressure and room temperature from $CpPt(CH_3)_3$. *Applied Physics Letters*, 53:1705–1708, 1988.

[43] M. K. Mazumder, Y. Takakuwa, and N. Miyamoto. Atmospheric photoassisted chemical vapor deposition of Si using ultraviolet-light irradiated H_2 carrier gas and nonexcited SiH_2Cl_2. *Applied Physics Letters*, 61:2881–2883, 1992.

[44] G. Reisse and R. Ebert. Titanium nitride thin film deposition by laser CVD. *Applied Surface Science*, 106:268–274, 1996.

[45] H. Dumont, J.-E. Bourée, A. Marbeuf, and O. Gorochov. Photo-assisted growth of ZnTe by metalorganic chemical vapour deposition. *Journal of Crystal Growth*, 130:600–610, 1993.

[46] W. Hamd, Y. C. Wu, A. Boulle, E. Thune, and R. Guinebretière. Microstructural study of SnO_2 thin layers deposited on sapphire by solgel dip-coating. *Thin Solid Films*, 518:1–5, 2009.

[47] U. Selvaraj, A. V. Prasadarao, S. Komarneni, and R Ro. Sol-Gel Fabrication of Epitaxial and Oriented TiO_2 Thin Films. *Journal of the American Ceramic Society*, 75:1167–1170, 1992.

[48] V. Patil, A. Patil, J.-W. Choi, Y.-P. Lee, Y. S. Yoon, H.-J. Kim, and S.-J. Yoo. $LiCoO_2$ thin film cathodes grown by solgel method. *Journal of Electroceramics*, 23:214–218, 2009.

[49] K. Tadanaga, N. Katata, and T. Minami. Formation Process of Super-Water-Repellent Al_2O_3 Coating Films with High Transparency by the SolGel Method. *Journal of the American Ceramic Society*, 80:3213–3216, 1997.

[50] R. Ashiri, Ali Nemati, M. Sasani Ghamsari, and H. Aadelkhani. Characterization of optical properties of amorphous $BaTiO_3$ nanothin films. *Journal of Non-Crystalline Solids*, 355:2480–2484, 2009.

[51] A. Stoch, C. Paluszkiewicz, T. Gibala, and A. Bolek. FTIR study of silica sol-gel deposited films on anodically oxidized aluminium. *Journal of Molecular Structure*, 293:287–290, 1993.

[52] R. Mizutani, Y. Oono, J. Matsuoka, H. Nasu, and K. Kamiya. Coating of polymethylmethacrylate with transparent SiO_2 thin films by a sol-gel method. *Journal of Materials Science*, 29:5773–5778, 1994.

[53] C. McDonagh, F. Sheridan, T. Butler, and B.D. MacCraith. Characterisation of sol-gel-derived silica films. *Journal of Non-Crystalline Solids*, 194:72–77, 1996.

[54] R. Rella, A. Serra, P. Siciliano, L. Vasanelli, G. Ded, and A. Licciulli. CO sensing properties of SnO_2 thin films prepared by the sol-gel process. *Thin Solid Films*, 304:339–343, 1997.

[55] C. Cobianu, C. Savaniu, O. Buiu, Dan Dascalua, M. Zaharescu, C. Parlog, A. van den Berg, and B Pecz. Tin dioxide solgel derived thin films deposited on porous silicon. *Sensors and Actuators B: Chemical*, 43:114–120, 1997.

[56] G. Guzman, R. Morineau, and Jacques Livage. Synthesis of vanadium dioxide thin films from vanadium alkoxides. *Materials Research Bulletin*, 29:509–515, 1994.

[57] C. D. E. Lakeman and D. A. Payne. Sol-gel processing of electrical and magnetic ceramics. *Materials Chemistry and Physics*, 38:305–324, 1994.

[58] G. Dubpernell. Chromium plating. *Journal of the Electrochemical Society*, 80:589–615, 1941.

[59] M. Stelter and H. Bombach. Process Optimization in Copper Electrorefining. *Advanced Engineering Materials*, 6:558–562, 2004.

[60] L. Weisberg and A. K.Graham. Gold Plating. *Journal of the Electrochemical Society*, 80:509–520, 1941.

[61] C. G. Fink and R. H. Lester. The Electrodeposition of Indium from Sulfate Baths. *Journal of the Electrochemical Society*, 78:349–372, 1940.

[62] F. C. Mathers and M. M. Felger. A New Addition Agent for the Electrolytic Refining of Tin and Lead. *Journal of the Electrochemical Society*, 90:81–84, 1946.

[63] S. K. Panikkar and T. L. Rama Char. Electroplating of Nickel from the Pyrophosphate Bath. *Journal of the Electrochemical Society*, 106:494–499, 1959.

[64] A. J. Appleby. Electroplating of Osmium. *Journal of the Electrochemical Society*, 117:1610, 1970.

[65] J. J. Becker. Some Observations on the Electroplating and Deplating of Silver. *Journal of the Electrochemical Society*, 111:480–482, 1964.

[66] J. L. Bray and F. R. Morral. Addition Agents in the Electrodeposition of Zinc. *Journal of the Electrochemical Society*, 78:309–316, 1940.

[67] E. P. DeGarmo, J. T. Black, and Ronald A. Kosker. *DeGarmo's materials and processes in manufacturing*. Wiley-Interscience, 2008.

[68] L. F. Oeming. Stream Pollution Problems of the Electroplating Industry. *Sewage Works Journal*, 18:678–685, 1946.

[69] A. Jaworek and A. T. Sobczyk. Electrospray route to nanotechnology: An overview. *Journal of Electrostatics*, 66:197–219, 2008.

[70] E. M. Kelder, O. C. J. Nijs, and J. Schoonman. Low-temperature synthesis of thin films of YSZ and $BaCeO_3$ using electrostatic spray pyrolysis (ESP). *Solid State Ionics*, 68:5–7, 1994.

[71] A. A. van Zomeren, E. M. Kelder, J. C. M. Marijnissen, and J. Schoonman. The production of thin films of $LiMn_2O_4$ by electrospraying. *Journal of Aerosol Science*, 25:1229–1235, 1994.

[72] D. A. Grigoriev, M. J. Edirisinghe, X. Bao, J. R. G. Evans, and Z. B. Luklinska. Preparation of silicon carbide by electrospraying of a polymeric precursor. *Philosophical Magazine Letters*, 81:285–291, 2001.

[73] H. A. Wyllie and G. C. Lowenthal. An electrospraying technique for coating radioactive sources with silver. *The International Journal of Applied Radiation and Isotopes*, 33:589–591, 1982.

[74] A. Lintanf-Salaüna and E. Djurado. Fabrication by electrostatic spray deposition and structural investigation of ultra thin and dense zirconia films. *Thin Solid Films*, 517:6784–6788, 2009.

[75] M. I. Boulos. Thermal Plasma Processing. *IEEE Transactions on Plasma Science*, 19:1078–1089, 1991.

[76] P. Fauchais, A. Vardelle, and A. Denoirjean. Reactive thermal plasmas: ultrafine particle synthesis and coating deposition. *Surface and Coatings Technology*, 97:66–78, 1997.

[77] C.-J. Li, G.-J. Yang, and A. Ohmor. Relationship between particle erosion and lamellar microstructure for plasma-sprayed alumina coatings. *Wear*, 260:1166–1172, 2006.

[78] E. E. Vidal and P. R. Taylor. Thermal Plasma Synthesis of $BaFe_{12}O_{19}$ (BaM) Films. *Plasma Chemistry and Plasma Processing*, 23:609–626, 2003.

[79] R. G. Castro, P. W. Stanek, K. E. Elliott, D. L. Youchison, R. D. Watson, and D. S. Walsh. The structure, properties and performance of plasma-sprayed beryllium for fusion applications. *Physica Scripta*, T64:77–83, 1996.

[80] K. A. Gross, C. C. Berndt, and H. Herman. Amorphous phase formation in plasma-sprayed hydroxyapatite coatings. *Journal of Biomedical Materials Research Part A*, 39:407–414, 1998.

[81] N. Yamaguchi, T. Hattori, K. Terashima, and T. Yoshida. High-rate deposition of $LiNbO_3$ films by thermal plasma spray CVD. *Thin Solid Films*, 316:185–188, 1998.

[82] S. A. Kulinich, H. Yamamoto, J. Shibata, K. Terashima, and T. Yoshida. Lithium niobatetantalate thin films on Si by thermal plasma spray CVD. *Thin Solid Films*, 407:60–66, 2002.

[83] J. Colmenares-Angulo, S. Zhao, C. Young, and A. Orlov. The effects of thermal spray technique and post-deposition treatment on the photocatalytic activity of TiO_2 coatings. *Surface and Coatings Technology*, 204:423–427, 2009.

[84] S. Grenier, K. Shanker, P. Tsantrizos, and F. Ajersch. Deposition of TiN films using a thermal plasma reactive forming technology. *Surface and Coatings Technology*, 82:311–316, 1996.

[85] R. Harnacha, P. Fauchais, and F. Nardou. Influence of dopant on the thermal properties of two plasma-sprayed zirconia coatings Part I: Relationship between powder characteristics and coating properties. *Journal of Thermal Spray Technology*, 5:431–438, 1996.

[86] S. Wuttiphan, A. Pajares, B. R. Lawn, and C. C. Berndt. Effect of substrate and bond coat on contact damage in zirconia-based plasma-sprayed coatings. *Thin Solid Films*, 293:251–260, 1997.

[87] H. Randhara. Review of plasma-assisted deposition processes. *Thin Solid Films*, 196:329–349, 1991.

[88] R. F. Bunshah and C. V. Deshpandey. Plasma assisted physical vapor deposition processes: A review. *Journal of Vacuum Science and Technology A*, 3:553–560, 1985.

[89] M. Saraiva, H. Chen, W. P. Leroy, S. Mahieu, N. Jehanathan, O. Lebedev, V. Georgieva, R. Persoons, and D. Depla. Influence of Al Content on the Properties of MgO Grown by Reactive Magnetron Sputtering. *Plasma Processes and Polymers*, 6:S751–S754, 2009.

[90] K.-R. Wu and C.-H. Hung. Characterization of N,C-codoped TiO_2 films prepared by reactive DC magnetron sputtering. *Applied Surface Science*, 256:1595–1603, 2009.

[91] A. Ricard, H. Michel, P. Jacquot, and M. Gantois. Analysis of a reactive sputter ion plating discharge for TiN deposition using optical emission spectroscopy. *Thin Solid Films*, 124:67–73, 1985.

[92] E. Kusano, J. A. Theil, and J. A. Thornton. Deposition of vanadium oxide films by direct-current magnetron reactive sputtering. *Journal of Vacuum Science and Technology A*, 6:1663–1667, 1988.

[93] L. Vasanelli, A. Valentini, and A. Losacco. Preparation of transparent conducting zinc oxide films by reactive sputtering. *Solar Energy Materials*, 16:91–102, 1987.

[94] U. Helmersson, M. Lattemann, J. Bohlmark, A. P. Ehiasarian, and J. T. Gudmundsson. Ionized physical vapor deposition (IPVD): A review of technology and applications. *Thin Solid Films*, 513:1–24, 2006.

[95] V. Kouznetsov. Method and apparatus for magnetically enhanced sputtering, patent number 6296742. US Patent Office, 1997.

[96] E. Wallin, T. I. Selinder, M. Elfwing, and U. Helmersson. Synthesis of α-Al_2O_3 thin films using reactive high-power impulse magnetron sputtering. *Europhysics Letters*, 82, 2008.

[97] T.I. Selinder, E. Coronel, E. Wallin, and U. Helmersson. αAlumina coatings on WC/Co substrates by physical vapor deposition. *International Journal of Refractory Metals & Hard Materials*, 27:507–512, 2009.

[98] S. Konstantinidis, J.P. Dauchot, and M. Hecq. Titanium oxide thin films deposited by high-power impulse magnetron sputtering. *Thin Solid Films*, 515:1182–1186, 2006.

[99] V. Straňák, M. Čada, M. Quaas, S. Block, R. Bogdanowicz, Š. Kment, H. Wulff, Z. Hubička, C. A. Helm, M. Tichý, and R. Hippler. Physical properties of homogeneous TiO_2 films prepared by high power impulse magnetron sputtering as a function of crystallographic phase and nanostructure. *Journal of Physics D: Applied Physics*, 42, 2009.

[100] S. Konstantinidis, A. Hemberg, J. P. Dauchot, and M. Hecq. Deposition of zinc oxide layers by high-power impulse magnetron sputtering. *Journal of Vacuum Science and Technology B*, 25:L19–L21, 2007.

[101] L. Niinistö and M. Leskelä. Atomic layer epitaxy: chemical opportunities and challenges. *Thin Solid Films*, 225:130–135, 1993.

[102] H. Kim, H.-B.-R. Lee, and W.-J. Maeng. Applications of atomic layer deposition to nanofabrication and emerging nanodevices. *Thin Solid Films*, 517:2563–2580, 2009.

[103] D. J. Lichtenwalner, V. Misra, S. Dhar, S.-H. Ryu, and A. Agarwal. High-mobility enhancement-mode 4H-SiC lateral field-effect transistors utilizing atomic layer deposited Al_2O_3 gate dielectric. *Applied Physics Letters*, 95:152113, 2009.

[104] J. Hämäläinen, E. Puukilainen, M. Kemell, L. Costelle, M. Ritala, and M. Leskelä. Atomic Layer Deposition of Iridium Thin Films by Consecutive Oxidation and Reduction Steps. *Chemistry of Materials*, 21:4868–4872, 2009.

[105] M. Putkonen, T. Aaltonen, M. Alnes, T. Sajavaara, O. Nilsenc, and H. Fjellvåg. Atomic layer deposition of lithium containing thin films. *Journal of Materials Chemistry*, 19:8767–8771, 2009.

[106] M. Popovici, S. Van Elshocht, N. Menou, J. Swerts, D. Pierreux, A. Delabie, B. Brijs, T. Conard, K. Opsomer, J. W. Maes, D. J. Wouters, and J. A. Kittl. Atomic Layer Deposition of Strontium Titanate Films Using $Sr(^tBu_3Cp)_2$ and $Ti(OMe)_4$. *Journal of the Electrochemical Society*, 157:G1–G6, 2010.

[107] M. Bosund, K. Mizohata, T. Hakkarainen, M. Putkonen, M. Söderlund, S. Honkanen, and H. Lipsanen. Atomic layer deposition of ytterbium oxide using β-diketonate and ozone precursor. *Applied Surface Science*, 256:847–851, 2009.

[108] Y.-T. Lin, P.-H. Chung, H.-W. Lai, H.-L. Su, D.-Y. Lyu, K.-Y. Yen, T.-Y. Lin, C.-Y. Kung, and J.-R. Gong. Self-limiting growth of ZnO films on (0 0 0 1) sapphire substrates by atomic layer deposition at low temperatures using diethyl-zinc and nitrous oxide. *Applied Surface Science*, 256:819–822, 2009.

[109] S. Yang, B. H. Lin, W.-R. Liu, J.-H. Lin, C.-S. Chang, C.-H. Hsu, and W. F. Hsieh. Structural Characteristics and Annealing Effect of ZnO Epitaxial Films Grown by Atomic Layer Deposition. *Crystal Growth and Design*, 9:5184–5189, 2009.

[110] H. Kawamoto, H. Sakaue, S. Takehiro, and T. Horrike. Study on Reaction Mechanism of Aluminium Selective Chemical Vapor Deposition with *in-situ* XPS Measurement. *Japanese Journal of Applied Physics*, 29:2657 – 2661, 1990.

[111] J. Sterner, J. Kessler, and L. Stolt. XPS instrument coupled with ALCVD reactor for investigation of film growth. *Journal of Vacuum Science and Technology A*, 20:278 – 284, 2002.

[112] L. Constant, C. Speisser, and F. Le Normand. Hfcvd diamond growth on Cu(111). Evidence for carbon phase transformations by in situ AES and XPS. *Surface Science*, 387:28 – 43, 1997.

[113] J-P. Lu, P. W. Chu, R. Raj, and H. Gysling. Ultrahigh vacuum chemical vapor deposition of rhodium thin films on clean and TiO_2-covered Si(111). *Thin Solid Films*, 208:172–176, 1992.

[114] R. W. Collins, Yue Cong, H. V. Nguyen, I. An, K. Vedam, T. Badzian, and R. Messier. Real time spectroscopic ellipsometry characterization of the nucleation of diamond by filament-assisted chemical vapor deposition. *Journal of Applied Physics*, 71:5287–5289, 1992.

[115] A. von Keudell, W. Jacob, and W. Fukarek. Role of hydrogen ions in plasma-enhanced chemical vapor deposition of hydrocarbon films, investigated by in situ ellipsometry. *Applied Physics Letters*, 66:1322–1324, 1995.

[116] C. W. Teplin, D. H. Levi, E. Iwaniczko, K. M. Jones, J. D. Perkins, and H. M. Branz. Monitoring and modeling silicon homoepitaxy breakdown with real-time spectroscopic ellipsometry. *Journal of Applied Physics*, 97, 2005.

[117] C N Banwell and E M McCash. *Fundamentals of Molecular Spectroscopy*. McGraw-Hill Book Company, 4th edition, 1994.

[118] P. W. Morrison and J. R. Haigis. *In situ* infrared measurements of film and gas properties during the plasma deposition of amorphous hydrogenated silicon. *Journal of Vacuum Science and Technology A*, 11:490–502, 1993.

[119] E. S. Aydil, R. A. Gottscho, and Y. J. Chabal. Real-time monitoring of surface chemistry during plasma processing. *Pure and Applied Chemistry*, 66:1381 – 1388, 1994.

[120] A. Campion and P. Kambhampati. Surface-enhanced Raman scattering. *Chemical Society Reviews*, 27:241–250, 1998.

[121] T. López-Ríos and E. Sandré. Application of SERS to study chemical vapour deposition processes: the example of diamond films. *Journal of Raman Spectroscopy*, 29:733–737, 1998.

[122] S. Jonas, W. S. Ptak, W. Sadowski, and E. Walasek. FTIR In Situ Studies of the Gas Phase Reactions in Chemical Vapor Deposition of SiC. *Journal of the Electrochemical Society*, 142:2357–2362, 1995.

[123] B. Zheng, G. Braeckelmann, K. Kujawski, I. Lou, S. Lane, and A. E. Kaloyeros. In Situ Mass Spectral and Infrared Studies of the Gas-Phase Evolution and Decomposition Pathways of $Cu^{II}(hfac)_2$. *Journal of the Electrochemical Society*, 142:3896–3903, 1995.

[124] S. R. Armstrong, M. E. Pemble R. D. Hoare, I. M. Povey, A. Stafford, A. G. Taylor, and J. O. Williams. The pyrolysis of precursors for GaAs MOCVD studied by in-situ and ex-situ Fourier transform infrared spectroscopy. *Journal of Crystal Growth*, 124:10–15, 1992.

[125] D. Vernardou, M. E. Pemble, and D. W. Sheel. In-situ FTIR studies of the growth of vanadium dioxide coatings on glass by atmospheric pressure chemical vapour deposition for VCl_4 and H_2O system. *Thin Solid Films*, 515:8768–8770, 2007.

[126] D. Vernardou, M. E. Pemble, and D. W. Sheel. In-situ Fourier transform infrared spectroscopy gas phase studies of vanadium (IV) oxide coating by atmospheric pressure chemical vapour deposition using vanadyl (IV) acetylacetonate. *Thin Solid Films*, 516:4502–4507, 2008.

[127] J. Nishizawa and N. Hayasaka. *In Situ* observation of plasmas for dry etching by IR spectroscopy and probe methods. *Thin Solid Films*, 92:189 – 198, 1982.

[128] T. A. Cleland and D. W. Hess. *In Situ* FTIR Diagnostics of the Radio-Frequency Plasma Decomposition of N_2O. *Plasma Chemistry and Plasma Processing*, 7:379 – 394, 1987.

[129] K. Kawaguchi, O. Baskakov, Y. Hosaki, Y. Hama, and C. Kugimiya. Time-resolved Fourier transform spectroscopy of pulsed discharge products. *Chemical Physics Letters*, 369:293 – 298, 2003.

[130] J. Y. Hwang, C. Park, M. Huang, and T. Anderson. Investigation of mass transport phenomena in an upflow cold-wall CVD reactor by gas phase Raman spectroscopy and modeling. *Journal of Crystal Growth*, 279:521 – 530, 2005.

[131] T. O. Sedgwick and J. E. Smith. Raman Scattering Spectroscopy Applied to the Study of Chemical Vapor Deposition Systems. *Journal of the Electrochemical Society*, 123:254–258, 1976.

[132] V. Zumbach, J. Schäfer, J. Tobai, M. Ridder, T. Dreier, T. Schaich, J. Wulfrum, B. Ruf, F. Behrendt, O. Deutschman, and J. Warnatz. Experimental investigation and computational modeling of hot filament diamond chemical vapor deposition. *Journal of Chemical Physics*, 107:5918–5928, 1997.

[133] N. Herlin, M.l Lefebvre, M. Péalat, and J. Perrin. Investigation of the Chemical Vapor Deposition of Silicon Carbide from Tetramethylsiiane by in Situ Temperature and Gas Composition Measurements. *Journal of Physical Chemistry*, 96:7063–7072, 1992.

[134] B. J. Phillips, S. D. Steidley, L. D. Lau, and R. G. Rodriguez. Coherent Raman Spectroscopic Monitoring of Pulsed Radio Frequency PECVD of Silicon Nitride Thin Films. *Applied Spectroscopy*, 55:946–951, 2001.

[135] K. P. Killeen. Reactive chemical intermediates in metalorganic chemical vapor deposition of GaAs. *Applied Physics Letters*, 61:1864–1866, 1992.

[136] W. W. Lee and P. S. Locke. Hydrogen-atom assisted CVD of copper at low temperatures and in-situ gas-phase spectroscopy studies. *Thin Solid Films*, 262:39–45, 1995.

[137] J.E. Butler, N. Bottka, R.S. Sillmon, and D.K. Gaskill. In situ, real-time diagnostics of omvpe using ir-diode laser spectroscopy. *Journal of Crystal Growth*, 77:163–171, 1986.

[138] S-I. Chou, D. S. Baer, R. K Hansen, W. Z. Collison, and T. Q. Ni. HBr concentration and temperature measurements in a plasma etch reactor using diode laser spectroscopy. *Journal of Vacuum Science Technology*, 19:477 – 484, 2000.

[139] S. Kim, P. Klimecky, J. B. Jeffries, F. L. Terry Junior, and R. K. Hansen. *In situ* measurements of HCl during plasma etching of poly-silicon using a diode laser absorption sensor. *Measurement Science and Technology*, 14:1662 – 1670, 2003.

[140] P. A. Martin, R. J. Holdsworth, D. W. Sheel, and R. Schlatmann. NIR diode laser spectroscopy of HF and HCl at multiple points in the atmospheric pressure CVD of tin oxide films. *Surface and Coatings Technology*, 201:9030–9034, 2007.

[141] N. Xu, D. R. Pirkle, J. B. Jeffries, B. McMillin, and R. K. Hansen. Near-infrared diode laser hydrogen flouride monitor for dielectric etch. *Journal of Vacuum Science Technology A*, 22:2479 – 2486, 2004.

[142] G. Duxbury, N. Langford, M. T. McCulloch, and S. Wright. Quantum cascade semiconductor infrared and far-infrared lasers: from trace gas sensing to non-linear optics. *Chemical Society Reviews*, 34:921–934, 2005.

[143] J. Röpcke, G. Lombardi, A. Rousseau, and P. B. Davies. Application of mid-infrared tuneable diode laser absorption spectroscopy to plasma diagnostics: a review. *Plasma Sources Science and Technology*, 15:S148 – S168, 2006.

[144] P. Ho, M. E. Coltrin, and W. G. Breiland. Laser-Induced Fluorescence Measurements and Kinetic Analysis of Si Atom Formation in a Rotating Disk Chemical Vapor Deposition Reactor. *Journal of Physical Chemistry*, 98:10138–10147, 1994.

[145] V. S. Ban. Transport Phenomena Measurements in Epitaxial Reactors. *Journal of the Electrochemical Society*, 125:317–320, 1978.

[146] V. S. Ban. Novel reactor for high volume low-cost silicon epitaxy. *Journal of Crystal Growth*, 45:97–107, 1978.

[147] E. P. Visser, C. A. M. Govers, and L. J. Giling. Measurement of gas-switching related diffusion phenomena in horizontal MOCVD reactors using biacetyl luminescence. *Journal of Crystal Growth*, 102:529–541, 1990.

[148] A. V. Kharchenko and D. Grésillon. Nonparticle laser velocimetry and permanent velocity measurement by enhanced light scattering. *Measurement Science and Technology*, 14:228–233, 2003.

[149] L. J. Giling. Gas Flow Patterns in Horizontal Epitaxial Reactor Cells Observed by Interference Holography. *Journal of the Electrochemical Society*, 129:634–644, 1982.

[150] P. Hariharan. *Optical Holography: Principles, techniques, and applications*. Cambridge University Press, 1996.

[151] J. E. Williams and R. W. Peterson. The application of holographic interferometry to the visualization of flow and temperature profiles in a MOCVD reactor cell. *Journal of Crystal Growth*, 77:128–135, 1986.

[152] E. J. Johnson, P. V. Hyer, P. W. Culotta, L. R. Black, I. O. Clark, and M. L. Timmons. Characterization of MOCVD fluid dynamics by laser velocimetry. *Journal of Crystal Growth*, 109:24–30, 1991.

[153] E. J. Johnson, P. V. Hyer, P. W. Culotta, and I. O. Clark. Evaluation of infrared thermography as a diagnostic tool in CVD applications. *Journal of Crystal Growth*, 187:463–473, 1998.

[154] J.E. Smith Jr and T.O. Sedgwick. Measurement of gas temperature gradients using Raman scattering spectroscopy. *Letters in Heat and Mass Transfer*, 2:285–357, 1975.

[155] M. Koppitz, O. Vestavik, W. Pletschen, A. Mircea, M. Heyen, and W. Richter. On the effect of carrier gas on growth conditions in MOCVD reactors; Raman study of local temperature. *Journal of Crystal Growth*, 68:136–141, 1984.

[156] I. Langmuir. Positive Ion Currents in the Positive Column of the Mercury Arc. *General Electric Review*, 26:731, 1923.

[157] I. Langmuir and H. A. Jones. A Simple Method for Quantitative Studies of Ionization Phenomena in Gases. *Science*, 59:380, 1924.

[158] R. M. Clements and P. R. Smy. Pulsed Langmuir Probe Measurement of Ionization in a High-Pressure Plasma. *IEEE Transactions on Instrumentation and Measurement*, 19:167 – 171, 1973.

[159] K.-T. Rie and J. Wöhle. Spectroscopic investigation of N_2-H_2-Ar-$TiCl_4$-assisted chemical vapour deposition discharge for plasma of TiN. *Materials Science and Engineering, A*, 139:37–40, 1991.

[160] R. Beckmann, S. Reinke, M. Kuhr, W. Kulisch, and R. Kassing. Investigation of gas phase mechanisms during deposition of diamond films. *Surface and Coatings Technology*, 60:506–510, 1993.

[161] L. Thomas, E. Tomasella, J. M. Badie, R. Berjoan, and M. Ducarroir. Electrical Measurements and Optical Emission Spectroscopy of Silicon-Carbon Alloys Grown by PACVD: Correlation with Film Microstructure. *Chemical Vapor Deposition*, 9:130–138, 2003.

[162] Z. Abd Allah, D. Sawtell, V. L. Kasyutich, and P. A. Martin. FTIR and QCL diagnostics of the decomposition of volatile organic compounds in an atmospheric pressure dielectric packed bed plasma reactor. *Journal of Physics: Conference Series*, 157, 2009.

[163] T. Oda. Non-thermal plasma processing for environmental protection: decomposition of dilute VOCs in air. *Journal of Electrostatics*, 57:293–311, 2003.

[164] F. S. Denes and S. Manolache. Macromolecular plasma-chemistry: an emerging field of polymer science. *Progress in Polymer Science*, 29:815 – 885, 2004.

[165] R. Foest, E. Kindel, A. Ohd, M. Steiberand, and K-D. Weltmann. Non-thermal atmospheric pressure discharges for surface modification. *Plasma Physics and Controlled Fusion*, 47:B525 – B536, 2005.

[166] S. E. Alexandrov and M. L. Hitchman. Chemical Vapor Deposition Enhanced by Atmospheric Pressure Non-thermal Non-equilibrium Plasma. *Chemical Vapour Deposition*, 11:457 – 468, 2005.

[167] Y. Shimomura and W. Spears. Review of the ITER project. *IEEE Transactions on Applied Superconductivity*, 14:1369 – 1375, 2004.

[168] W. Siemens. eber die elektrostatische Induction und die Verzgerung des Stroms in Flaschendrhten. *Poggendorff's Annual Physical Chemistry*, -:66 – 122, 1857.

[169] A. Bogaerts, E. Neyts, R. Gijbels, and J. van der Mullen. Gas discharge plasmas and their applications. *Spectrochimica Acta Part B*, 57:609 – 658, 2002.

[170] F. Paschen. Ueber die zum Funkenübergang in Luft, Wasserstoff und Kohlensäure bei verschiedenen Drucken erforderliche Potentialdifferenz. *Annalen der Physik*, 273:69–75, 1889.

[171] M A Lieberman and A J Lichtenberg. *Principles of plasma discharges and materials processing*. Wiley-Interscience, 1994.

[172] D. B. Hibbert and A. J. B. Robertson. The Emission of Electrons from Glass Induced by a Strong Electric Field and the Mechanism of the Silent Electric Discharge. *Proceedings of the Royal Society of London. Series A, Mathematical and Physical Sciences*, 349:63–79, 1976.

[173] Y B Golubovskii, V A Maiorov, P Li, and M Lindmayer. Effect of the barrier material in a Townsend barrier discharge in nitrogen at atmospheric pressure. *Journal of Physics D: Applied Physics*, 39:1574 – 1583, 2006.

[174] M A Lieberman and A J Lichtenberg. *Principles of plasma discharges and materials processing*. Wiley-Interscience, 2nd edition, 2005.

[175] J. W. Coburn and H. F. Winters. Plasma etching - A discussion of mechanisms. *Journal of Vacuum Science and Technology*, 16:391–403, 1979.

[176] J. W. Coburn and H. W. Winters. Etching in reactive plasmas. *Journal of Vacuum Science and Technology*, 16:1613–1614, 1979.

[177] A. von Keudell. Surface processes during thin-film growth. *Plasma Sources Science and Technology*, 9:455–467, 2000.

[178] D. B. Graves. Plasma Processing. *IEEE Transactions on Plasma Science*, 22:31 – 42, 1994.

[179] F. E. Haworth. Electrode Reactions in the Glow Discharge. *Journal of Applied Physics*, 22:606 – 609, 1951.

[180] U. Kogelschatz, B. Eliasson, and W. Egli. From ozone generators to flat television screens: history and future potential of dielectric-barrier discharges. *Pure and Applied Chemistry*, 71:1819–1828, 1999.

[181] S. Liu and M. Neiger. Electrical modelling of homogeneous dielectric barrier discharges under an arbitrary excitation voltage. *Journal of Physics D: Applied Physics*, 36:3144 – 3150, 2003.

[182] C. Tendero, C. Tixier, P. Tristant, J. Desmaison, and P. Leprince. Atmospheric pressure plasmas: A review. *Spectrochimica Acta Part B*, 61:2 – 30, 2006.

[183] N Gherardi, G Gouda, E Gat, A Ricard, and F Massines. Transition from glow silent discharge to micro-discharges in nitrogen gas. *Plasma Sources Science and Technology*, 9:340–346, 2000.

[184] A. Fridman and L. A. Kennedy. *Plasma Physics and Engineering*. Taylor and Francis, 2004.

[185] U. Kogelschatz. Filamentary, Patterned, and Diffuse Barrier Discharges. *IEEE Transactions on Plasma Science*, 30:1400 – 1408, 2002.

[186] Y. Kim, M. S. Cha, W-H. Shin, and Y-H. Song. Characteristics of Dielectric Barrier Glow Discharges with a Low-Frequency Generator in Nitrogen. *Journal of the Korean Physical Society*, 43:732–727, 2003.

[187] Y. H. Choi, J. H. Kim, and Y. S. Hwang. One-dimensional discharge simulation of nitrogen DBD atmospheric pressure plasma. *Thin Solid Films*, 506 - 507:389–395, 2006.

[188] U. Kogelschatz. Dielectric-barrier Discharges: Their History, Discharge Physics, and Industrial Applications. *Plasma Chemistry and Plasma Processing*, 23(1):1–46, March 2003.

[189] F. Massines, A. Rabehi, P. Decomps, R. B. Gadri, P. Segur, and C. Mayoux. Experimental and theoretical study of a glow discharge at atmospheric pressure controlled by dielectric barrier. *Journal of Applied Physics*, 83:2950 – 2957, 1998.

[190] Y. Honda, F. Tichikubo, and S. Uchida. Initial Growth Process of Barrier Discharge in Atmospheric Pressure Helium for Glow Discharge Formation. *Japanese Journal of Applied Physics*, 41:1256–1258, 2002.

[191] G. Nersisyan, T. Morrow, and W. G. Graham. Measurements of helium metastable density in an atmospheric pressure glow discharge. *Applied Physics Letters*, 85:1487 – 1489, 2004.

[192] A. Sublet, C. Ding, J-L. Dorier, Ch. Hollenstein, P. Fayet, and F. Coursimault. Atmospheric and sub-atmospheric dielectric barrier dissipated in helium and nitrogen. *Plasma Sources Science and Technology*, 15:627 – 634, 2006.

[193] F. Massines, P. Segur, N. Gherardi, C. Khamphan, and A. Ricard. Physics and chemistry in a glow dielectric barrier discharge at atmospheric pressure: diagnostics and modelling. *Surface and Coatings Technology*, 174 - 175:8 – 14, 2003.

[194] E. Aldea, P. Peeters, H. De Vries, and M. C. M. Van De Sanden. Atmospheric glow stabilization. Do we need pre-ionization? *Surface and Coatings Technology*, 200:46 – 50, 2005.

[195] V. Hopfe and D. W. Sheel. Atmospheric-Pressure Plasmas for Wide-Area Thin-Film Deposition and Etching. *Plasma Processes and Polymers*, 4:253–265, 2007.

[196] Yu. B. Golubovskii, V. A. Maiorov, J. Behnke, and J. F. Behnke. Modelling of the homogeneous barrier discharge in helium at atmospheric pressure. *Journal of Physics D: Applied Physics*, 36:39–49, 2003.

[197] X. T. Deng and M. G. Kong. Frequency Range of Stable Dielectric-Barrier Discharges in Atmospheric He and N_2. *IEEE Transactions on Plasma Science*, 32:1709 – 1715, 2004.

[198] S. Okazaki, M. Kogoma, M. Uehara, and Y. Kimura. Appearance of stable glow discharge in air, argon, oxygen and nitrogen at atmospheric pressure using a 50 Hz source. *Journal of Physics D: Applied Physics*, 26:889 – 892, 1993.

[199] J. R. Roth, S. Nourgostar, and T. A. Bonds. The One Atmosphere Uniform Glow Discharge Plasma (OAUGDP) - A Platform Technology for the 21st Century. *IEEE Transactions on Plasma Science*, 35:233 – 250, 2007.

[200] I. Enache, N. Naude, J. P. Cambronne, N. Gherardi, and F. Massines. Electrical model of the atmospheric pressure glow discharge (APGD) in helium. *The European Physical Journal Applied Physics*, 33:15 – 21, 2006.

[201] N. Gherardi and F. Massines. Mechanisms Controlling the Transition from Glow Silent Discharge to Streamer Discharge in Nitrogen. *IEEE Transactions on Plasma Science*, 29:536 – 544, 2001.

[202] N. Naude, J-P. Cambronne, N. Gherardi, and F. Massines. Electrical model of an atmospheric pressure Townsend-like discharge (APTD). *The European Physical Journal Applied Physics*, 29:173 – 180, 2005.

[203] E. Schrödinger. An undulatory theory of the mechanics of atoms and molecules. *Physical Review*, 28:1049–1070, 1926.

[204] G. Herzberg. Molecular electronic spectra. *Annual Reviews in Physical Chemistry*, 9:315 – 338, 1958.

[205] J. Cooper. Plasma spectroscopy. *Reports on Progress in Physics*, 29:35 – 130, 1966.

[206] A. Thorne. *Spectrophysics*. Chapman and Hall, 1974.

[207] S Förster, C Mohr, and W Viöl. Investigations of an atmospheric pressure plasma jet by optical emission spectroscopy. *Surface and Coatings Technology*, 200:827–830, 2005.

[208] H. R. Griem, M. Baranger, A. C. Kolb, and G. Oertel. Stark Broadening of Neutral Helium Lines in a Plasma. *Physical Review*, 125:177 – 195, 1962.

[209] G. Herzberg. *Infrared and Raman Spectra*. D. Van Nostrond Company, 1945.

[210] P. R. Griffiths and J. A. de Haseth. *Fourier Transform Infrared Spectrometry*. Wiley-Interscience, second edition, 2007.

[211] S. W. Sharpe, T. J. Johnson, R. L. Sams, P. M. Chu, G. C. Rhoderick, and P. A. Johnson. Gas-Phase Databases for Quantitative Infrared Spectroscopy. *Applied Spectroscopy*, 58:1452 – 1461, 2004.

[212] P. Atkins and J. de Paulo. *Atkins' Physical Chemistry*. Oxford University Press, 2002.

[213] C. R. Webster, R. T. Menzies, and E. D. Hinkley. *Laser Remote Chemical Analysis*, chapter 3: Infrared Laser Absorption: Theory and Applications, pages 163–272. John Wiley and Sons, 1988.

[214] L. S. Rothman, D. Jacquemart, A. Barbe, D. Chris Benner, M. Birk, L. R. Brown, M. R. Carleer, C. Chackerian Jr., K. Chance, L. H. Coudert, V. Dana, V. M. Devi, J.-M. Flaud, R. R. Gamache, A. Goldman, J.-M. Hartmann, K. W. Jucks, A. G. Maki, J.-Y. Mandin, S. T. Massie, J. Orphal, A. Perrin, C. P. Rinsland, M.A.H. Smith, J. Tennyson, R. N. Tolchenov, R. A. Toth, J. Vander Auweraf, P. Varanasi, and G. Wagner. The HITRAN 2004 molecular spectroscopic database. *Journal of Quantitative Spectroscopy & Radiative Transfer*, 96:139 – 204, 2005.

[215] F. Mandl. *Statistical Physics*. John Wiley and Sons, 1995.

[216] S. R. Drayson. Rapid computation of the Voigt profile. *Journal of Quantitative Spectroscopy and Radiative Transfer*, 16:611 – 614, 1976.

[217] J. Humlicek. An efficient method for evaluation of the complex probability function: The voigt function and its derivatives. *Journal of Quantitative Spectroscopy and Radiative Transfer*, 21:309 – 313, 1979.

[218] J. Humlicek. Optimized computation of the voigt and complex probability functions. *Journal of Quantitative Spectroscopy and Radiative Transfer*, 27:437 – 444, 1982.

[219] R. J. Noll and A. Pires. A New Nonlinear Least Square Algorithm for Voigt Spectral Lines. *Applied Spectroscopy*, 34:351 – 360, 1980.

[220] W. H. Press, S. A. Teukolsky, W. T. Vetterling, and B. P. Flannery. *Numerical Recipes: The Art of Scientific Computing*. Cambridge University Press, 2007.

[221] D. W. Marquardt. An Algorithm for Least-Squares Estimation of Nonlinear Parameters. *Journal of the Society of Industrial and Applied Mathematics*, 11:431–441, 1963.

[222] J. Hecht. *The Laser Guidebook*. TAB Books, 2nd edition, 1992.

[223] J. P. Gordon, H. J. Zeiger, and C. H. Townes. The MaserNew Type of Microwave Amplifier, Frequency Standard, and Spectrometer. *Physical Review*, 99:1264–1274, 1955.

[224] A. L. Schawlow and C. H. Townes. Infrared and optical masers. *Physical Review*, 112:1940–1949, 1958.

[225] A. Einstein. Zur Quantentheorie der Strahlung. *Physikalische Zeitschrift*, 18:121–128, 1917.

[226] A. W. Mantz. A review of spectroscopic applications of tunable semiconductor lasers. *Spectrochimica Acta Part A*, 51:2211 – 2236, 1995.

[227] T. Bao, P. W. Morrison Jr, and W. A. Woyczynski. Parametric optimisation of microhardness of diamond-like carbon films prepared by plasma enhanced chemical vapor deposition. *Thin Solid Films*, 485:27 – 41, 2005.

[228] T.-C. Wei and C.-H. Liu. Evaluation of plasma deposited fluorocarbon films using experimental design methodology. *Surface and Coatings Technology*, 200:2214–2222, 2005.

[229] N. Gomathi, C. Eswaraiah, and S. Neogi. Surface modification of polycarbonate by radio-frequency plasma and optimization of the process variables with response surface methodology. *Journal of Applied Polymer Science*, 114:1557–1566, 2009.

[230] K. D. Allen and H. H. Sawin. The Plasma Etching of Polysilicon with CF_3Cl/Argon Discharges. *Journal of the Electrochemical Society*, 133:2315, 1986.

[231] P. Klimecky, C. Garvin, C. G. Galarza, B. S. Stutzman, P. P. Khargonekar, and F. L. Terry. Real-Time Reactive Ion Etch Metrology Techniques to Enable *In Situ* Response Surface Process Characterization. *Journal of the Electrochemical Society*, 148:C34–C40, 2001.

[232] P. Simeonova, S. Tsakovski, P. Mandjukov, V. Simeonov, and V. Lovchinov. High-temperature superconducting thin films: A multivariate statistical approach. *Microchimicta Acta*, 124:151–165, 1996.

[233] H. M. Walker. Degrees of freedom. *Journal of Educational Psychology*, 31:253–269, 1940.

[234] I. J. Good. What are Degrees of Freedom? *The American Statistician*, 27:227–228, 1973.

[235] D. C. Montgomery. *Design and Analysis of Experiments*. John Wiley and Sons, 2001.

[236] R. G. Brereton. *Chemometrics: Data Analysis for the Laboratory and Chemical Plant*. John Wiley and Sons, 2003.

[237] D. Sawtell, P. A. Martin, and D. W. Sheel. Enhanced AP-PE-CVD Process Understanding and Control by Application of Integrated Optical, Electrical and Modelling Diagnostics. *Plasma Processes and Polymers*, 6:S637S642, 2009.

[238] B.G.M. Vandeginste, C. Sielhorst, and M. Gerritsen. The NIPALS algorithm for the calculation of the principal components of a matrix. *TrAC Trends in Analytical Chemistry*, 7:286–287, 1988.

[239] Paul Gemperline, editor. *Practical guide to chemometrics*. Taylor and Francis, 2006.

[240] D. Sawtell, V.L. Kasyutich, R.J. Holdsworth, D. W Sheel, and P. A. Martin. 2D Species Concentration Mapping of Thermal AP-CVD Reactors for Monitoring, Control and Design. *ECS Transactions*, 25:501–506, 2009.

[241] M. Batzill and U. Diebold. The surface and materials science of tin oxide. *Progress in Surface Science*, 79:47 – 154, 2005.

[242] E. A. G. Hamers, M. N. van den Donker, B. Stannowski, R. Schlatmann, and G. J. Jongerden. Helianthos: Roll-to-Roll Deposition of Flexible Solar Cell Modules. *Plasma Processes and Polymers*, 4:275–281, 2007.

[243] S. Suh, Z. Zhang, W-K. Chu, and D. M. Hoffman. Atmospheric-pressure chemical vapor deposition of flourine-doped tin oxide thin films. *Thin Solid Films*, 345:240–243, 1999.

[244] S. C. Ray, M. K. Karanjai, and D. Dasgupta. Preparation and study of doped and undoped tin dioxide films by the open air chemical vapour deposition technique. *Thin Solid Films*, 307:221–227, 1997.

[245] G. R. Alcott, T. A. M. B. van Mol, and K. C. I. M. A. Spee. Evaluation of Chemometric Models in an FTIR Study of the Gas Phase During Atmospheric-Pressure CVD of Tin Oxide Thin Films. *Chemical Vapor Deposition*, 6:261 – 268, 2000.

[246] J. J. Robbins, R. T. Alexander, W. Xiao, T. L. Vincent, and C. A. Wolden. An investigation of tin oxide plasma-enhanced chemical vapor deposition using optical emission spectroscopy. *Thin Solid Films*, 406:145 – 150, 2002.

[247] A. Al-Kaoud, T. Wen, A. Gilmore, V. Kaydanov, T. R. Ohno, C. Wolden, L. Feng, and J. Xi. Atmospheric pressure chemical vapor deposition of SnO_2: Processing and properties. *AIP Conference Proceedings*, 462:212–217, 1999.

[248] R. G. Dhere, H. R. Moutinho, S. Asher, D. Young, X. L, R. Ribelin, and T. Gessert. Characterization of SnO_2 films prepared using tin tetrachloride and tetra methyl tin precursors. *AIP Conference Proceedings*, 462:242–247, 1999.

[249] C. Morales, H. Juarez, T. Diaz, Y. Matsumoto, E. Rosendo, G. Garcia, M. Rubin, F. Mora, M. Pacio, and A. Garca. Low temperature SnO_2 films deposited by APCVD. *Microelectronics Journal*, 568:588, 2008.

[250] T. C. Xenidou, A. G. Boudouvis, D. M. Tsamakis, and N. C. Markatos. An experimentally assisted computational analysis of tin oxide deposition in a cold-wall apcvd reactor. *Journal of the Electrochemical Society*, 151:C757–C764, 2004.

[251] A. G. Zawadzki, C. J. Giunta, and R. G. Gordon. Kinetic modeling of the chemical vapor deposition of tin oxide from tetramethyltin and oxygen. *The Journal of Physical Chemistry B*, 96:5364–5379, 1992.

[252] C. J. Giunta, D. A. Stricker, and R. G. Gordon. Kinetic Modelling of the Chemical Vapor Deposition of Tin Oxide from Dimethyltin Dichloride and Oxygen. *Journal of Physical Chemistry*, 97:2275 – 2283, 1993.

[253] Y. Chae, W. G. Houf, A. H. McDaniel, J. Troup, and M. D. Allendorf. Stagnation Flow Reactor Investigation of Tin Oxide CVD from Monobutyltin Trichloride. *Journal of the Electrochemical Society*, 151:C527–C534, 2004.

[254] R. Y. Korotkov, P. Ricou, and A. J. E. Farran. Preferred orientations in polycrystalline SnO_2 films grown by atmospheric pressure chemical vapor deposition. *Thin Solid Films*, 502:79–87, 2006.

[255] D. Russo, C. McKown, C. Roger, J. Brotzman, and J. Stricker. The influence of film composition on the optical and thermal properties of solar control coatings. *Thin Solid Films*, 398:65–70, 2001.

[256] J.-F. Huang, Y.-F. Lee, and L.-S. Lee. Vapor-Liquid Equilibrium Measurements for Tetraethyl Orthosilicate and Ethanol at 24.00 kPa and 53.32 kPa. *Journal of Chemical and Engineering Data*, 49:11751179, 2004.

[257] A. M. B. van Mol, J. P. A. M. Driessen, J. L. Linden, M. H. J. M. de Croon, C. I. M. A. Spee, and J. C. Schoute. Vapor Pressures of Precursors for the CVD of Titanium Nitride and Tin Oxide. *Chemical Vapor Deposition*, 7:101–104, 2001.

[258] T. Rugină and L. Săcărescu. Isobaric Vapor-Liquid Equilibria for the Binary Systems CH_3SiHCl_2 with $(CH_3)_3SiHCl$, $(CH_3)_2SiHCl_2$, CH_3SiHCl_3, or $SiCl_4$. *Journal of Chemical Engineering Data*, 37:143 – 145, 1992.

[259] P. Wright, N. Terzijaa, J. L. Davidson, S. Garcia-Castillo, C. Garcia-Stewart, S. Pegrum, S. Colbourne, P. Turner, S. D. Crossley, T. Litt, S. Murray, K. B. Ozanyan, and H. McCann. High-speed chemical species tomography in a multi-cylinder automotive engine. *Chemical Engineering Journal*, 158:2–10, 2010.

[260] D. Sawtell, D. W Sheel, and P. A. Martin. The Application of Advanced Spectroscopic Diagnostics with Chemometric Modelling to Optimise Thin Film Properties Grown by Atmospheric Pressure PECVD. *ECS Transactions*, 25:491–499, 2009.

[261] D. A. DeCrosta, J. J. Hackenberg, and J. H. Linn. Characterization of High Oxygen:Tetraethylorthosilicate Ratio Plasma-Enhanced Chemical Vapor Deposited Films. *Journal of the Electrochemical Society*, 143:1079 – 1084, 1996.

[262] S S Han, M Ceiler, A Bidstrup, and P Kohl. Modeling the Properties of PECVD Silicon Dioxide Films Using Optimized Back-Propagation Neural Networks. *IEEE*

Transactions on Components, Packaging, and Manufacturing Technology - Part A, 17(2):174–182, June 1994.

[263] A. Pfuch, A. Heft, R. Weidl, and K. Lang. Characterization of SiO2 thin films prepared by plasma-activated chemical vapour deposition. *Surface and Coatings Technology*, 201:189 – 196, 2006.

[264] I. T. Emesh, G. D'Asti, J. S. Mercier, and P. Leung. Plasma-Enhanced Chemical Vapor Deposition of Silicon Dioxide Using Tetraethylorthosilicate (TEOS). *Journal of the Electrochemical Society*, 136:3404 – 3408, 1989.

[265] M. E. Coltrin, P. Ho, H. K. Moffat, and R. J. Buss. Chemical kinetics in chemical vapour deposition: growth of silicon dioxide from tetraethoxysilane (TEOS). *Thin Solid Films*, 365:251 – 263, 2000.

[266] L. D. Flores and J. E. Crowell. Boundary Layer Chemistry Probed by in Situ Infrared Spectroscopy during SiO_2 Deposition at Atmospheric Pressure from Tetraethylorthosilicate and Ozone. *Journal of Physical Chemistry B*, 109:16544 – 16553, 2005.

[267] N. Hirashita, S. Tokitoh, and H. Uchida. Thermal Desorption and Infrared Studies of Plasma-Enhanced Chemical Vapor Deposited SiO Films with Tetraethylorthosilicate. *Japanese Journal of Applied Physics*, 32:1787 – 1793, 1993.

[268] M. T. Kim. Deposition kinetics of silicon dioxide from tetraethylorthosilicate by PECVD. *Thin Solid Films*, 360:60 – 68, 2000.

[269] T. Mori, K. Tanaka, T. Inomata, A. Takeda, and M. Kogoma. Development of silica coating methods for powdered pigments with atmospheric pressure glow plasma. *Thin Solid Films*, 316:89 – 92, 1998.

[270] D. Pech, P. Steyer, A.-S. Loir, J. C. Snchez-Lpez, and J.-P. Millet. Analysis of the corrosion protective ability of PACVD silica-based coatings deposited on steel. *Surface and Coatings Technology*, 201:347 – 352, 2006.

[271] G. B. Raupp and T. S. Cale. The role of oxygen excitation and loss in plasma-enhanced deposition of silicon dioxide from tetraethylorthosilicate. *Journal of Vacuum Science and Technology B*, 10:37 – 45, 1992.

[272] P. J. Stout and M. J. Kushner. Monte Carlo simulation of surface kinetics during plasma enhanced chemical vapor deposition of SiO_2 using oxygen/tetraethoxysilane chemistry. *Journal of Vacuum Science and Technology A*, 11:2562 – 2571, 1993.

[273] I. Enache, H. Caquineau, N. Gherardi, T. Paulmier, L. Maechler, and F. Massines. Transport Phenomena in an Atmospheric-Pressure Townsend Discharge Fed by N_2/N_2O/HMDSO Mixtures. *Plasma Processes and Polymers*, 4:806–814, 2007.

[274] M. T. Kim. Deposition behaviour of hexamethyldisiloxane films based on the FTIR analysis of Si-O-Si and $SiCH_3$ bonds. *Thin Solid Films*, 311:157 – 163, 1997.

[275] F. Fracassi, R. d'Agostino, F. Fanelli, A. Fornelli, and F. Palumbo. GC-MS Investigation of Hexamethyldisiloxane-Oxygen Fed Plasmas. *Plasmas and Polymers*, 8:259 – 269, 2003.

[276] A. Milella, F. Palumbo, J. L. Delattre, F. Fracassi, and R. d'Agostino. Deposition and Characterization of Dielectric Thin Films from Allylmethylsilane Glow Discharges. *Plasma Processes and Polymers*, 4:425 – 432, 2007.

[277] A. Milella, J. L. Delattre, F. Palumbo, F. Fracassi, and R. d'Agostino. From Low-*k* to Ultralow-*k* Thin-Film Deposition by Organosilicon Glow Discharges. *Journal of the Electrochemical Society*, 153:F106 – F114, 2006.

[278] A. Yanguas-Gil, A. Barranco, J. Cotrino, P. Groning, and A. R. Gonzalez-Elipe. Plasma Characterization of Oxygen-Tetramethylsilane Mixtures for the Plasma-Enhanced CVD of $SiO_xC_yH_z$ Thin Films. *Chemical Vapor Deposition*, 12:728 – 735, 2006.

[279] F. Siffer, A. Ponche, P. Fioux, J. Schultz, and V. Roucoules. A chemometric investigation of the effect of the process parameters during maleic anhydride pulsed plasma polymerization. *Analytica Chimica Acta*, 539:289 – 299, 2005.

[280] A. Qayyum, S. Zeb, M. A. Naveed, S. A. Ghauri, and M. Zakaullah. Diagnostics of nitrogen plasma by trace rare-gas-optical emission spectroscopy. *Journal of Applied Physics*, 89:103303, 2005.

[281] G. Socrates. *Infrared Characteristic Group Frequencies: Tables and Charts*. John Wiley and Sons, 1994.

[282] S. Romet, M. F. Couturier, and T. K. Whidden. Modeling of Silicon Dioxide Chemical Vapour Deposition from Tetraethoxysilane and Ozone. *Journal of the Electrochemical Society*, 148:G82 – G90, 2001.

[283] A. Goullet, C. Charles, P. Garcia, and G. Turban. Quantitative infrared analysis of the stretching peak of SiO_2 films deposited from tetraethoxysilane plasmas. *Journal of Applied Physics*, 74:6876– 6882, 1993.

[284] S A Nair, T Nozaki, and K Okazaki. In Situ Fourier Transform Infrared (FTIR) Study of Nonthermal-Plasma-Assisted Methane Oxidative Conversion. *Industrial and Engineering Chemistry Research*, 46:3486 – 3496, 2007.

[285] T. de los Arcos, M. Castillo, C. Domingo, V. J. Herrero, M. M. Sanz, and I. Tanarr. Fast Processes in a N_2O-Modulated Hollow Cathode Discharge: Excitation and Diffusion. *The Journal of Physical Chemistry A*, 104:8183–8193, 2000.

Appendix A

Raw Data

This appendix presents the raw data used for the chemometric models presented in chapters seven and eight. The experimental plan for both experiments is presented in table A.1.

Number	Voltage$_{pk-pk}$	TEOS:O2	Frequency
	x_1	x_2	x3
1	-1	-1	-1
2	0	0	0
3	0	-1	0
4	1	1	1
5	-1	1	1
6	1	1	-1
7	-1	1	-1
8	0	0	0
9	1	-1	1
10	0	0	0
11	0	0	1
12	1	0	0
13	0	0	-1
14	1	-1	-1
15	0	0	0
16	-1	-1	1
17	-1	0	0
18	0	0	0
19	0	1	0
20	0	0	0

Table A.1: Experimental plan followed in chapters eight and nine.

Experiment	Excitation Temperature / K	TEOS decomposition / %	Acetaldehyde / ppm	CO / ppm	CO_2 / ppm	N_2O / ppm
Error	± 300	± 7.5	± 88	± 52	± 18.5	± 2.5
1	1500	81	130	12	12	0
2	2400	80	277	137	73	7
3	1800	80	267	135	41	4
4	4600	95	133	238	108	19
5	4900	75	233	284	66	4
6	5600	77	240	201	52	10
7	4500	60	324	110	21	3
8	2900	82	211	56	55	6
9	2000	78	112	130	62	7
10	2500	74	253	159	64	11
11	2000	78	258	155	84	11
12	2100	74	302	130	58	7
13	2300	59	337	106	40	6
14	2000	73	220	92	32	4
15	2900	89	101	150	92	10
16	1800	66	217	107	37	2
17	2100	67	309	74	28	3
18	2600	77	218	121	68	8
19	4400	77	187	241	81	13
20	2300	-	-	-	-	-

Table A.2: Spectroscopic results for the TEOS chemometric experiments.

Experiment	Power / watts	Phase shift / degrees
Error	$\pm$ 17.5	$\pm$ 1.4
1	21	83.9
2	59	69.3
3	56	68.0
4	446	20.3
5	139	19.3
6	60	83.0
7	24	83.7
8	51	70.0
9	580	18.0
10	57	69.0
11	357	18.0
12	53	70.0
13	40	83.5
14	59	83.1
15	86	67.3
16	216	16.3
17	31	73.6
18	51	70.1
19	51	71.3
20	54	69.5

Table A.3: Electrical results for the TEOS chemometric experiments.

Experiment	Growth rate / nm min^{-1}	Mohs Hardness	Absolute Hardness	Refractive index	Contact Angle / degrees
Error	$\pm$ 2.0	$\pm$ 1.1	$\pm$ 15	$\pm$ 0.03	$\pm$ 3.5
1	15.7	4.8	36	1.51	33
2	24.4	3.4	13	1.47	31
3	28.5	3.7	17	1.49	30
4	27.2	3.6	15	1.54	30
5	21.7	4.4	28	1.57	23
6	25.7	2.7	6	1.42	26
7	18.5	2.6	6	1.50	23
8	23.4	4.1	22	1.49	29
9	34.9	2.4	5	1.50	27
10	23.9	2.6	6	1.50	29
11	30.9	2.9	8	1.51	29
12	30.4	4.8	36	1.38	22
13	13.6	3.0	9	1.53	25
14	25.3	5.3	49	1.53	20
15	27.4	4.8	36	1.48	28
16	25.2	3.0	9	1.56	20
17	18.8	2.4	5	1.48	30
18	24.8	3.8	18	1.44	25
19	43.3	2.8	7	1.44	36
20	24.1	4.1	22	1.45	32

Table A.4: Thin film results for the TEOS chemometric experiments.

Experiment	Excitation Temperature / K	DDS decomposition / %	Formic Acid / ppm	CO / ppm	CO_2 / ppm	HCl / ppm	HCl *in situ* / ppm
Error	± 750	± 4.5	± 6	± 19	± 3	± 75	± 950
1	2800	47	56	192	15	373	4400
2	3300	54	131	235	45	482	6700
3	2500	51	89	241	29	473	6900
4	13800	55	180	252	58	343	9200
5	4800	40	98	271	25	563	4800
6	8600	53	114	279	45	464	3600
7	6000	20	69	230	14	536	3400
8	3300	55	124	234	45	616	5000
9	2500	48	115	240	59	401	5300
10	2900	50	112	232	43	536	6800
11	2400	48	48	201	28	350	5500
12	5000	64	153	264	81	603	7200
13	2200	26	80	179	25	400	4600
14	2700	41	103	220	39	334	4000
15	4200	50	123	249	48	493	5700
16	2300	36	64	191	23	367	6000
17	3000	35	92	234	25	628	5000
18	3600	48	121	212	49	456	4900
19	7500	45	132	277	44	491	3500
20	2600	46	119	228	42	498	6600

Table A.5: Spectroscopic results for the DDS chemometric experiments.

Experiment	Power / watts	Phase shift / degrees
Error	$\pm$ 12.5	$\pm$ 3
1	30	39
2	121	39
3	115	33
4	241	36
5	79	37
6	97	35
7	32	41
8	146	37
9	216	37
10	144	35
11	118	40
12	164	36
13	58	38
14	78	39
15	135	32
16	84	34
17	81	34
18	124	38
19	118	36
20	132	35

Table A.6: Electrical results for the DDS chemometric experiments.

Experiment	Growth rate / nm min^{-1}	Mohs Hardness	Absolute Hardness	Refractive index	Contact Angle / degrees
Error	$\pm$ 11	$\pm$ 0.4	$\pm$ 9	$\pm$ 0.025	$\pm$ 4.5
1	35	2.4	35	1.22	74
2	96	2.7	96	1.17	63
3	126	2.4	126	1.20	59
4	112	4.6	112	1.23	52
5	107	2.7	107	1.27	67
6	56	3.1	56	1.12	59
7	19	4.4	19	1.19	76
8	91	3.2	91	1.20	57
9	120	2.8	120	1.20	49
10	77	3.2	77	1.21	65
11	117	3.4	117	1.20	51
12	126	3.6	126	1.09	51
13	29	4.0	29	1.23	2
14	73	3.3	73	1.22	68
15	79	3.5	79	1.18	62
16	87	3.0	87	1.26	61
17	46	2.8	46	1.18	57
18	73	3.5	73	1.15	59
19	60	3.2	60	1.15	46
20	78	3.4	78	1.15	62

Table A.7: Thin film results for the DDS chemometric experiments.